Characterisation of dye sensitised photovoltaic cells

Wijayantha, Kahagala Gamage Upul

Award date:
2001

Awarding institution:
University of Bath

CHARACTERISATION OF DYE SENSITISED PHOTOVOLTAIC CELLS

submitted by **Kahagala Gamage Upul Wijayantha**

for the degree of PhD

of the University of Bath

2001

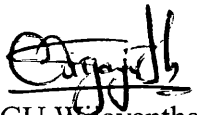

KGU Wijayantha

ProQuest LLC
789 East Eisenhower Parkway
P.O. Box 1346
Ann Arbor, MI 48106-1346

Dedicated to..

My parents

My Brothers and Sisters

My wife Nirmala and little son Sankha

University of Bath

Department of Chemistry

Doctor of Philosophy

CHARACTERISATION OF DYE SENSITISED PHOTOVOLTAIC CELLS

by

Kahagala Gamage Upul Wijayantha

ABSTRACT

Highly efficient dye sensitised nanocrystalline TiO_2 photovoltaic (DSN) cells were constructed. The generation, transport and recombination of electrons in the cells were studied by intensity modulated photocurrent and photovoltage spectroscopies (IMPS and IMVS), small amplitude laser pulse excitation and a novel charge extraction technique.

The electron lifetime τ_n and electron diffusion coefficient D_n of photoinjected electrons have been measured in DSN cells over 5 orders of magnitude of intensity using IMPS and IMVS. τ_n was found to be inversely proportional to the square root of the steady state light intensity, I_0, whereas D_n varied with $I_0^{0.68}$. The intensity dependence of D_n is attributed to trapping/detrapping involving a distribution of trapping levels. The square root intensity dependence of τ_n is interpreted as evidence that the back reaction of electrons with I^-_3 may be second order with respect to electron density. This is consistent with a back reaction mechanism involving the formation of $I_2^{\bullet-}$ as an intermediate. Since τ_n and D_n vary with intensity in opposite senses, the calculated electron diffusion length $L_n = (D_n \tau_n)^{1/2}$ falls by less than a factor of 5 when the intensity is reduced by 5 orders of magnitude. The incident photon to current efficiency (IPCE) is predicted to decrease by

less than 10% over the same range of intensity, and the experimental results agree well with this prediction.

τ_n and D_n have also been measured by small amplitude laser pulse excitation at different light intensities. Confirming the results obtained using frequency resolved techniques it was found that both D_n and τ_n are vary with light intensity ($D_n \propto j_{dc}^{0.068}$ and $\tau_n \propto j_{dc}^{-0.62}$).

The kinetics of the back reaction of electrons in DSN cells with I^-_3 ions were also studied by charge extraction technique. The analysis of the time dependence electron density measured by this technique further confirms that electron decay is second-order with electron concentration.

Several solid-state versions of DSN cells were constructed and characterised. It was found that even for dye sensitised solid-state cells both D_n and τ_n are intensity dependent parameters suggesting a trap dominant electron transport process and trap occupancy dependent interfacial electron transfer rate constant.

ACKNOWLEDGEMENTS

It is with great pleasure, that I express my deep gratitude to my supervisor Professor Laurence M. Peter for his guidance, encouragement, constructive advice and untiring assistance throughout the last three years. In fact, his great patience enabled me to cope with the strenuous task and made my work rewarding.

I wish to convey my sincere thanks to Dr. G.J.Price, Dr. D.J.Riley, and Dr.A.C.Fisher who were closely associated with my work. I would also like to make use of this opportunity to convey my appreciation and thanks to all present and past members in our research group, who were in some way associated with my work, Noel, Gamini, June, Gabriella, Ruilin, Khaled, Alice, Rachel, Dan, Shin, Nia, Fulian, Kamran, Kerry and Andy.

Special thanks are due to Prof. Laurie Peter, Dr. Noel Duffy and Dr.A.C. Fisher who carried out some measurements and most calculations presented in this thesis. I am also very grateful to Dr. M.Bailes not only for his continuous technical support, but also for spending his valuable time reading the draft of this thesis. Thanks are also due to Mrs. P.M.Croft for her kind assistance in many ways.

I wish to convey my sincere thanks to the Engineering and Physical Sciences Research Council (EPSRC) who provided me with the most important funding throughout the last three years. It will be a major failure if I do not mention the tremendous support given by all the academic and non-academic staff members of the Department of Chemistry, University of Bath.

I would like to thank Dr.R. Potter (Johnson Matthey Technology Center) and Prof.J.Utley (Queen Mary & Westfield College) for providing materials. Also special thanks to Dr.J.Riley (University of Bristol), Prof. W. Flavell and Mr.A.R.Kumarasinghe (UMIST) for performing the SEM and synchrotron AFM measurements on TiO_2 films. I also

appreciate the technical support given by Mr. Mike Lock, Mr. Les Steele and Mr. H.R.Perrott.

I wish to express my thanks to Prof. K.Tennakone, Prof. O.A.Illeperuma Prof. R.M.G. Rajapakse and Prof.R.N.Pathirana, Sri Lanka for their keen interest in my work.

Finally a big thanks should go to my loving wife Nirmala for her encouragement, great patience and for relieving me from most of my family work. I should also remember my son little Sankha who joined us dramatically at the very final stage of this work.

Glossary of symbols

E_F	Fermi Level
S	Ground Energy Level of the Sensitiser Dye
S*	Excited Energy Level of the Sensitiser Dye
S^+	Oxidised Dye Molecule
E_C	Conduction Band Energy
E_V	Valence Band Energy
U_{photo}	Open circuit voltage
η_{cell}	Overall power conversion efficiency
η	Efficiency of collecting electrons in the external circuit
ϕ	Quantum yield for net charge injection
q	Elementary Charge
${}_nE_F$	Electron quasi Fermi Level
E_{redox}	Nernst potential of the redox couple
Δn	the excess electron density generated by illumination
n_0	the equilibrium electron density (in dark)
i_{sc}	the short circuit photocurrent
ff	the fill factor
VB	Valance Band
CB	Conduction Band
T	charge trapping
R	charge recombination
ΔE	Energy difference between bonding and antibonding orbitals
$f(E)$	Fermi-Dirac probability distribution function
$(N(E_C))$	density of occupied states in the conduction band
$(N(E_V))$	density of occupied states in the valence band
N	number of electrons per unit volume
N_C	effective density of states in conduction band
N_V	effective density of states in valence band
Δp	excess hole density under illumination

p_0	hole density at equilibrium
${}_pE_F$	hole quasi Fermi level
E_{ox}	Energy level of oxidised species
E_{red}	Energy level of reduced species
λ	reorganisation energy
$E^{\theta}{}_{redox}$	the standard redox Fermi level
J_A	the diffusional flux of species A
D_A	the diffusion coefficient of species A
$d\phi/dx$	the electric field arising from the potential gradient
J_m	the migratory flux
u_C	the mobility of charged species C
${}_{SC}\bar{\mu}_e$	electrochemical potential of the semiconductor
${}_{redox}\bar{\mu}$	electrochemical potential of the redox electrolyte
μ_i	chemical potential of species i
Φ	inner Galvani potential
μ_i^{θ}	standard chemical potential of species i
a_i	activity of species i
O	oxidised species
R	reduced species
$[O]$	concentration of oxidised species
$[R]$	concentration of reduced species
$\Delta\Phi_{sol,SC}$	the electrical potential drop across the semiconductor/electrolyte interface
$\bar{\mu}_O$	electrochemical potential of the oxidised species
$\bar{\mu}_e$	electrochemical potential of electrons
$\bar{\mu}_R$	electrochemical potential of the reduced species
$\Delta\Phi^{\theta}{}_{sol,SC}$	the standard electrical potential drop across the semiconductor/electrolyte interface

W	width of the space charge layer
Ns	charge of the space charge layer
ε	relative permitivity
ε_0	permitivity of free space
N_d	doping density
$\Delta\phi_{SC}$	surface charge
C_{sc}	space charge layer capacitance
U_{FB}	flat band potential
$\Delta\phi_H$	potential drop across the Helmholtz layer
$\Delta\phi_G$	potential drop across the Gouy-Chapman layer
L	diffusion length
α	absorption coefficient
$1/\alpha$	light penetration depth
L_p	hole diffusion length
L_n	electron diffusion length
u_p	mobility of holes
τ_p	lifetime of holes
X	occupied interfacial bandgap states
X^+	unoccupied interfacial bandgap states
β_n	electron trapping rate
β_n	hole trapping rate
K_{ETtrap}	trapped hole transfer rate constant
K_{ETtrap}	free hole transfer rate constant
$p(o)$	concentration of free holes
$n(o)$	concentration of free electrons
r_B	Bohr radius
m*	the effective mass
L_D	the Debye length
r_0	radius of the semiconductor particle
d_H	diffuse layer thickness

G	volume injection rate
τ_n	the electron lifetime
I_0	incident photo flux
$n(x,t)$	distance and time dependent electron density under illumination
V	applied voltage
ΔV	maximum amplitude of the input voltage
ω	angular frequency
ϕ	phase shift
i	$\sqrt{-1}$
Z	impedance
R	resistor
C	capacitor
Q	charge
I	current
Z_R	impedance of a resistor
Z_C	impedance of a capacitor
$\|Z\|$	magnitude of impedance
J_0	the exchange current density
η	overpotential
α	transfer coefficient
$I_0(EE)$	incident photon flux from electrolyte side
$I_0(SE)$	incident photon flux from substrate side
$I_T(EE)$	transmitted photon flux from electrolyte side
$I_T(SE)$	transmitted photon flux from substrate side
n_{free}	the density of free conduction band electrons
k_{trap}	first-order rate constant for electron trapping
k_{detrap}	first-order rate constant for electron detrapping
D_{eff}	effective diffusion coefficient
σ	the capture cross section
$v_{thermal}$	the thermal velocity of electrons

τ_{trap}	the lifetime for recombination of trapped electrons with tri-iodide
τ_{eff}	the effective electron lifetime
k_{ext}	charge extraction rate
ω_{min}	the angular frequency corresponding to the minimum in the complex plane
C_{cb}	conduction band capacitance
Q_{cb}	conduction band charge
C_t	surface states capacitance
Q_t	trapped charge
k_{dssp}	rate of disproportionation reaction of $I_2^{\bullet-}$
k_{et}	direct electron transfer rate from $I_2^{\bullet-}$
f_{min}	the frequency corresponding to the minimum in the complex plane
D_n	electron diffusion length
τ_n	the electron lifetime
$t_{1/2}$	the half lifetime
$\delta(t)$	delta function
d	film thickness
Q_{photo}	photo charge
t_d	delay time

Abbreviations

AM	Air Mass
PEC	Photoelectrochemical
IPCE	Incident Photon to Current Conversion Efficiency
SCE	Standard Calomel Electrode
UV	Ultra-violet
UV-Vis	Ultra-violet Visible
DSN	Dye sensitisd Nanocrystalline
IR	Infra red
MLCT	Metal to Ligand Charge Transfer
LUMO	Lower Unoccupied Molecular Orbital
HOMO	Highest Occupied Molecular Orbital
SCR	Space Charge Region
OHP	Outer Helmholtz Plane
QNR	Quasi Neutral Region
MBE	Molecular Beam Epitaxy
MOCVD	Metal-organic Chemical-vapour Deposition
HCM	Hole Conducting Media
IMPS	Intensity Modulated Photocurrent Spectroscopy
IMVS	Intensity Modulated Photovoltage Spectroscopy
EIS	Electrochemical Impedance Spectroscopy
SEM	Scanning Electron Microscopy
AFM	Atomic Force Microscopy
PPV	poly(p-phenylene vinylene)
PVK	poly(vinylcarbazole)
PANI	poly(aniline)
FRA	Frequency Response Analyser
LED	Light Emitting Diode
VMOS	V-Metal Oxide Semiconductor

DSO	Digital Storage Oscilloscope
QFL	Quasi Fermi Level

Index

Chapter 1

Introduction

1.1 Conversion of light into electricity

It has long been accepted that world demand for energy will increase steadily for the foreseeable future, but until now more intensive exploitation of conventional sources seemed able to provide an adequate supply. However, the situation has changed entirely. Non-renewable fuels need to be conserved and are ecologically unpopular; nuclear power presents social and political problems; renewable sources such as wind and tidal power still present technological difficulties. The earth receives from the sun more than 10 000 times the amount of energy required for man's activity. In these circumstances, direct conversion of sunlight into electricity is an attractive goal to pursue. In fact exploring solar energy is a very topical subject, not only because of the immense energy available but also because the sun is an environmentally clean energy supply.

The solar irradiance on earth depends on the so-called air mass, which is determined by atmospheric conditions. Relative quantities of water, ozone, oxygen, carbon dioxide and dust are the main factors effecting on air mass. The solar spectrum reaching the earth is defined as AMn where $n = 1/\cos\theta$. θ is the angle between the position of sun and zenith. Therefore, solar spectra are referred to as AM1, AM1.5, AM2, AM3 etc. The AM1.5 spectral solar irradiance corresponding to a sun-facing surface-titled 37^{o} from the horizontal is used as the standard and shown in Figure 1.1.

The total solar intensity can be obtained by integrating the whole AM1.5 spectrum and is ~ 96.4 mW/cm^2. An ideal solar energy conversion device should absorb the photon flux all the way up to a threshold wavelength of approximately 900 nm. Considerable efforts have been devoted to convert sunlight into electricity in the last three decades. Solid-state technology, applying semiconductors to absorb sunlight, has been spectacularly successful in achieving high efficiencies for conversion of light to electrical power. The

best known semiconductor, silicon, as used in microelectronics and transistors, has been used to fabricate solar cells with conversion efficiency approaching very high levels.

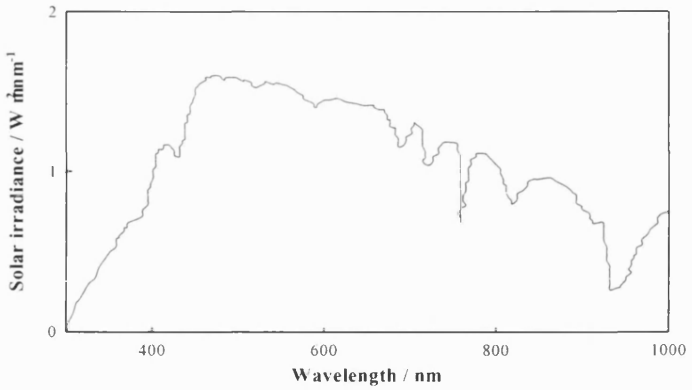

Figure 1.1 *AM1.5 solar spectrum*

[1, 2]. Taking into account energy losses before and during energy conversion, crystalline silicon solar cells exhibit a relatively high conversion efficiency of 24% on laboratory scale [2]. Today commercial solar cell panels and solar-powered devices are available in the market. Nearly all of the solar cell panels and solar power devices are fabricated using solar cells made from crystalline silicon wafers. Solar powered devices include anything from simple heat collectors for domestic water tanks, to solar-powered watches, calculators and buildings, multi-megawatt generators, space vehicles and satellites. However, the large scale use of silicon solar cells for electricity generation is prohibitively expensive at present mainly due to their economically intractable production cost; generation from existing commercial devices costs about ten times more than conventional methods. The best ever cell efficiency is held by a gallium arsenide-gallium antimonide cell made by the Boeing Company, which converts 33% of the sunlight it receives into electricity [3]. Although useful for powering space shuttle instruments and other 'hi-tech' applications, GaAs-GaSb is far too costly for most terrestrial applications. Therefore, the prospect of a new photovoltaic technology capable of challenging the established solid-state devices and using other semiconductors is of considerable interest.

1.2 The photoelectrochemical option

Photoelectrochemical energy conversion is a widely known option, continuing to receive much attention as an alternative method of harnessing sunlight [4-8]. Liquid junction or photoelectrochemical solar cells (PEC cells) are examples of this option.

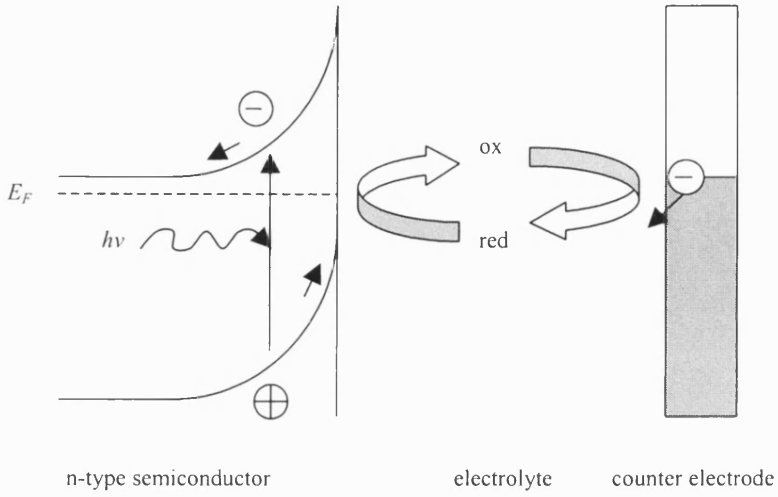

Figure 1.2 *An example of a photoelectrochemical (PEC) solar cell. An n-type semiconductor electrode is in contact with an electrolyte containing a redox couple.*

Several attractive features of PEC cells are:

(a). Easy fabrication.
(b). Feasibility of use of polycrystalline materials.
(c). Ability to form a space charge region spontaneously by contact with an electrolyte.

However, inherent problems such as photocorrosion had a negative impact on the advancement of PEC cells. Intensive research in this area has revealed that the most convenient way of circumventing photocorrosion is the fabrication of PEC cells using wide bandgap semiconductor materials [4]. Even though they are themselves insensitive

to the visible spectrum, the spectral response can be extended by employing a suitable light absorbing material such as organic molecular dyes and inorganic quantum sized low bandgap semiconductor particles [9, 10]. The process of extension of the spectral response by using an organic molecular dye is called 'dye-sensitisation'.

1.3 Dye sensitisation – the history

The phenomenon of dye-sensitisation of the semiconductor surface was first reported more than a century ago when Vogel made the important discovery that dye-coated silver halide grains sensitise the photographic film to the absorption spectrum of the dye [11]. The mechanism for the dye-sensitisation was first proposed by Gurney and Mott. The argument was that the process originates from an electron transfer by the excited dye molecule to the conduction band of the silver halide [12]. In 1968 Gerischer and Tributsch reported a dye-sensitised PEC cell that consists of a Rhodamine B sensitised ZnO electrode and a liquid electrolyte [4]. They found that the photocurrent action spectrum was identical with the absorption spectrum of the sensitiser dye. Confirming the Gurney and Mott argument, Gerischer and Tributsch extended the theory of the dye-sensitisation process. They argued that only a relatively weak interaction is needed for electron transport to occur between two distinguishable quantum states as electron injection takes place in a very short time scale (less than 10^{-13} sec). Furthermore they pointed out that under such circumstance the Frank-Condon principle could be applied in the electron transfer process [4, 6]. Matsumura and Tsubomura carried out a systematic study of dye-sensitisation for some n-type semiconductors (mainly ZnO) and dyes (Rose Bengal, Rhodamine B, cyanines etc.) in the late seventies [13, 14]. A number of studies have also been reported on dye-sensitisation of p-type semiconductor materials [15-18]. However, the conversion efficiencies of such assemblies were extremely low mainly due to the low light harvesting. The reported light-harvesting efficiencies were well below 1% and too low to be of practical interest. On a smooth surface, a monomolecular layer of sensitiser dye absorbs less than 1% of incident monochromatic light. Attempts to harvest more light by using multi-layer dye coverage have been unsuccessful, mainly because of the concentration quenching and electrical resistance of thick dye layers. Only

the first monolayer of adsorbed dye exhibits efficient charge injection into the semiconductor. The remaining option is to increase the roughness of the semiconductor surface so that a large number of dye molecules can be adsorbed onto the semiconductor surface, which directly contacts a liquid electrolyte solution that contains a redox shuttle. Memming and Tributsch observed a relatively high IPCE for a dye-sensitised rough GaP electrode [19]. Alonso *et al.* employed sintered ZnO electrodes in their dye-sensitised photovoltaic device [20]. Willig *et al.* reported high quantum yields for the dye-sensitisation of SnS_2 [21]. However, the global efficiency (under AM 1.5 solar illumination) remained still well below 1% for all these devices. The poor stability of the employed dyes was also a major problem in the above systems.

1.4 Grätzel's approach

In his early studies Grätzel has employed number of different sensitisers such as porphyrins [22], $Ru(bipy)^{2+}_3$ [23] and $Fe(CN)^{4-}_6$ [24] surface-derivatised TiO_2 particles and observed the sensitisation effect. Later in 1991, by using semiconductor films consisting of nanometer-sized TiO_2 particles, together with newly developed charge-transfer dyes, Grätzel and O'Regan attempted to increase the efficiency and stability of the PEC cell [25]. The prototype dye that was employed at that time by Grätzel was $RuL_2(\mu\text{-}(CN)Ru(CN)L'_2)_2$ where L is 2,2' bipyridine-4,4'-dicarboxylic acid and L' is 2,2'-bipyridine. In the nano-crystalline film, each TiO_2 nano-particle is covered with dye at a monolayer coverage. As the incident light intercepts many dye coated TiO_2 particles, the effective light absorption cross-section is increased, at the same time avoiding de-activation of excited dye molecules by mutual interactions (concentration quenching). Optical excitation of the adsorbed dye leads to injection of an electron from the excited dye to the conduction band of TiO_2. The oxidised dye is subsequently reduced back to its native state by an external donor (I^-) present in the electrolyte, and the resulting tri-iodide ions are reduced back to I^- at the Pt-coated counter electrode (see Fig 1.3). Since the presence of liquid electrolyte in the porous TiO_2 film limits the electrical field in the solid phase to small values, the collection of photo-injected electrons takes place by diffusion. This novel dye-sensitised nanocrystalline PEC cell which was fabricated by Grätzel and

co-workers, was a major breakthrough and recorded 7.9% overall power conversion efficiency with a remarkable stability sustaining at least five million turnovers without decomposition, which corresponds to 15 years of exposure to sunlight [25]. The discovery was widely recognised in the scientific community as the first solar energy conversion device operating on a molecular level that showed the stability and the efficiency that is required for potential practical applications [26].

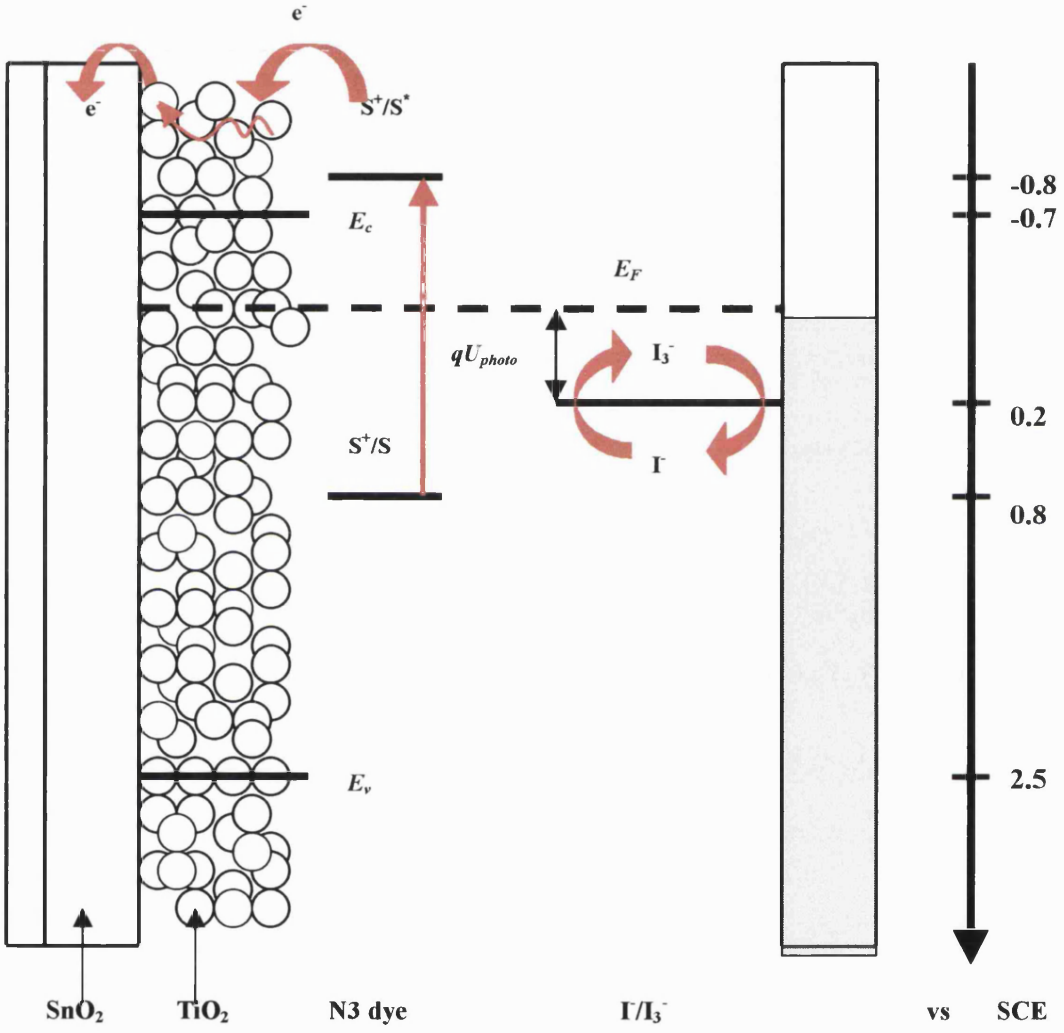

Figure 1.3 *Schematic diagram of a nanocrystalline dye-sensitised solar cell [16].*

1.4.1 Why titanium dioxide?

Titanium dioxide is a wide indirect band-gap n-type semiconductor material. It is transparent to visible light and absorbs light in the ultra-violet (UV) region (~ 370nm). It is polymorphous existing in three different structural modifications, rutile, anatase and brookite. Only the rutile and anatase modifications are of any note, technically or commercially. The most thermodynamically stable polymorph of TiO_2 is rutile, which crystallises in the tetragonal structure. As illustrated in Figure 1.4, each titanium atom is coordinated by six oxygen atoms at the corners forming a slightly distorted octahedral shape around the titanium with four shorter and two longer Ti-O bonds. The refractive index of rutile is second only to diamond hence it is widely used as a pigment for providing brightness, whiteness and opacity in products such as paints, coatings, plastics, papers, inks, fibers, foods and cosmetics [27].

The anatase form has a very similar tetragonal structure but with different packing (see Figure 1.4). It is less closely packed compared to rutile and this difference clearly explains the different densities. The density of anatase is about 3.89 g cm^{-3} whereas the density of rutile is about 4.26 g cm^{-3} [28]. This difference influences many electrical and optical properties.

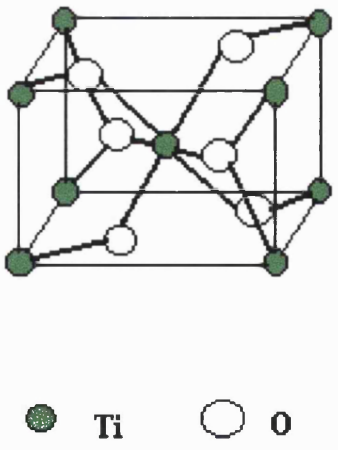

Figure 1.4(a) *The unit cell of rutile (TiO_2)*

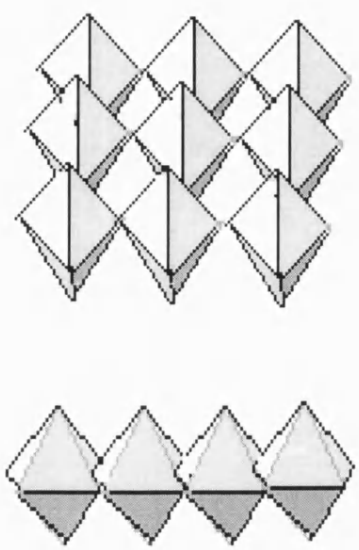

Figure 1.4(b) (***above***) *: Anatase polymorphous of TiO_2.* (***below***)*: Rutile form of TiO_2 Ti ions are in a distorted octahedral environment and formally have a Ti^{4+} ($3d^0$) electronic configuration.*

In the electronic band structure of TiO_2, the valence band is composed of oxygen $2p$ orbitals hybridised with titanium $3d$ orbitals, whereas the conduction band is composed of titanium $3d$ orbitals [28-32]. The crystal structures of rutile and anatase (see Figure 1.4) have been calculated by a number of methods [33-35]. However, experimental data that are comparable to the accurately calculated electronic band structures were not reported for a long time. The difficulty in the theoretical prediction of the properties of TiO_2 arises from the influence of traps originating from defects in the crystal structures of these oxides. However, later several works appeared using a tight-binding linear-combination of atomic orbitals Hamiltonian method and reported the bandgaps for both rutile and anatase more accurately [36, 37]. For rutile the bandgap is about 3.05 eV [36] and for anatase it is about 3.2 eV [37].

The optical and electrical properties of both anatase and rutile have been examined and strong photoluminescence at 500nm was found for anatase, but no emission from rutile. The luminescence is explained by the emission of self-trapped excitons localised on TiO_6-octahedra, demonstrating the importance of the local atomic structure in these metal oxides [38, 39]. It was found that oxygen vacancies leads to in-gap states at energy levels of 1-1.4 eV below the conduction band edge [40, 41]. These states and others resulting from defects and impurities in the TiO_2 lattice can explain absorption tails at the fundamental absorption edge, seen in the ultraviolet-visible (UV-Vis) transmission spectra for both anatase and rutile single crystals [38].

Despite the existence of in-gap energy states, defects and impurities, polycrystalline TiO_2 has been shown remarkable photo stability in organic and aqueous liquid electrolyte media [42, 43]. This contrasts to the observations of III-V and II-VI compounds, as they have exhibited readily photocorrosive and photooxidative properties in contact with aqueous or organic liquid [44, 45]. However, nanocrystalline thin-film TiO_2 electrodes have been shown very unusual properties in contact with liquid electrolytes. They have been recognised as functional subunits with a series of interesting properties such as high surface area, surface affinity to certain functional groups, semiconductor properties, conductivity and transparency [27]. Assuming that TiO_2 nanoparticles are in spherical shape, one can estimate the surface area to volume ratio in nanocrystalline electrode as follows. The total surface area of a 3-dimensional TiO_2 particle network with N number of particles is given by $4N\pi r^2$. The total volume, including inter-particle voids is $4N\pi r^3/3f$, where f is the packing fraction. Therefore, the surface area to volume ratio is $3f/r$. For the average particle size of 10 nm, it is of the order of 10^6 cm^{-1} (the packing fraction for a cubic-closed packed array is 74%). Therefore, a 1 cm^2 10 μm thick nanocrystalline electrode can have an internal surface area of 1000 cm^2. However, the active area could be less than the estimated value due to the inter-particle necking during sintering process as sintering required to guarantee adequate electrical contact. Upon modification of the surface with appropriate molecular components, these electrodes show the envisaged macroscopic function enhanced by the roughness factor. For

example, the absorbance of a nanocrystalline TiO_2 electrode surface-modified with a functional groups such as porphyrins [22], $Ru(bipy)^{2+}_3$ [23], corresponds to the absorbance of several hundred monolayers of them.

The main purpose of this sub-section is to describe the use of nanocrystalline anatase TiO_2 electrodes in dye-sensitised solar cells. Therefore, it would be worth discussing briefly the advantages and disadvantages of rutile form, as anatase is always contaminated with a certain degree of rutile form. It has been reported that the use of the rutile form of TiO_2 (which is photoactive at wavelengths of >400 nm) in nanocrystalline TiO_2 electrodes need to be strictly restricted in terms of getting maximum use of sensitiser organic dye and long-term stability of the cell [46]. The argument was any rutile particles in the semiconductor TiO_2 substrate get excited in the UV region creating electrons in the conduction band and leaving holes in the valence band. The photogenerated holes are strong oxidising agents and must be reduced by iodide ions in the electrolyte within a few picoseconds [47]. However, some holes in the valence band could lead to irreversible oxidation of the electrolyte and the organic sensitiser dye molecules. This has a deleterious effect on the long-term performance of the cell. The foundation for this argument was the absorption edge of the anatase form is blue shifted by 20 nm hence it gives enough security margin in this respect [48]. Nevertheless, one can argue that 20 nm is not a fairly enough security margin and therefore, the impact from rutile particles present in the TiO_2 film may not be very effective. In fact, studies have reported that successfully working DSN TiO_2 cells can also made with rutile form of TiO_2 films [49]. Some studies have also revealed that adding a very small amount of large rutile particles to the nanocrystalline anatase substrate increases the ability to scatter light [46]. The scattering of light increases the path length of the photons inside the TiO_2 electrode and, thus, increases the probability of light absorption by dye molecule [46, 48]. This is especially important in the red and near infra red (IR) region of the solar spectrum (wavelength ~ 700 - 800 nm), where the *cis*-$[Ru(dcbH_2)_2(NCS)_2]$ (N3) dye possesses relatively low absorption coefficient ($dcbH_2$ = 4,4'-dicarboxy-2,2'-bipyridine). (see the Fig 1.5 in the next section for the molecular structure and a typical absorption spectrum for the N3 dye)

1.4.2 Molecular sensitisers and the role of the N3 dye

As already described in section 1.2, sensitisers can be categorised into two main groups. They are organic molecular sensitisers [25, 27] and inorganic semiconductor quantum dot particles [9, 10, 50, 51]. The present study is focused only on the molecular dye-sensitised photovoltaic devices.

In principle, a molecular sensitiser consists of an anchoring group, a linker and a light absorber (chromophoric group). However, in reality, it is not possible to distinguish these functional groups in every molecular sensitiser except a few of them such as *cis*-$[Ru(dcbH_2)_2(NCS)_2]$ (N3 dye), tri (cyanato)-2,2'2''-terpyridyl-4,4',4''-tricarboxylate)Ru(II) (black dye). The cyclic process of the molecular sensitiser is as follows. Following excitation by an incoming photon ($S \rightarrow S^*$) the excited dye molecule injects an electron into the conduction band of the TiO_2. As a consequence the dye becomes oxidised ($S^* \rightarrow S^+$) and is regenerated by the reduced supersensitiser (see Fig. 1.3).

In order to be utilised in a dye-sensitised photovoltaic cell, the molecular sensitiser needs to fulfill the following requirements.

(a) efficient light absorption in the visible and near IR region. An ideal molecular sensitiser should absorb all the light of AM 1.5 sunlight below a threshold wavelength of approximately 920 nm (see section 1.1).
(b) an excited-state redox potential negative enough for electron injection into the conduction band of TiO_2.
(c) a ground-state redox potential as positive as possible, while satisfying (a) and (b).
(d) small reorganisational energy for excited and ground state redox processes, so as to minimise free energy losses in primary and secondary electron transfer steps .

(e) the rate of reduction of oxidised dye by semiconductor conduction band electrons should be much slower than the rate of reduction of oxidised dye by redox species in electrolyte, so that net electron injection efficiency from the dye is very high.
(f) stable oxidised state to minimise loss of dye by decomposition.
(g) the ability to anchor firmly on the TiO_2 surface.
(h) easy synthesis and low cost.

The sensitisation of TiO_2 with different types of molecules has been widely studied. Phthalocyanins [52, 53], coumarin [54], and xanthene [55] are examples. Natural pigment molecules, such as chlorophyll derivatives [56, 57], cyanin [58, 59], and cyanidin (cyanin without the sugar moiety) [60-62] have also been used to extend the spectral response of TiO_2. However, the reported incident photon-to-current conversion efficiencies for these systems are relatively low at the peak pigment absorption. The losses in photocurrent efficiency have been explained by giving two reasons. One is the increased dye aggregation on semiconductor film and the second reason is electron recapture by the electrolyte mediator, possibly involving intermediate trapping steps [58]. In addition to that the isolation of these natural pigment molecules from natural product samples involves very difficult steps.

The most efficient sensitiser dye molecules used so far are based on polypyridine complexes of d^6 metal ions, such as Ru(II), Os(II) and Re(I) exhibiting highly efficient metal to ligand charge transfer transitions in the visible region, leading to MLCT states [26]. So far, polypyridine complexes of Ru(II) have shown the best performance in the charge transfer process [63]. Sensitiser dye molecules of Ru(II) complexes, which contain carboxylate and phosphonate anchoring groups guarantee a tight electronic overlap between the lowest unoccupied molecular orbital (LUMO) of the dye molecule and the vacant *3d* orbitals of Ti(IV). This tight overlap results in efficient charge injection kinetics. The back reaction of the injected electron with an oxidised dye molecule involves a *d*-orbital localised on the ruthenium, and this orbital has a poor overlap with the wave function of the conduction band electrons. In addition to this poor overlap, the

orbitals on the ruthenium contract once an electron has been transferred from the dye to the TiO_2, making it even more difficult for the back reaction to occur. This leads to slow back reaction kinetics [64].

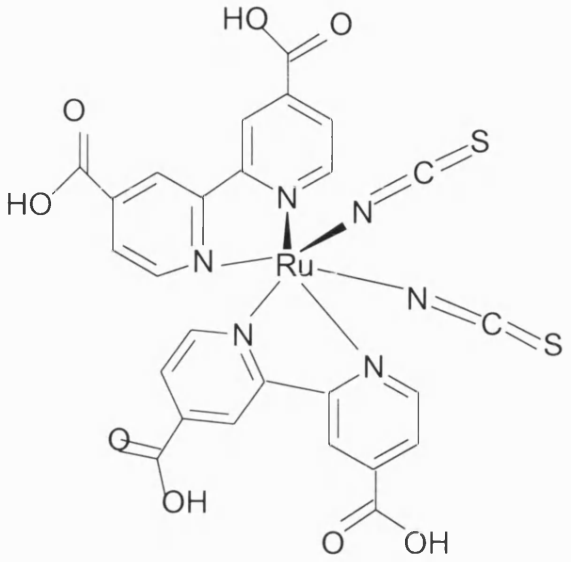

Figure 1.5a *Molecular structure of cis-[Ru(dcbH$_2$)$_2$(NCS)$_2$] (N3) dye.*

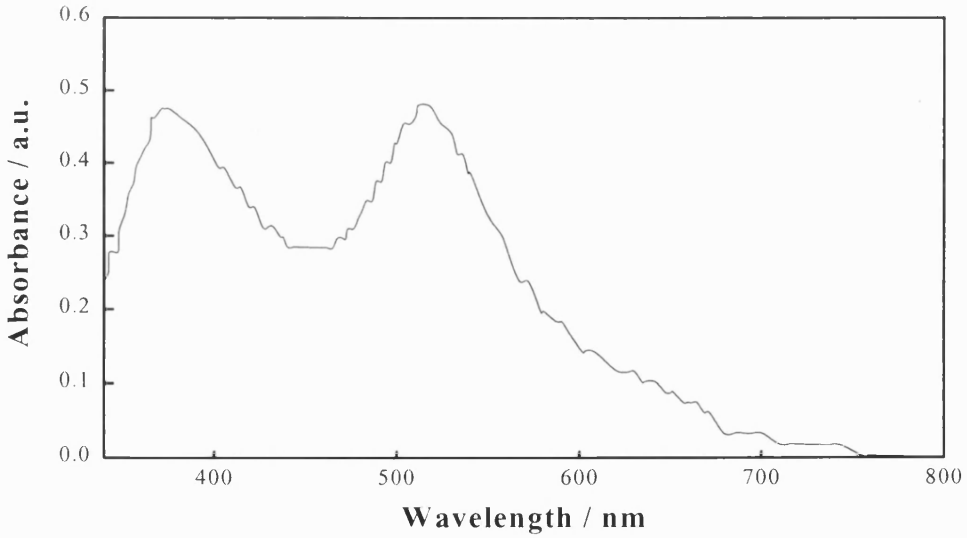

Figure 1.5b *A typical absorption spectrum cis-[Ru(dcbH$_2$)$_2$(NCS)$_2$] (N3) dye in ethanolic solution.*

The performance of the Ru(II) complex *cis*-[Ru(dcbH$_2$)$_2$(NCS)$_2$], known as N3 dye, in dye-sensitised nanocrystalline photovoltaic solar cells was found to be outstanding and unmatched by any other sensitiser [65, 66]. The fully protonated N3 has absorption maxima at 518 and 380 nm, the extinction coefficients being 1.3 and 1.33 x 10^4 $M^{-1}cm^{-1}$, respectively (see Figure 1.5b). The complex emits at 750 nm, the lifetime being 60 ns. The optical transition possesses typical MLCT character, and excitation of the N3 molecule involves transfer of an electron from the Ru(II) to the π^* orbital of the surface anchored carboxylated bipyridyl ligand, from where it is released within less than 50 femtoseconds into the *3d* orbital of Ti(IV) [67-71]. It has been reported that the sensitiser adsorbs onto the TiO_2 surface through two of the four carboxylate groups and at least one covalent link requires for the ultrafast charge injection [70, 72, 73]. Obviously the next interesting question is whether the transfer involves both bpy ligands, or whether it is localised on one. Work by McCusker shows that it is very difficult to establish the argument that the charge localised in only one bpy even though the reported ultrafast injection time scale is too rapid for sampling another ligand [73]. However, once MLCT and charge injection occurred, it is interesting to see how the sensitiser molecule resists the back electron transfer and promotes the regeneration. The d_π Ru orbitals interact strongly with the π orbitals of NCS, resulting in molecular orbitals of a mixed nature. In particular, hole delocalisation across the NCS ligands can thus be responsible for an increased rate constant of the reductive process mediated by I^-, which regenerates the sensitiser. This may explain the observed unit quantum yield [70].

Other Ru complexes have also been tested and failed to show the performance of N3 [74-76]. The introduction of phenyl groups in the chromophoric ligands [74] and the utilisation of supramolecular species [75] are examples of those attempts. However, it is only recently that a potential challenger (tri (cyanato)-2,2'2''-terpyridyl-4,4',4''-tricarboxylate)Ru(II)) (black dye – see Figure 1.6) has been identified [77, 78]. This dye extends the absorption further to the near IR region and thereby improves the spectral match of the sensitised device to the incident solar radiation.

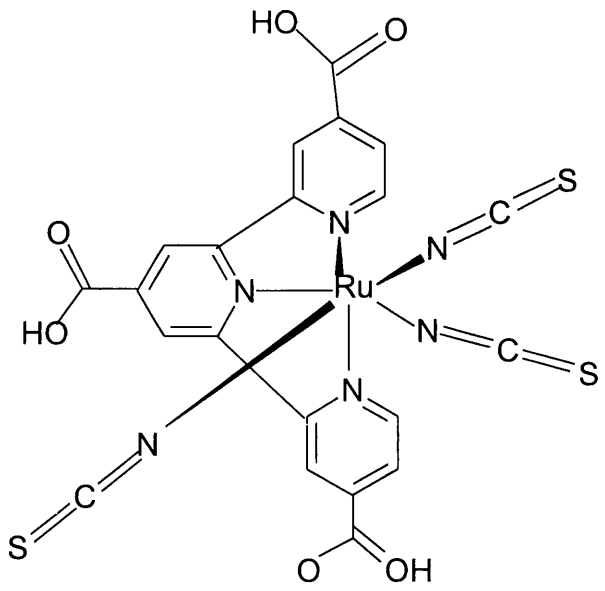

Figure 1.6 *Molecular structure of (tri (cyanato)-2,2'2''-terpyridyl-4,4',4''-tricarboxylate)Ru(II)) (black dye).*

1.4.3 Redox shuttle

Today dye-sensitised nanocrystalline TiO_2 cells employ iodide/tri-iodide redox couple, dissolved in organic solvents. The attractive features of the iodide/tri-iodide system are as follows:

(a). high stability.

(b). good reversibility at Pt counter electrode, but not at SnO_2 or TiO_2 surfaces as DSN solar cells work due to differential kinetics.

(c). low absorption coefficient in the visible region.

(d). reasonably high diffusion coefficient [79].

However, its redox potential is not well matched to that of the presently employed sensitisers such as N3 dye. The voltage loss resulting from the mismatch of the ground state energy level of the N3 dye and the redox potential of the iodide/tri-iodide system is about 0.4 V (see Fig. 1.3), which is a considerable fraction of the currently reported open

circuit photovoltage (~ 0.7 V). Overcoming this loss would mean that the power conversion efficiency of the N3 dye sensitised cell would increase from 10% to 17%. One of the challenges for chemists today is to explore new redox systems that are better matched with the sensitisers such as the N3 dye and it is only recently an attempt was reported towards this goal [80].

1.4.4 The exchange current process and the counter electrode

The counter electrode is needed to transfer electrons arriving from the external circuit back to the I_3^- ions in the electrolyte medium. This process is called the exchange current process. To achieve an efficient exchange current density at the counter electrode, it must not only be a good conductor but also be a catalytically active surface for the $I_3^- \rightarrow 3I^-$ reaction. Otherwise, it will not be able to reach a current density about 20 mA/cm^2 (corresponding to AM 1.5 solar emission) without significant overvoltage.

Up to now platinum has been the most widely used material since it fulfils both requirements. It has been reported that the exchange current density at a platinum coated SnO_2 surface is six orders of magnitude higher than that of a bare SnO_2 surface [81]. However, for an economical approach, cheap materials need to be introduced or the amount of platinum needs to be minimised [82]. Although the amount of platinum has been kept low (< 0.1 g/m^2) by finely dispersing it as a very thin layer on top of the SnO_2 coated glass substrate, it is still an expensive component. Furthermore, the catalytic activity of platinum was found to diminish following desorption of loosely bound dye molecules into the liquid electrolyte which then adsorb on Pt counter electrode, probably blocking of its surface [48]. There is some concern that a small amount of platinum could dissolve in organic electrolyte solvents such as acetonitrile by oxidation and form complexes such as PtI_4 and H_2PtI_6 [48]. If this happens, there is a possibility of redeposition of dissolved platinum on bare SnO_2 sites of the working electrode, which could then catalyse the $I_3^- \rightarrow 3I^-$ reaction. This is a potential problem because the DSN solar cell works on differential kinetics (the back reaction, $I_3^- \rightarrow 3I^-$ needs to be essentially slow at TiO_2 and highly doped SnO_2 coated glass electrodes compared to the

rate of the same reaction (then it also called as the iodine regenerative reaction) on Pt counter electrode).

An attractive low-cost alternative for platinum is carbon [48]. Sufficient conductivity, corrosion resistance and electrocatalytic activity for the $I_3^- \rightarrow 3I^-$ reaction are among the relevant properties of carbon. By employing a porous carbon film as the counter electrode, the number of catalytically active sites could also be increased. However, providing a transparent Pt counter electrode facilitates an additional advantage to the cell since it can be illuminated from either side. Therefore, the platinum coated SnO_2 electrode is still the best option.

1.5 Progress in developing the dye-sensitised nanocrystalline solar cells

Colloid chemistry has greatly advanced in the last decade. It is now possible to control the processing parameters of fabrication of nanocrystalline semiconductor substrates so that optimisation of semiconductor films to get the maximum power output from the DSN solar cell is much easier. After extensive research on the DSN solar cell over the last ten years, 10% power conversion efficiency (under AM 1.5 solar emission) has been achieved for optimised cells [70, 79].

In the light of Grätzel's discovery, other wide band gap n-type nanocrystalline semiconductor materials have also received attention as alternative materials to nanocrystalline TiO_2 [83-86]. As will be explained later, the electron trapping plays a dominant role in electron transport within the nanocrystalline TiO_2 phase and influence cell performance. Therefore, semiconductor materials with low defect densities would be of interest. Materials such as ZnO [83], SnO_2 [84, 85], Nb_2O_5 [86] and $SrTiO_3$ [87] have been investigated and promising results have been obtained. The open circuit voltage (U_{photo}) equals to the difference in energy between the electron quasi-Fermi level of the semiconductor photoelectrode under illumination and the redox potential of the electrolyte. Assuming that flatband potential can approximate to the quasi Fermi level,

one can employ semiconductor materials with flatband potentials higher than anatase TiO_2 in photoelectrode, in order to increase the U_{photo} [87].

In a different approach, a dye-sensitised SnO_2 and ZnO composite film has been employed as the photoactive anode along with the I^-/I_3^- redox shuttle and Pt counter electrode, achieving 8% power conversion efficiency under direct sunlight [88, 89]. Another interesting idea is the fabrication of a tandem cell, which consists of two photoactive electrodes; one is anodically sensitised and other is cathodically sensitised [90]. The principle of the tandem cell is interesting as it uses two active electrodes that can in principle give a high power conversion efficiency that cannot be achieved in conventional dye-sensitised PEC cells that consist of only one active electrode.

The photovoltaic properties of most of the above assemblies are promising. However, despite the high level of photoresponse, a comprehensive fundamental understanding of all the systems (including the dye-sensitised nanocrystalline TiO_2 system) has not been achieved yet.

1.6 Important parameters and factors that determine the cell performance

There are several important parameters that quantify the performance of the DSN solar cell. They are incident photon to current conversion efficiency (IPCE), open circuit photovoltage (U_{photo}) and the overall power conversion efficiency (η_{cell}).

1.6.1 Incident photon to current conversion efficiency (IPCE)

The IPCE measures how efficiently incident photons convert into electrons. The wavelength dependent IPCE can be expressed as a product of the quantum yield for net charge injection (ϕ), the efficiency of collecting electrons in the external circuit (η), and the light harvesting efficiency or the fraction of radiant power absorbed by the material.

$$IPCE(\lambda) = LHE(\lambda)\phi\eta \tag{1.1}$$

The light harvesting efficiency depends on the wavelength dependence dye extinction coefficient, while the net charge injection efficiency depends on the competition between conduction band electron and iodide ions reacting with oxidised dye molecules provided that the radiative and non-radiative intramolecular decay of the excited state of the dye is much slower than electron injection. The charge collection efficiency depends on competition between electron diffusion and back reaction.

1.6.2 Open circuit photovoltage (U_{photo})

As already explained the maximum open-circuit photovoltage attainable in the dye sensitised solar cell is the difference between the electron quasi-Fermi level of the semiconductor under illumination and the Nernst potential of the redox couple in electrolyte. It can be given as follows.

$$qU_{photo} = {}_nE_F - E_{redox} \tag{1.2}$$

Here, ${}_nE_F$ is given by the following relationship.

$$\frac{n_0 + \Delta n}{N_C} = e^{-\frac{{}_nE_F - E_F}{kT}} \tag{1.3}$$

n_0 is the equilibrium electron density (in dark) and Δn is the excess electron density generated by illumination. N_C is the total number of states in the conduction band.

1.6.3 Overall power conversion efficiency (η_{cell})

The overall power conversion efficiency of the photovoltaic cell, η_{cell} , is given by the following equation.

$$\eta_{cell} = \frac{i_{sc} \times U_{photo} \times ff}{I} \tag{1.4}$$

where, i_{sc} is the short circuit photocurrent, U_{photo} is the open circuit photovoltage, ff is the cell fill factor and I is the intensity of the incident light. By designing the geometry of the DSN solar cell for optimal current collection and taking care to minimise ohmic losses, η_{cell} can be increased [91].

As already explained, the N3 sensitiser dye injects electrons into the conduction band with unit quantum efficiency. Innovation of sensitiser dyes that absorb all light below a threshold wavelength of 920 nm and controlling the porosity of the semiconductor film would enhance the light harvesting efficiency. However, a proper understanding of the charge transport within the semiconductor film and investigation of the back reaction of injected electrons with iodide ions is very important in optimisation of the cell performance. Therefore, one purpose of this study was to investigation of the electron transport within the TiO_2 substrate and an understanding of the back reaction kinetics.

1.6.4 Electron transport within the nanocrystalline TiO_2 phase

A unique feature of nanocrystalline semiconductor systems including nanocrystalline TiO_2 is, they consist of a three dimensional network of small particles. The consequence is a large surface-area-to-volume ratio (~ 10^6 cm^{-1} for a 10 nm sized particle network- see section 1.4.1) [92, 93]. So, the particulate electrodes are sponge-like highly porous networks. Therefore, nanocrystalline electrodes are entirely different from compact bulk semiconductor electrodes in the following ways:

(a) the conductivity of the film in the dark is very low,

(b) the semiconductor particles are very small and the dopant density is low hence the built-in electric field is very weak when the electrode comes into contact with the liquid electrolyte [94],

(c) the liquid electrolyte penetrates the porous electrode all the way to the back-contact forming a three-dimensional network.

Electron transport may be strongly influenced by interfacial properties. An interesting feature of the dye sensitised nanocrystalline TiO_2 solar cell is that the photogenerated electrons move without back reacting through hundreds of nanocrystalline TiO_2 particles to reach the conducting SnO_2 substrate. During their passage to the substrate (which can take several seconds at very low light intensities), electrons are never more than ~ 10 nm away from the oxidised redox species in liquid electrolyte.

Several studies have investigated the transient response of electron transport in nanocrystalline substrates. Solbrand *et al.* [95], Schwarzburg *et al.* [96] and Levy *et al.* [97] recorded the photocurrents transients under pulse illumination and found that the response time is very slow (~ millisecond scale). Parallel to the above studies, Cao *et al.* [98] and Sommeling *et al.* [99] studied nanocrystalline TiO_2 electrodes with stepped illumination and reported a similar time scale response, which is in contrast to the response of bulk TiO_2. It also became clear that the characteristic rise or decay time of the response is dependent upon the illumination light intensity [96-98, 100]. This observation led to comparisons of the transient responses with and without electrolyte, and revealed that it is the TiO_2 phase, not the organic electrolyte, that was limiting the response [100, 101]. In contrast, Solbrand *et al.* reported that the electron transport properties in nanostructured system depend more on the properties of liquid electrolyte and less on the type of semiconductor material used to build the nanoporous film [95].

Localised in-gap energy states due to grain boundaries, defects and impurities can act as electron traps. So, the electron transport in nanocrystalline TiO_2 may be influenced by bulk and surface trapping as well as scattering, and the result is a very slow transient response [92]. Chapters 5 and 6 address the question of how the electron transport properties influence the performance of the DSN solar cell.

1.6.2 Back reaction of photogenerated electrons with tri-iodide ions

The photo-injected electrons can back react with oxidised dye molecules as well as tri-iodide ions in electrolyte (see the k_1 and k_2 reaction routes in Figure 1.7). However, the

reaction of electrons and oxidised dye molecules may not be an important factor limiting the short circuit photocurrent due to the unique features of *cis*-[$Ru(dcbH_2)_2(NCS)_2$] (N3) molecular sensitiser dye (see the section 1.4.2). As already explained in previous section, nanocrystalline porous electrodes exhibit very slow electron transport properties. Such slow transport may lead to very long residence times of electrons in the network that could eventually promote the back transfer of electrons to an oxidised species present in the electrolyte solution. So, it is believed that recombination via back reaction is also an important limiting factor that influences the performance of the DSN solar cell [102]. Chapters 5, 6 & 7 of this study consider unresolved questions that remain in the back electron transfer process.

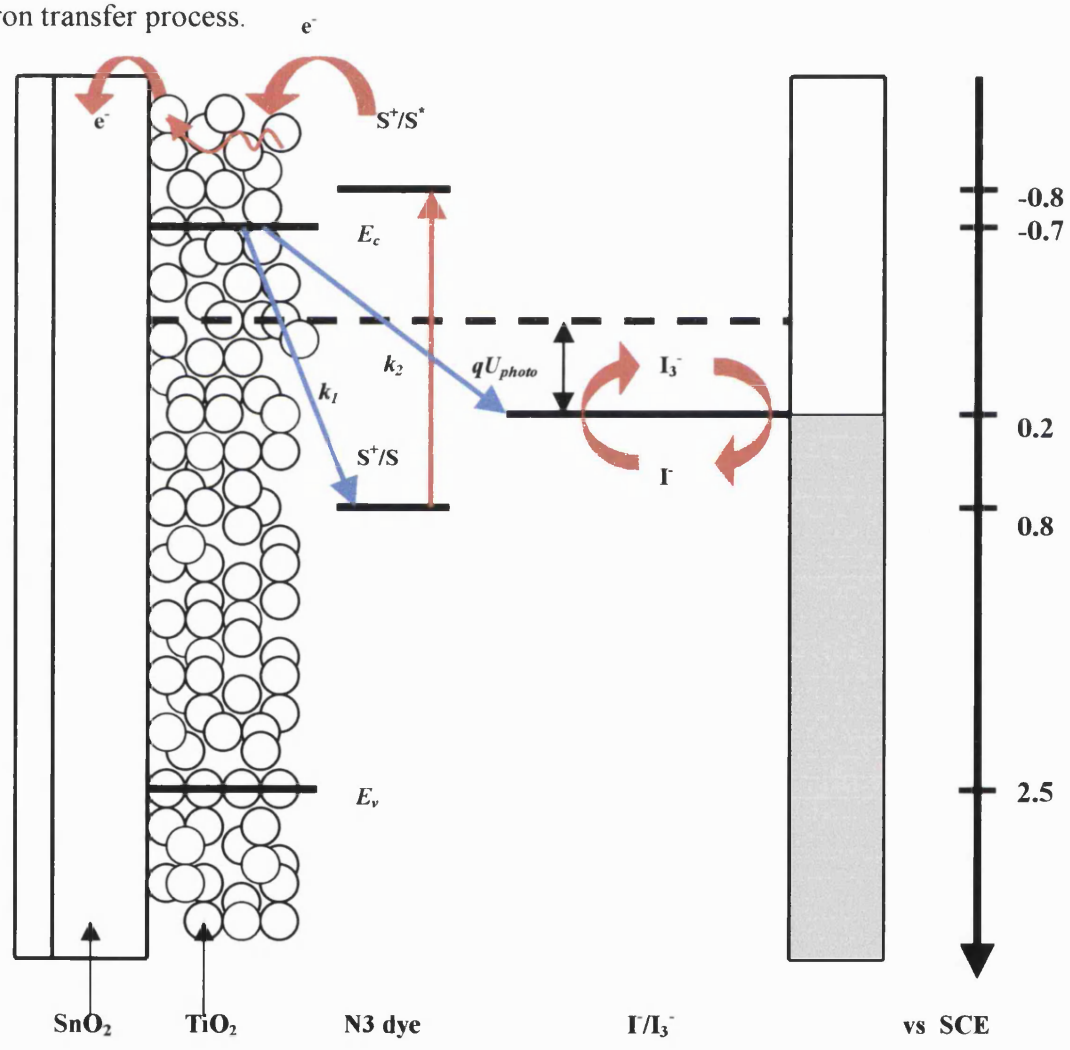

Figure 1.7 *k_1 and k_2 are the possible back reaction routes for photogenerated electrons dye sensitised nanocrystalline solar cell.*

1.7 The future prospects for the dye-sensitised nanocrystalline solar cell

Today the maximum reported power conversion efficiency for DSN solar cells under AM 1.5 solar illumination is around 10%. Therefore, the challenge today is to enhance the performance of DSN solar cell. Some research fronts that are opened for thorough investigation in future towards a high efficient DSN solar are;

(1) Development of a molecular sensitiser that fulfills the following properties.

(a) sensitiser must contain anchoring groups such as carboxylates or phosphonates.
(b) upon excitation, the sensitiser should inject electrons into the conduction band of nanocrystalline semiconductor material with a unit quantum yield while resisting to the back electron injection process.
(c) it should absorb all light in the solar spectrum below a threshold wavelength of about 920 nm.
(d) sensitiser molecule has to be stable enough to sustain at least 10^8 turnover cycles corresponding to 20 years of exposure to light.

It may be possible to replace the molecular sensitiser dye with inorganic semiconductor nanoparticles that also satisfy the requirements given in (b), (c) and (d).

(2) Exploring other redox systems that overcome the voltage loss resulting from mismatch of the ground state energy level of sensitiser dye and the Nernst potential of the redox couple.

(3) Broadening the studies towards semiconductor materials with efficient electron transport properties.

(4) Minimising the dark current and ohmic losses.

(5) Minimising the electron back reaction with redox species.

1.7.1 Existing problems of the dye-sensitised nanocrystalline solar cell

In spite of already mentioned attractive features of the DSN TiO_2 liquid junction solar cells, they faces following scientific and techniological hurdles that must be overcome before introduce as a practical low cost device.

(1) An inefficient dye regeneration process can also cause the desorption of chemically bound sensitiser dye from TiO_2 surface to the liquid electrolyte media.

(2) Sealing of cells and containment of liquid electrolytes are further technological problems as solvent degradation and evaporation are the direct results of them [103].

(3) In principle, any trace amount of water present in liquid electrolyte could lead to organic sensitiser dye degradation via photogenerated holes (by UV light) in TiO_2. (As it can be seen in the Figure 1.1, the UV region in the solar spectrum is not negligible)

1.7.2 Strategies to overcome existing problems

It is clear that many of the problems in DSN cells originate from the liquid phase. These potential problems have stimulated research into solid-state analogues of the DSN cell, in which the liquid electrolyte is replaced by a suitable solid-state material that penetrates into the dye-sensitised nano-porous network. However, in order to achieve this goal the prospective solid-state material needs to fulfill the following requirements.

(1). To be a viable candidate, the solid-state material must be transparent in the visible spectrum, where the sensitiser dye absorbs light. Therefore it must be a high bandgap material.

(2). The VB (if the material is a p-type semiconductor) or HOMO (if the material is a conductive polymer) must lie above the ground state energy of the sensitiser dye.

(3). The material should be photostable [104].

(4). A convenient method must be available for filling the nanocrystalline TiO_2 porous network without decomposing the absorbed organic sensitiser dye.

(5). A proper sealing method is required to guarantee the long-term stability of the cell.

(6). p-type semiconductors, partially oxidised hole conducting polymers, redox polymers, ionic conducting polymers are several examples for suitable solid-state materials. However, the prospective material should possess good hole transport properties.

1.7.3 Solid-state analogues of dye-sensitised nanocrystalline solar cells

In the light of the recent improvement of the performance of DSN solar cell, extensive work has been carried out on use of transparent p-type semiconductors as hole conducting materials [60, 61, 105-108]. But the overall energy conversion efficiencies are still very low owing to the difficulty to provide intimate contacts with all the adsorbed dye molecules in the nano-porous three-dimensional network. For efficient charge transfer process each molecular sensitiser must be in intimate contact with both electron and hole conducting phases [60, 106]. Chapter 8 describes the fabrication and characterisation of a solid-state dye-sensitised cell made by using CuI as the p-type semiconductor. Figure 1.8 shows a schematic diagram of the solid-state dye-sensitised cell made by replacing the liquid electrolyte by p-type CuI.

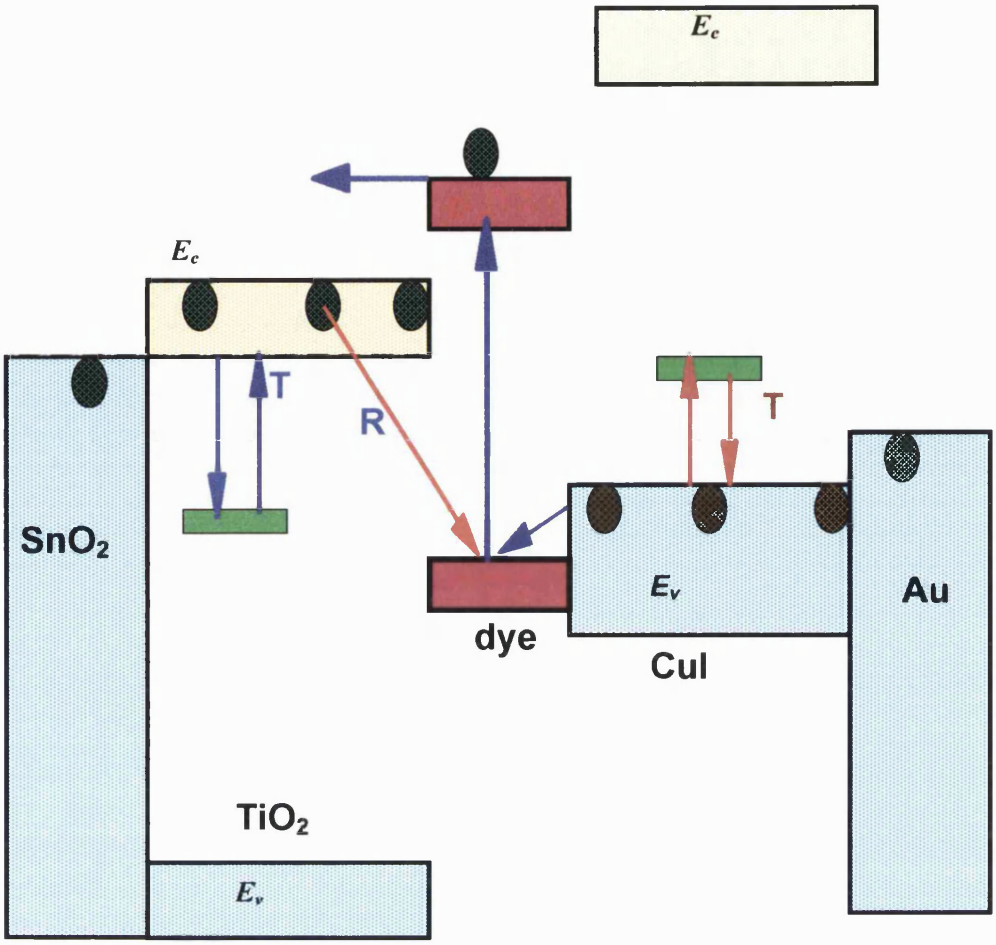

Figure 1.8 *An schematic representation of dye sensitised solid state photovoltaic cel made p-type CuI as the hole conducting material. R –recombination routes, T – charge trapping*

In terms of employing a stable hole conducting material in solid-state type dye-sensitised solar cell, conductive polymers could play a major role. On the other hand in general they are light absorbing materials, which renders them less suitable for this purpose. However, recent approaches to thin film cells involving the use of organic compounds [109] or of polymer materials [110-115] have excited considerable interest since they offer the possibility of fine-tuning material properties such as solubility and hole conductivity via chemical substitution. In this type of device, charge generation/separation takes place at

solid-solid interface and charge transport occurs in different organic and inorganic phases. In this work attempts were made to fabricate a photovoltaic cell based on an organoceramic nanocomposite. This organo-inorganic hybrid comprises two distinct, interpenetrating and mutually contiguous phases; one, a network of dye sensitised semiconductor nanocrystallites and the other, a photostable hole conducting polymer. Within the composite, the effective area of the sensitiser-nanocrystallite interface is high, maximising both the efficiency of incident light absorption by the sensitiser and the efficiency of light induced interfacial charge separation. The principle of this device is illustrated in the following schematic diagram (see Fig.1.9). Chapter 8 also discusses dye sensitised nanocomposite organoceramic cell fabrication strategies and characterisation.

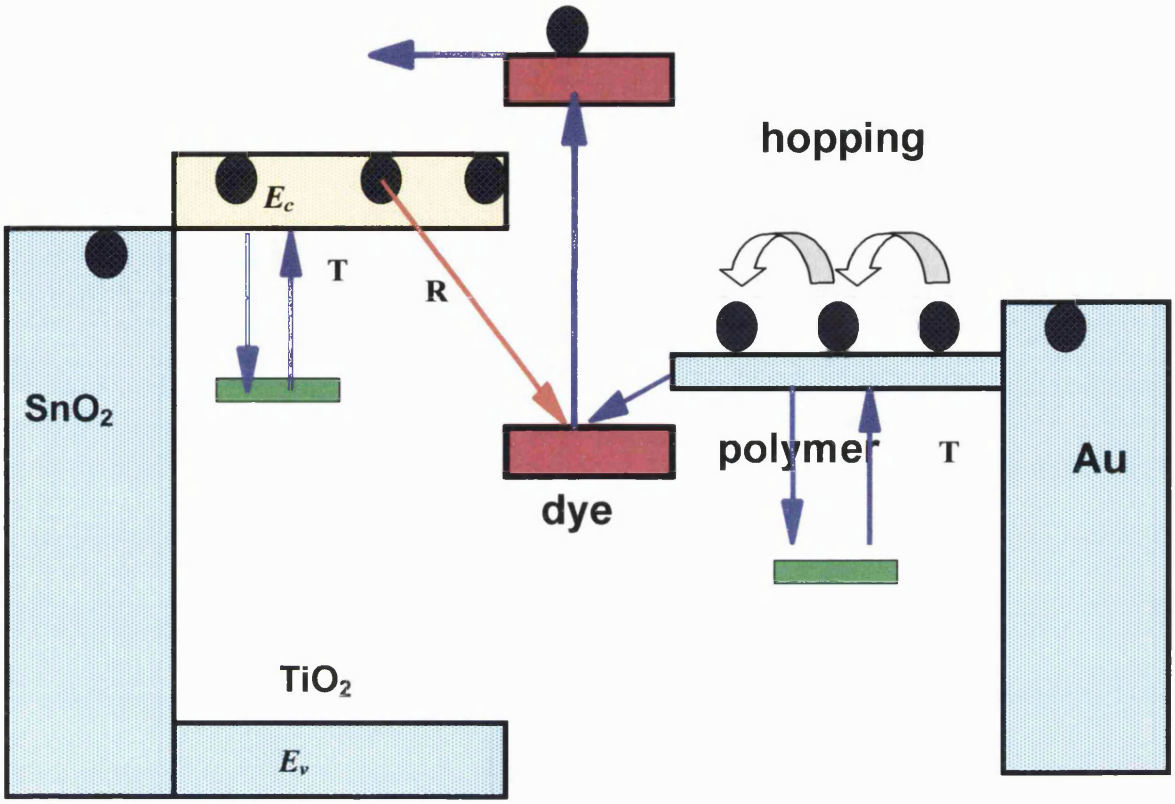

Figure 1.9 *An schematic diagram of dye sensitised nanocomposite organoceramic photovoltaic cell. R –recombination routes, T – charge trapping*

1.8 References

1. P. J. Verlinden, R. M. Swanson, and R. A. Crane, Progress in Photovoltaics and Applications 2:143 (1994).
2. J. Zhao, A. Wang, P. Altermalt, and M. A. Green, Applied Physics Letters 66:3636 (1995).
3. C. O'Driscoll, Chemistry in Britain 34:44 (1998).
4. H. Gerischer and H. Tributsch, Berichte der Bunsen-gesellschaft-Physical Chemistry Chemical Physics 72:437 (1968).

5. H. Gerischer, Top Current Chemistry 61:31 (1976).
6. H. Gerischer, Photochemistry and Photobiology 16:243 (1972).
7. A. J. Bard and M. S. Wrighton, Journal of Electrochemical Society 124:1706 (1977).
8. S. Licht and D. Peramunage, Journal of Physical Chemistry 100:9082 (1996).
9. R. Vogel, P. Hoyer, and H. Weller, Journal of Physical Chemistry 98:3183 (1994).
10. C. Rost, I. Sieber, C. Fischer, M. C. Lux-Steiner, and R. Konenkamp, Materials Science and Engineering B-Solid State Materials for Advanced Technology 69:570 (2000).
11. H. W. Vogel, Berichte der Bunsen-gesellschaft-Physical Chemistry Chemical Physics 6:1320 (1873).
12. R. W. Gurney and N. Mott, in Proceedings of Roral Society A, Vol. 164, 1938, p. 151.
13. M. Matsumura, Y. Nomura, and H. Tsubomura, Bulletin of Chemical Society of Japan 82:1559 (1979).
14. H. Tsubomura, M. Matsumura, Y. Nomura, and T. Amamia, Nature 261:402 (1979).
15. K. Tennakone, M. Kahanda, C. Kasige, P. Abeysooriya, R. H. Wijayanayaka, and P. Kaviratna, Journal of the Electrochemical Society 131:1574 (1984).
16. K. Tennakone, J. Karunamuni, and M. Dewasurendra, Solar Energy Materials 13:447 (1986).
17. K. Tennakone, G. S. S. Pushpa, S. Punchihewa, and G. Epa, Electrochimica Acta 31:315 (1986).
18. K. Tennakone, C. A. N. Fernando, M. S. Kariapper, and M. Dewasurendre, Journal of Physics D-Applied Physics 19:L125 (1986).
19. R. Memming and H. Tributsch, Journal of Physical Chemistry 75:562 (1971).
20. N. Alonso, M. Beley, P. Chartier, and V. Ern, Revue De Physique Appliquee 16:5 (1981).
21. F. Willig, R. Eichberger, N. S. Sundaresan, and B. A. Parkinson, Journal of the American Chemical Society 112:2702 (1990).

22. K. Kalyanasundaram, N. Vlachopoulos, V. Krishnan, A. Monnier, and M. Gratzel, Journal of Physical Chemistry 91 (1987).
23. J. Desilvestro, M. Gratzel, L. Kavan, J. Moser, and J. Augustynski, Journal of American Chemical Society 107:2988 (1985).
24. E. Vrachnou, N. Vlachopoulos, and M. Gratzel, Journal of Chemical Society Chemical Communication:868 (1987).
25. B. Oregan and M. Gratzel, Nature 353:737 (1991).
26. C. A. Bignozzi, R. Argazzi, and C. J. Kleverlaan, Chemical Society Reviews 29:87 (2000).
27. T. Gerfin, M. Gratzel, and L. Walder, Molecular Level Artificial Photosynthetic Materials 44:345 (1997).
28. J. K. Burdett, T. Hughbanks, G. J. Miller, J. W. Richardson, and J. V. Smith, Journal of the American Chemical Society 109:3639 (1987).
29. B. Silvi, N. Fourati, R. Nada, and C. R. A. Catlow, Journal of Physics and Chemistry of Solids 52:1005 (1991).
30. K. M. Glassford and J. R. Chelikowsky, Physical Review B-Condensed Matter 46:1284 (1992).
31. K. M. Glassford and J. R. Chelikowsky, Physical Review B-Condensed Matter 45:3874 (1992).
32. A. Fahmi, C. Minot, B. Silvi, and M. Causa, Physical Review B-Condensed Matter 47:11717 (1993).
33. S. Munnix and M. Schmeits, Physical Review B-Condensed Matter 30:2202 (1984).
34. K. M. Glassford, N. Troullier, J. L. Martins, and J. R. Chelikowsky, Solid State Communications 76:635 (1990).
35. B. Poumellec, P. J. Durham, and G. Y. Guo, Journal of Physics-Condensed Matter 3:8195 (1991).
36. D. W. Bullett, ed., in Solid State Physics, Acedamic, New York, vol. 35, 129, 1980.
37. R. I. Bickley, Chemical Physics Solid Surfaces 7:118 (1978).

38. H. Tang, H. Berger, P. E. Schmid, and F. Levy, Solid State Communications 92:267 (1994).
39. H. Tang, H. Berger, P. E. Schmid, F. Levy, and G. Burri, Solid State Communications 87:847 (1993).
40. S. Kodaira, Y. Sakisaka, T. Maruyama, Y. Haruyama, Y. Aiura, and H. Kato, Solid State Communications 89:9 (1994).
41. F. Cao, G. Oskam, P. C. Searson, J. M. Stipkala, T. A. Heimer, F. Farzad, and G. J. Meyer, Journal of Physical Chemistry 99:11974 (1995).
42. M. K. Nazeeruddin, P. Liska, J. Moser, N. Vlachopoulos, and M. Gratzel, Helvetica Chimica Acta 73:1788 (1990).
43. K. Hashimoto, T. Kawai, and T. Sakata, Nouveau Journal De Chimie-New Journal of Chemistry 7:247 (1983).
44. A. Kraft, M. Rottmann, and K. H. Heckner, Solar Energy Materials and Solar Cells 45:97 (1997).
45. L. B. Feng, H. Q. Wang, Z. S. Jin, Q. L. Li, and M. Y. Shi, Journal of Photochemistry and Photobiology a-Chemistry 56:89 (1991).
46. C. J. Barbe, F. Arendse, P. Comte, M. Jirousek, F. Lenzmann, V. Shklover, and M. Gratzel, Journal of the American Ceramic Society 80:3157 (1997).
47. D. J. Fitzmaurice, M. Eschle, H. Frei, and J. Moser, Journal of Physical Chemistry 97:3806 (1993).
48. A. Kay and M. Gratzel, Solar Energy Materials and Solar Cells 44:99 (1996).
49. N. G. Park, G. Schlichthorl, J. van de Lagemaat, H. M. Cheong, A. Mascarenhas, and A. J. Frank, Journal of Physical Chemistry B 103:3308 (1999).
50. S. Hotchandani and P. V. Kamat, Journal of Physical Chemistry 96:6834 (1992).
51. D. Liu and P. V. Kamat, Journal of Physical Chemistry 97:10769 (1993).
52. M. K. Nazeeruddin, R. Humphry-Baker, M. Gratzel, D. Wohrle, G. Schnurpfeil, G. Schneider, A. Hirth, and N. Trombach, Journal of Porphyrins and Phthalocyanines 3:230 (1999).
53. M. K. Nazeeruddin, R. Humphry-Baker, M. Gratzel, and B. A. Murrer, Chemical Communications:719 (1998).

54. H. N. Ghosh, J. B. Asbury, and T. Lian, Journal of Physical Chemistry 102:6482 (1998).

55. K. Sayama, M. Sugino, H. Sugihara, Y. Abe, and H. Arakawa, Chemistry Letters:753 (1998).

56. A. Kay and M. Gratzel, Journal of Physical Chemistry 97:6272 (1993).

57. A. Kay, R. Humphrybaker, and M. Gratzel, Journal of Physical Chemistry 98:952 (1994).

58. N. J. Cherepy, G. P. Smestad, M. Gratzel, and J. Z. Zhang, Journal of Physical Chemistry B 101:9342 (1997).

59. G. P. Smestad and M. Gratzel, Journal of Chemical Education 75:752 (1998).

60. K. Tennakone, G. Kumara, A. R. Kumarasinghe, K. G. U. Wijayantha, and P. M. Sirimanne, Semiconductor Science and Technology 10:1689 (1995).

61. K. Tennakone, G. Kumara, I. R. M. Kottegoda, and K. G. U. Wijayantha, Semiconductor Science and Technology 12:128 (1997).

62. K. Tennakone, A. R. Kumarasinghe, G. Kumara, K. G. U. Wijayantha, and P. M. Sirimanne, Journal of Photochemistry and Photobiology a-Chemistry 108:193 (1997).

63. M. Gratzel and K. Kalyanasundaram, Current Science 66:706 (1994).

64. P. Liska, N. Vlachopoulos, M. K. Nazeeruddin, P. Comte, and M. Gratzel, Journal of the American Chemical Society 110:3686 (1988).

65. M. K. Nazeeruddin, A. Kay, I. Rodicio, R. Humphrybaker, E. Muller, P. Liska, N. Vlachopoulos, and M. Gratzel, Journal of the American Chemical Society 115:6382 (1993).

66. R. Argazzi, C. A. Bignozzi, T. A. Heimer, F. N. Castellano, and G. J. Meyer, Inorganic Chemistry 33:5741 (1994).

67. J. M. Lanzafame, R. J. D. Miller, A. A. Muenter, and B. A. Parkinson, Journal of Physical Chemistry 96:2820 (1992).

68. B. Burfeindt, T. Hannappel, W. Storck, and F. Willig, Journal of Physical Chemistry 100:16463 (1996).

69. J. M. Rehm, G. L. McLendon, Y. Nagasawa, K. Yoshihara, J. Moser, and M. Gratzel, Journal of Physical Chemistry 100:9577 (1996).

70. M. Gratzel, Current Opinion in Colloid & Interface Science 4:314 (1999).
71. J. B. Asbury, R. J. Ellingson, H. N. Ghosh, S. Ferrere, A. J. Nozik, and T. Q. Lian, Journal of Physical Chemistry B 103:3110 (1999).
72. K. S. Finnie, J. R. Bartlett, and J. L. Woolfrey, Langmuir 14:2744 (1998).
73. J. K. Mccusker.
74. O. Kohle, S. Ruile, and M. Gratzel, Inorganic Chemistry 35:4779 (1996).
75. M. T. Indelli, C. A. Bignozzi, A. Harriman, J. R. Schoonover, and F. Scandola, Journal of the American Chemical Society 116:3768 (1994).
76. C. A. Bignozzi, R. Argazzi, M. T. Indelli, and F. Scandola, Solar Energy Materials and Solar Cells 32:229 (1994).
77. S. M. Zakeeruddin, M. K. Nazeeruddin, P. Pechy, F. P. Rotzinger, R. HumphryBaker, K. Kalyanasundaram, M. Gratzel, V. Shklover, and T. Haibach, Inorganic Chemistry 36:5937 (1997).
78. M. K. Nazeeruddin, P. Pechy, and M. Gratzel, Chemical Communications:1705 (1997).
79. M. Gratzel, Progress in Photovoltaics 8:171 (2000).
80. B. A. Gregg, F. Pichot, S. Ferrere, and C. L. Fields, Journal of physical Chemistry B 105:1422 (2001).
81. N. J. Show, in Ph.D. Thesis, Department of Chemistry, University of Bath, Bath, 1999.
82. N. Papageorgiou, W. F. Maier, and M. Gratzel, Journal of the Electrochemical Society 144:876 (1997).
83. P. Hoyer and H. Weller, Journal of Physical Chemistry 99:14096 (1995).
84. S. Ferrere, A. Zaban, and B. A. Gregg, Journal of Physical Chemistry B 101:4490 (1997).
85. P. V. Kamat, I. Bedja, S. Hotchandani, and L. K. Patterson, Journal of Physical Chemistry 100:4900 (1996).
86. K. Sayama, H. Sugihara, and H. Arakawa, Chemistry of Materials 10:3825 (1998).
87. S. Burnside, J. E. Moser, K. Brooks, M. Gratzel, and D. Cahen, Journal of Physical Chemistry B 103:9328 (1999).

88. K. Tennakone, V. P. S. Perera, I. R. M. Kottegoda, and G. Kumara, Journal of Physics D-Applied Physics 32:374 (1999).

89. K. Tennakone, G. Kumara, I. R. M. Kottegoda, and V. P. S. Perera, Chemical Communications:15 (1999).

90. J. J. He, H. Lindstrom, A. Hagfeldt, and S. E. Lindquist, Solar Energy Materials and Solar Cells 62:265 (2000).

91. M. Gratzel, in Semiconductor Nanoclusters, Vol. 103 (P. V. Kamat and D. Meisel, eds.), Elsevier Science B.V., 1996, p. 353.

92. L. M. Peter and D. Vanmaekelbergh, in Advances in Electrochemical Science and Engineering, Vol. 6 (D. M. Alkire and D. Kolb, eds.), VCH Wiley, New York, 1999, p. 77.

93. L. M. Peter, E. A. Ponomarev, G. Franco, and N. J. Shaw, Electrochimica Acta 45:549 (1999).

94. A. Hagfeldt, H. Lindstrom, S. Sodergren, and S. E. Lindquist, Journal of Electroanalytical Chemistry 381:39 (1995).

95. A. Solbrand, H. Lindstrom, H. Rensmo, A. Hagfeldt, S. E. Lindquist, and S. Sodergren, Journal of Physical Chemistry B 101:2514 (1997).

96. K. Schwarzburg and F. Willig, Applied Physics Letters 58:2520 (1991).

97. B. Levy, W. Liu, and S. E. Gilbert, Journal of Physical Chemistry B 101:1810 (1997).

98. F. Cao, G. Oskam, G. J. Meyer, and P. C. Searson, Journal of Physical Chemistry 100:17021 (1996).

99. P. M. Sommeling, H. C. Rieffe, J. M. Kroon, J. A. M. Van Roosmalen, A. Schonecker, and W. C. Sinke, in Proceeding of he 14th EC Photovoltaic Solar Energy Conference (H. Ossenbrink, P. Helm, and H. Ehmann, eds.), H. S. Stephens and Associates, Bedford, 1997, p. 1816.

100. L. Dloczik, O. Ileperuma, I. Lauermann, L. M. Peter, E. A. Ponomarev, G. Redmond, N. J. Shaw, and I. Uhlendorf, Journal of Physical Chemistry B 101:10281 (1997).

101. A. Hagfeldt, S. E. Lindquist, and M. Gratzel, Solar Energy Materials and Solar Cells 32:245 (1994).

102. H. Lindstrom, H. Rensmo, S. Sodergren, A. Solbrand, and S. E. Lindquist, Journal of Physical Chemistry 100:3084 (1996).
103. R. Grunwald and H. Tributsch, Journal of Physical Chemistry B 101:2564 (1997).
104. K. G. U. Wijayantha, in Department of Chemistry, M. Phil thesis, University of Ruhuna, Matara, 1997, p. 141.
105. K. Tennakone, G. Kumara, I. R. M. Kottegoda, K. G. U. Wijayantha, and V. P. S. Perera, Journal of Physics D-Applied Physics 31:1492 (1998).
106. B. O'Regan and D. T. Schwartz, Chemistry of Materials 10:1501 (1998).
107. U. Bach, D. Lupo, P. Comte, J. E. Moser, F. Weissortel, J. Salbeck, H. Spreitzer, and M. Gratzel, Nature 395:583 (1998).
108. U. Bach, Y. Tachibana, J. E. Moser, S. A. Haque, J. R. Durrant, M. Gratzel, and D. R. Klug, Journal of the American Chemical Society 121:7445 (1999).
109. D. Wohrle and D. Meissner, Advanced Materials 3:129 (1991).
110. G. Yu and A. J. Heeger, Journal of Applied Physics 78:4510 (1995).
111. G. Yu, J. Gao, J. C. Hummelen, F. Wudl, and A. J. Heeger, Science 270:1789 (1995).
112. J. J. M. Halls, C. A. Walsh, N. C. Greenham, E. A. Marseglia, R. H. Friend, S. C. Moratti, and A. B. Holmes, Nature 376:498 (1995).
113. J. J. M. Halls, K. Pichler, R. H. Friend, S. C. Moratti, and A. B. Holmes, Applied Physics Letters 68:3120 (1996).
114. A. Kohler, D. A. dos Santos, D. Beljonne, Z. Shuai, J. L. Bredas, A. B. Holmes, A. Kraus, K. Mullen, and R. H. Friend, Nature 392:903 (1998).
115. M. Granstrom, K. Petritsch, A. C. Arias, A. Lux, M. R. Andersson, and R. H. Friend, Nature 395:257 (1998).

Chapter 2

Fundamental Aspects of Semiconductor Photoelectrochemistry

2.1 Introduction

The liquid electrolyte based dye-sensitised nanocrsytalline solar cell comprises 3-dimensional inter-connected dye coated semiconductor nanocrystallites in contact with liquid electrolyte, which contains a redox shuttle. Therefore, in order to study the properties of the DSN solar cell, it is important to understand electronic conduction in solids, the energy distribution of redox species in liquid electrolyte solution and electron transfer at the semiconductor/liquid electrolyte interface. This chapter starts with a brief introduction to the different types of solids and their electronic properties, which also includes fundamental features of solid-state band theory (section 2.2). Section 2.3 of this chapter mainly deals with the Fermi energy in a semiconductor (at equilibrium and non-equilibrium) and the energy distribution of redox species in a solution. Section 2.4 reviews electron transfer at the semiconductor electrode/electrolyte interface in equilibrium and non-equilibrium situations.

The solid-state dye-sensitised solar cell comprises two distinct, interpenetrating and mutually contiguous phases; one, a 3-dimensional network of dye sensitised semiconductor nanocrystallites for electron transport and the other, a hole conducting material. Therefore, it is essential to understand how the interfacial properties of a semiconductor solid-solid heterojunction differ from those of its the semiconductor/liquid counterpart. This is dealt with in the final section of this chapter.

2.2 Solids

Atoms of a solid are vibrated with small amplitude about a fixed equilibrium position. The immobility of atomic equilibrium positions gives a solid a fixed structure and

distinguishes it from a liquid or a gas. Any given solid material may be either crystalline, amorphous or polycrystalline, depending on how it is prepared.

2.2.1 Crystalline solids and Band theory

In crystals, atomic equilibrium positions form a geometric pattern that is exactly repeated throughout the solid without change in composition, dimension, or orientation. The different electrical conducting properties in crystalline solids can be explained using band theory. Applying molecular orbital theory to small, finite-sized molecules and extending the treatment to infinite, three-dimensional structures, solid-state band theory can be built up. In the molecular orbital theory of diatomic molecules (the simplest case), an atomic orbital formed from valence shell electrons of atom one overlaps with a similar atomic orbital on atom two, resulting in the formation of two molecular orbitals that are delocalised over both atoms. One of the molecular orbitals is 'bonding' and has lower energy than that of the atomic orbitals. The other is 'antibonding' and is of higher energy (see Figure 2.1).

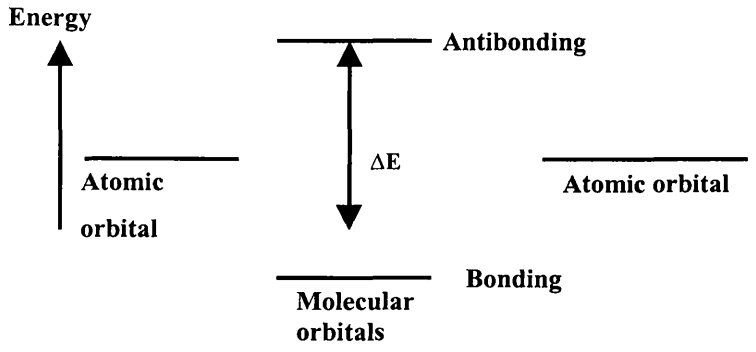

Figure 2.1 *Formation of a molecular orbital from atomic orbitals.*

Extension of this approach to larger molecules leads to an increase in the number of molecular orbitals. As the number of molecular orbitals increases, the average energy gap between adjacent molecular orbitals decreases. At the same time the gap between bonding and antibonding orbitals also decreases until the situation is reached in which there is essentially a continuum of energy levels. Taking into account the formation of an

aluminium metal crystal from individual aluminium atoms, the idea of continuum energy levels is shown in Figure 2.2.

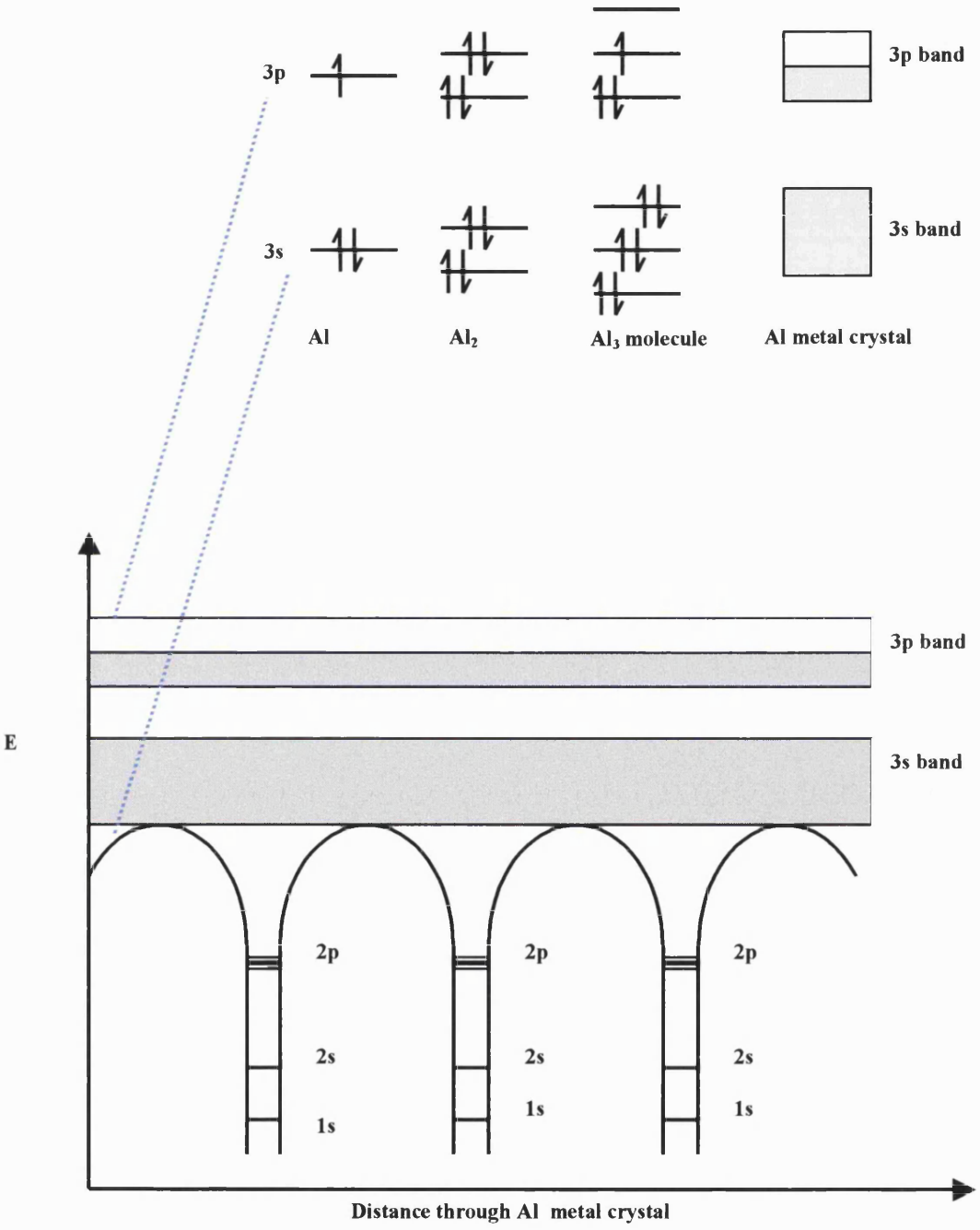

Figure 2.2 *Formation of an aluminium metal crystal from individual aluminium atoms.*

The band structure of other crystalline solids may be regarded in a similar way.

The electrical conductivity in crystalline solids mainly depends on:

(a) whether the valence bands are full, partly filled or empty,

(b) the magnitude of the forbidden energy gap (bandgap) between full and empty bands,

Solids are categorised into three groups as metals, semiconductors and insulators.

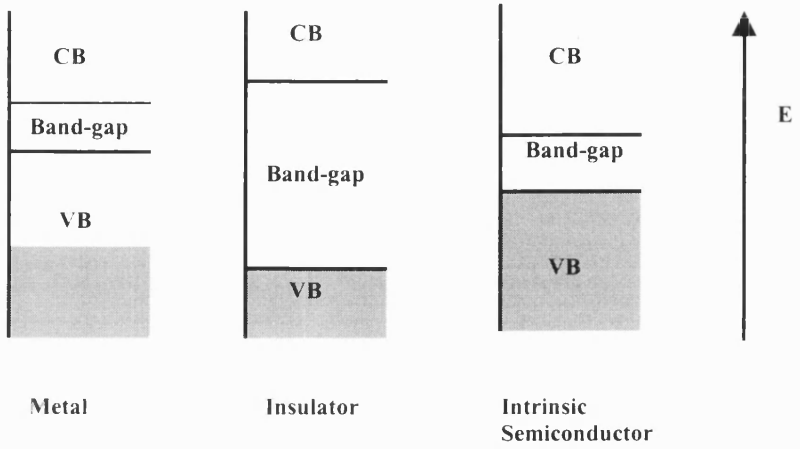

Figure 2.3 *Forbidden energy gaps for a metal, a semiconductor and an insulator.*

Metals

Metals are characterised by a band structure in which the highest occupied band, is only partly filled. As described in Figure 2.2, in aluminium the inner core electrons (1s, 2s, 2p) are localised in discrete atomic orbitals in individual aluminium atoms. However, the 3s and 3p electrons that form the valence shell occupy energy levels that are delocalised over the whole of the metal crystal. Thus in an aluminium crystal that contains N atoms, each atom contributes one 3s orbital and the result is a band that contains N closely spaced energy levels and is called a 3s valence band. The 3p levels are similarly present

as a delocalised 3p band of energy levels and are partly filled. This band is responsible for electrical conduction in aluminium.

Insulators

At absolute zero, the valence band in insulators is completely full. It is separated by a large bandgap from the next energy band, which is empty. For example, diamond is an insulator with a bandgap of ~ 6 eV. Therefore, at 0 K, these materials do not display any conduction because the valence band is filled while the conduction band is empty. However, as the temperature rises, electrical conduction appears due to thermal excitation. However, having a completely filled valence band is not the only requirement for a solid to be an insulator. The best example is beryllium. In beryllium both 1s and 2s bands are completely filled. However, the 2s and 2p bands overlap each other which allows 2s electrons to move to the 2p band. Therefore, beryllium shows metallic character (zero bandgap).

Semiconductors

Intrinsic semiconductors have a similar band structure to insulators but the bandgap is smaller. There is no clear margin to distinguish the bandgap of semiconductors and insulators but usually it is in the range 0.5 to 3.0 eV for semiconductors. The result of having a relatively small bandgap is that at room temparature electrons have sufficient thermal energy to be promoted into the next empty band and become freely mobile. Semiconductors may be divided into two groups as intrinsic and extrinsic. Intrinsic semiconductors are pure materials. The number of electrons in the conduction band in intrinsic semiconductors is entirely governed by the magnitude of the bandgap, the temperature and the intensity of illumination. Pure silicon is an example of an intrinsic semiconductor. However, extrinsic semiconductors are not pure materials, and the conductivity is mainly controlled by added dopants. Silicon is the most common example in distinguishing both intrinsic and extrinsic semiconductors. Pure silicon (an intrinsic semiconductor) can easily be converted into an extrinsic semiconductor by doping with

atoms from either Group III or Group V elements of the periodic table (e.g. gallium, arsenic). As a result, silicon can either be n-type or p-type depending on the dopant. The donor or acceptor levels that are introduced by foreign atoms increase the number of electrons or holes that are available for electrical conduction (see Figure 2.4). The electronic conductivity in extrinsic semiconductors can also be increased by illumination with light and by increasing the temperature.

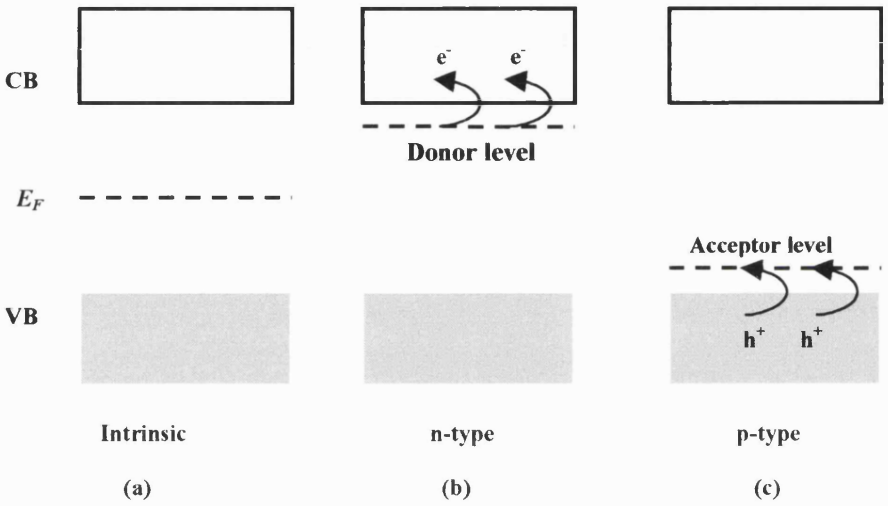

Figure 2.4 *Formation of donor and acceptor levels due to foreign atoms.*

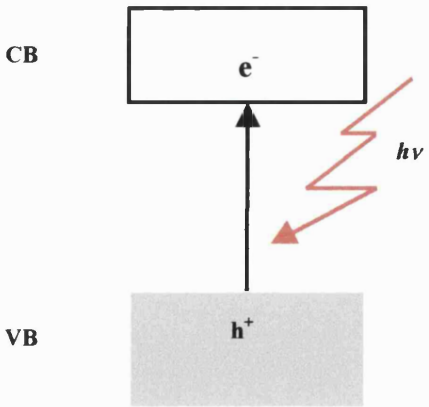

Figure 2.5 *Creation of electron-hole pairs by illumination.*

Two types of electrical conduction mechanism may be distinguished in both intrinsic and extrinsic semiconductors. As shown in Figure 2.5, any electrons that are promoted into the conduction band from the filled valence band can move freely and be responsible for electrical conduction. The electron vacancies that are left behind in the valence band may be regarded as positive holes and can move freely in the valence band, and so they are also responsible for electrical conduction.

2.2.2 Amorphous Solids and Glasses

A solid can either be crystalline or be amorphous depending on the cooling rate during its transition from liquid to solid. If the liquid cools sufficiently slowly for the atoms to assume orderly arrangements like the ones shown in Figure 2.2, a crystal results. If the temperature is dropped abruptly, restricting the motion of the atoms before they can reorganise themselves, then a disorganised structure called a glass or an amorphous solid may result. This insufficient reorganisation time may lead to wide composition ranges and deviations from stoichiometric composition, whereas in crystalline systems the composition of the crystal is usually stoichiometric. Amorphous silicon and glassy $As_2 S_3$ are examples of amorphous solids. The interpretation of electrical conduction in amorphous solids is rather difficult [1].

2.2.3 Polycrystalline solids

A polycrystalline solid is made up of a large number of small crystals, called crystallites. Each crystallite forms from a large number of atoms with a highly ordered structure and is therefore crystalline. However, the orientation of the crystal lattice changes abruptly at crystallite boundaries. Nanocrystalline TiO_2, which was used in the present study, is an example of a polycrystalline solid. The electrical conduction properties of polycrystalline materials depend not only on the bulk properties of the solid but also on intergrain contacts; If the crystals are very small, quantum confinement effects may change the electrical and optical properties (for more details see section 2.4.3) [2].

2.2.4 Polymers

Polymers are materials that contain very large molecules (typically 10^4 to 10^6 atoms). They can be either inorganic (e.g. CuSCN) or organic (e.g. cellulose, starch, rubber). In early stage, polymers were regarded as amorphous materials as they do not possess well-ordered structures. However, recent studies reveal that they are crystalline in many cases [3]. Polymers are often non-conducting materials, and consequently have found widespread application as insulators. However, in 1977 Chiang *et al.* discovered that the conductivity of trans-polyacetylene films could be enhanced by ten million times when electrons were removed from the conjugated trans-polyacetylene chain by oxidation with iodine vapor [4].

Conducting polymers

When large numbers of atoms are brought together to form polymers, the electronic states mix to form bands; each band consisting of electronic states whose energies form a continuous range (see Figure 2.6). This situation is analogous to the formation of continuum energy levels in crystalline solids. However, the weak interaction between polymer strands results poor electronic conductivity. For example, the conductivities of polyethylene, cis-polyacetylene, trans-polyacetylene are 10^{-16}, 10^{-8}, 10^{-5} Scm^{-1} respectively at room temperature. The discovery of transformation of trans-polyacetylene from poor conductor to a lustrous polymer with a conductivity approaching that of metals, paved the way of exploiting other polymers as conductors [4].

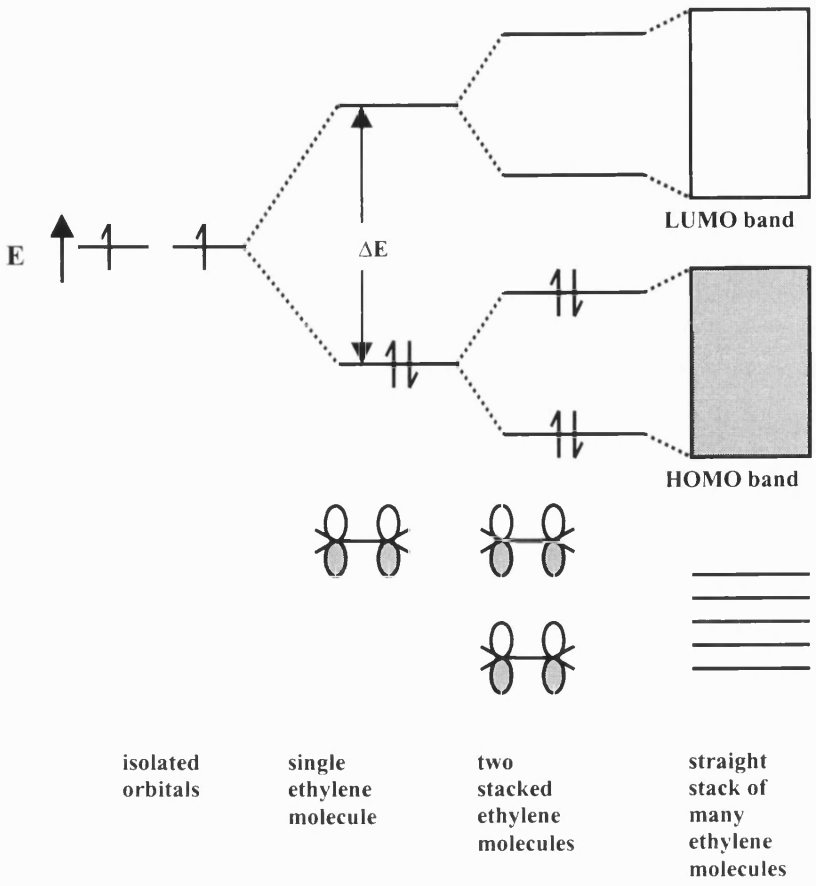

Figure 2.6 *Formation of HOMO and LUMO energy levels in polyethylene*

The reactions which induce enhancements in the conductivity of polyacetylene have been termed p-doping or n-doping processes, by analogy with classical semiconductor terminology. However, these processes may be more correctly described as redox reactions, which involve oxidising or reducing agents with the formation of polyanions or polycations whose charge is balanced by the counterions. For instance, exposure to an oxidising agent, say X (e.g. I, Br), leads p-doping and forms positively charged polymer complex:

$$(CH)_n + (ny)X \rightarrow [(CH^{y+})]_n + (ny)X^- \rightarrow [(CH^{y+})X_y^-]_n$$

Similarly, exposure to a reducing agent, say M (e.g. Na, Li), results n-doping and forms negatively charge polymer complexes as described below.

$$(CH)_n + (ny)M \rightarrow [(CH^{y-})]_n + (ny)M^+ \rightarrow [M_y^+(CH^{y-})]_n$$

The doping process can also be applied to other polymers such as polypyrrole, polyaniline and polythiophene. An additional important feature of the heterocyclic polymers lies in the fact that the polymerisation as well as doping processes can also be driven by electrochemically. However, it is noteworthy to emphasis two notable differences between doping inorganic materials and doping polymers. The first is the difference of the amount of dopant (doping levels) that requires for doping process ('y' in above schemes). Typically, for inorganic semiconductors, the doping level is less than 10 ppm whereas for polymers it is about 0.5. The low dimensional conductivity due to weak inter-chain interactions, localisation of charge within polymer chains due to possible defects sites such as cross-links, chain ends and bends may be responsible for required higher amount of doping levels for polymers. The second important difference is the impurities or doping agents do not become part of structure in polymers. This contrasts with the formation of structural-related donor or acceptor levels in inorganic semiconductors (recall section 2.2.1). In polymers, inserted doping agents within the polymer chains can be easily removed by applying an opposite electrical driving force. Consequently and most significantly, the doping processes of conducting polymers are reversible and may be monitored by an external polarisation, which may be promoted and controlled in suitable electrochemical cells.

In oxidised heterocyctic polymers the radical cation (which is partially delocalised over the polymer segment and is stabilised by polarising the surrounding medium) is called *polaron*. Similarly, *polarons* with opposite charge may form in reduced heterocyclic polymers. It is energetically described as *polaron* levels situated at approximately 0.5 eV from HOMO or LUMO levels [5-7] (see Figure 2.8). When further electrons are removed from oxidised chain, dications (in the case of re-reduction, dianions) are formed and called as *bipolarons*. At sufficiently high doping levels, the bipolaronic bands may

overlap with HOMO and LUMO levels, thus approaching the metallic regime [8]. These polaron and bipolarons are said to be responsible for electrical conductance in heterocyclic polymers (see Figure 2.8).

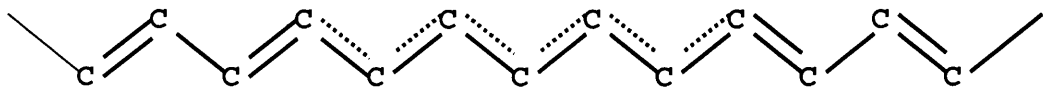

Figure 2.7 *Formation of transition zone in polyacetylene chain.*

The electrical conductance in polyacetylene is somewhat different from heterocyclic polymers. Polyacetylene has a degenerative ground state and it possesses two geometric having exactly the same energy (recall the 'kekule structure' for benzene ring) and differing only in the carbon-carbon single and double bonds. Since both structures are chemically and energetically equivalent, it is possible that in long chains one part tends to assume one version of structure and another part the other version with a transition zone in between (see Figure 2.7). In the transition zone, the resulting bond length alternation (double bonds gradually become longer whereas single bonds become shorter) leads to a structural distortion. The electronic state which; due to the symmetry of the electronic distribution lies precisely at middle of the HOMO-LUMO gap and termed as *neutral soliton* (see Figure 2.8). Similarly, oxidised polyacetylene chain acquires *positive solitons* and reduced polyacetylene acquires *negative solitons*.

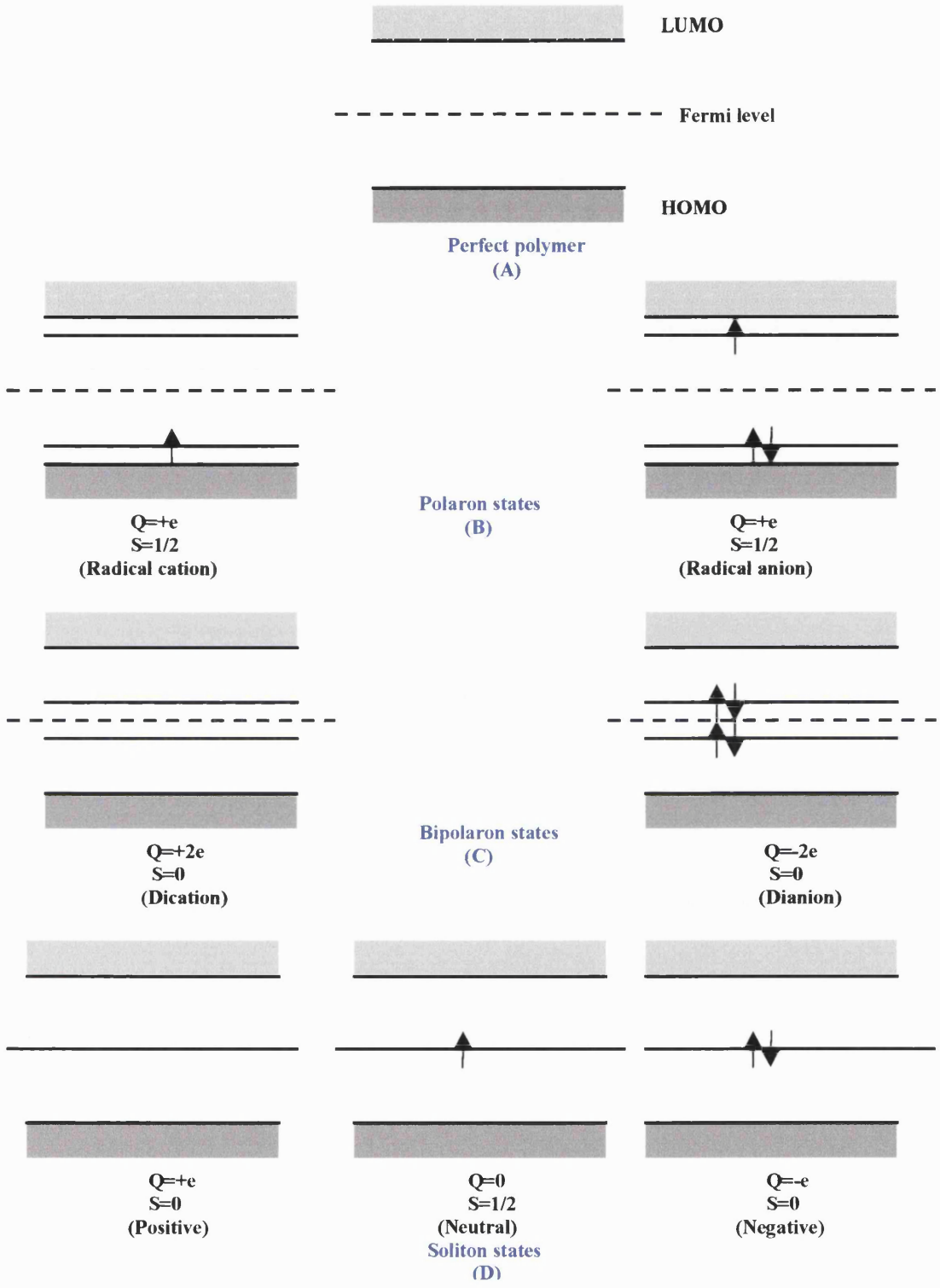

Figure 2.8 *Electronic energy levels associated with perfect polymers, polarons, bipolarons and solitons.*

Generally, the charge carrier movement along the conjugated polymers by polarons (positive or negative), bipolarons (dications or dianions) or solitons (neutral, positive or negative) can be described as follows.

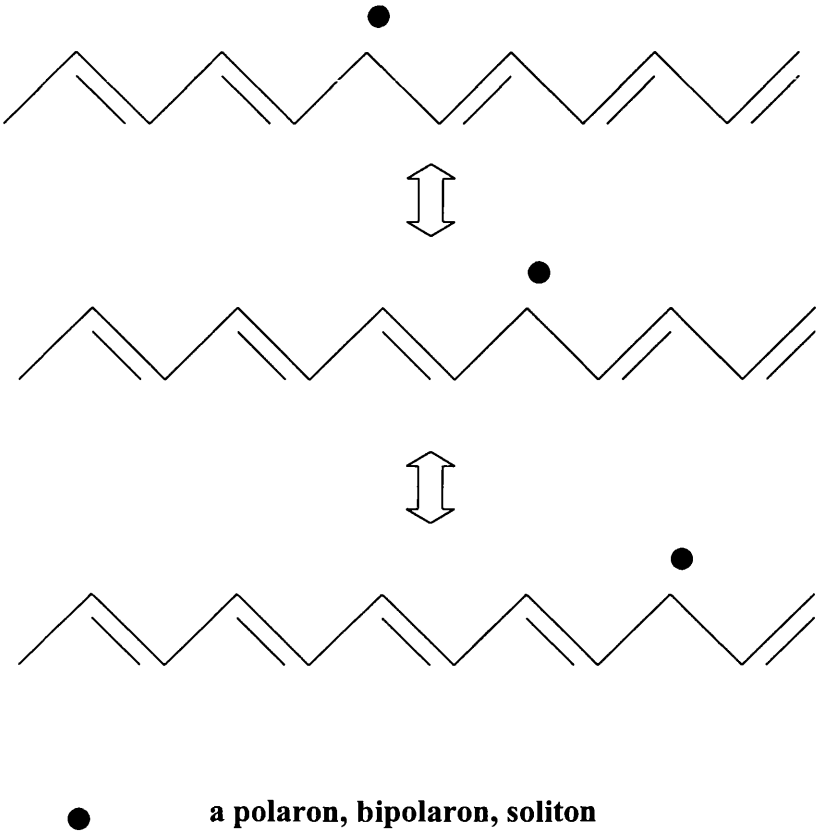

● **a polaron, bipolaron, soliton**

Figure 2.9 *Charge carrier movement along the conjugated polymer chain.*

2.3 Distribution of Electronic Energy States in Semiconductors and Liquid Electrolytes, and Charge Transport

2.3.1 The Fermi Energy (E_F)

The Fermi energy (also known as electrochemical potential of electrons) describes the distribution of electrons and holes in the available energy levels of a solid in

thermodynamic equilibrium. The Fermi-Dirac probability distribution function, *f(E)*, which expresses the probability that a level at energy E is occupied by an electron.

$$f(E) = \frac{1}{1 + e^{(E-E_F)/kT}} \tag{2.1}$$

where k is the boltzmann constant, T is the absolute temperature, E_F is the Fermi energy and E is the energy level of interest. The position of the Fermi level relative to the bands of a solid distinguishes a metal from a semiconductor or an insulator. For example, if the Fermi energy is in a region of the band with a very high density of states, then the material is metal. If the Fermi level is in a forbidden region, the material is either a semiconductor or an insulator. At absolute zero of temperature, $f(E) = 1$ for $E < E_F$ and $f(E) = 0$ for $E > E_F$. (approximations at 0 K is useful for simple descriptions)

The probability that the energy states at the bottom of the conduction band and the top of the valence band are occupied by an electron is given by equations (2.2) and (2.3) respectively.

$$f(E_C) = \frac{1}{1 + e^{(E_C-E_F)/kT}} \tag{2.2}$$

$$f(E_V) = \frac{1}{1 + e^{(E_V-E_F)/kT}} \tag{2.3}$$

Assuming that only electrons occupying energy states at the top of the valence band can gain sufficient energy to transfer to energy states at the bottom of the conduction band, the density of occupied states in the conduction band ($N(E_C)$) and the density of energy states that remain occupied in the valence band ($N(E_V)$) at temperature T are given by

$$N(E_C) = Nf(E_C) = \frac{N}{1 + e^{(E_C-E_F)/kT}} \tag{2.4}$$

$$N(E_V) = Nf(E_V) = \frac{N}{1 + e^{(E_V - E_F)/kT}} \tag{2.5}$$

where N is the number of electrons per unit volume in the semiconductor that gained sufficient energy to transfer from the bottom of the valence band to the top of the conduction band at absolute zero. However

$$N(E_C) = N - N(E_V) \tag{2.6}$$

This follows,

$$E_F = \frac{1}{2}(E_V + E_C) \tag{2.7}$$

Therefore, the Fermi energy lies halfway between the top of the valence band and the bottom of the conduction band in an intrinsic semiconductor at absolute zero temperature (see Figure 2.10).

However, in the case of an extrinsic semiconductor that contains donor atoms the Fermi energy lies between the donor state and the conduction band at absolute zero (recall Figure 2.4b). On the other hand in an extrinsic semiconductor that contains acceptor atoms the Fermi energy lies between the acceptor state and the valence band at absolute zero (recall Figure 2.4c).

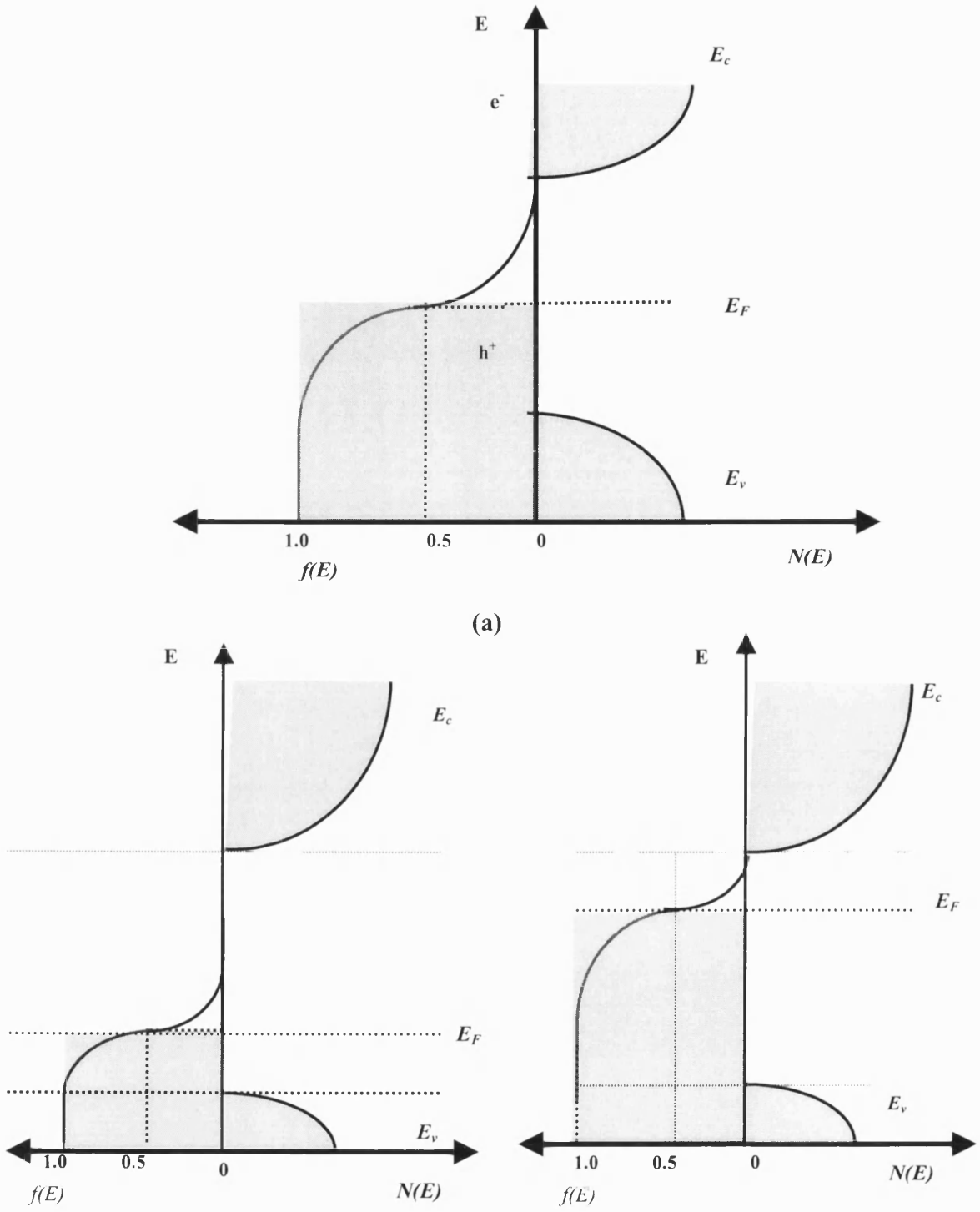

Figure 2.10 *Fermi-Dirac probability distribution function (at T K) and density of states function for (**a**). Intrinsic semiconductor (**b**). p-type semiconductor (c) n-type semiconducor. (note that the tinted grey region in f(E) in all three cases shows the occupation of levels at T=0 K.)*

2.3.2 The Quasi Fermi Level (QFL)

If a semiconductor electrode is illuminated with light of an energy higher than the bandgap energy, then the photogeneration of electrons and holes leads shift of the energy reference levels relavent to the charge carriers. This is a thermodynamically non equilibrium situation, but under steady-state conditions it can be described by the introduction of the quasi Fermi level concept. In the case of electrons the quasi Fermi level is given by

$$\frac{n_0 + \Delta n}{N_C} = e^{-(E_C - {}_nE_F)/kT} \tag{2.8}$$

where Δn is the excess electron density under illumination. The quasi Fermi level of holes is given by

$$\frac{p_0 + \Delta p}{N_V} = e^{-({}_pE_F - E_V)/kT} \tag{2.9}$$

where Δp is the excess hole density under illumination. However, in a dye-sensitised n-type semiconductor electrode, only the electron density increases under illumination, and the electron quasi Fermi level, ${}_nE_F$ reflects the newly acquired non-equilibrium energy level.

2.3.3 The Redox Energy Level in a Liquid Electrolyte Solution

As already discussed, in an n-type semiconductor, conduction band electrons (in the case of p-type semiconductor, holes) are essentially delocalised, moving about freely in the regular periodic environment of the crystal lattice. However, in the other side of a semiconductor/liquid interface the situation is somewhat different, since the electrons are localised on the orbitals of individual ionic or molecular species and conduction involves the migration of ions. The absence of long range order in an electrolyte solution results to a situation which is subject to random thermal fluctuations; ions are free to move, and they are surrounded by other ions and dipoles that are in a situation that is constant thermally perturbed. Consequently, the electronic energy levels of a particular ion will change with time over a range of values around its most probable value which is determined by the interactions of the ion with its local environment, placing important restrictions on the probability of electron transfer to and from energy levels in the adjacent semiconductor electrode. This very complicated situation lead to introduction of the following simplified model [9-11]. However, it is worth noting here that the fluctuations stem from ionic or molecular motion which is slow enough the ions and molecules to be considered frozen during the charge transfer process. The fluctuations arise from the polarisation of electron shells which is very rapid and averages out during the charge transfer process (Franck-Condon principle).

In this model, the fluctuating energy levels of oxidised and reduced species are defined by a Gaussian distribution that reflects the temporal energy fluctuation of each level. The distribution of energies about the most probable energy level of oxidised species in the solution is given by

$$W(E) = [4\pi\lambda kT]^{-1/2} \exp - \left[\frac{(E_{ox} - E)^2}{4\lambda kT} \right] \qquad (2.10)$$

Similarly, the distribution of energies about the most probable energy level of reduced species in the solution is given by

$$W(E) = [4\pi\lambda kT]^{-1/2} \exp - \left[\frac{(E_{red} - E)^2}{4\lambda kT} \right] \tag{2.11}$$

where, λ is the 'reorganisation energy' associated with the energy fluctuations. The differing polarisation of the dielectric for the oxidised and reduced species leads to a splitting of the energy levels given by

$$E_{ox} - E_{red} = 2\lambda \tag{2.12}$$

The reorganisation energy , λ is also known as the activation energy of reduction or oxidation reaction. The redox reactions faster when activation energy, λ lower. However, one cannot excite an electron, either thermally or optically, from the lower Gaussian (the reducing agent) directly to the upper Gaussian (the oxidising agent) because the reducing agent and the oxidising agent are separated in the solution space. The standard redox Fermi level, E^{θ}_{redox} is then defined as

$$E^{\theta}_{redox} = \frac{1}{2}(E_{ox} - E_{red}) \tag{2.13}$$

Figure 2.11 shows the accepted model of energy levels in an electrolyte solution that contains a redox couple.

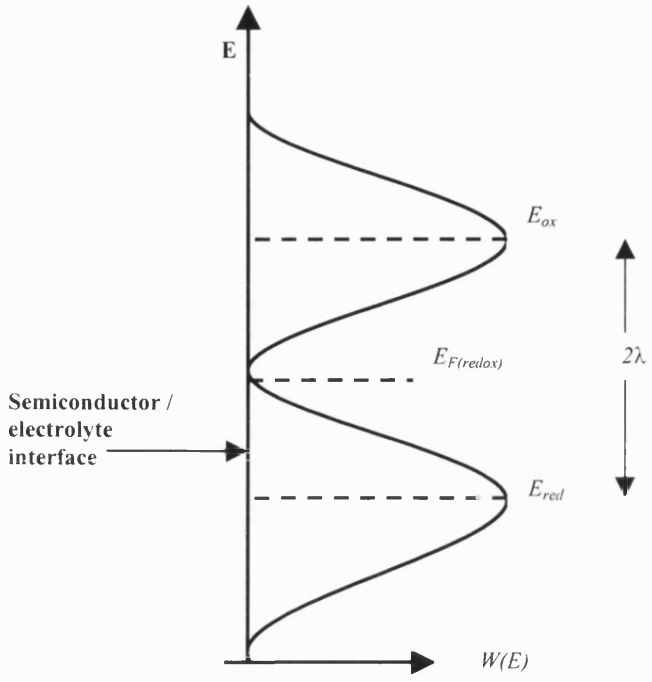

Figure 2.11 *Gaussian distributions of the energies of oxidised and reduced species in an electrolyte solution.*

2.3.4 Charge Transport

In general, three modes of charge transport can be described in electrochemical systems. They are diffusion, migration and convection. However, in photoelectrochemical systems, where the influence of mechanical forces is absent, the charge transport occurs either by one of the first two modes (diffusion or migration) or by both.

Diffusion

Diffusion is the movement of neutral or charged species down a concentration gradient. When a concentration is unevenly distributed due to a homogeneous or heterogeneous chemical reaction, diffusion takes place to smooth out the concentration inhomogeneities and maximise the entropy. The rate of diffusion of a particular species at a given point

depends upon the concentration gradient of that particular species at that point. According to Fick's first law (in one direction),

$$J_A = -D_A \frac{\partial [A]}{\partial x} \tag{2.14}$$

Where J_A is the diffusional flux of species A, D_A is the diffusion coefficient of species A, [A] is the concentration of species A and x is the distance. The change in concentration at a given point as a function of time can be expressed by Fick's second law (in one direction),

$$\frac{\partial [A]}{\partial t} = D_A \left[\frac{\partial^2 [A]}{\partial x^2} \right] \tag{2.15}$$

Migration

The movement of charged species due to a potential gradient is called migration. The electric field arising from the potential gradient, $d\phi/dx$ exerts electrostatic forces on charged species so that they migrate. In mathematical terms, the migration can be written for the one dimensional case as follows,

$$J_m = -u_C [C] \left[\frac{\partial \phi}{\partial x} \right] \tag{2.16}$$

where J_m is the migratory flux, u_C is the mobility of charged species C, [C] is the concentration of species C, and ϕ is the electrical potential.

2.4 The Semiconductor Electrode / Liquid Electrolyte Interface

The understanding of the semiconductor/electrolyte junction is based mainly on consideration of the electron energy levels in both bulk phases. The orderly arranged solid phase defined by the band model differs considerably from the disordered solution phase, which is responsible for large temporal fluctuations in the electron energy levels associated with redox species. As shown in Figure 2.12, when an n-type semiconductor and a redox couple in a liquid electrolyte solution are brought together ($E_F > E_{redox}$), electrons will flow from semiconductor phase to liquid electrolyte until Fermi levels in both phases become to a same energy level.

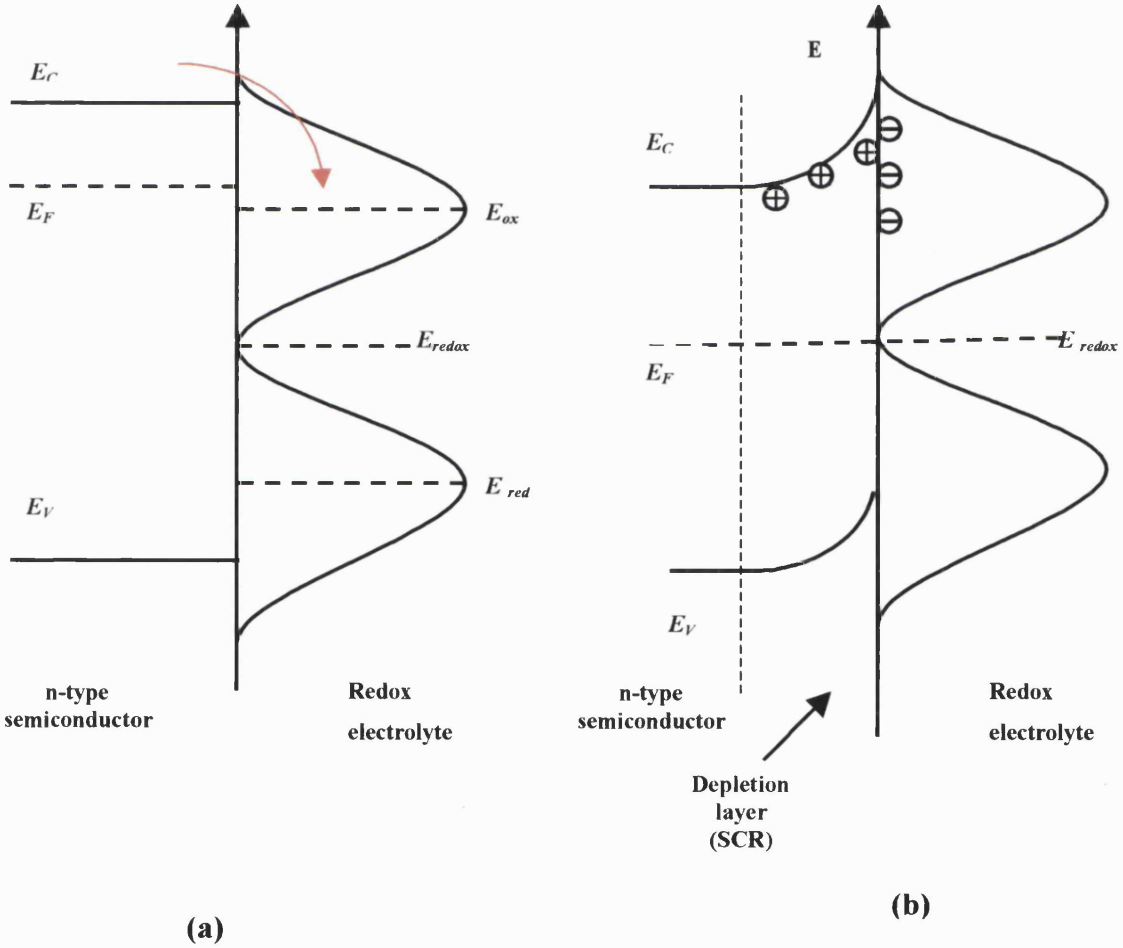

Figure 2.12 *(a) Semiconductor/electrolyte system before contact* ***(b)*** *the system after achieving equilibrium.*

At equilibrium, the Fermi energy (the electrochemical potential) must be constant throughout the system. Therefore,

$$_{sc}\bar{\mu}_e = {}_{redox}\bar{\mu} \tag{2.17}$$

where $_{sc}\bar{\mu}_e$ is the electrochemical potential of the semiconductor and $_{redox}\bar{\mu}$ is the electrochemical potential of redox electrolyte. At this point it is worth to recall the definition of the electrochemical potential of a given species *i*.

$$\bar{\mu}_i = \mu_i + z_i F\Phi \tag{2.18}$$

where μ_i is the chemical potential of the species *i*, and $z_iF\Phi$ is the electrical component (z_iF corresponds to the charge per mole of species *i* and Φ is referred to as the inner (or Galvani) potential of the phase.) The chemical potential of a species *i*, μ_i is given by

$$\mu_i = \mu_i^{\theta} + RT\ln a_i \tag{2.19}$$

where μ_i^{θ} is the standard chemical potential of species *i* and a_i is the activity of species *i*. For an ideal solution, a_i can be replaced by the concentration of species *i*, [*i*].

The injected electrons from the n-type semiconductor participate in redox reactions as follows.

$$O + e \leftrightharpoons R \tag{2.20}$$

At equilibrium, the electrochemical potential of the reactant and products must be equal. Therefore,

$$\overline{\mu}_O + \overline{\mu}_e = \overline{\mu}_R \tag{2.21}$$

where $\overline{\mu}_O$, $\overline{\mu}_e$ and $\overline{\mu}_R$ are the chemical potentials of oxidised species, electrons and , reduced species respectively.

$$\overline{\mu}_e = \overline{\mu}_R - \overline{\mu}_O = \overline{\mu}_{redox} \tag{2.22}$$

Equation (2.22) can be expanded using equation (2.18) to give,

$$\mu_e - F\Phi_{SC} = (\mu_R + z_R F\Phi_{sol}) - (\mu_O + z_O F\Phi_{sol}) \tag{2.23}$$

$$(Z_R - Z_O)F\Phi_{sol} + F\Phi_{SC} = \mu_e + \mu_O - \mu_R \tag{2.24}$$

as $z_O - z_R = 1$,

$$\Phi_{SC} - \Phi_{sol} = \frac{1}{F}(\mu_e + \mu_O - \mu_R) \tag{2.25}$$

Equation (2.25) can be expanded using equation (2.19).

$$\Delta\Phi_{sol,SC} = \frac{1}{F}\{\mu_e + \mu_O^\theta + RT\ln[O] - \mu_R^\theta - RT\ln[R]\} \tag{2.26}$$

where $\Delta\Phi_{sol,SC}$ is the electrical potential drop across the semiconductor/electrolyte interface. The $[O]$ and $[R]$ are the concentrations of oxidised and reduced species respectively.

$$\Delta\Phi_{sol,SC} = \frac{1}{F}\left[\mu_e + \mu_O^\theta - \mu_R^\theta\right] + \frac{RT}{F}\ln\frac{[O]}{[R]} \tag{2.27}$$

This follows,

$$\Delta\Phi_{sol,SC} = \Delta\Phi^{\theta}_{sol,SC} + \frac{RT}{F}\ln\frac{[O]}{[R]} \tag{2.28}$$

where $\Delta\Phi^{\theta}_{sol,SC} = \frac{1}{F}\left[\mu_e + \mu^{\theta}_O - \mu^{\theta}_R\right]$. The equation (2.28) is the Nernst equation and can be presented in the usual form as follows.

$$E = E^{\theta} + \frac{RT}{F}\ln\frac{[O]}{[R]} \tag{2.29}$$

where $E = \Delta\Phi_{sol,SC}$ and $E^{\theta} = \Delta\Phi^{\theta}_{sol,SC}$.

2.4.1 Double layers on Semiconductor / Electrolyte Interfaces

The electron exchange that takes place at the semiconductor/electrolyte interface to achieve thermodynamic equilibrium leads to rearrangement of charged species in adjacent phases so that the system becomes electrically neutral. At a semiconductor/electrolyte interface, there are three types of double layer to consider: the space charge, the Helmholtz and the Gouy-Chapman double layers [12, 13].

The space charge layer

Before contact has been made between an n-type semiconductor and a liquid electrolyte that contains a redox couple, the band model might appear as in Figure 2.12(a). In this particular case, the electrochemical potential of electrons, E_F, is higher in the semiconductor than the redox potential, E_{redox} in the liquid electrolyte. However, when contact is made, electrons will flow from the semiconductor to the liquid electrolyte to establish equilibrium, leaving positively charged donors in the semiconductor and charging the solution phase negative. Therefore, the electrons are depleted from the semiconductor surface region, and the region is termed a *depletion* layer or a *space charge layer*. The potential change as a function of distance in the depletion layer region

leads to the band bending. However, when the system reaches equilibrium, the electron flow from the semiconductor to the electrolyte equals the flow from the electrolyte to the semiconductor and the band diagram at the interface must have the form of Figure 2.12(b). An equivalent *depletion layer* occurs when holes are extracted from a p-type semiconductor by electron injection from a reduced solution species.

Another case at the semiconductor/liquid electrolyte interface is the formation of an *accumulation layer*. An accumulation layer forms as a result of injection of electrons into the conduction band of an n-type semiconductor by a strong donor or extraction of electrons from (injection of holes into) the valence band of a p-type semiconductor by a strong acceptor. An accumulation layer can also form under externally applied appropriate voltage (negative voltage for an n-type semiconductor electrode). Finally, a third and important case is the formation of an *inversion layer*, where the band bending is so strong that the Fermi energy at the semiconductor surface is closer to the minority carrier band than the majority carrier band. Then the surface is *inverted* from an n-type bulk to a p-type surface or from p-type bulk to an n-type surface.

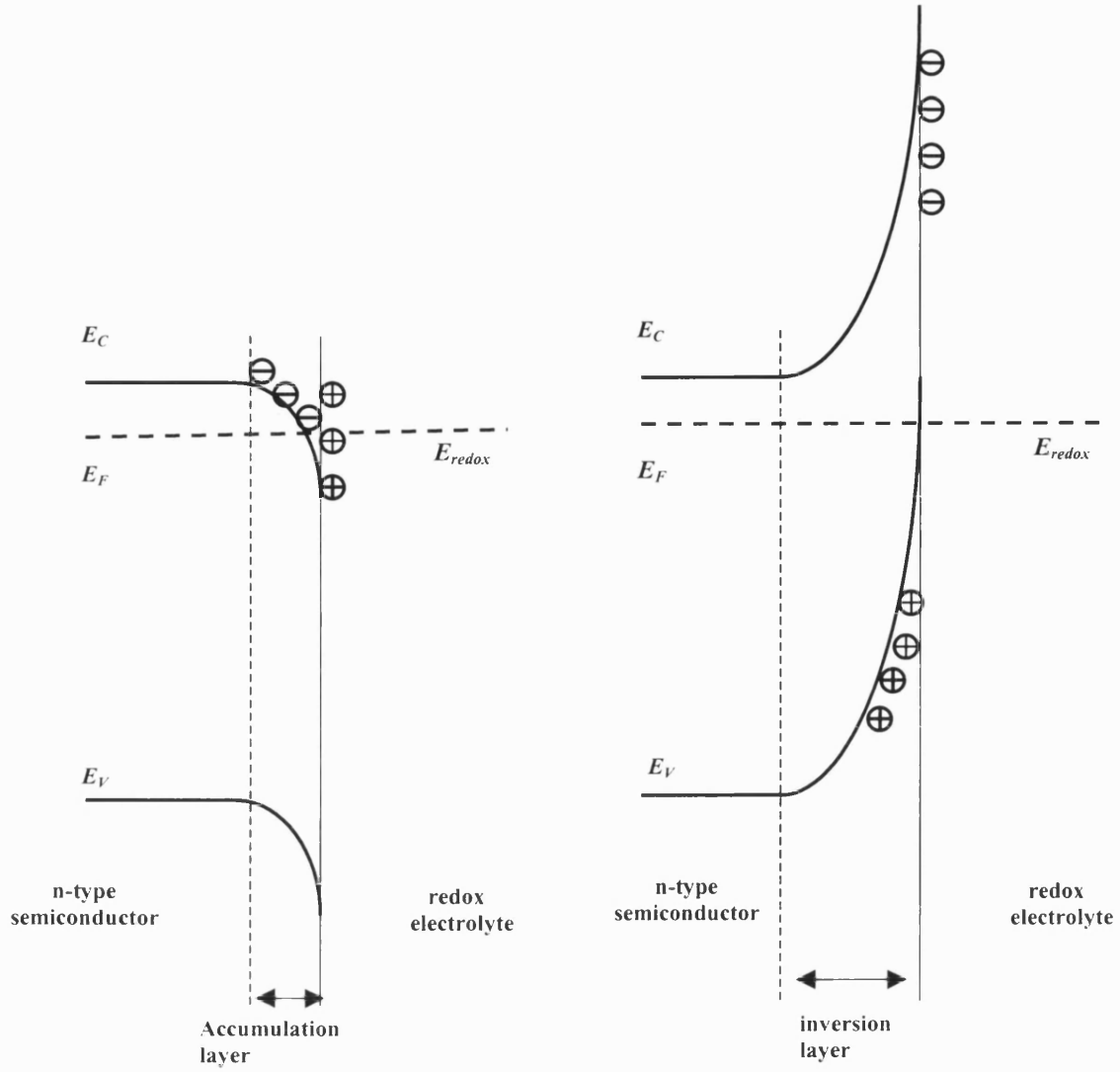

Figure 2.13 ***(a)*** *Formation of an accumulation layer* ***(b)*** *Formation of an inversion layer*

Figure 2.13 illustrates the formation of accumulation and inversion layers at thermodynamic equilibrium at an interface of n-type semiconductor/redox electrolyte solution. Formation of *depletion*, *accumulation* and *inversion* layers at thermodynamic equilibrium at an interface of p-type semiconductor/redox electrolyte solution can also be illustrated in similar fashion. The width of the *accumulation layer* is very thin compared with that of *depletion* and *inversion layers*. This is due to the fact that electrons (or holes) are delocalised throughout the Fermi energy state of the semiconductor and can move freely, whereas the donor ions are fixed in the semiconductor lattice.

The space charge double layer is made up of charged donors or acceptors in the space charge region. The potential throughout the space charge region is given as a function of distance by Poisson's equation [12, 13]. By making the 'abrupt depletion approximation' and then solving the Poisson's equation, one obtains the following expressions for the width (W) and charge (N_S) of the space charge region (for depletion region) in n-type semiconductor.

$$W = \left[\frac{2\Delta\phi_{sc}\varepsilon\varepsilon_0}{qN_d} \right]^{1/2} \tag{2.30}$$

$$N_s = \left[\frac{2\Delta\phi_{sc}\varepsilon\varepsilon_0 N_d}{q} \right]^{1/2} \tag{2.31}$$

where ε is the relative permitivity, ε_o is the permittivity of free space, N_d is the doping density, q is the elementary charge and $\Delta\phi_{sc}$ is the surface charge. For a n-type semiconductor the capacitance of the space charge layer (C_{sc}) is given by the following equation [12, 13]

$$C_{sc} = \sqrt{\left(\frac{\varepsilon\varepsilon_0 q^2 N_d}{2kT} \right)} \frac{\left[\exp\left(-\frac{e}{kT}\Delta\phi_{sc} \right) - 1 \right]}{\sqrt{\left\{ \frac{q}{kT}\Delta\phi_{sc} + \left[\exp\left(-\frac{e}{kT}\Delta\phi_{sc} \right) - 1 \right] \right\}}} \tag{2.32}$$

The variation of C_{sc} with applied potential (in the non-equilibrium situation) is described by the Mott-Schottky equation [13].

$$C_{sc}^{-2} = \frac{2}{\varepsilon\varepsilon_0 q N_d} \left(\Delta\phi_{sc} - \frac{kT}{q} \right) \tag{2.33}$$

The equation (2.33) can also be written as the following useful way.

$$C_{sc}^{-2} = \frac{2}{\varepsilon\varepsilon_0 q N_d}\left(U - U_{FB} - \frac{kT}{q}\right) \tag{2.34}$$

where U is the applied potential and U_{FB} is the flatband potential. Plots of C_{sc}^{-2} versus the applied potential are used to determine the flatband potential and the doping density. It is of practical interest to estimate the thickness of the space charge layer. For a semiconductor with a doping density of the order of 10^{23} m^{-3}, a relative permitivity of 10, and U-U_{FB} = 1 V, one estimates the space charge layer thickness to be about 1000 Å. Figure 2.14 illustrates the potential distribution across space charge region, Helmholtz and Gouy-Chapman regions at an n-type semiconductor/liquid electrolyte interface.

The Helmholtz Layer

The Helmholtz double layer on a semiconductor in general is composed of a sheet of ions adsorbed at the surface and ions of the opposite sign attracted to the surface by the adsorbed ions. On a semiconductor surface, it has a high charge per unit area. In principle up to a monolayer of ions can be adsorbed. The free ions in the solution can move close to the adsorbed surface charge, so the effective capacity of the double layer is high. In aqueous solution the adsorbed ions are usually H^+ and OH^-, with one of these dominating. The dominant species (either H^+ or OH^-) is depending on the solution pH. The adsorption of H^+ and OH^- is high if the electrode is a reasonably polar material, either an oxide semiconductor or a non-polar semiconductor with a polar oxide layer. In that case each positive lattice ion (Ti^{4+} on a TiO_2 surface) attracts an OH^- ion as an adsorbate and each negative ion (usually O^{2-}) attracts an H^+ ion so that both species are adsorbed. However, a slight imbalance in the concentration of H^+ and OH^- leads to large net surface charge.

The variation of the Helmholtz potential with solution pH depends on how polar the electrode material. Strong ionic solid will strongly adsorb H^+ and OH^- ions and the Helmholtz potential will vary in a Nernstian fashion, 59 mV per pH unit [12]. However,

materials like silicon with a thin oxide layer is only partially polar and the Helmholtz potential vary by 30 mV per pH unit [12]. Metals, if not oxidised, can show negligible pH dependence of the Helmholtz potential.

However, the situation in non-aqueous solution is entirely different. As the present study mainly deals with dye adsorbed semiconductor electrodes in non-aqueous media, it is worth of looking at such a situation. Usually redox potentials of most dyes are pH-independent. However, when they get adsorbed on semiconductor surface, can become pH-dependent if they are mostly sitting inside the Helmholtz layer [14]. This is because a part of the potential difference between the electrode and the solution drops across the adsorbed dye layer. However, such a case, the redox potentials of adsorbed dyes can be pH-independent if other ions in the solution (solution ions or redox ions) deeply penetrate into the semiconductor surface, resulting in residing them in between semiconductor surface and adsorbed dye molecules. This situation can only arise if the solution contains small cations such as Li^+ so that they can easily penetrate into the semiconductor surface. When cations such as Li^+ get adsorbed on the semiconductor surface the Helmholtz potential drops across them resulting dye redox potential is pH independent. In some cases strong adsorption of small cations such as Li^+ are also shift the semoconductor band edges [14]. However, large ions such as Ca^{2+} and R_4N^+ do not penetrate into the semiconductor surface because of the blocking effect of large dye molecules. On the other hand if adsorbed dye molecules are mostly sitting outside the Helmholtz layer, the redox potentials of them still can be pH-independent [14].

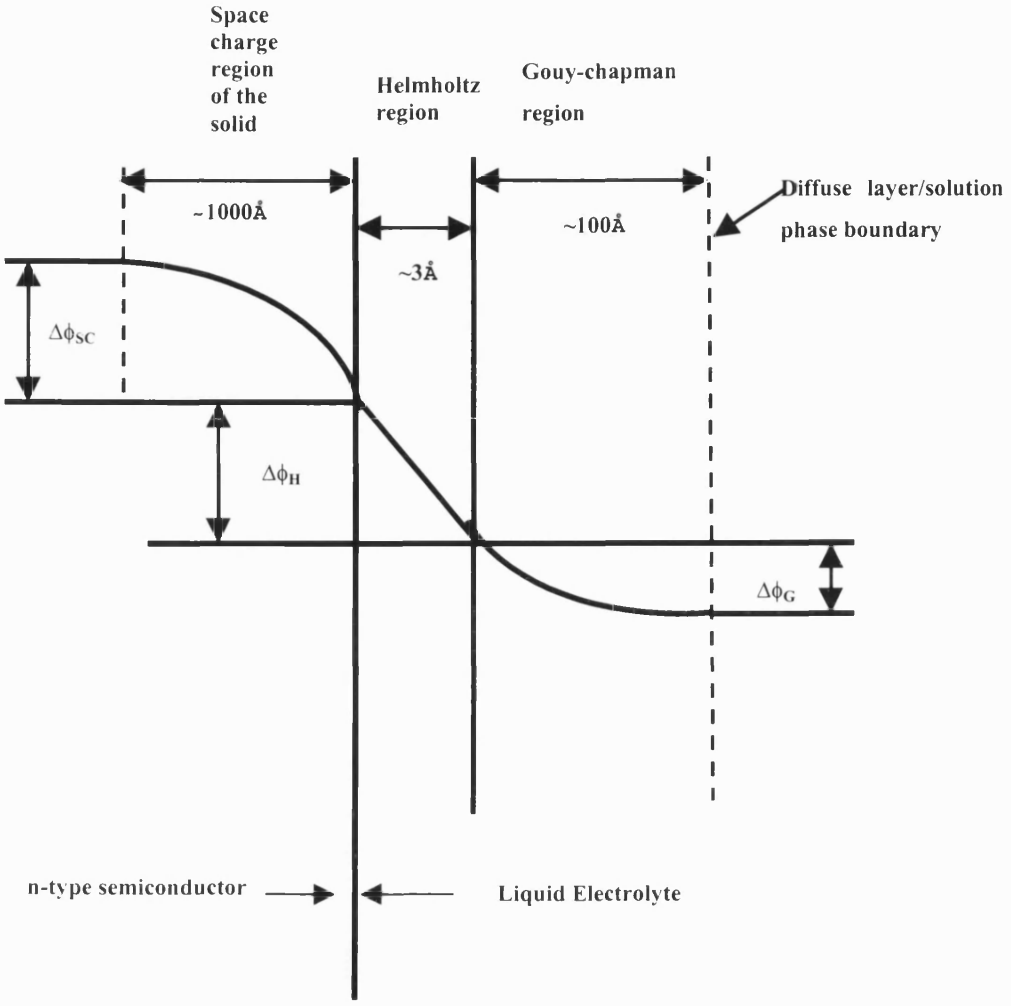

igure 2.14 *Potential distribution across the semiconductor/liquid electrolyte interface. Here, $\Delta\phi_H$ and $\Delta\phi_G$ are potential drops across the Helmholtz and the Gouy-Chapman layers.*

The Gouy-Chapman Layer

Finally, the Gouy-Chapman layer is formed when the charge on the OHP is not enough to compensate the charge on the electrode, hence charge with opposite sign to that on the electrode extends further into the solution. If the solution is very concentrated, the influence of the Gouy-Chapman double layer becomes negligible.

2.4.2 Photo induced electron transfer at a Flat Semiconductor Electrode / Liquid Electrolyte Interface

So far this section has discussed the situation of a semiconductor/liquid electrolyte at thermodynamic equilibrium. However, an important question in semiconductor electrochemistry is, how an electrochemical system behaves when it is not in thermodynamic equilibrium. Illumination of the semiconductor/liquid electrolyte junction or the application of an external voltage to a semiconductor electrode in contact with a liquid electrolyte are examples of non-equilibrium situations. This sub-section deals with photo induced electron transfer at a flat-semiconductor/electrolyte interface.

Consider the simplest photoelectrochemical (PEC) cell that consists of an n-type semiconductor working electrode and a metal counter electrode, both in contact with a liquid electrolyte (again in this particular case, $E_F > E_{redox}$). In the dark, the system is in thermodynamic equilibrium and the Fermi energy is constant throughout the system. Therefore, band bending occurs and the space charge region (SCR) forms (in this particular case, a *depletion* layer forms). When the semiconductor electrode is illuminated with light of energy greater than the bandgap energy, photon absorption results in the creation of electron-hole pairs. In the case of an n-type semiconductor, light absorption increases the hole concentration substantially above the dark value while the increase in the electron concentration is negligible compared to its dark value. This drives the PEC cell away from thermodynamic equilibrium. At open-circuit, the photovoltage is determined by the potential difference between electron quasi Fermi level and the redox level in the solution. When the PEC cell is shifted into short-circuit condition, it is the depletion layer (also referred to as the Schottky barrier), which plays an important role in photo-induced charge separation. The local electrostatic field in the depletion layer contributes to the driving force to separate the photo-generated electron-hole pairs. In this system, the direction of the field is such that holes migrate to the surface, where they undergo chemical reaction (take part in oxidation reactions etc.), while the electrons drift through the bulk to the back contact of the semiconductor and subsequently through the

external circuit to the counter electrode. Figure 2.15 shows the photo-induced charge separation and recombination at a semiconductor working electrode.

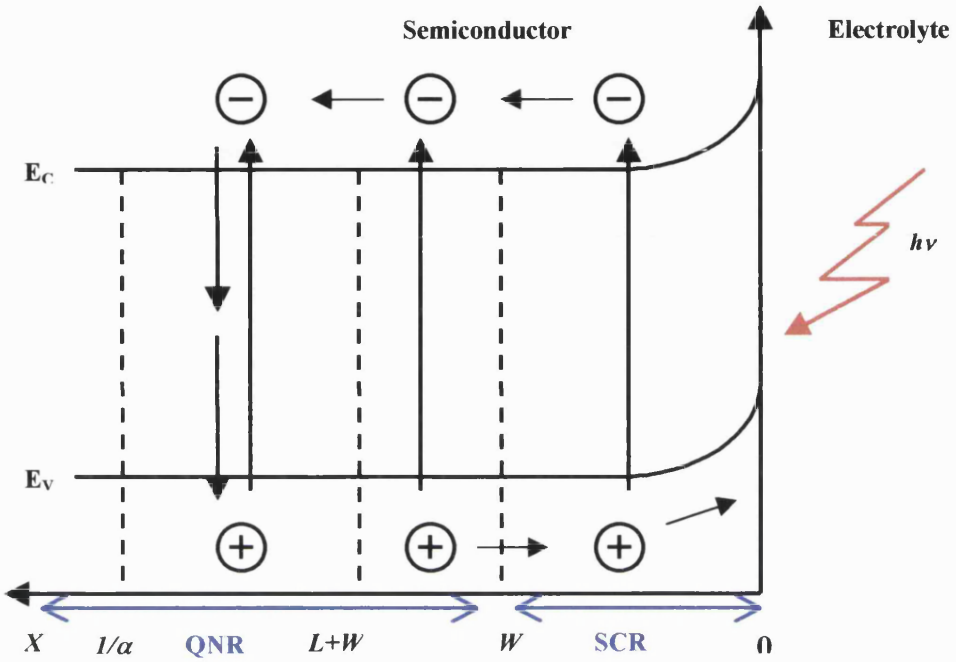

Figure 2.15 *Photo-induced electron-hole pair separation and recombination in the semiconductor electrode.*

In this type of PEC cell (also referred to as a Schottky device or a minority carrier device) the flux of photogenerated holes that migrate towards the surface depends on the width of the SCR, the optical absorption coefficient of the semiconductor material and the diffusion length of the holes. In semiconductors with a low defect concentration, and if the lifetime of the electron-hole pairs is long enough to allow for some holes to diffuse to the SCR, holes generated in the quasi-neutral region (QNR; in the semiconductor electrode this region is extended all the way to the back contact but the electric field is very tiny) can also contribute to the hole flux before they undergo recombination. However, this contribution is very small, due to the tiny electric field in the QNR region. Therefore, the electron-hole pairs generated in the neutral bulk region (i.e. at $x > W + L_p$)

are mainly subjected to recombination resulting in heat evolution (see Figure 2.15). Therefore, in semiconductors with low optical absorption coefficients, hence a long light penetration depth, and a small minority carrier diffusion length, bulk recombination plays an important role. If the increase in the density of photogenerated electrons in this PEC is negligible, the recombination rate is first order with respect to hole concentration and characterised by a minority carrier life time, τ_p (electrons are the majority carriers in this case). An effective diffusion length, L_p can be defined within which electron-hole pair separation is achieved.

$$L_P = (D_P \tau_P)^{1/2} = (kT u_P \tau_P)^{1/2} \tag{2.35}$$

where, L_p is the hole diffusion length, D_p is the diffusion coefficient of the holes, u_p is the corresponding mobility of the holes and τ_p is the lifetime of the holes. Considering the *depletion* situation in a p-type semiconductor electrode, one can derive the corresponding expression for the electron diffusion length, L_n.

If recombination within the SCR is neglected and minority carriers effectively undergo chemical reactions at the interface, the photocurrent only depends on the generation and collection. Considering this ideal situation and solving the generation and collection problem using the appropriate boundary values, Gärtner obtained an expression for the photocurrent density.

$$J_{photo} = qI_O \left[1 - \frac{e^{-\alpha W}}{1 + \alpha L_P} \right] \tag{2.36}$$

where I_0 is the incident photon flux corrected for reflection losses and α is the absorption coefficient of the semiconductor material. The ratio of j_{photo}/qI_0 is also known as the photocurrent conversion efficiency, Φ. The minority carrier diffusion length and the absorption coefficient can be obtained using the plots of ln (1-Φ) versus W.

However, it has been found that the experimental photocurrent-voltage plots always deviate from equation (2.36) [15, 16]. This may be due to the influence of the

recombination processes within the SCR, QNR and the interface, which have been neglected in the derivation of equation (2.36). The effects of recombination are particularly evident when the band bending in the semiconductor is relatively small, as in the case close to the flatband potential, where the detected steady-state current is small [15, 16]. This is because the minority carriers are trapped at defects and impurity states (surface states) at the semiconductor/electrolyte interface where they undergo recombination, resulting in a flux of majority carriers into the interface. Under extreme conditions, the majority carrier flux towards the interface can be equal to the minority carrier flux, resulting in no net photocurrent. Most the minority carrier recombination takes place at the surface and in the near surface region rather than in the bulk [17]. In some cases, recombination of electron-hole pairs results in photoluminescence [18, 19]. In such cases photoluminescence can be used as a probe to determine the proportion of photoinduced charge carriers that recombine [18-20]. Figure 2.16 contrasts the ideal photocurrent-voltage curve (predicted by the Gärtner model) with real curves for the cases where surface recombination takes place.

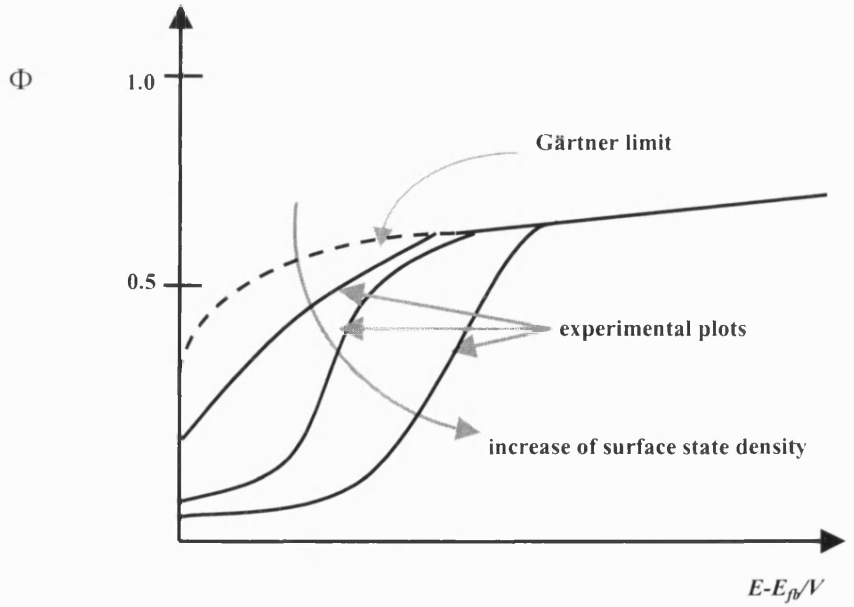

Figure 2.16 *Comparison of photocurrent-voltage plots predicted by Gärtner equation with experimental plots*

Despite the poor agreement with experimental photocurrent densities in the flatband region, equation (2.36) is successful in explaining the photocurrent-voltage characteristics of many single crystalline semiconductor electrodes in the region where band bending is relatively large. This behavior can be explained as follows. When the band bending is relatively large, the trapped majority carrier density at the surface is small (see Figure 2.17). As the recombination occurs at the semiconductor surface, in such condition the available majority carriers for recombination process is relatively low. On the other hand, the strong local electrostatic field present in the SCR effectively separates the photo-generated electron-hole pairs (electrons to the interior and holes to the surface) suppressing the recombination.

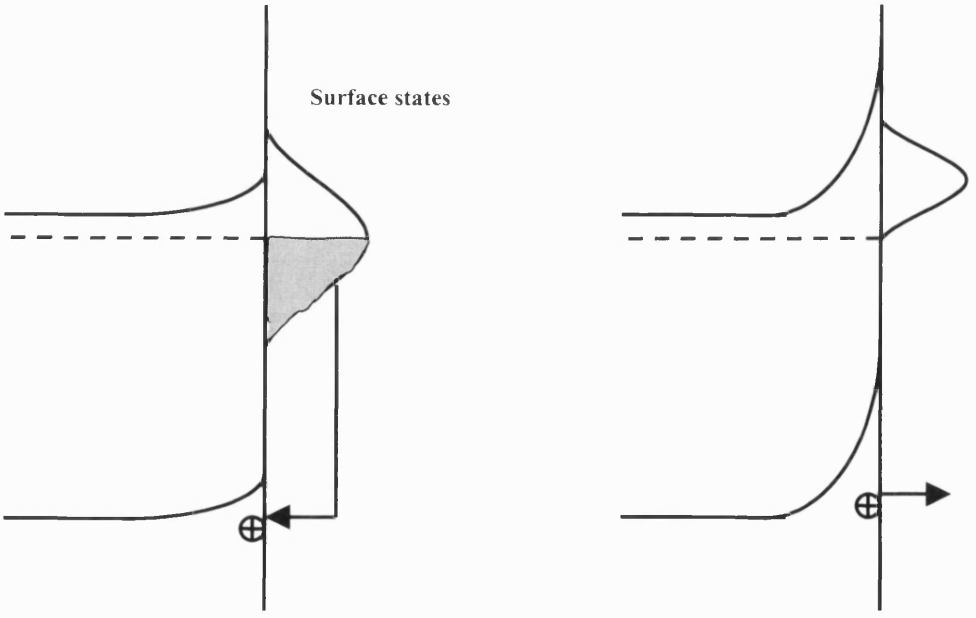

Figure 2.17 *The trapped majority carrier density at the surface* ***(a)*** *close to flatband potential* ***(b)*** *in photocurrent saturation region.*

The other assumption made in deriving the equation (2.36) is that the minority carriers are consumed by rapid electron transfer reactions at the interface. If the Gaussian energy distribution of the reduced species coincides with the energy of the valence band (E_v) it would guarantee an efficient oxidation reaction at the interface. In reality, the degree of this overlap can be varied from one system to the other, and in extreme cases the degree of overlap may be very much less, resulting in inefficient charge transfer at the interface. In such a case holes (electrons for a p-type semiconductor) can be trapped initially in an in-gap energy state before being transferred across. Therefore, trapping at an interfacial bandgap state may compete with the charge transfer. When it considers the trapping/charge transfer/recombination processes, there are three options to be discussed. They can be considered as follows.

(1) The X-X$^+$ formalism

In this case, the trapping states are considered as an unlimited supply (i.e. they are always available as the trap filling is neglected). Then, the trapping/charge transfer/recombination processes can be given by the following scheme.

$$X + h_{(vb)} \xrightarrow{\beta_p} X^+ \qquad (2.37a)$$

$$X^+ + e_{(cb)} \xrightarrow{\beta_n} X \qquad (2.37b)$$

$$X^+ + R \xrightarrow{K_{ETtrap}} O \qquad (2.37c)$$

$$h_{(vb)} + R \xrightarrow{K_{ETfree}} O \qquad (2.37d)$$

Here, X and X^+ are respectively occupied and unoccupied interfacial bandgap states. In this case, the number of available states depends on potential.

(2) A set of states that all have the same energy

This case considers a set of states that all have the same energy. Therefore, the number of available states to trap holes is equal to $N \times f(E)$.

(3) Other states distributions

The interfacial trap states can have other distributions such as exponential or Gaussian (see Figure 7.8 in chapter 7, which shows an exponential trap distribution). In such case, the number of available states is given by $\int_{E_v}^{E_c} N(E)f(E)$.

Interfacial states can either be similar to localised bulk states or they may arise from localised (chemisorbed at the electrode surface) redox states. The hole trapping rate (i.e. the rate of the step (2.37*a*) in this scheme) at an energy E can be given as follows.

$$\text{The rate of hole trapping per state} = \beta_p p(o) f(E) \qquad (2.38)$$

Where β_p is the rate constant of this process and it can be given as the product of the thermal velocity of free electrons and the capture cross section [21-25]. *p(o)* is the concentration of free holes and *f(E)* is the density of occupied states in the bandgap. The trapped holes may also be thermally released back to the valence band (i.e. drive to the reverse direction in the step (2.37*a*) of this scheme). The rate of this process per state at an energy E is described by

$$\text{The rate of thermal release of hole per state} = \beta_p N_v \exp\left[\frac{-(E-E_v)}{kT}\right][1-f(E)] \qquad (2.39)$$

Generally a trapped hole at the interface can undergo two processes. The first is donation of an electron from the reducing agent present in the adjacent solution phase (step (2.37*c*) of the given scheme) and the second is capture of a free electron (step (2.37*b*) of the given scheme). Figure 2.18 shows a schematic representation of interfacial processes.

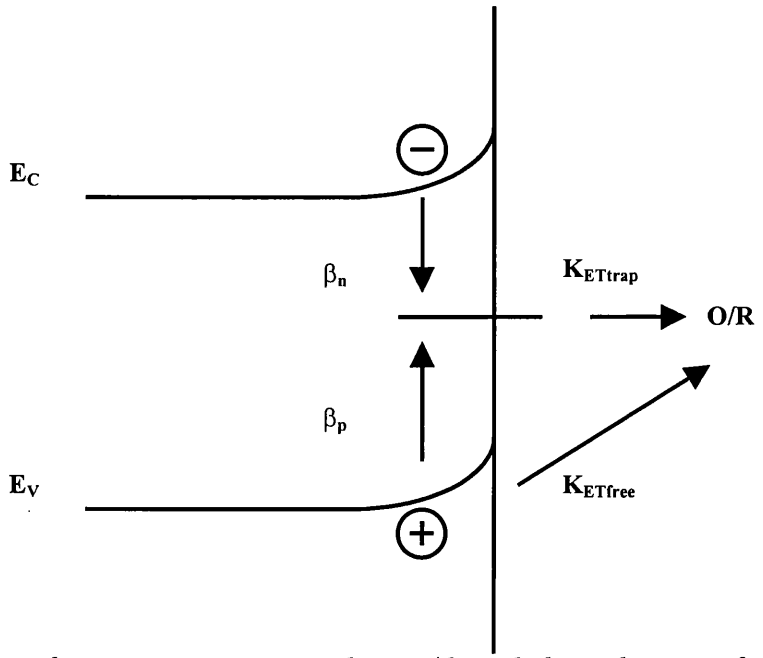

Figure 2.18 *Interfacial processes at semiconductor / liquid electrolyte interface.*

The first process (given by the step (2.37*c*) in the scheme) involves isoenergetic electron tunnelling and sinks holes at the interface participating to the electron transfer cycle. The rate of the second process (given by the step (2.37*b*) in the scheme) can be expressed as follows.

$$\text{The electron capture rate per state} = \beta_n n(o)[1 - f(E)] \qquad (2.40)$$

where *n(o)* is the concentration of free electrons at the surface. As for the case of trapped holes, trapped electrons can also be thermally released and the rate per state is given as follows.

$$\text{The rate of thermal release of electron per state} = \beta_n N_C \exp\left[\frac{-(E_C - E)}{kT}\right] f(E) \qquad (2.41)$$

Competition between thermal release and recombination of trapped electrons and holes within the interfacial bandgap region has been approached by defining a *demarcation level* [26, 27]. This is defined by assuming that electrons above *the demarcation level* are excited into the conduction band, while the ones below recombine. In the case of holes, recombination takes place above *the demarcation level*, while the thermal release takes place below it.

Surprisingly, in some PEC systems, the observed photocurrent quantum yield exceeds the Gärtner limit given by equation (2.36) [28, 29]. This process is referred to as photocurrent multiplication and attributed to majority carrier injection in an electrochemical process initiated by photogenerated minority carriers so that the observed photocurrent density is much higher than the expected maximum. Generally the photo-induced charge transfer process in a PEC can be summarised as described in Figure 2.19.

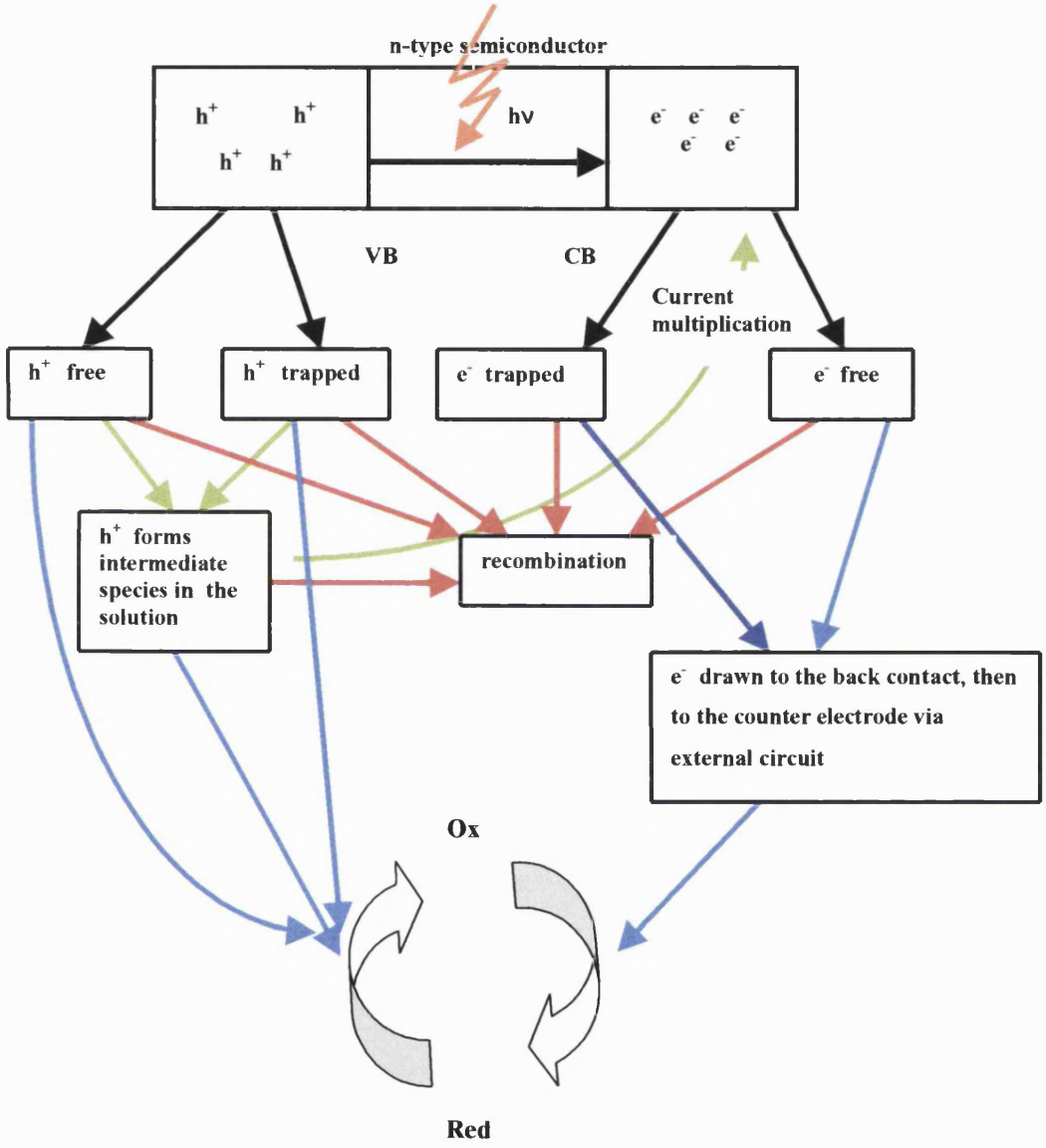

Figure 2.19 *A summary of photo-induced charge transfer process in a PEC.*

2.4.3 Behavior of an Illuminated Nanocrystalline Semiconductor Electrode / Liquid Electrolyte Interface

Now attention is turned towards the nanocrystalline semiconductor electrode/liquid electrolyte interface to discuss the salient features of these types of electrodes and their electron transfer processes, as the present study is mainly concerned with the dye-sensitised nanocrystalline TiO_2 solar cell.

Nanocrystalline semiconductor electrodes consisting of interconnected particles with dimensions in the nanometer range have attracted considerable scientific interest [30-32]. One fascinating application of nanocrystalline semiconductor electrodes is in the dye-sensitised nanocrystalline TiO_2 solar cell as the photo-active electrode [32].

The obvious difference between a flat semiconductor/liquid electrolyte junction (two dimensional) and a nanostructured semiconductor/liquid electrolyte interface (three dimensional) is, the latter is composed of interconnected nanocrystalline particles with a large number of grain boundaries, whereas the former can be represented by a conventional continuous band model. The difficulties of defining the flat semiconductor/electrolyte interface have been pointed out already in the previous section. The description of the junction at the nano-scale is even more complicated. However, it is useful to compare the physical dimensions of nanocrystalline networks with the characteristic lengths used to describe charge distribution in the solid and electrolyte phases first.

When the individual particle size becomes sufficiently small, quantum confinement effects can lead to widening the bandgap, shifting the fundamental absorption edge towards higher energy. However, the quantum confinement effect only occurs when the Bohr radius of the first exciton in the semiconductor becomes commensurate with or larger than that of the particle [33]. The Bohr radius (r_B) of the first exciton is given by,

$$r_B = \frac{h^2 \varepsilon \varepsilon_0}{c^2 \pi m^*} \tag{2.42}$$

where m* is the effective mass of the electron in the semiconductor material and c is the speed of light. For TiO_2, $m^*_{e^-} = 30\ m_{e^-}$ and $\varepsilon = 80$ yielding $r_B = 1.4$ Å. As the nanocrystalline TiO_2 electrodes are composed of particles with size of 10-50 nm they are too large to exhibit quantum confinement.

The other characteristic length that is used to describe the behaviour of nanocrystalline semiconductor electrodes is the extrinsic Debye length, L_D. It is given by

$$L_D = \left(\frac{kT\varepsilon\varepsilon_o}{q^2 N_d} \right)^{\frac{1}{2}} \tag{2.43}$$

Generally the Debye length is greater than the individual particle diameter in nanocrystalline electrodes so that there is no appreciable potential gradient within the particles caused by ionised donor or acceptor states [34]. This situation is shown in Figure 2.20, which considers the band bending in macro and nano-scale semiconductor particles [35]. This contrasts with conventional semiconductor electrodes where photogenerated electron-hole pairs are separated rapidly by the local electric field present in the SCR [36]. It follows that the conventional ways of treating PEC systems are not applicable to nanocrystalline semiconductor/liquid electrolyte interfaces. Therefore, in nanocrystalline semiconductor electrodes, the dominant driving force for the movement of charge carriers in the solid phase may be the existence of a gradient of electron concentration that arises from the light absorption profile, so that diffusion could be more important than migration. (The electron transport through the nanocrystalline phase is treated in more detail later in this section.)

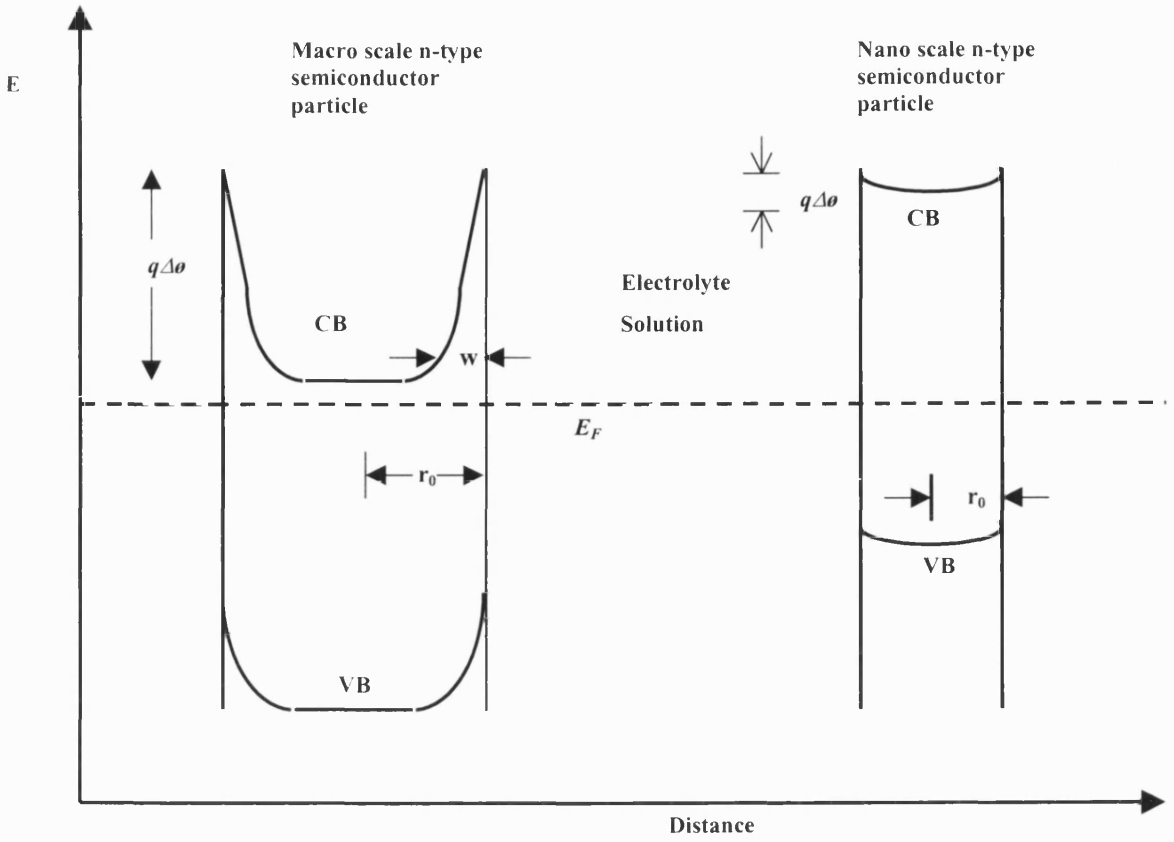

Figure 2.20 *Comparison of band bending in macro and nano particles.*

The third characteristic length that is relevant to the electronic transport properties of nanocrystalline electrodes is the excess carrier diffusion length $L = (D\tau)^{1/2}$ (cf. the equation (2.35) in the previous section which described minority carrier diffusion length). Here D is the excess carrier diffusion coefficient and τ is the excess carrier lifetime.

It is becoming clear that in nanocrystalline electrodes the width of the SCR can no longer be defined since the physical dimension of an individual nano particle is much smaller than the typical width of the SCR. However, as the Helmholtz electrical double layer thickness approach (or become less than) diameter of the structural units (r_0 in the Figure 2.20), the molecular dimensional Helmholtz electrical double layer can be formed throughout the large internal surface area of the nanoporous network. It follows that

under accumulation conditions nanoporous semiconductor electrodes behave as 'supercapacitors'. This unusual behavior has been exploited by using of simple linear sweep measurements to estimate the internal surface area of porous silicon [37]. However, this surface area measurements only valid if the solution is very concentrated. For dilute solutions the Gouy-Chapman layer may become comparable with diameter of the structural units. Figure 2.21 describes this situation.

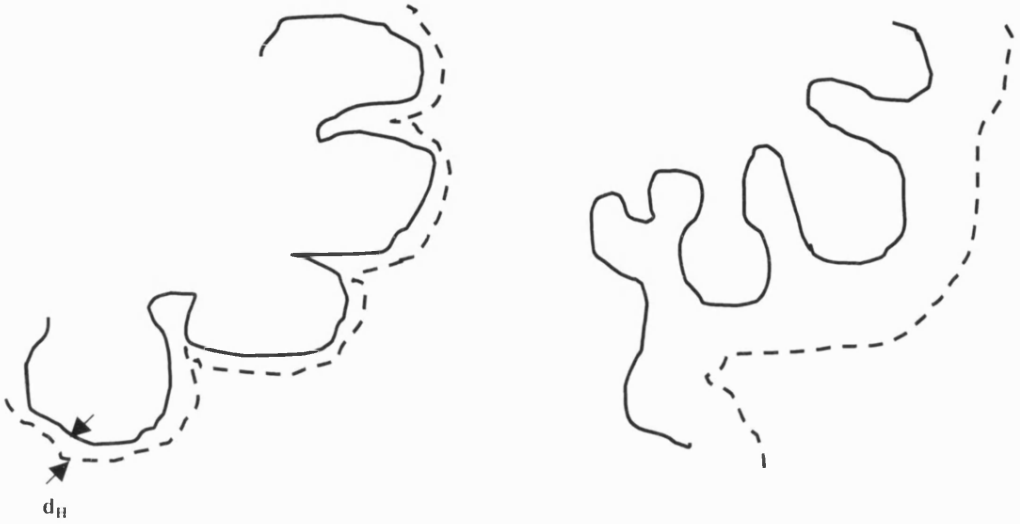

Figure 2.21 *Diffuse layer* ***(a)*** *in high concentrated electrolyte solution and* ***(b)*** *in diluted electrolyte solution.*

In the dark, the Fermi level of the nanocrystalline semiconductor electrode is in equal to E_{redox} of the electrolyte and is independent of the spatial co-ordinate x normal to the substrate. It can be assumed that the density of electrons in the nanocrystalline solid phase is negligible in the dark. Figure 2.22 describes this situation.

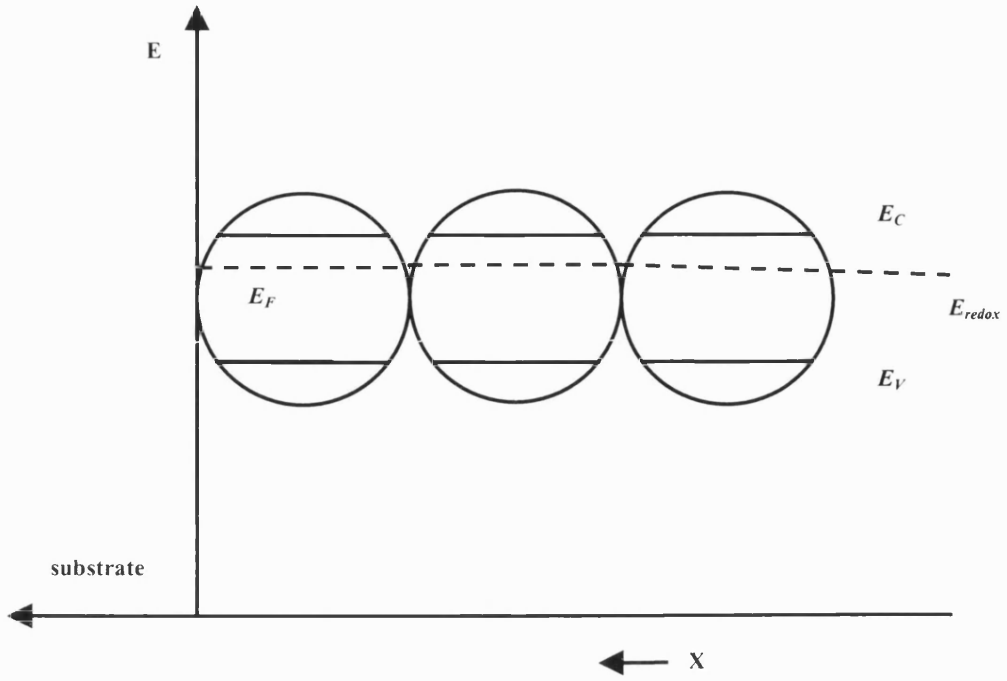

Figure 2.22 *Nanocrystalline semiconductor electrode/liquid electrolyte interface at equilibrium.*

Illumination of the nanocrystalline semiconductor electrode with a constant light intensity establishes a non-equilibrium steady-state situation (see Figure 2.24). Charge generation in the dye-sensitised nanocrystalline electrode can result from two different mechanisms: one is electron-hole generation due to the excitation above the fundamental absorption edge of the semiconductor and the other is the injection of electrons from the excited dye molecules (see Figure 2.23). However, according to Figure 1.1 in chapter 1, the AM 1.5 solar irradiance around the fundamental bandgap absorption edge for TiO_2 (~ 360 nm) is very low compared to where the sensitiser dye absorbs. (For example, the sensitiser N3 dye absorbs the whole AM 1.5 spectrum except the red and near IR region). Therefore, in dye-sensitised nanocrystalline semiconductor electrodes, it is reasonable to assume that the contribution of photo-induced charge from semiconductor band to band excitation is negligible compared to that of injection from excited dye molecules.

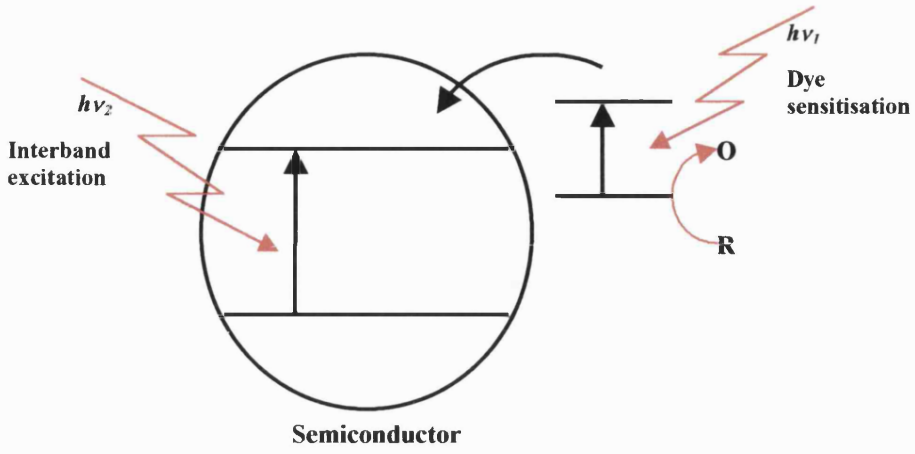

Figure 2.23 *Charge generation mechanisms in dye-sensitised semiconductor particle.*

For a simple steady-state situation and homogeneous illumination, the following relationship can be obtained.

$$\frac{dn}{dt} = G - kn \tag{2.44}$$

Here G is the volume injection rate ($cm^{-3}s^{-1}$). k is the first-order rate constant for back reaction of electrons with tri-iodide ions. n is the electron concentration.

$$\frac{dn}{dt} = G - \frac{n}{\tau_n} \tag{2.45}$$

τ_n is the electron lifetime . Under steady-state condition

$$n = G\tau_n \tag{2.46}$$

It means that increase in n cause ${}_nE_F$ to rise up. However, it is necessary to consider trapped as well as free electrons in order to obtain a relationship between G, τ_n, and U_{photo}.

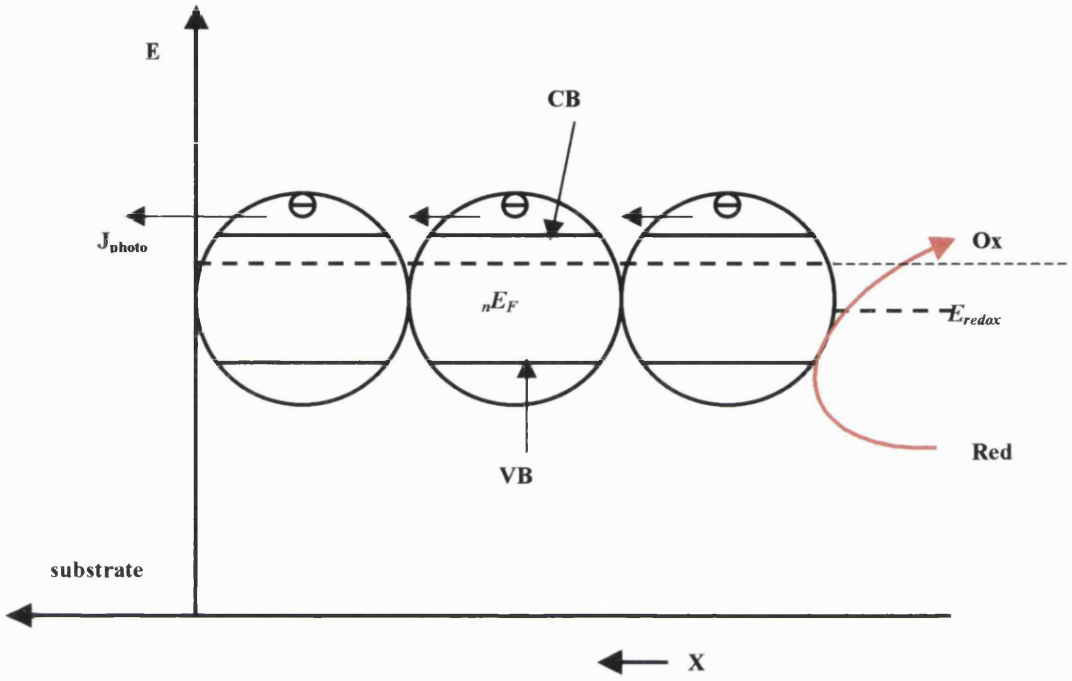

Figure 2.24 *Dye-sensitised nanocrystalline semiconductor electrode/liquid electrolyte Interface in the non-equilibrium steady-state situation brought about by illumination.*

As shown in Figure 1.3, in the DSN TiO_2 solar cell, the photogenerated electrons must travel through hundreds of nanocrystalline TiO_2 particles to reach the conducting SnO_2 substrate. During their entire passage to the SnO_2 conducting substrate, which takes several milliseconds at typical solar illumination levels, the electrons are within a few nanometers of the oxidised species (I_3^-) in the liquid electrolyte. The flux of electrons to the back contact is proportional to the gradient of the electron quasi-Fermi level. The driving force for electron movement may be due to a gradient in the potential energy of the electrons or to a gradient in their concentration, or may be due to both. The gradient

of the electrochemical potential (or gradient of the quasi-Fermi level of electrons can be obtained as follows. The electrochemical potential of species *i* is given by $\bar{\mu}_i = \mu_i + z_i F\phi$ (recall equation 2.18) where μ_i is the chemical term (recall equation 2.19) and $z_i F\phi$ is the electrical term. Hence the electrochemical potential gradient of species *i* is given by

$$\frac{d\,\bar{\mu}_i}{dx} = RTd\ln C_i + z_i F\frac{d\phi}{dx} \tag{2.47}$$

For electrons this can be rewritten as follows.

$$\frac{\partial\mu}{\partial x} = \frac{\partial E_{F,n}(x,t)}{\partial x} = \frac{kT}{n(x,t)}\frac{\partial n(x,t)}{\partial x} - e\frac{\partial\phi}{\partial x} \tag{2.48}$$

where μ is the electrochemical potential, *n(x,t)* is the distance and time dependent electron concentration, $\partial\phi/\partial x$ is the electric field that exists normal to the direction x (see Figure 2.24). The term $\frac{kT}{n(x,t)}\frac{\partial n(x,t)}{\partial x}$ represents spatially non-uniform concentration of free electrons in the TiO_2 phase, which arises from constant photogeneration in the network and electron removal at the TiO_2/SnO_2 boundary. Therefore, the first term on the right hand side accounts for diffusion and the second term represents migration.

The concentrated liquid electrolyte that penetrates into the dye-sensitised nanostructured TiO_2 phase screens the electron charge preventing the establishment of any substantial macroscopic electric field normal to the direction x. Therefore, it may be permissible to assume that electrons are collected by diffusion, so that the first term in equation (2.48) is dominant. In an interesting study, Solbrand et al. excited the nanocrystalline TiO_2 films with pulsed illumination [38]. They found that the time to peak current, varies with the square of the film thickness. As the diffusion time is given by $\tau_D = d^2/D$, where d is the film thickness and D is the diffusion coefficient, their study suggests that the electron

transport in nanocrystalline TiO_2 is diffusion controlled. However, it has been shown that the contribution from the second term in equation (2.48) for the electron transport cannot be completely ruled out at high light intensities, where the electron concentration in the nanostructured semiconductor electrode is very high [34].

The relatively high density of surface states present in the nanocrystalline electrode may play an important part in the electron transport. In flat semiconductor electrodes the typical density of surface states is about $10^{12} - 10^{13}$ cm^{-2}, whereas in nanoporous electrodes it becomes $10^{18} - 10^{19}$ cm^{-3} (note the unit difference which arises from the shift from a 2 dimensional system to a 3 dimensional system as the surface-to-volume ratio in nanocrystalline phase is about 10^6 cm^{-1} if the average particle size is 10 nm. see the section 1.4.1 for more details). Such a high density of surface states has also been evidenced from the detection of electrons at sub-bandgap illumination [39-41]. As electron transfer at the 3-dimentsional dye-sensitised TiO_2 interface is governed by interfacial rather than bulk properties, the increased density of surface states may enhance surface trapping of photogenerated electrons resulting in trapping/detrapping dominated electron transport. As shown in Figure 2.25, electrons can be temporarily localised in unoccupied traps in between the demarcation level and conduction band, during their passage to the SnO_2 substrate. Supporting this argument, several studies have reported that the electron diffusion coefficient in nanocrystalline semiconductor electrodes is several orders of magnitude smaller than that in flat semiconductor electrodes [42, 43]. If this is the case, the time taken for an electron to reach the substrate is the sum of the residence times in the traps. As the trapped electron is released by thermal excitation, the residence time depends on the trap depth (recall equation (2.41)). It follows that the electron diffusion coefficient is an intensity dependent parameter, which contradicts its original definition. Interestingly several studies have shown that the electron diffusion coefficient increases as the illumination intensity adjusts to higher levels [42-46].

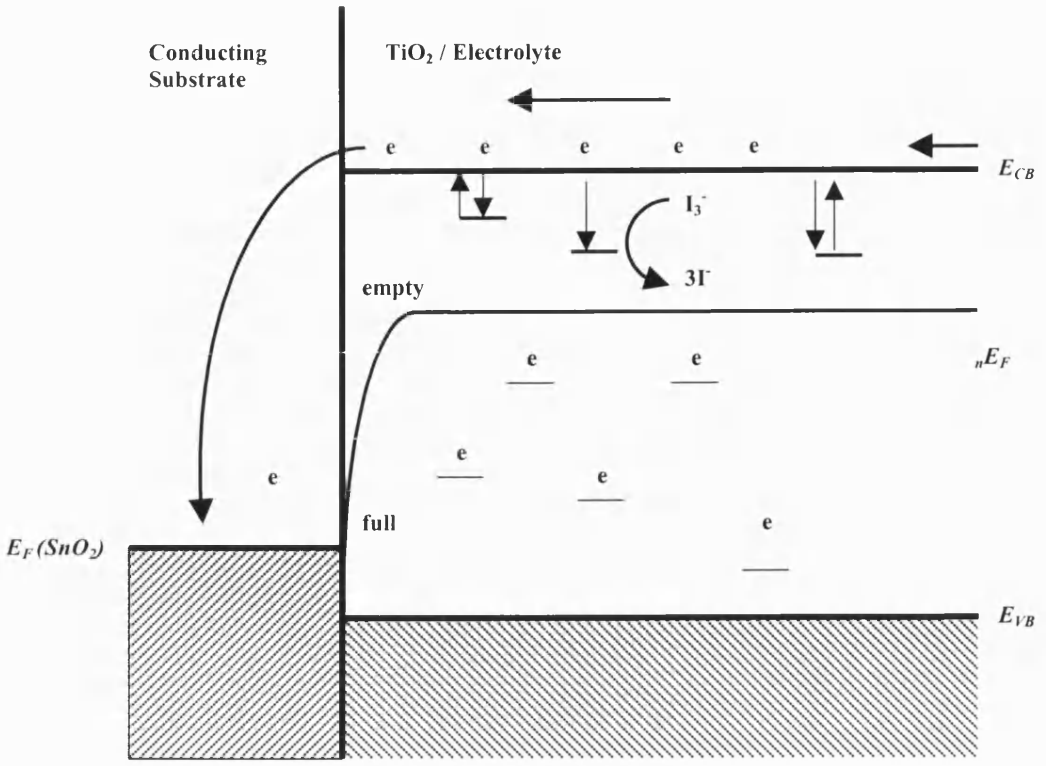

Figure 2.25 *Trapping / detrapping dominated electron transport in nanocrystalline semiconductor phase.*

Most work on electron transport in nanostructured films has assumed that the driving force for the majority carrier transport to the substrate is due to diffusion. Sodergren *et al.* have solved the generation/collection problem in DSN TiO_2 solar cells for steady-state conditions and illumination from either side of the cell [47]. The generation/collection problem can be formulated in terms of the continuity equation.

$$\frac{\partial n(x,t)}{\partial t} = \eta\alpha I_0 e^{-\alpha x} + D_n \frac{\partial^2 n(x,t)}{\partial x^2} - \frac{n(x,t) - n_0}{\tau_n} \qquad (2.49)$$

where D_n is the electron diffusion coefficient, τ_n is the electron lifetime determined by back reaction with I_3^-. This process is commonly referred to as recombination, and its rate is assumed to be first order in electron density, although it may not be first order as it was

found in present study (see chapter 5, 6 and 7). α is the absorption coefficient determined by the dye coverage, light scattering and the surface area/volume ratio of the nanocrystalline electrode and I_o is the incident photon flux corrected for reflection losses. The first term considers the rate of electron generation by photoexcited dye molecules for the case where light is incident from the substrate side. η is the net electron injection efficiency. Recalling equation (2.15), it is realised that the second term on the right hand side of equation (2.49) is familiar as Fick's second law. The third term takes into account the fact that photoinjected electrons may react with tri-iodide ions before they reach the SnO_2 substrate. $n(x,t) - n_o$ is the excess electron concentration generated by illumination. $n(x,t)$ is distance and time dependent electron density under illumination, and n_o is the equilibrium (dark) electron concentration determined by the redox Fermi level of the I^-/I_3^- couple.

However, this approach does not take into account the fact that the diffusion coefficient (D) and the electron lifetime (τ_n) depend on trapping and detrapping hence they are functions of distance. Under high incident light intensity and a trapping/detrapping dominant diffusional electron transport process, the net electron injection efficiency, η, for DSN electrodes could also depend on the total electron density and hence on distance [45, 48]. Under non-stationary conditions, the measured photocurrent density can also be affected by the RC time constant of the cell (this will be discussed in section 3.3.1). Incorporating the kinetics of electron extraction into the boundary conditions and introducing distance dependence parameters Dloczik *et al.* have extended the above model [42]. The analysis of the frequency-resolved measurements in the present study has been done on the basis of the Dloczik model and analytical expressions for the steady state and small amplitude techniques responses (i.e.IMPS) will discussed in section 3.3.

2.5 The Dye-sensitised Semiconductor / Solid Heterojunction

Until now this chapter has considered semiconductor/liquid electrolyte junctions and their photo-induced charge transfer processes. For particular applications such as solid-state dye-sensitised solar cells, it may be very useful to consider junctions between two

different semiconductors or junctions between semiconductor and polymer with different energy gaps. If the two semiconductors, although containing different chemical elements, are similar concerning the nature of the crystalline binding and the lattice structure, it is possible to form ideal (or nearly ideal) heterostructures. Molecular beam epitaxy (MBE) and metal-organic chemical-vapour deposition (MOCVD) have allowed the realisation of several such nearly ideal heterojunctions. One good example is the formation of GaAs /Al_xGa_{1-x} As heterojunction (here as x changes from 0 to 1, the bandgap of Al_xGa_{1-x} As goes from 1.42 to 2.17 eV, while the lattice constants of the two solids are basically the same within less than 0.1%) [49].

However, describing a DSN semiconductor/solid junction is rather complicated compared to nearly ideal heterostructures such as the one mentioned above. Here two hypothetical situations are considered very briefly: the first is a dye-sensitised nanocrystalline n-type semiconductor/nanocrystalline p-type semiconductor junction and the second is a dye-sensitised nanocrystalline n-type semiconductor/conducting polymer junction. Chapter 8 will treat these situations in more detail including experimental results.

Assuming the individual nanocrystalline semiconductor particles in both n-type and p-type phases are comparable in size and they interpenetrate each other making intimate contact, the first hypothetical situation can be described schematically as follows.

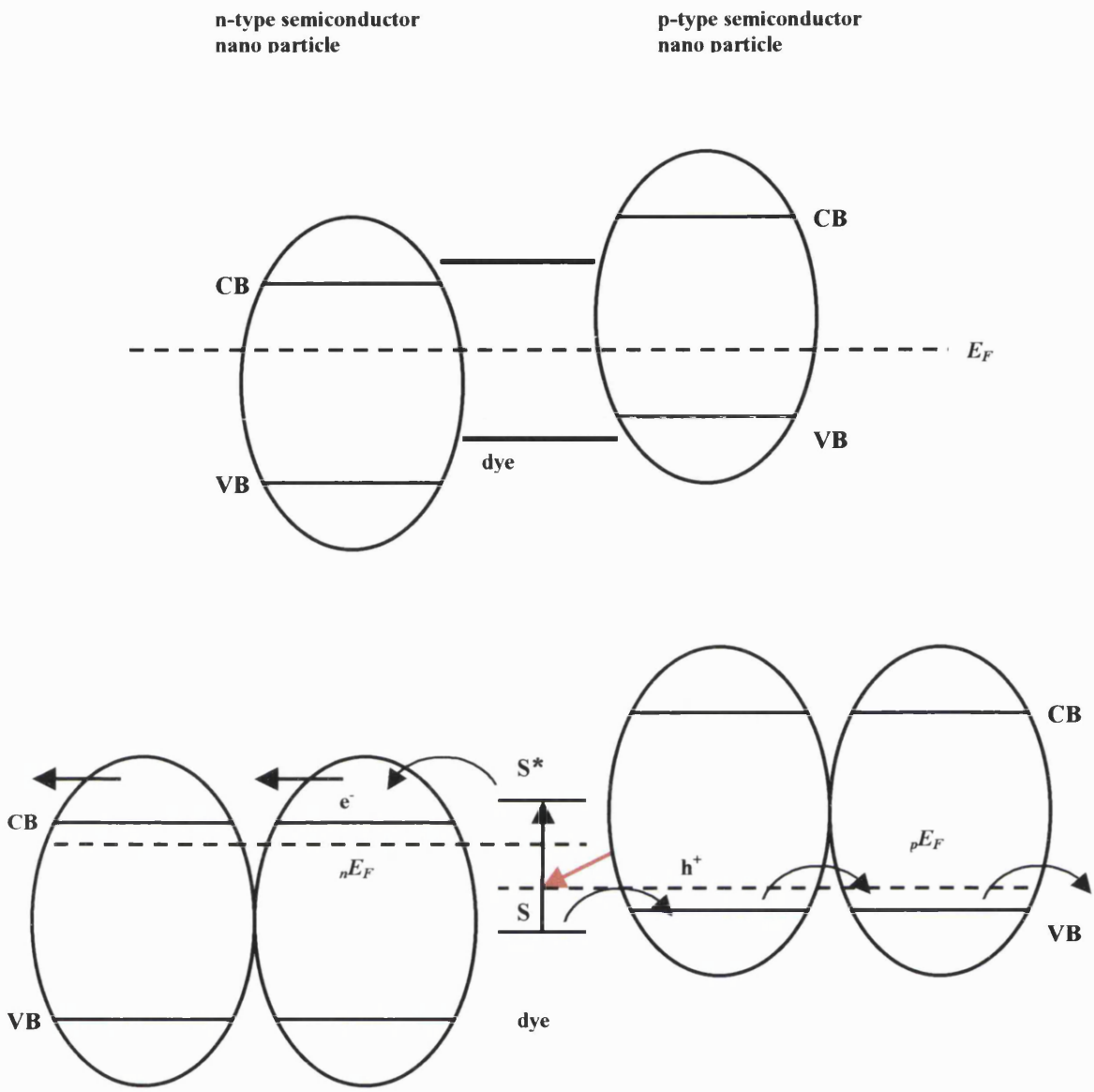

Figure 2.26 *The dye-sensitised nanocrystalline n-type semiconductor / nanocrystalline p-type semiconductor heterojunction :* ***(upper)*** *: at equilibrium,* ***(lower)*** *: at non-equilibrium.*

It has already been established that the electron injection from excited sensitiser N3 dye molecules into the conduction band of the nanocrystalline TiO_2 occurs at unit quantum efficiency [50]. If the regeneration of oxidised dye molecules takes place efficiently (as shown is Figure 2.26 this happens as a result of hole injection into the valence band of nanocrystalline p-type semiconductor), then the limiting processes in this system are

charge transport in n-type and p-type semiconductor phases. Electron and hole transport in respective phases (electron transport in n-type semiconductor phase and hole transport in p-type semiconductor phase) may be trapping/detrapping dominated processes. However, the n-type semiconductor/dye/p-type semiconductor system sharply contrasts from the dye-sensitised nanocrystalline semiconductor/liquid electrolyte junction by following points. Lattice mismatch effects, formation of voids inside the porous system during the filling process (lack of full penetration, see Figure 2.27) and the creation of uncompensated electrical fields that oppose the charge separation (this situation arises as a result of the absence of mobile electrolyte ions) are them. In fact, these problems are common even in other solid state dye-sensitised versions such as dye-sensitised nanocrystalline n-type semiconductor/conducting polymer junction.

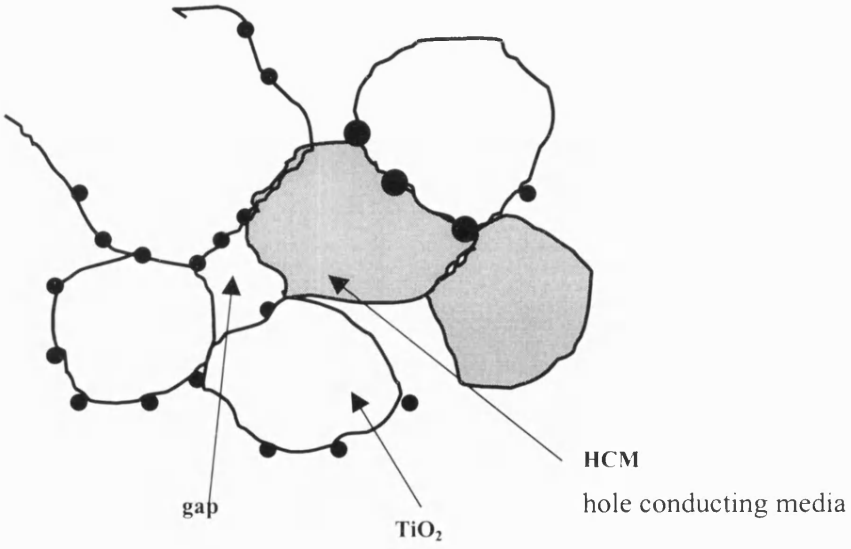

Figure 2.27 *Formation of voids inside the dye coated porous semiconductor system.*

The dye-sensitised nanocrystalline n-type semiconductor/conducting polymer junction and the n-type semiconductor/dye/p-type semiconductor system are discussed briefly in chapter 8, which also contains the experimental results.

2.6 References

1. A. R. West, Solid state chemistry and its applications, John Wiley & Sons, Chichester, 1985.
2. S. Hayashi, N. Nakamori, H. Kanamori, Y. Yodogawa, and K. Yamamoto, Surface Science 86:665 (1979).
3. M. Kryszewski, in International symposium on polymers for advanced technologies (M. Lewin, ed.), VCH Verlagsgesellschaft mbH, Jerusalem, Israel, 1987, p. 199.
4. C. K. Chiang, Y. W. Park, A. J. Heeger, H. Shirakawa, E. J. Louis, and A. G. MacDiarmid, physical Review Letters 39:1098 (1977).
5. J. L. Bredas and G. B. Street, Acc. Chem. Res. 18:309 (1985).
6. T. A. Skotheim, Hand book of Conducting Polymers, Marcel Dekker Inc., New York, 1986.
7. B. Scrosati, Progress Solid State Chemistry 18:1 (1988).
8. M. G. Kanatzidis, Chemical & Engineering news 68:36 (1990).
9. H. Gerischer, Z.Phys.Chem (Frankfurt) 26:233 (1960).
10. H. Gerischer, Z.Phys.Chem (Frankfurt) 27:40 (1961).
11. R. A. Marcus, Journal of Chemical Physics 24:966 (1956).
12. S. R. Morrison, in Semiconductor Micromaching, Vol. 1 (S. A. Campbell and H.-J. Lewerenz, eds.), John Wiley & Sons Ltd, Chichester, 1998.
13. S. R. Morrison, in Electrochemistry at Semiconductor and Oxidized Metal Electrodes, Plenum Press, New York, 1980.
14. A. Zaban, S. Ferrere, and B. A. Gregg, Journal of physical Chemistry B 102:452 (1998).
15. L. M. Peter, in Photocatalysis and Environment (M. Schiavello, ed.), Kluwer Academic Publishers, Dorc, 1988, p. 243.
16. R. Peat and L. M. Peter, Ber. Bunsenges. Phys. Chem. 91:381 (1987).
17. J. Li, R. Peat, and L. M. Peter, Journal of Electroanalytical Chemistry 165:41 (1984).

18. N. Serpone, D. K. Sharma, M. A. Jamieson, M. Gratzel, and J. J. Ramsden, Chemistry Physics Letters 115:473 (1985).
19. A. B. Ellis and B. R. Kavas, Journal of American Chemical Society 101:236 (1979).
20. K. Beckmann and R. Memming, Journal of Electrochemiscal Society 116:368 (1969).
21. W. Shockley and W. T. Read, Physical Review 87:835 (1952).
22. R. N. Hall, Physical Review 87:387 (1952).
23. A. Rose, Progress in Semiconductor 2:211 (1956).
24. R. H. Bube and F. Cardon, Journal of Applied Physics 35:2712 (1964).
25. J. G. Simmons and G. W. Taylor, Physical Review B4:502 (1971).
26. R. H. Bube, Photoelectric Properties of Semiconductors, Cambridge University Press, 1992.
27. L. M. Peter and D. Vanmaekelbergh, in Advances Electrochemical Science and Engineering, Vol. 6 (R. C. Alkire and D. M. Kolb, eds.), VCH Wiley, New York, 1999, p. 77.
28. R. Peat and L. M. Peter, Electrochemical Acta 31:731 (1986).
29. R. Peat and L. M. Peter, Journal of Electroanalytical Chemistry 209:307 (1986).
30. J. D. Joannopoulos, P. R. Villeneuve, and S. Fan, Nature 386:143 (1997).
31. C. G. Granquist, Handbook of Inorganic Electrochemistry, Elsevier, Amsterdam, 1995.
32. M. Gratzel, Proceedings of the Indian Academy of Sciences-Chemical Sciences 107:607 (1995).
33. M. Gratzel, Heterogeneous photochemical electron transfer, CRC press, Fluorida, 1989.
34. L. M. Peter, E. A. Ponomarev, G. Franco, and N. J. Shaw, Electrochimica Acta 45:549 (1999).
35. W. J. Albery and P. N. Bartlett, Journal of Electrochemiscal Society 131:315 (1984).
36. A. Heller, Science 223:1141 (1984).

37. L. M. Peter, D. J. Riley, and R. I. Wielgosz, Applied Physics Letters 66:2355 (1995).

38. A. Solbrand, H. Lindstrom, H. Rensmo, A. Hagfeldt, S. E. Lindquist, and S. Sodergren, Journal of Physical Chemistry B 101:2514 (1997).

39. B. H. Erne, D. Vanmaekelbergh, and J. J. Kelly, Advanced Materials 7:739 (1995).

40. F. Iranzo Marin, M. A. Hamstra, and D. Vanmaekelbergh, Journal of Electrochemiscal Society 143:1137 (1997).

41. J. van de Lagemaat, D. Vanmaekelbergh, and J. J. Kelly, Journal of Applied Physics 83:6089 (1998).

42. L. Dloczik, O. Ileperuma, I. Lauermann, L. M. Peter, E. A. Ponomarev, G. Redmond, N. J. Shaw, and I. Uhlendorf, Journal of Physical Chemistry B 101:10281 (1997).

43. F. Cao, G. Oskam, G. J. Meyer, and P. C. Searson, Journal of Physical Chemistry B 100:17021 (1996).

44. L. M. Peter and K. G. U. Wijayantha, Electrochemistry Communications 1:576 (1999).

45. G. Schlichthorl, N. G. Park, and A. J. Frank, Journal of Physical Chemistry B 103:782 (1999).

46. G. Schlichthorl, S. Y. Huang, J. Sprague, and A. J. Frank, Journal of Physical Chemistry B 101:8141 (1997).

47. S. Sodergren, A. Hagfeldt, J. Olsson, and S. E. Lindquist, Journal of Physical Chemistry B 98:5552 (1994).

48. S. Y. Huang, G. Schlichthorl, A. J. Nozik, M. Gratzel, and A. J. Frank, Journal of Physical Chemistry B 101:2576 (1997).

49. G. Grosso and G. P. Parravicini, Solid State Physics, Academic Press, Cambridge, 2000.

50. M. Gratzel, Current Opinion in Colloid & Interface Science 4:314 (1999).

Chapter 3

Theory of the Small Amplitude Responses of Dye-sensitised Nanocrystalline TiO_2 Solar cells

3.1 Introduction

In the DSN TiO_2 solar cell, upon light absorption, the excited dye injects an electron into the conduction band of the semiconductor in the sub-picosecond time scale. In a comparison of time scales, the injected electrons and the I_3^- require a time of the order of milliseconds to reach their respective electrodes, making them by far the slowest part of the overall process (see section 1.4 of chapter 1). The dynamics of reactions in DSN solar cells such as the electron injection from excited dye molecules to the conduction band of the semiconductor have been extensively studied using picosecond and femtosecond transient laser techniques [1, 2]. The present study is mainly concerned with the slower steps involving electron transport and recombination of the photogenerated electrons in dye-sensitised liquid junction and solid-state cells. Characterisation of a nanocrystalline semiconductor/electrolyte junction (or even a flat semiconductor/electrolyte junction) using steady-state techniques gives only limited information about the dynamics of electron transport and recombination kinetics [3-6]. Therefore, the present study mainly involves non-steady-state techniques. The steady-state techniques (current voltage characteristics and photocurrent measurements) that were used for the preliminary solar cell characterisation, will not be discussed in this section. However, before moving on to analytical expressions for non-steady state techniques, some basic understanding of a.c. theory is necessary. Section 3.2 will briefly introduce a.c. theory.

Two small amplitude modulation frequency-resolved techniques have been employed in the present work. One is intensity modulated photocurrent spectroscopy (IMPS), which involves modulation of the intensity of the illuminating light and measurement of the magnitude and phase shift of the resulting photocurrent at different frequencies [7, 8]. The other frequency-resolved technique that is closely related to IMPS is intensity

modulated photovoltage spectroscopy (IMVS), which involves modulation of the intensity of the illumination light and measurement of the magnitude and phase shift of the resulting modulated photovoltage [9, 10]. Section 3.3.1 discusses the analytical expressions for the steady state and small amplitude responses of IMPS. Section 3.3.2 deals with intensity modulated photovoltage spectroscopy.

3.2 A.C. Theory

The Transfer Function

In an electrochemical or photoelectrochemical system, the *input function* and *output function* can be related by the *transfer function*. The following table summarises several examples for such systems.

Input Function	**Output Function**	**Transfer Function**	**Related Technique**
a.c. voltage, V	a.c. voltage, V	gain,V/V (dimensionless)	
a.c. voltage, V	a.c. current, I	impedance, V/I (Ω)	EIS
a.c. current, I	a.c. voltage, V	admittance, I/V(Ω^{-1})	
a.c. photon flux, $cm^{-2}s^{-1}$	a.c.electron flux, $cm^{-2}s^{-1}$	quantum efficiency, Φ (dimensionless)	IMPS
a.c. photon flux, $cm^{-2}s^{-1}$	a.c. voltage, V	impedance, V/(photon flux x q)	IMVS

In order to characterise DSN TiO_2 solar cells using techniques such as IMPS and IMVS, some basic understanding of a.c. theory is necessary. Consider a system where the input function is a sinusoidal voltage and the output function is a current. In most cases the current will be sinusoidal and of the same frequency (higher harmonics will not be considered in this brief introduction. However, the amplitude and phase of the resulting

current can be different from that of the applied sinusoidal voltage. The applied sinusoidal voltage can be given by

$$V = \Delta V \sin \omega t \tag{3.1}$$

where $\omega=2\pi f$, f is the modulation frequency, ΔV is the maximum amplitude of the input voltage. The output function (sinusoidal current) can be represented by

$$I = \Delta i \sin(\omega t + \phi) \tag{3.2}$$

where ϕ is the phase shift with respect to the input voltage and Δi is the maximum amplitude of the output current. Both input voltage and output current can be represented using a phasor diagram as shown in Figure 3.1. As the frequencies of the input voltage and the output current are the same, they can also be represented in V-t and I-t form separately as shown below.

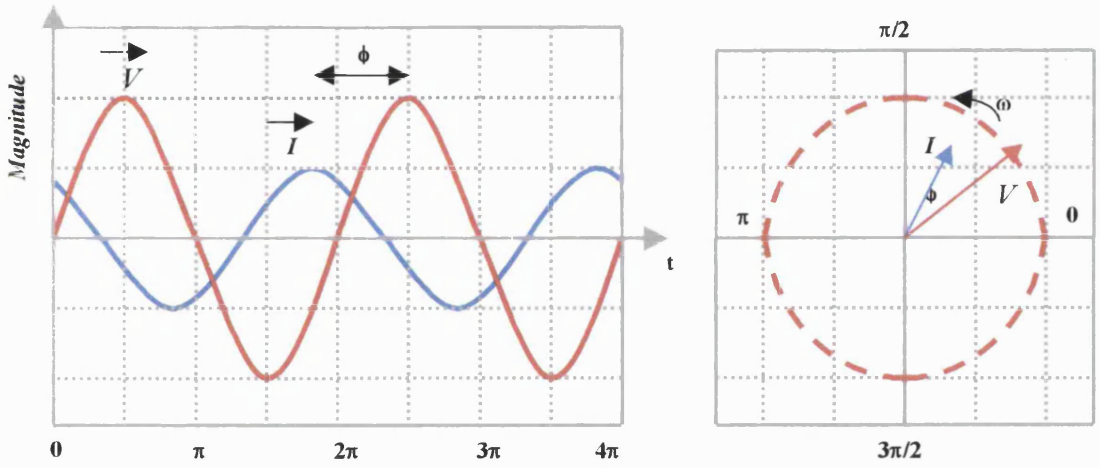

Figure 3.1 *The phasor diagram representation , V-t and I-t forms of input voltage [$\Delta V \sin \omega t$] and output current [$\Delta i \sin(\omega t + \phi)$].*

However, the situation is more complicated when a transfer function such as impedance, is recorded at a series of frequencies. Therefore, a convenient method is required to represent the relative magnitude and phase of the transfer function at different frequencies. It can be done using a complex plane diagram. To use a complex plane diagram, it is convenient to replace the more familiar sinusoidal form of input voltage by the complex form $V = V_o e^{i\omega t}$ where the complex number, $e^{i\omega t} = \cos\omega t + i \sin\omega t$ and i

$= \sqrt{-1}$. The real component of the input voltage is $cos\omega t$ and the imaginary component is $sin\omega t$. Similarly, the complex form of output current can be given by $I = I_o e^{(i\omega t+\phi)} = I_o e^{i\omega t} e^{\phi}$. Here, the first term, I_o contains the magnitude information and the second term, $e^{i\omega t}$ shows the rotating vector. The third term, e^{ϕ} contains phase information with respect to the input voltage. For example, if the transfer function is impedance, Z

$$Z = \frac{V}{I} = \frac{V_o e^{i\omega t}}{I_o e^{i\omega t+\phi}} = \left(\frac{V_o}{I_o}\right) e^{-\phi} \tag{3.3}$$

The magnitude of the impedance, |Z| is (V_o/I_o) and the phase shift of the current with respect to input voltage is $-\phi$. Now the impedance at a given frequency can be represented in the complex diagram as follows.

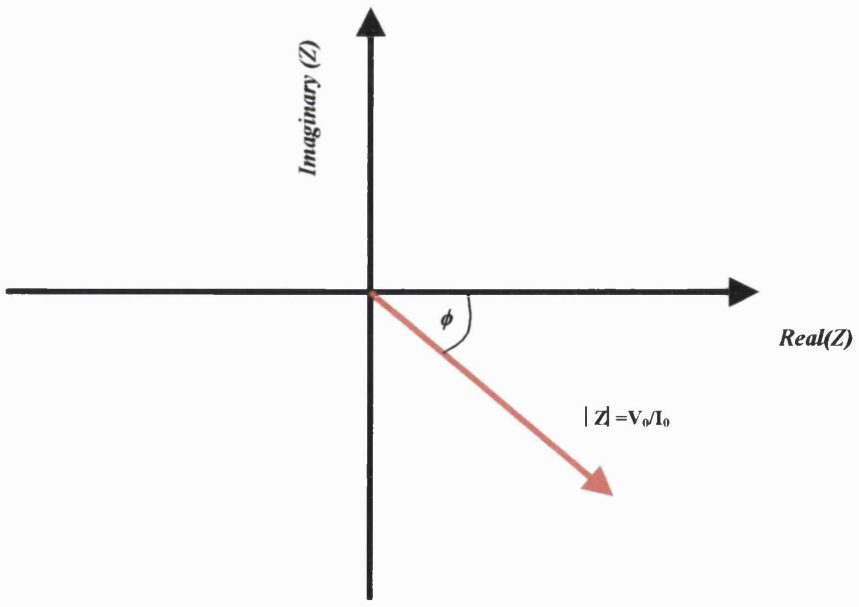

Figure 3.2 *Impedance response for a given frequency can be represented as a vector in the complex plane.*

Similarly, the impedance of the system for a range of frequencies can be represented in the complex plane. In IMPS, the real and imaginary components of the photocurrent can be recorded on the complex plane at different frequencies in a similar fashion.

Now it is useful to consider some simple electronic circuit elements and their frequency responses (impedance), as most of the electrochemical systems closely mimic these simple electronic circuit elements or their different combinations. As an example, impedance responses for a resistor, capacitor, resistor-capacitor series and parallel combinations will be discussed.

Resistor

Applying an a.c. voltage, V (i.e. $V = V_o e^{i\omega t}$) across a resistor will cause a current, I (i.e. $I = I_o e^{i\omega t}$) to flow, with a magnitude maximum of $I_o = V_o/R$, where R is the resistance of the resistor.

$$Z_R = \frac{V}{I} = \frac{V_o e^{i\omega t}}{\left(V_o / R\right) e^{i\omega t}} = R \tag{3.4}$$

Therefore, it is clear that the alternation in both V and I are *in phase* (i.e. both V and I obey ohms law, $V = IR$). Figure 3.3 shows the phasor notation, *I-t* and *V-t* forms of a current response for an applied sinusoidal voltage at a given frequency across a resistor.

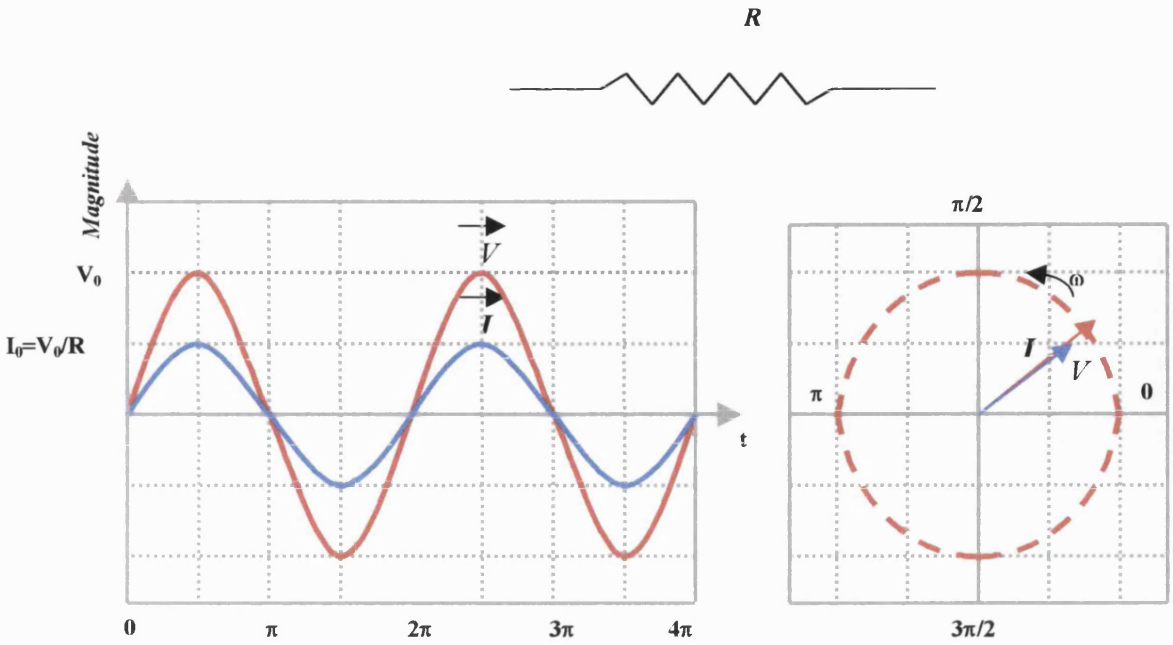

Figure 3.3 *The phasor notation, I-t and V-t forms of the current response for an applied sinusoidal voltage,* $V = V_o e^{i\omega t}$.

Clearly, at any given frequency the impedance of a resistor is equal to its resistance, *R*. The complex notation of impedance response of a resistor is shown in Figure 3.4. It is also possible to represent the vector forms of magnitude and phase angle as a function of logarithmic frequency (Bode plots). Figure 3.4 also describes the Bode plots corresponding to the impedance response of a resistor.

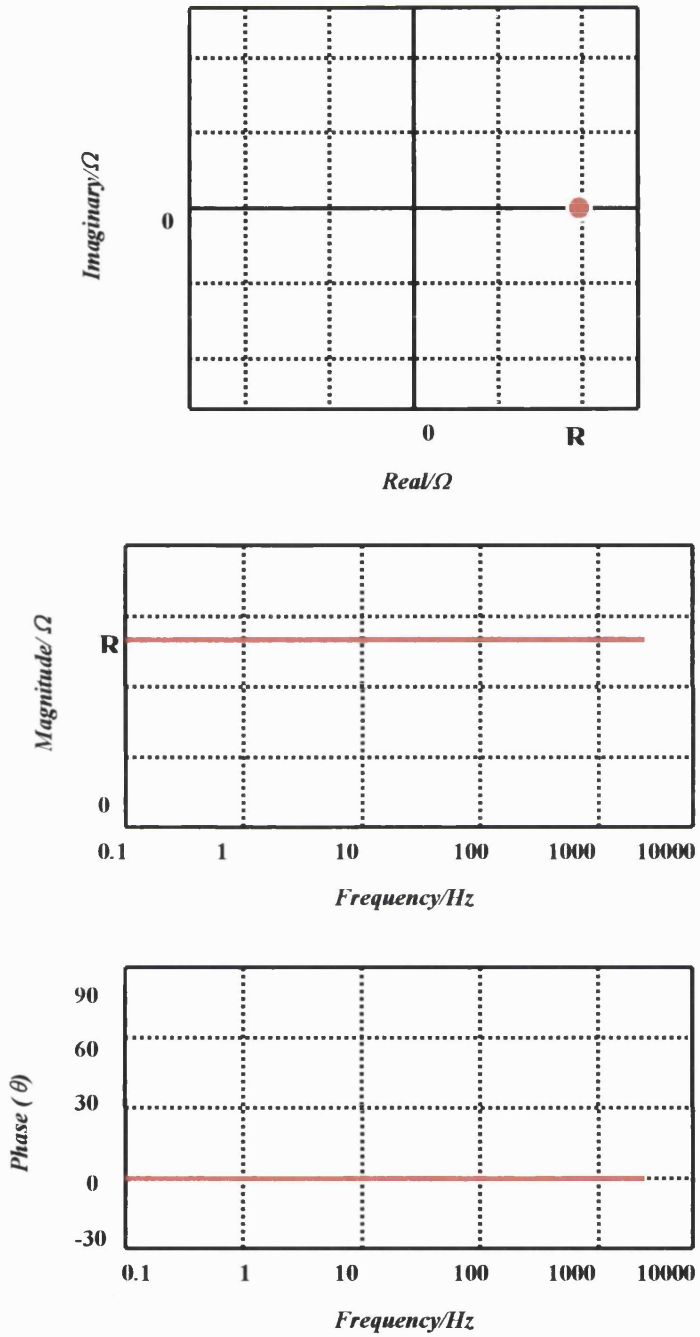

Figure 3.4 *The complex notation and corresponding Bode plots of impedance response of a resistor.*

Capacitor

For a capacitor, the current response to an applied a.c. voltage can be related by the expression $Q = CV$, where C is the capacitance of the capacitor.

$$Q = CV \tag{3.5}$$

$$I = \frac{dQ}{dt} = C\frac{dV}{dt} \tag{3.6}$$

Equation (3.6) shows that a capacitor will only pass a current if the applied voltage, V, is time dependent (i.e. a.c. voltage). The current response for an applied a.c. voltage, V (i.e. $V = V_o e^{i\omega t}$) across a capacitor would be an alternating current, $I = i\omega C\ V_o e^{i\omega t} = V_o \omega C e^{i\omega t + \pi/2}$. Therefore, the current appears to have been moved $\pi/2$ forward with respect to the applied voltage and is said to lead the voltage by $\pi/2$. If the applied voltage, V is in the composite form of $V = V_o + V_1 sin\ \omega t$, then the current passed will be $I = \omega C V_1 cos\ \omega t$ and the steady-state component of the applied voltage, V_o has no influence on the output current. Figure 3.5 shows this situation in phasor notation and I-t and V-t forms of the current response for an applied composite form ($V = V_o + V_1 sin\ \omega t$) sinusoidal voltage across a capacitor.

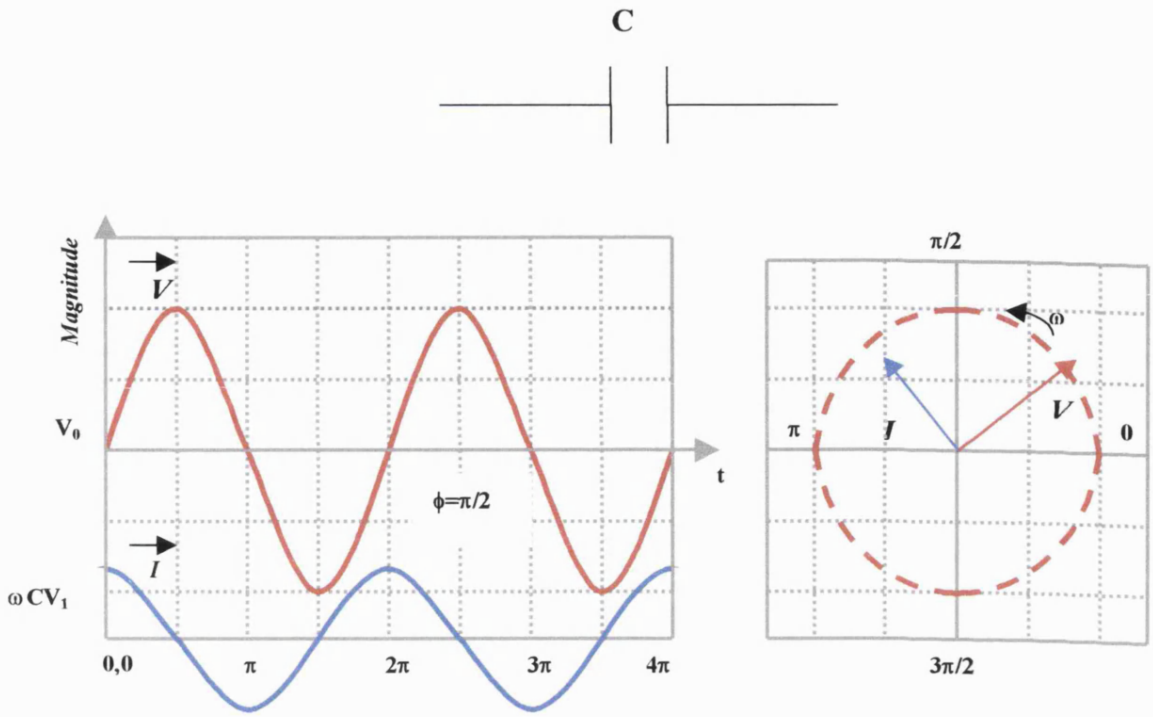

Figure 3.5 *The phasor notation, I-t and V-t forms of the current response for an applied sinusoidal voltage across a capacitor.*

The details of the impedance response of a capacitor can be obtained by the following equations (3.7) and (3.8).

$$Z_C = \frac{V}{I} = \frac{V_o e^{i\omega t}}{i\omega C e^{i\omega t}} = \frac{1}{i\omega C} = \frac{-i}{\omega C} \tag{3.7}$$

$$Z_C = \frac{V}{I} = \frac{V_o e^{i\omega t}}{V_o \omega C e^{i\omega t + \pi/2}} = \frac{1}{\omega C} e^{-\pi/2} \tag{3.8}$$

As can be seen from equation (3.7) and (3.8), the phase angle of the impedance response of a capacitor is not only lagging behind by $\pi/2$ with respect to that of the applied voltage but also it does not contain a real component. Figure 3.6 describes the complex notation of the typical impedance response of a capacitor and the typical shape of Bode plots.

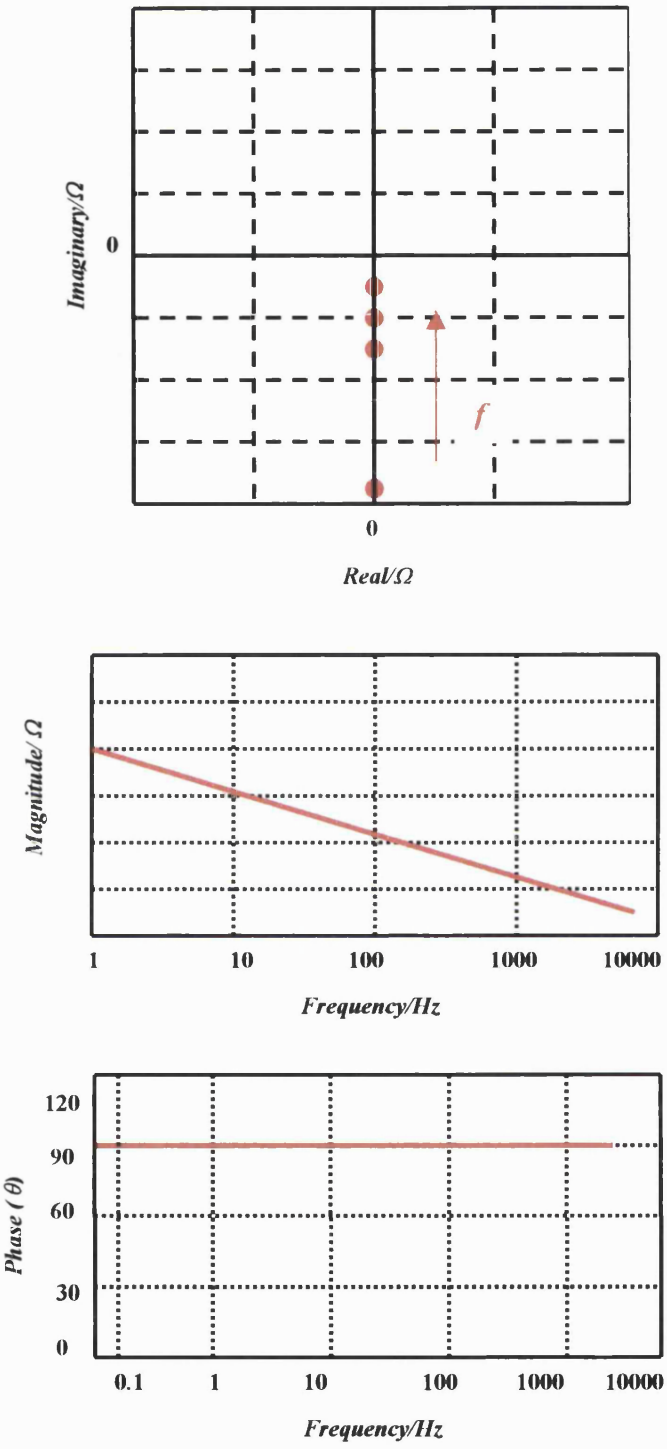

Figure 3.6 *The complex plane plot of the typical impedance response of a capacitor and the typical shape of Bode plots.*

Resistor-capacitor combination in series

For electronic circuit elements containing both resistors and capacitors, the total impedance is obtained using Kirchoff's laws. According to Kirchoff's laws, the sum of the voltage drops around a closed loop must be zero and the sum of currents into any node must be equal to zero.

In a resistor-capacitor series combination, an applied a.c. voltage, V (i.e. $V = V_o e^{i\omega t}$) results in a current, which has to pass through both resistor and capacitor. Therefore, the total impedance of such a combination can be obtained by adding the impedance of each component.

$$Z_{total} = Z_R + Z_C = R + \frac{1}{i\omega C} = R - \frac{i}{\omega C} \tag{3.9}$$

Applying Ohm's law and manipulating the complex variables, it can be shown that the current passing through the resistor-capacitor series combination is in the form of

$$I = \left(\frac{V}{|Z|}\right) e^{i(\omega t + \alpha)} \tag{3.10}$$

where $|Z| = (1 + \omega^2 C^2 R^2)^{1/2}/\omega C$ and $\alpha = tan^{-1}(1/\omega CR)$. According to equation (3.9), at low frequencies the circuit element behaves like a pure capacitor but at high frequencies it converts into a resistor. Figure 3.7 shows the general shape of the impedance response for a resistor ($1000\,\Omega$) – capacitor ($1\ \mu$ F) series combination.

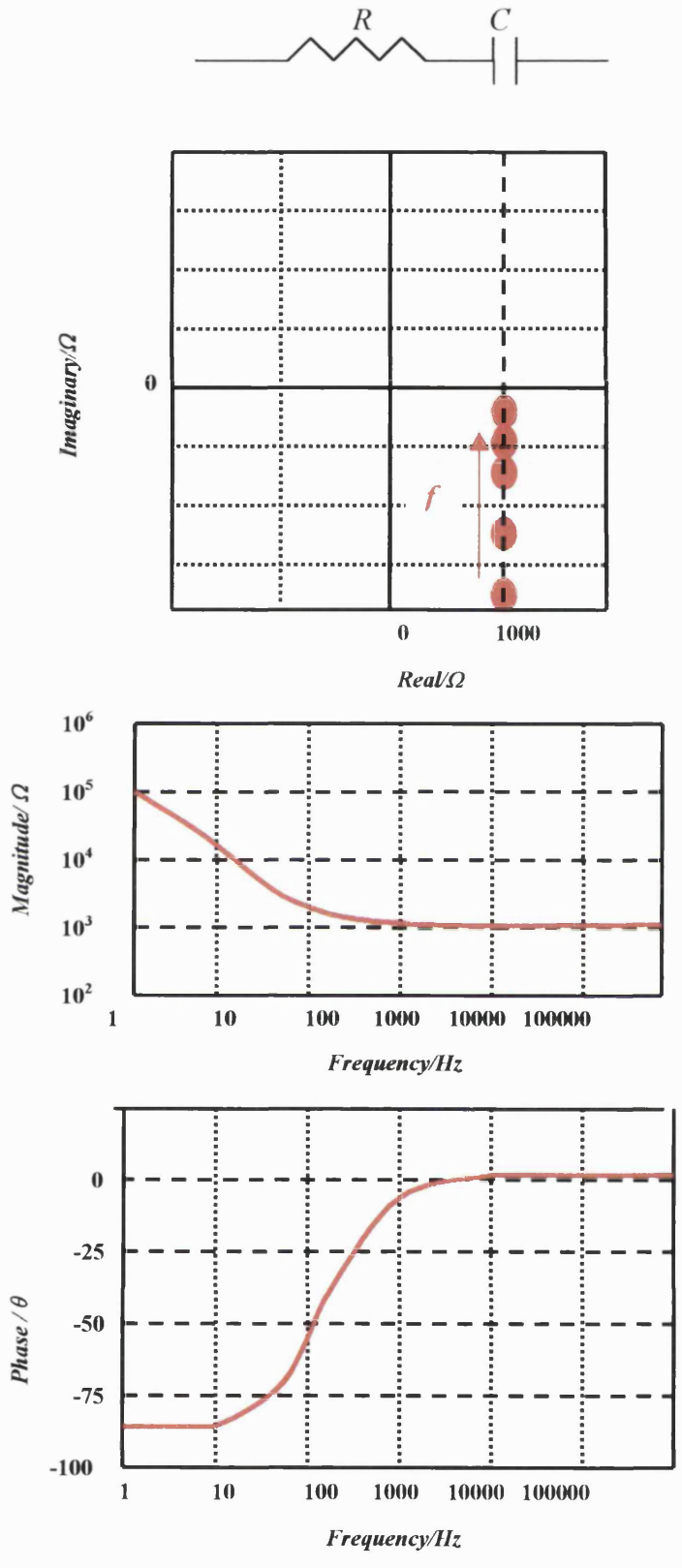

Figure 3.7 *The impedance response and Bode plots for a resistor (1000 Ω) – capacitor (1 μ F) series combination.*

Resistor-capacitor combination in parallel

The total impedance of a resistor-capacitor parallel combination can be obtained as follows.

$$\frac{1}{Z_{total}} = \frac{1}{R} + i\omega C \tag{3.11}$$

$$Z = \left(\frac{R}{1+R^2\omega^2C^2}\right) - i\left(\frac{\omega R^2 C}{1+R^2\omega^2C^2}\right) \tag{3.12}$$

Therefore, at the low frequency limit the impedance response of the resistor-capacitor parallel combination approaches R and at the high frequency limit it approaches zero. When the angular frequency, ω is equal to $1/RC$, the real and imaginary components of the impedance response are equal to $R/2$ and $-R/2$ respectively. Figure 3.8 shows the impedance response and Bode plots for a resistor (1000 Ω) – capacitor (1 μ F) parallel combination.

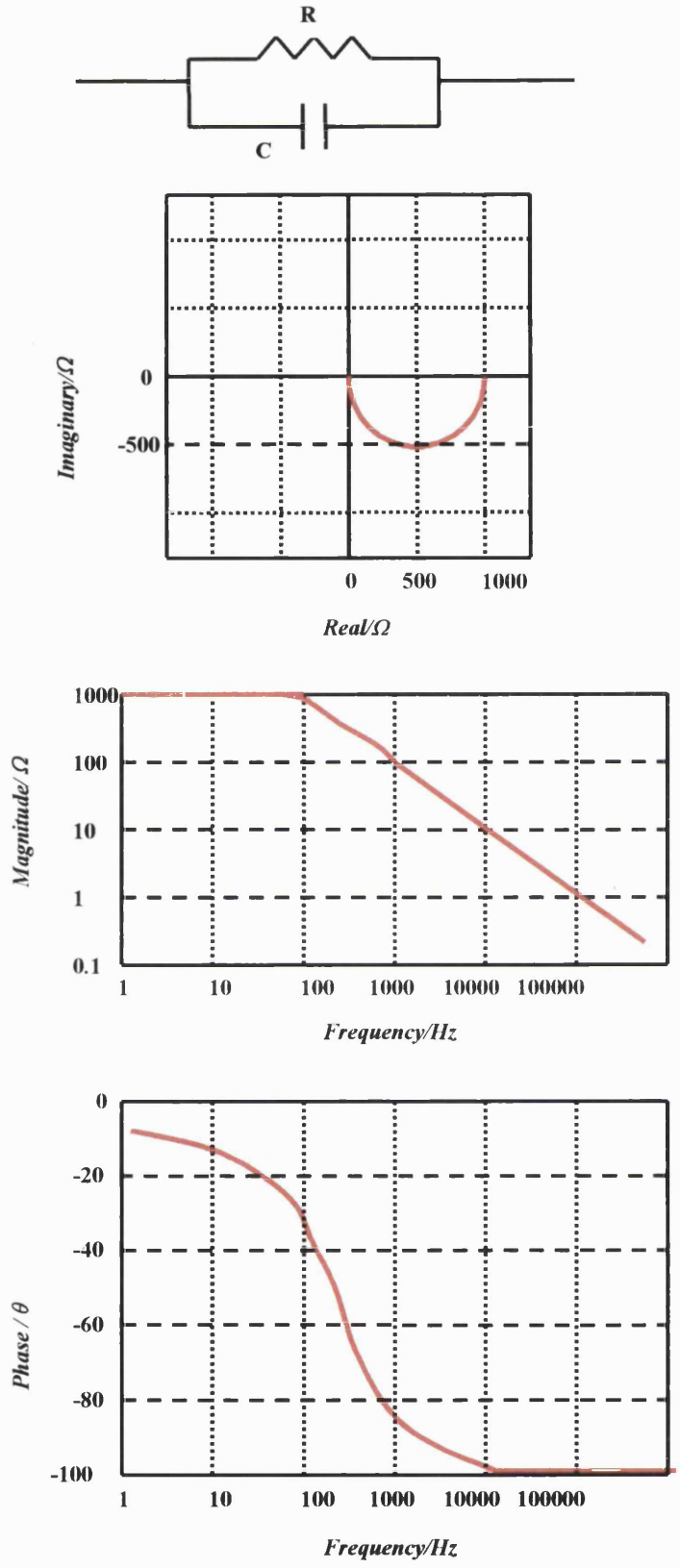

Figure 3.8 *The impedance response and Bode plots for a resistor (1000 Ω) – capacitor (1 μ F) parallel combination.*

At this stage it is worth noting that in electrochemical systems, the rates of elementary reaction steps are exponentially dependent upon the potential (see equation (3.13)). Therefore, electrochemical processes are non-linear. On the other hand a.c.theories can only be applied to linear systems. Therefore, in order to explain the frequency responses using models developed based on linearised a.c.theories, the exciting signal applied to the system must be kept small enough so that the system can be regarded as linear. As described later, applying small potential perturbations about the equilibrium potential or applying small potential perturbations on top of a large d.c. potential can convert a non-linear system into a linear system. The experimentally obtained frequency responses (i.e. impedance) from such systems can be interpreted using linear analytical expressions.

The linearisation of a non-linear system can be explained in mathematical terms as follows. Generally, in a system, the current response of an electron transfer reaction can be given as a function of overpotential and transfer coefficient using the Butler-Volmer equation.

$$j = j_0 \left[e^{(1-\alpha)nF\eta/RT} - e^{-\alpha nF\eta/RT} \right] \qquad (3.13)$$

where j is the current response, j_0 is the exchange current density, F is the Faraday constant, n is the number of electrons involved in the electron transfer reaction, α is the transfer coefficient, η is the overpotential (deviation from the equilibrium potential in the system). Therefore, the system response is non-linearly related to the applied potential. The first exponential term represents the cathodic current component at any potential and the second exponential term corresponds to the anodic current contribution. Figure 3.9 shows a typical j versus η plot.

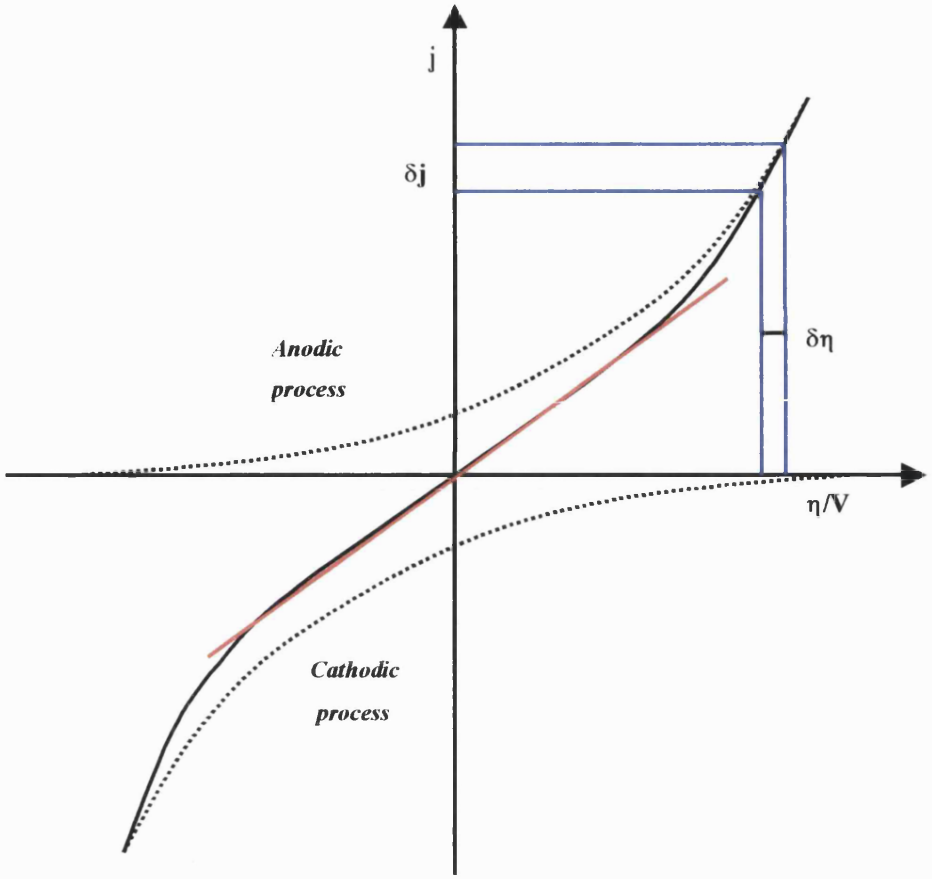

Figure 3.9 *Example of current-overpotential plot assuming that $\alpha = 0.5$, $n = 1$ in equation (3.13), electron transfer is rate-limiting and concentrations of oxidised and reduced species are equal.*

Two limiting forms of the Butler-Volmer equation are important. They are, the current response of the system at both small and large overpotentials.

Linearisation of the system response about the equilibrium potential

As shown in Figure 3.9, for small potential perturbations about equilibrium potential the response is linearly related to the overpotential. Therefore, in the limit of about equilibrium potential, the exponential term in equation (3.13) can be expanded as follows (i.e. for small x, $e^x = 1 + x$).

$$j = j_0\left[\left(1+\frac{(1-\alpha)nF\eta}{RT}\right)-\left(1-\frac{\alpha nF\eta}{RT}\right)\right] \qquad (3.14)$$

It follows that,

$$j = \left(\frac{j_0 nF}{RT} \right) \eta \tag{3.15}$$

Therefore, the current is directly proportional to the overpotential for small amplitude perturbations about the equilibrium potential.

Linearisation of the system response about at a large applied potential

The other limiting form of the Butler-Volmer equation describes the system response for small amplitude perturbations at large overpotentials. In this situation, the current is logarithmically related to overpotential. Either at large positive or negative overpotentials, the net current density coincides with the partial current density (see Figure 3.9), resulting a domination of the corresponding exponential term in equation (3.13). In this situation, the Tafel approximation is valid.

For example, at a large overpotential for a reductive (cathodic) process, the exponential term corresponding to the anodic process in equation (3.13) can be neglected. In such a situation, the equation (3.13) can be rewritten as follows,

$$j = j_0 \left[e^{-\alpha nF\eta / RT} \right] \tag{3.16}$$

Considering a small perturbation, the equation (3.16) can be modified as;

$$j + \delta j = j_0 \left[e^{-\alpha nF(\eta + \delta\eta) / RT} \right] \tag{3.17}$$

$$j + \delta j = j_0 \left[e^{-\alpha nF\eta / RT} . e^{-\alpha nF\delta\eta / RT} \right] \tag{3.18}$$

For $\delta\eta$, the second exponential term in equation (3.18) can be expanded as follows.

$$j + \delta j = j_0\left[e^{-\alpha nF\eta/RT}\left(1 - \frac{\alpha nF}{RT}\delta\eta\right)\right] \tag{3.19}$$

$$j + \delta j = j_0\left[e^{-\alpha nF\eta/RT} - e^{-\alpha nF\eta/RT}\left(\frac{\alpha nF}{RT}\right)\delta\eta\right] \tag{3.20}$$

Therefore,

$$\delta j = j_0\left[-e^{-\alpha nF\eta/RT}\left(\frac{\alpha nF}{RT}\right)\delta\eta\right] \tag{3.21}$$

$$\delta j = j\left(\frac{-\alpha nF}{RT}\right)\delta\eta \tag{3.22}$$

Again the small perturbation about a larger d.c. overpotentials, linearises the system response. The linearised output functions such as admittance ($\delta j/\delta\eta$), impedance ($\delta\eta/\delta j$) can be derived from equation (3.22). Therefore, in general, the system response of non-linear electrochemical or photoelectrochemical systems can be linearised for small amplitude perturbations.

3.3 Theory of Steady state and Small Amplitude Responses for the Dye-sensitised Nanocrystalline TiO_2 Solar cell

3.3.1 Intensity Modulated Photocurrent Spectroscopy (IMPS)

In section 2.4.3, the generation/collection equation (continuity equation) of DSN solar cells used by Sodergren *et al.* was introduced. Incorporating the kinetics of electron extraction into the boundary conditions and introducing distance dependent parameters

Dloczik *et al.* have extended the Sodergren model [8, 11]. Firstly, this section will briefly discuss the basic features and notable differences between the Sodergren and Dloczik models (assumptions etc.). Then it will present the analytical expressions derived in Dloczik model for the steady state and small amplitude responses. These analytical solutions have been used to analyse the frequency-resolved measurements obtained in the present study, which subsequently provide the information about the electron transport and back reaction kinetics in DSN TiO_2 solar cells. This section will also briefly consider the case in which the back reaction of electrons with tri-iodide is second order in electron concentration.

For illumination from the substrate side, the electron generation and collection in DSN solar cells is given by the continuity equation [8, 10, 12]:

$$\frac{\partial n(x,t)}{\partial t} = \eta\alpha I_o e^{-\alpha x} + D_n \frac{\partial^2 n(x.t)}{\partial x^2} - \frac{n(x,t) - n_o}{\tau_n} \tag{3.23}$$

A detailed description of each term in equation (3.23) is given in section 2.4.3. The notable absentee from the continuity equation is the drift term. This is because the electronic charge in the solid is shielded by the ionic species in liquid electrolyte media, the electric field in the direction of the substrate is small [13, 14] (see section 2.4 for more details).

To derive the continuity equation, Sodergren *et al.* have made the following assumptions [11]. The electron transport occurs due to normal diffusion and the kinetics of the back reaction of electrons with I_3^- species in the electrolyte are pseudo first order with respect to electron density [11]. No distinction was made between free and trapped electrons [11]. However, these assumptions were thoroughly examined in the Dloczik model [8].

The first term (generation term) represents the electron generation for illumination from the substrate side. In the Dloczik model, the thin film of nanocrystalline semiconductor is assumed to be uniformly sensitised with dye ($1/\alpha >> d$) so that the adsorption coefficient, α is independent of distance. Light absorption by I_3^- in pores is not considered, and light

scattering by the nanocrystalline phase is treated semiempirically by defining an effective absorption coefficient. For illumination from the electrolyte side, x in exponent term in equation (3.23) must be replaced by d-x, where d is the thickness of the TiO_2 film (see Figure 3.10).

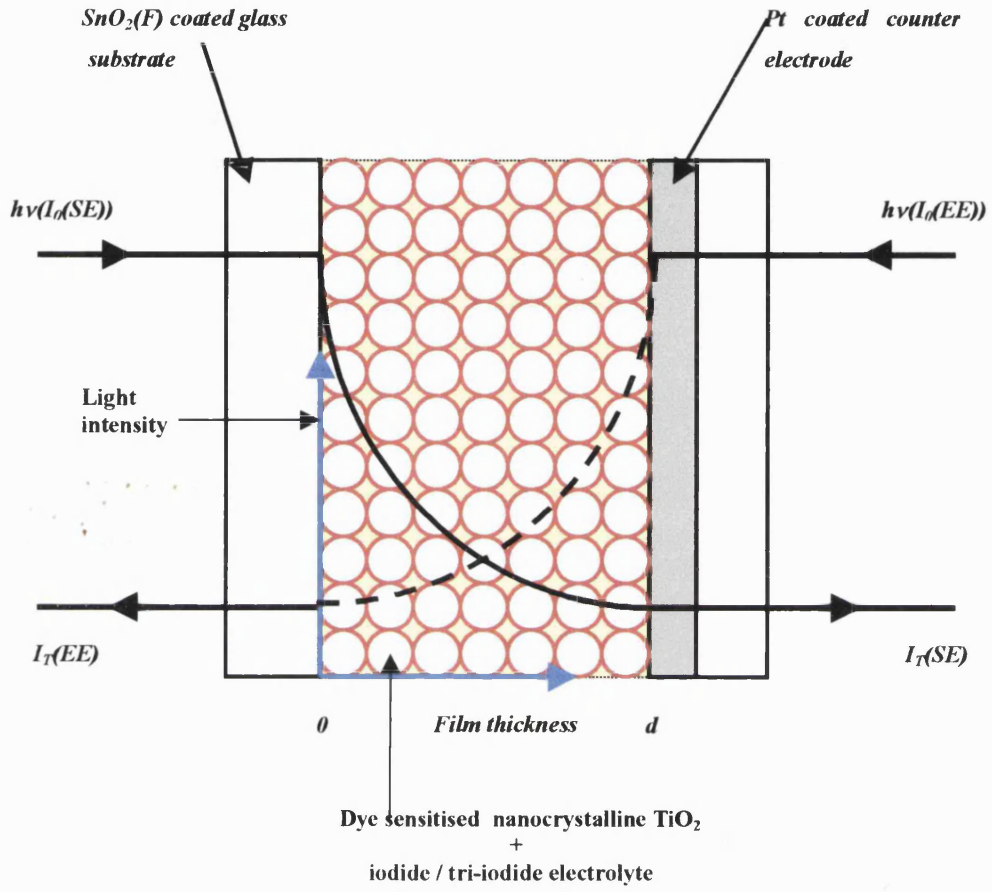

Figure 3.10 *An schematic representation of light absorption profile in DSN solar cell.*

As far as concerns the assumption of normal diffusion electron transport in the Sodergren model, the actual situation in DSN cell is rather different. This is because the trapping and thermal release of electrons at bulk and surface defects gives rise to a distribution of transit times that result in dispersive diffusion. At high electron densities (i.e. at high illumination), deep trapping states are filled and trapping occurs only in shallow traps so that electron transport is fast. The situation at low electron densities (i.e. at low light intensities) is different as electron trapping at deep levels becomes more important, and

transport is slower because the trap depth determines the thermal release rate (recall equation (2.32)). Therefore, diffusion cannot be described by Fick's laws as it represented by the second term in equation (3.23). In effect D_n is a function of the electron concentration, n. Therefore, the effect of electron trapping is considered and related to an effective diffusion coefficient of electrons, D_{eff}, determined by the expression

$$D_{eff} = D\frac{n_{free}}{n_{total}} = D\frac{k_{detrap}}{k_{trap} + k_{detrap}} \tag{3.24}$$

where n_{free} is the density of free conduction band electrons, n_{total} is the total density of free and trapped electrons, and k_{trap} and k_{detrap} are first order rate constants for trapping and detrapping of electrons.

Since the electron lifetime depends on illumination intensity, the next assumption concerning the kinetics of the back reaction in Sodergren model is also not quite correct. Recombination of electrons with I_3^- is a two-electron process:

$$I_3^- + 2e \rightarrow 3I^- \tag{3.25}$$

The studies presented in this thesis provides some evidence that this back reaction involves the formation of $I_2^{\bullet-}$ as an intermediate, and the rate may be second order in electron concentration [15-17] (see also chapter 5,6 and 7 for more details). If this is the case, the last term in equation (3.23) needs to be replaced by the corresponding second order term (see the equation (3.48)). Even if the back reaction is first order in electron density, the back electron transfer rate may be intensity dependent. Furthermore, the recombination with I_3^- is possible for both free and trapped electrons, and the Dloczik model considers this situation. In fact, as both electron diffusion coefficient and lifetime are intensity-dependent quantities, equation (2.23) is non-linear.

The impedance measurements have revealed that electron accumulation in DSN TiO_2 films at potentials near the open circuit photovoltage gives rise to a capacitance of the

order of 1 mF cm^{-2} [8], whereas in the absence of electron accumulation (i.e. at short circuit) and in the dark, it is about 10 μFcm^{-2}. In fact, the experimental results have been shown that the IMPS response is modified by the *RC* time constant even under short circuit conditions as electrons may accumulate at particles furthest from the SnO_2 substrate in high efficient cells [8, 13, 18, 19]. Therefore, the influence of the *RC* time constant of the system has also considered in the Dloczik model (also see Figure 3.11).

Considering all these features, incorporating the kinetics of electron extraction into the boundary conditions and introducing distance dependence parameters in continuity equation, Dloczik *et al.* have extended the Sodergren model and obtained the analytical expressions for the steady state and small amplitude responses (for both trap influenced and trap free cases).

The Trap Free Situation

In order to obtain the analytical solutions for the equation (3.23), two boundary conditions need to be defined. Since photogenerated electrons are extracted only at the SnO_2 substrate, the electron concentration gradient, $\partial n/\partial x$ must be zero when the TiO_2 film thickness approaches *d* (i.e. x = d). However, when x = 0, the electron flux must be equal to the rate of electron extraction, $k_{ext}n(0,t)$.

$$\left.\frac{\partial n(x,t)}{\partial x}\right|_{x=d} = 0 \tag{3.26}$$

$$D\left.\frac{\partial n}{\partial x}\right|_{x=0} = k_{ext}n(0.t) \tag{3.27}$$

As both electron diffusion coefficient and lifetime are intensity-dependent quantities, equation (2.23) is non-linear. However, the system can be converted into a linear system by applying a very small sinusoidal illumination of top of a much larger d.c. level (i.e. $I(t) = I_0 + I_0 e^{i\omega t}$), where ω is the angular frequency ($2\pi f$). The time-dependent electron concentration can be given by

$$n(x,t) = u(x)e^{i\omega t} \tag{3.28}$$

Then, the equation (3.23) and boundary values convert into the following form.

$$u'' = u\left(\frac{1}{D\tau} + \frac{i\omega}{D}\right) - \alpha\frac{I_0}{D}e^{-\alpha x} \tag{3.29}$$

$$u'(d) = 0 \tag{3.30}$$

$$Du'(0) = k_{ext}u(0) \tag{3.31}$$

The solution takes the following form

$$u(x) = Ae^{\gamma x} + Be^{-\gamma x} + Ce^{-\alpha x} \tag{3.32}$$

where α is the effective absorption coefficient and

$$\gamma = \sqrt{\left(\frac{1}{D\tau} + \frac{i\omega}{D}\right)} \tag{3.33}$$

$$C = \frac{\alpha I_0 / D}{\gamma^2 - \alpha^2} \tag{3.34}$$

$$A = C\frac{\alpha e^{-\alpha d}(k_{ext} + \gamma D) - \gamma e^{-\gamma d}(k_{ext} + \alpha D)}{\gamma[k_{ext}(e^{\gamma d} + e^{-\gamma d}) + D\gamma(e^{\gamma d} - e^{-\gamma d})]} \tag{3.35}$$

$$B = -C\frac{\alpha e^{-\alpha d}(k_{ext} + \gamma D) + \gamma e^{\gamma d}(k_{ext} + \alpha D)}{\gamma[k_{ext}(e^{\gamma d} + e^{-\gamma d}) + D\gamma(e^{\gamma d} - e^{-\gamma d})]} \tag{3.36}$$

The a.c. component of the photocurrent is given by

$$j(\omega) = D\left(\frac{\partial u}{\partial x}\right)\Big|_{x=0} = D(A\gamma - B\gamma - C\alpha) \tag{3.37}$$

For illumination from the electrolyte side, the a.c. photocurrent conversion efficiency $\Phi(\omega) = j_{photo}/qI_0$ is given by

$$\Phi(\omega) = \frac{\alpha}{\alpha + \gamma}\frac{\left(e^{(\gamma-\alpha)d} - e^{-(\alpha+\gamma)d}\right) + 2\alpha\left(\frac{e^{(\gamma-\alpha)d} - 1}{\gamma - \alpha}\right)}{\left(e^{\gamma d} + e^{-\gamma d}\right) + \frac{D\gamma}{k_{ext}}\left(e^{\gamma d} - e^{-\gamma d}\right)} \tag{3.38}$$

For large k_{ext} values, the response becomes diffusion-limited. In that case, the equation (3.38) can be written as

$$\Phi(\omega) = \frac{\alpha}{\alpha+\gamma} \frac{\left(e^{(\gamma-\alpha)d} - e^{-(\alpha+\gamma)d}\right) + 2\alpha\left(\frac{e^{(\gamma-\alpha)d}-1}{\gamma-\alpha}\right)}{\left(e^{\gamma d} + e^{-\gamma d}\right)} \tag{3.39}$$

For illumination from the substrate side, the ac photocurrent conversion efficiency is given by

$$\Phi(\omega) = \frac{\alpha}{\alpha+\gamma} \frac{\left(e^{\gamma d} - e^{-\gamma d}\right) + 2\alpha\left(\frac{e^{-\alpha d} - e^{-\gamma d}}{\gamma-\alpha}\right)}{\left(e^{\gamma d} + e^{-\gamma d}\right) + \frac{D\gamma}{k_{ext}}\left(e^{\gamma d} - e^{-\gamma d}\right)} \tag{3.40}$$

The diffusion-controlled solution for illumination from substrate side can be obtained by setting the k_{ext} large in equation (3.40)

$$\Phi(\omega) = \frac{\alpha}{\alpha+\gamma} \frac{\left(e^{\gamma d} - e^{-\gamma d}\right) + 2\alpha\left(\frac{e^{-\alpha d} - e^{-\gamma d}}{\gamma-\alpha}\right)}{\left(e^{\gamma d} + e^{-\gamma d}\right)} \tag{3.41}$$

The steady-state solutions for illumination from the either side for the diffusion-controlled limit can be obtained by setting $\omega = 0$ (i.e. setting $\gamma = (D\tau)^{-1/2}$)

The Influence of Electron Trapping and Detrapping

The Dloczik model has also considered the influence of electron trapping and detrapping for the illumination from the substrate side when the system is in diffusion controlled [8]. The first-order rate constant of electron trapping can be expressed as the product of number density of vacant traps ($N_{trap}(1-f_t)$), capture cross section (σ) and thermal velocity of electrons ($v_{thermal}$).

$$k_{trap} = N_{trap}(1-f_t)\sigma v_{thermal} \tag{3.42}$$

Since increasing the illumination intensity fills electron traps, one can expect a decrease of the value of k_{trap} with increase of light intensity. On the other hand, as the electron quasi-Fermi level varies throughout the TiO_2 film, k_{trap} may be distance dependent. The rate of release of trapped electrons can be given by a first-order rate constant, k_{detrap} is determined by the trap depth and the temperature (recall the equation (2.41)). This means that the variation of electron quasi-Fermi level throughout the TiO_2 film may also influence on k_{detrap}. However, for simplicity, Dloczik *et al.* have assumed that both k_{trap} and k_{detrap} are constant throughout the TiO_2 film.

When trapping and detrapping are considered, the diffusion equation for the conduction band electrons under illumination from substrate side becomes

$$\frac{\partial n}{\partial t} = D\frac{\partial^2 n}{\partial x^2} - \frac{n}{\tau_{cb}} - k_1 n + k_2 N + \eta\alpha I_0 e^{-\alpha x} e^{i\omega t} \tag{3.43}$$

where n is excess electron concentration, N is the density of trapped electrons and τ_{cb} is the lifetime for recombination of free electrons with I_3^-. The density of trapped electrons is given by

$$\frac{\partial N}{\partial t} = k_{trap} n - k_{detrap} N - \frac{N}{\tau_{trap}} \tag{3.44}$$

where τ_{trap} is the lifetime for recombination of trapped electrons with I_3^-. The analytical solution for the equation (3.43) takes the same form as that obtained in the absence of trapping, except that γ is different from the trap free case (i.e. equation (3.33)). The γ for the trapped influenced case is given by

$$\gamma^2 = \frac{1}{D_{cb}\tau_{cb}} + \frac{\dfrac{k_{trap}}{\tau_{trap}}\left(k_{detrap} + \dfrac{1}{\tau_{trap}}\right) + \omega^2}{D_{cb}\left(k_{trap} + \dfrac{1}{\tau_{trap}}\right)^2 + \omega^2} + \frac{i\omega}{D}\left(1 + \frac{k_{trap}k_{detrap}}{\left(k_{trap} + \dfrac{1}{\tau_{trap}}\right)^2 + \omega^2}\right) \tag{3.45}$$

However, if k_{trap} and k_{detrap} are much larger than the modulation frequency (k_{trap} and k_{detrap} >>ω), then the original expressions can be recovered with the effective electron lifetime τ_{eff} and effective diffusion coefficient D_{eff} defined by

$$\frac{1}{\tau_{eff}} = \frac{1}{\tau_{cb}} + \frac{k_{trap}}{1 + k_{detrap}\tau_{trap}} \tag{3.46}$$

$$D_{eff} = \frac{D}{1 + \frac{k_{trap}k_{detrap}}{\left(k_{detrap} + \frac{1}{\tau_{trap}}\right)^2}} \tag{3.47}$$

However, in the case of second-order back reaction of photogenerated electrons with tri-iodide, the continuity equation must be modified with the corresponding second-order back reaction term as follows.

$$\frac{\partial n(x,t)}{\partial t} = \eta\alpha I_o e^{-\alpha x} + D_n \frac{\partial^2 n(x.t)}{\partial x^2} - k(n - n_0)^2 \tag{3.48}$$

The boundary conditions applied in solving the equation (3.23), are also applied in this case. Equation (3.48) can solved numerically by the fully implicit finite difference method [20] to obtain the steady-state electron profiles and the steady-state photocurrents.

Linearisation of the decay kinetics lead definition of an effective first order electron lifetime. However, if the recombination of photogenerated electrons with I_3^- is second order with respect to electron concentration, the effective electron lifetime, τ_n is inversely proportional to the steady-state electron concentration, n as shown below.

For a second order decay;

$$\frac{dn}{dt} = G - kn^2 \tag{3.49}$$

where G is the generation term and k is the second order rate constant. For small perturbation of electron concentration;

$$n = n + \delta n \tag{3.50}$$

$$\frac{d(n+\delta n)}{dt} = G - k(n+\delta n)^2 \tag{3.51}$$

$$\frac{dn}{dt} + \frac{d\delta n}{dt} = G - k(n^2 + 2n\delta n + \delta n^2)^2 \tag{3.52}$$

For $\delta n \rightarrow 0$, δn^2 can be neglected. Equation (3.49) allows to obtain

$$\frac{d\delta n}{\delta t} = -2kn\delta n \tag{3.53}$$

$$\int \frac{1}{\delta n} d\delta n = -2knt \tag{3.54}$$

Integration gives the relation $\ln \delta n = -2knt + const$. Using the boundary condition that t = 0, $\delta n = \delta n_0$ gives the solution

$$\delta n(t) = \delta n_0 e^{-t/\tau_n} \tag{3.55}$$

where

$$\tau_n = \frac{1}{2kn} \tag{3.56}$$

Figure 3.11 shows the theoretically calculated and experimentally obtained IMPS plots. The notable difference between the theoretical and experimental IMPS plots is, the experimental plots have distorted at high frequencies. This may be due to the effect of RC attenuation or by inhomogeneous dye distribution [8, 14, 21].

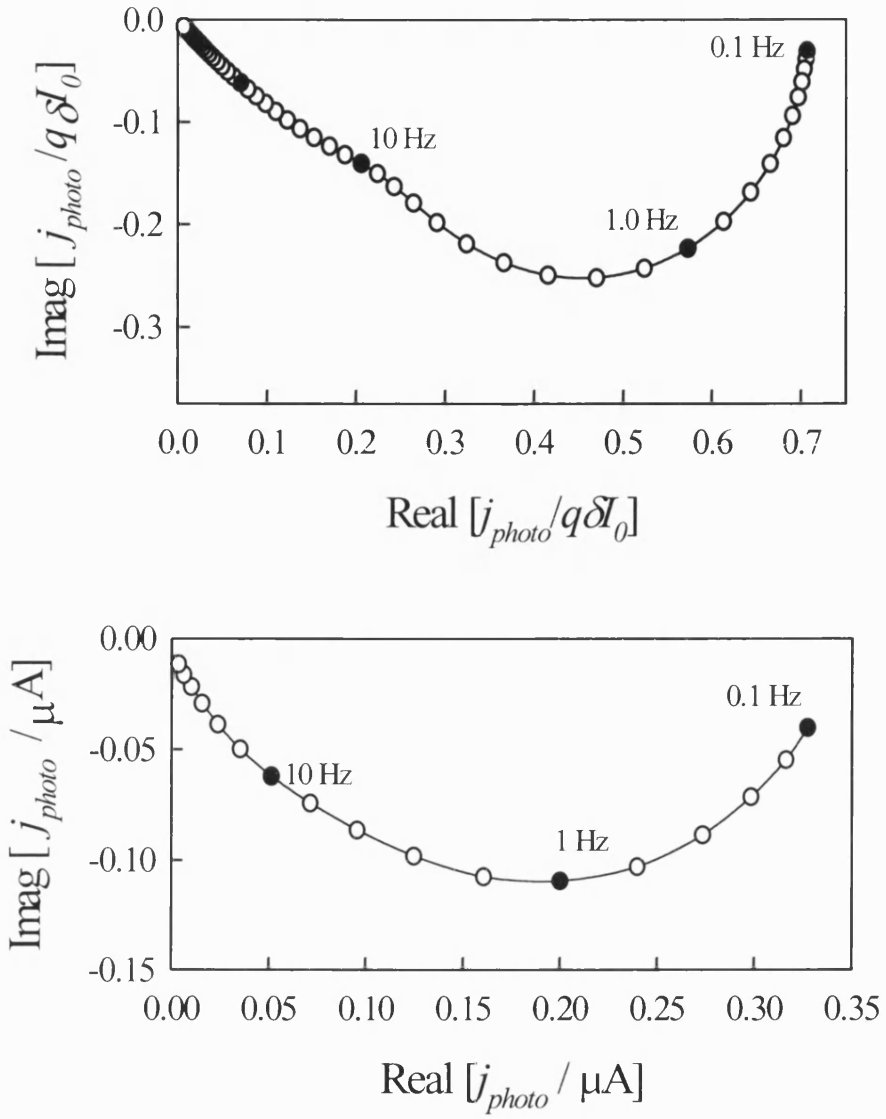

Figure 3.11 ***(upper)*** *An IMPS response calculated from equation (3.28) to (3.36) for 5 μm thick DSN TiO_2 film cell (where α = 2500 cm^{-1}, D_n= 10^{-6} cm^2s^{-1}, τ_n= 10 s obtained from the IMVS plot corresponding to same illumination intensity).* ***(lower)*** *Experimentally determined IMPS plot for a DSN TiO_2 cell with a 6 μm thick film.*

3.3.2 Intensity Modulated Photovoltage Spectroscopy (IMVS)

Intensity modulated photovoltage spectroscopy measures the perturbations of the photovoltage in response to the modulation of incident light intensity on top of a large d.c. illumination. Generally IMVS measurements can be performed at different constant current conditions through the external circuit (i.e. galvanostatic), but in the present study the measurements were obtained at zero current through the external circuit (i.e., $k_{ext} = 0$). Analytical solutions for the equation (2.23) in IMVS case, can be obtained by setting the limit $k_{ext} = 0$. The electron density at x = 0, $n_{x=0}(\omega)$ for open circuit is characterised by a semicircle in the lower complex plane with a minimum at $\omega_{min}=1/\tau_n$. Therefore, the electron lifetime can be obtained by ω_{min} of semicircle.

Figure 3.12 illustrates the calculated and experimentally obtained IMVS plots. This Figure represents the modulated voltage response rather than modulated electron density response. However, from equation (3.64) it is clear that for small modulations, δn is proportional to δU_{photo}.

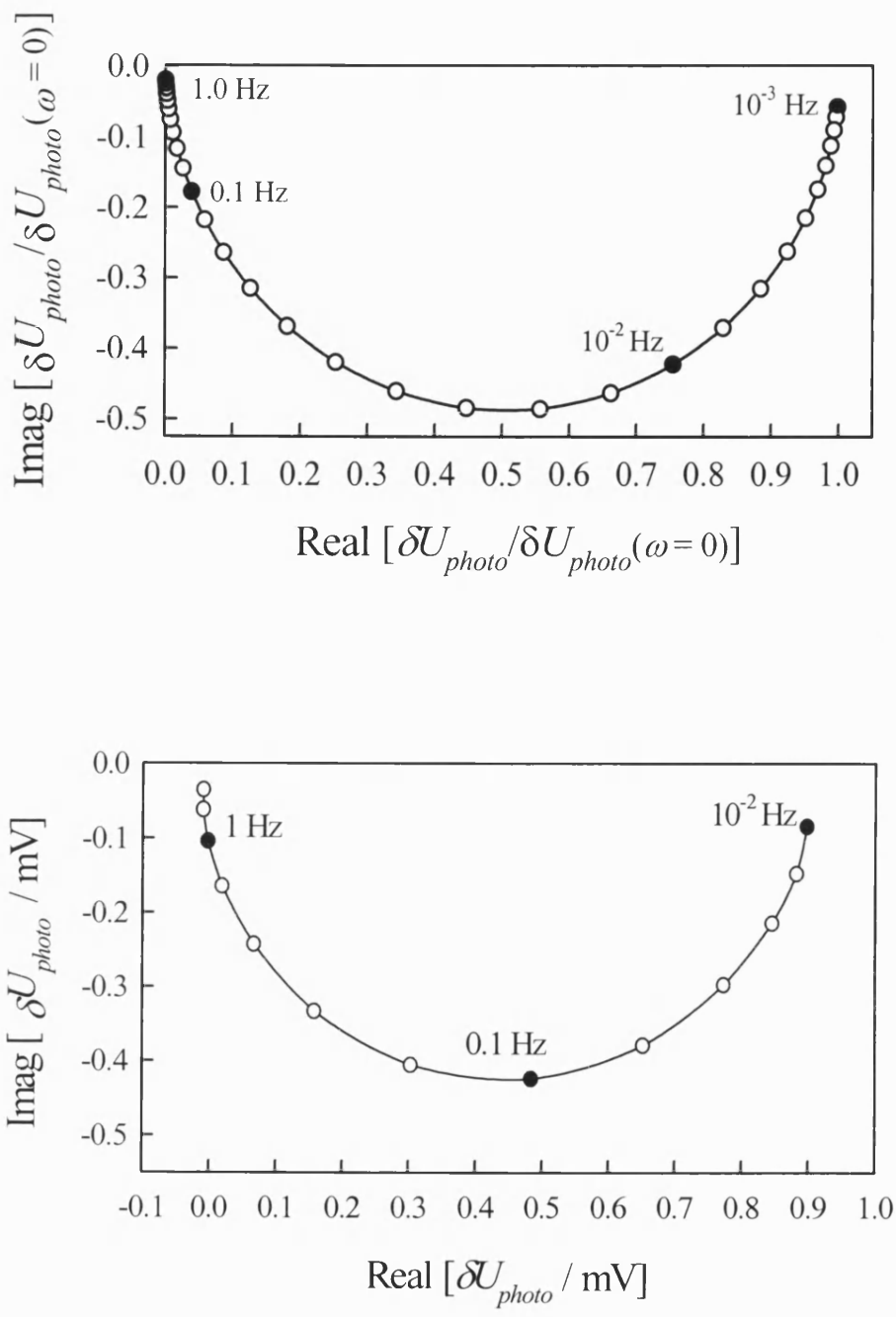

Figure 3.12 ***(upper)*** *An IMVS response calculated from equation (3.28) to (3.36) for 5 μm thick DSN TiO_2 film cell (where α = 2500 cm^{-1}, D_n= 10^{-6} cm^2s^{-1}).* ***(lower)*** *Experimentally determined IMVS plot for a DSN TiO_2 cell with a 6 μm thick film.*

Schlichthorl *et al.* have presented a detailed treatment on IMVS [9]. In that treatment they have discussed the relationship between the small amplitude-modulated photovoltage and corresponding modulation of free electron density (i.e., conduction band capacitance) and trapped electron density (i.e., surface state capacitance) [9]. The origin of the conduction band capacitance and surface states capacitance can be described as follows.

As described in Figure 2.18, in the dark, the Fermi levels of SnO_2, TiO_2 and I^-/I_3^- redox electrolyte are equal. The equilibrium electron density in the TiO_2 conduction band, is given by

$$\frac{n_0}{N_c} = e^{-\frac{(E_c - E_F)}{kT}} \tag{3.57}$$

As already shown by the equation (2.8), under illumination, the total electron density in the TiO_2 conduction band, $(n_0+\Delta n)$ is given by

$$\frac{n_0 + \Delta n}{N_c} = e^{-\frac{(E_c - {}_nE_F)}{kT}} \tag{3.58}$$

The photovoltage is a measure of the difference of Fermi level in the TiO_2 between the dark and illumination condition. Therefore the photovoltage can be given by

$$qU_{photo} = {}_nE_F - E_F \tag{3.59}$$

One has to consider the fact that at open circuit condition, the electron quasi-Fermi level, ${}_nE_F$, varies throughout the TiO_2 film, resulting a distance dependent U_{photo}. However, for a uniformly dye sensitised nanocrystalline TiO_2 cell (i.e., $1/\alpha = d$), the ${}_nE_F$ is independent of distance. In such condition, the U_{photo} is independent of distance. In such a situation, the equations (3.58) and (3.59) allow to obtain the following relationship.

$$\frac{n_0 + \Delta n}{N_c} = e^{-\frac{(E_c - E_F - qU_{photo})}{kT}} = e^{-\frac{(E_c - E_F)}{kT}} . e^{\frac{qU_{photo}}{kT}} \tag{3.60}$$

For a situation, in which a small periodic intensity modulation is superimposed on the background d.c. level, the equation (3.60) takes the following form.

$$\frac{n_0 + \Delta n + \delta n}{N_c} = e^{-\frac{(E_c - E_F)}{kT}} . e^{\frac{qU_{photo}}{kT}} . e^{\frac{q\delta U_{photo}}{kT}} \tag{3.61}$$

where δn is the periodic component of the excess electron density and δU_{photo} is the periodic photovoltage. Linear expansion of the last term in equation (3.61) gives

$$\frac{n_0 + \Delta n + \delta n}{N_c} = e^{-\frac{(E_c - E_F)}{kT}} . e^{\frac{qU_{photo}}{kT}} . \left[1 + \frac{q\delta U_{photo}}{kT}\right] \tag{3.62}$$

It follows that,

$$\frac{\delta n}{N_c} = e^{-\frac{(E_c - E_F)}{kT}} . e^{\frac{qU_{photo}}{kT}} . \left[\frac{q\delta U_{photo}}{kT}\right] \tag{3.63}$$

For a cell with a film of thickness d, the modulation of the conduction band free charge per unit area (δQ_{cb}) is given by

$$\delta Q_{cb} = qd\delta n = \frac{q^2 N_c d}{kT} . e^{-\frac{(E_c - E_F)}{kT}} . e^{\frac{qU_{photo}}{kT}} . \delta U_{photo} \tag{3.64}$$

The conduction band capacitance has been defined [10] as follows.

$$C_{cb} = \frac{q^2 N_c d}{kT} . e^{-\frac{(E_c - E_F)}{kT}} . e^{\frac{qU_{photo}}{kT}} \tag{3.65}$$

Equations (3.64) and (3.65) lead to the following relationship of the intensity modulated photovoltage and the corresponding perturbation of the free electron charge.

$$\delta Q_{cb} = C_{cb} \delta U_{photo} \tag{3.66}$$

Furthermore, the small periodic intensity modulation also perturbs the trapped electron density, n_t. For a complete treatment, one has to consider the perturbation of both free

and trapped electron density. In the dark at equilibrium, the trapped electron density is given by

$$n_t^0 = \int_{E_v}^{E_c} N(E) f(E) dE \approx \int_{E_v}^{E_F} N(E) dE \tag{3.67}$$

Under illumination, the trapped electron density is determined by the electron quasi Fermi level. Considering the equation (3.67) at open circuit condition and under illumination,, the trapped electron density, n_t can be approximately obtained by the following relation.

$$n_t = \int_{N_v}^{{}_nE_F} N(E) dE \tag{3.68}$$

The change in the trapped electron density for the small periodic intensity modulation at the electron quasi Fermi level, δn_t, is given by

$$\delta n_t = N({}_nE_F)\delta {}_nE_F = N({}_nE_F) q \delta U_{photo} \tag{3.69}$$

where $N({}_nE_F)$ is the trapped electron density at the electron quasi Fermi level. Similar to the case of conduction band free electron charge, the modulated trapped charge per unit area (δQ_t) can be obtained as follows (recall the equation (3.64)).

$$\delta Q_t = qd\delta n_t = q^2 dN({}_nE_F) q \delta U_{photo} \tag{3.70}$$

The surface state capacitance has been defined [10] as

$$C_t = q^2 dN({}_nE_F) \tag{3.71}$$

Therefore, equation (3.70) can be rewritten as

$$\delta Q_t = C_t \delta U_{photo} \tag{3.72}$$

Considering equations (3.66) and (3.72), the total photomodulated charge in the nanocrystalline electrode can be given by

$$\delta Q_{total} = (C_{cb} + C_t)\delta U_{photo} = C_{total}\delta U_{photo} \tag{3.73}$$

where C_{total} is the total capacitance (sum of the conduction band capacitance and surface states capacitance) of the nancrystalline electrode under illumination.

3.4 References

1. B. Oregan, J. Moser, M. Anderson, and M. Gratzel, Journal of Physical Chemistry 94:8720 (1990).
2. Y. Tachibana, J. E. Moser, M. Gratzel, D. R. Klug, and J. R. Durrant, Journal of Physical Chemistry 100:20056 (1996).
3. W. J. Albery and P. N. Bartlett, Journal of Electroanalytical Chemistry 129:2254 (1982).
4. J. Li, R. Peat, and L. M. Peter, Journal of Electroanalytical Chemistry 165:41 (1984).
5. J. Li and L. M. Peter, Journal of Electroanalytical Chemistry 193:27 (1985).
6. J. Li and L. M. Peter, Journal of Electroanalytical Chemistry 199:1 (1986).
7. P. E. de Jongh and D. Vanmaekelbergh, Physical Review Letters 77:3427 (1996).
8. L. Dloczik, O. Ileperuma, I. Lauermann, L. M. Peter, E. A. Ponomarev, G. Redmond, N. J. Shaw, and I. Uhlendorf, Journal of Physical Chemistry B 101:10281 (1997).
9. G. Schlichthorl, S. Y. Huang, J. Sprague, and A. J. Frank, Journal of Physical Chemistry B 101:8141 (1997).
10. G. Franco, J. Gehring, L. M. Peter, E. A. Ponomarev, and I. Uhlendorf, Journal of Physical Chemistry B 103:692 (1999).
11. S. Sodergren, A. Hagfeldt, J. Olsson, and S. E. Lindquist, Journal of Physical Chemistry 98:5552 (1994).
12. H. Lindstrom, H. Rensmo, S. Sodergren, A. Solbrand, and S. E. Lindquist, Journal of Physical Chemistry 100:3084 (1996).
13. D. Vanmaekelbergh and P. E. de Jongh, Journal of Physical Chemistry B 103:747 (1999).

14. L. M. Peter and D. Vanmaekelbergh, in Advances in Electrochemical Science and Engineering, Vol. 6 (D. M. Alkire and D. Kolb, eds.), VCH Wiley, New York, 1999, p. 77.
15. L. M. Peter and K. G. U. Wijayantha, Electrochemistry Communications 1:576 (1999).
16. A. C. Fisher, L. M. Peter, E. A. Ponomarev, A. B. Walker, and K. G. U. Wijayantha, Journal of Physical Chemistry B 104:949 (2000).
17. L. M. Peter and K. G. U. Wijayantha, Electrochimica Acta 45:4543 (2000).
18. L. M. Peter, E. A. Ponomarev, G. Franco, and N. J. Shaw, Electrochimica Acta 45:549 (1999).
19. D. Vanmaekelbergh, F. Iranzo Marin, and J. van de Lagemaat, Ber. Bunsen-Ges. Phys.Chem. 100:616 (1996).
20. A. C. Fisher and R. G. Compton, Journal of Physical Chemistry 90:247 (1986).
21. G. Franco, L. M. Peter, and E. A. Ponomarev, Electrochemistry Communications 1:692 (1999).

Chapter 4

Experimental methods

4.1 Introduction

As already discussed in chapter 1, dye-sensitised nanocrystalline solar cells have shown promising photovoltaic properties and attracted considerable attention from the scientific community all over the world [1-8]. The basic operating principles of the dye-sensitised solar cell are reasonably well understood [9]. However, a much-needed comprehensive fundamental understanding of the system has not been achieved yet. Several aspects such as electron transport within the nanocrystalline TiO_2 film, and the mechanism of the back reaction of electrons with I^-_3, still remain unresolved. The situation has directly affected further progress, as it is not clear what limits the cell performance.

In the present work, dye-sensitised nanocrystalline solar cells were studied using steady-state techniques, transient techniques and periodic perturbations to answer several key questions [10-12]. Steady state techniques such as I-V curves and IPCE plots were used for the preliminary characterisation of DSN solar cells. Small amplitude laser pulse excitation transient measurements and the charge extraction technique were the transient techniques that were used to characterise the electron transport and back reaction kinetics in DSN solar cells. Periodic techniques such as IMPS and IMVS were very useful to determine electron diffusion coefficients and electron life times of the dye-sensitised nanocrystalline TiO_2 solar cells. The combination of frequency-resolved technique studies and time-resolved technique studies gave a good basis for understanding the electron transport and back reaction kinetics in DSN solar cells.

Sections 4.2 and 4.3 of this chapter deals with the preparation of the dye-sensitised nanocrystalline TiO_2 solar cell and their solid state analogues. The rest of the chapter describes the techniques that were used to characterise the dye-sensitised nanocrystalline TiO_2 solar cells.

4.2 Fabrication of the Dye-sensitised Nanocrystalline TiO_2 Solar cell

4.2.1 Preparation of Nanocrystalline TiO_2 colloid

Nanocrystalline TiO_2 colloid was prepared by the following sol-gel method [3]. First a volume of 37 mL of titanium (IV) isopropoxide (Aldrich, 99.9%) was mixed with 10 mL of 2-propanol (Aldrich, anhydrous 99.8+%). This solution was added dropwise over 30 min into a stirred mixture of 80 mL of glacial acetic acid (BDH, 100%) and 250 mL of de-ionised water contained in a conical flask at 0 °C. The resulting solution contained in the conical flask was placed on a hot plate and heated up to 80 °C for 8 hours while stirring vigorously. The resulting gel-like solution was transferred into a PTFE lined titanium autoclave (Parr General Purpose Acid Digestion Bomb, Model No. 4744) and heated to 230 °C using a thermostatic heating pad (Electrothermal, 200 W) for 12 hours.

Figure 4.1 *The PTFE lined titanium autoclaving system.*

Upon removal from the titanium autoclave, the solution was sonicated for 5 min with an approximate power of 250 W (KERRY, 250 W ultrasonicator). The solution was then concentrated to 150 g/L by a rotary evaporator (BÜCHI, R-114). 4 g of Carbowax (Riedel-de Haen, Carbowax 20000) was added to the solution and it was stirred overnight. The resulting nanocrystalline TiO_2 colloidal solution was kept in a sealed container in a refrigerator and used for the nanoporous TiO_2 film preparation.

4.2.2 Deposition of Nanocrystalline TiO_2 film

Fluorine-doped conductive glass substrates (Libby Owens Ford TEC-10, 10 Ω $Sn O_2$) were cleaned by overnight immersion in a solution of KOH (Aldrich, 85+%) in isopropanol, rinsed with deionised water, and dried in an air stream. In order to prevent direct contact between the liquid electrolyte and the conducting substrate a few drops of 1% titanium (IV) isopropoxide in isopropanol solution were applied to the dried film. Finally the coated plates were fired at 450 °C for 30 min in an air stream (STEINEL, Hot-air gun Model HG 3000 SLE) (see Figure 4.2). The glass chamber temperature was measured using a type K thermocouple (DIGITRON, Model 3900). The thin dense layer of TiO_2 is intended to prevent direct contact of liquid electrolyte with conducting SnO_2 substrate. Some cells were also fabricated and studied without the thin dense TiO_2 layer.

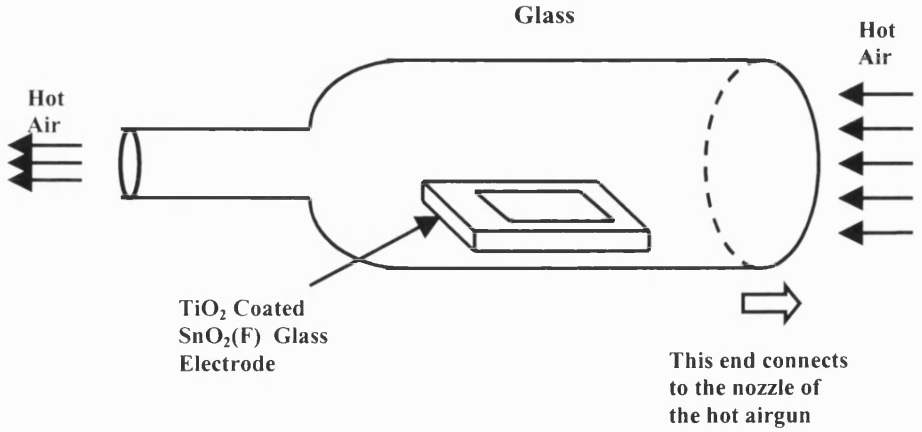

Figure 4.2 *Glass chamber for heat treatment of substrates.*

A 1 cm x 3 cm strip on the conducting substrate was masked out by 3M Scotch adhesive tape as described in Figure 4.3a. The masked area can later be used to provide the electrical contacts to the working electrode. The Scotch adhesive tapes form a mould or channel about 40-50 μm deep into which the nanocrystalline TiO_2 colloidal solution can flow.

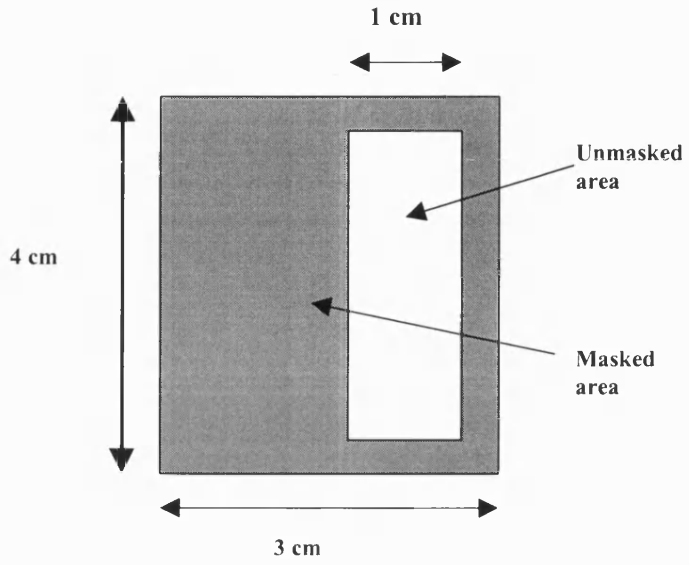

Figure 4.3a *Dimensions of the working electrode.*

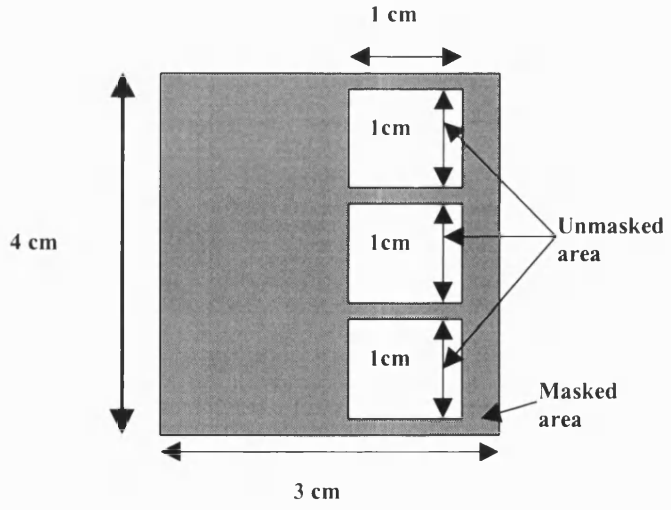

Figure 4.3b *The design of a 3-active area electrode*

In some cases 3 active area dye-sensitised nanocrystalline solar cells were also fabricated. The object was to prepare 3 rectangular TiO_2 films on the same conducting glass plate, so 3 unmasked rectangular areas were left in this case as shown in Figure 4.3b. The nanocrystalline TiO_2 colloidal solution was then distributed uniformly over the whole electrode by sliding a glass rod over the electrode as shown in Figure 4.4.

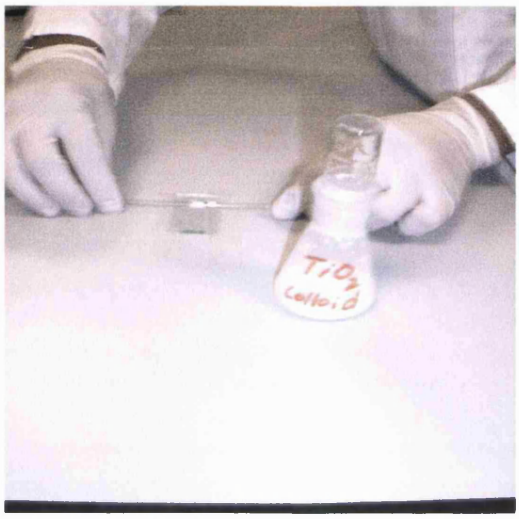

Figure 4.4 *Spreading the nanocrystalline TiO2 colloidal solution over the masked area of the electrode.*

The film was then allowed to dry in air for a few minutes. Then the tape was carefully removed and the resulting rectangular TiO_2 film annealed in an air stream at 450 °C for 30 min. This resulted in an almost transparent nano-structured TiO_2 film. (see section 4.3, which describes the surface morphology and particle size studies on the nanocrystalline TiO_2 films by SEM and AFM micrographs.)

4.2.3 Coating the Nanocrystalline TiO_2 film with Dye

After annealing the TiO_2 film in the hot air flow for 30 min at 450 °C, the nozzle temperature of the hot air gun was slowly brought down to about 80 °C. Then the TiO_2 film was removed and immediately immersed in a 3 x 10^{-4} M solution of the N3 dye (cis-

di (thiocyanato)-N, N-bis (2,2'-dicarboxylate) ruthenium (II)) (SOLARONIX SA) in dry ethanol (Aldrich, anhydrous, denatured with 5% isopropyl alcohol and 5% methyl alcohol) while the film was still hot (~ 80 °C). After being immersed, the TiO_2 electrode was left for 12 hours in the dark for dye adsorption. Dry argon was bubbled through the ethanolic N3 dye solution for 30 min to remove all traces of oxygen just prior to use.

It is worth noting here that in the presence of water, hydroxyl radical ions (OH^{o}) are formed at UV illuminated TiO_2. These can easily oxidise and destroy the organic molecular sensitiser N3 dye [13]. It has also been reported that water co-ordinates with the TiO_2 surface reducing the number of available TiO_2 sites that anchor with carboxylic groups of N3 dye [14, 15]. Removal of all the traces of oxygen is also essential as oxygen produces super-oxide radical ion (O_2^{o-}) under the band gap illumination of TiO_2. Super-oxide radical ion is strong enough to completely oxidise the organic molecular sensitiser N3 dye [16, 17]. Therefore, it is necessary to keep the system in the dark during the dye adsorption process to ensure that the nanocrystalline TiO_2 is photocatalytically inactive.

After 12 hours of dye adsorption, the electrode was taken out and washed with dry ethanol and dried in a dry N_2 stream. The dye-coated nanocrystalline TiO_2 electrode was stored under argon for later use in the final solar cell assembly step.

4.2.4 Preparation of the counter-electrode

A second fluorine-doped conductive glass substrate (Libby Owens Ford TEC 10, 10 Ω SnO_2) was cleaned by overnight immersion in a solution of KOH in isopropanol, rinsed with de-ionised water, and dried in an air stream. Two holes (diameter ~ 2 mm) were drilled through the glass plate using a diamond drill (RS Scientific, 9-18 V DC), so that the liquid electrolyte could be introduced at a later stage. Figure 4.5 shows the top view of the counter electrode after drilling the holes.

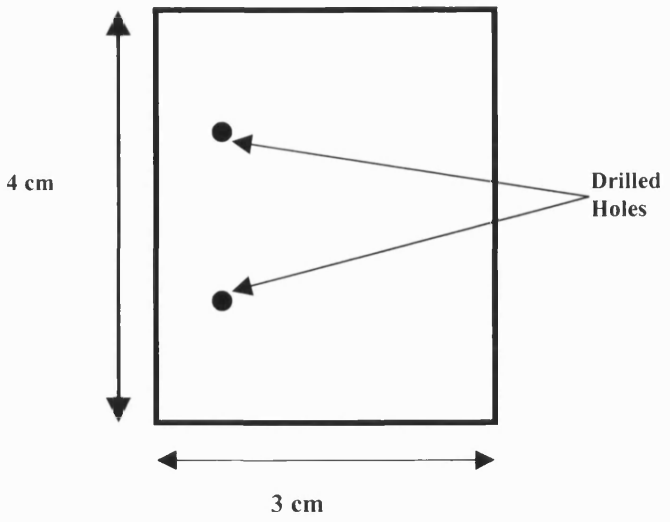

Figure 4.5 *The top view of the secondary electrode after drilling holes.*

Then a semi-transparent thin layer of platinum was sputter-deposited on the conductive surface of the glass plate using an Agar Sputter coater (Agar Scientific, B7340). The freshly coated Pt catalytic film was annealed in an air stream at 250 °C for 10 min. This was done in order to make sure that sputter-deposited Pt particles adhere onto the SnO_2 layer and are scratch resistant. The counter electrode was stored under argon for later use in the final solar cell assembly step. Storing under argon prevents adsorption of impurities on the surface of the Pt film from the gas phase. Figure 4.6 shows the counter electrode after completion.

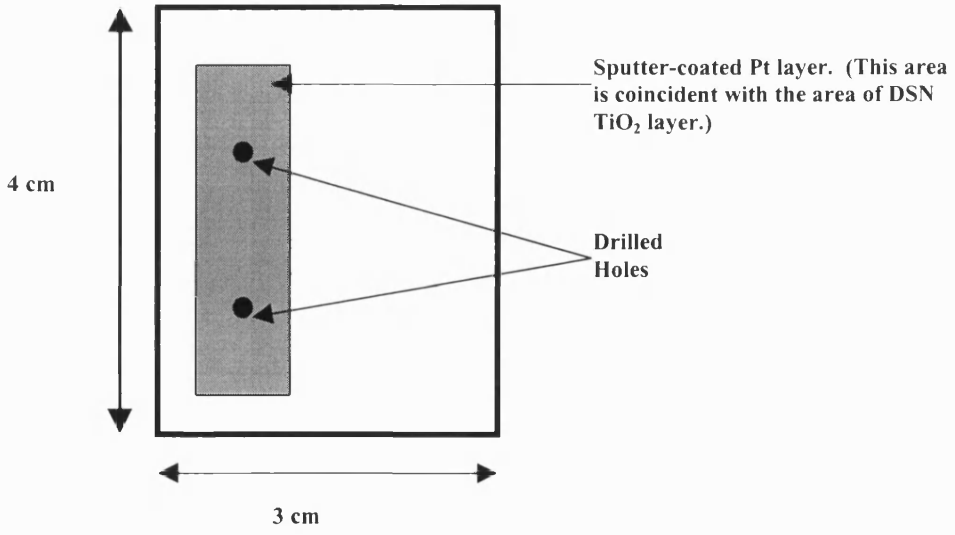

Figure 4.6 *The top view of the counter electrode after completion.*

4.2.5 Assembly of the Dye-sensitised Nanocrystalline TiO_2 Solar cell

The dye adsorbed nanocrystalline TiO_2 electrode and Pt coated counter electrode were sandwiched together. Care was taken to offset the two electrodes so that all of the TiO_2 coated area of the working electrode is covered by the Pt coated area of the counter electrode, while ensuring that enough space is left on both electrodes for applying a strip of silver conducting paint (RS Scientific) so that contacts could be made using crocodile clips on each electrode. The sandwiched electrodes were separated by transparent Surlyn® 1702 (Dupont, ionomer polyethylene resin, 25 μm thick). This was done in such a way that the dye adsorbed TiO_2 layer and sputter-deposited Pt layer faced one another and were not covered by the Surlyn® 1702 film. Dupont polyethylene resins are available as either a Sodium or a Zinc ionomer where polyethylene chain substituted with metal carboxylate groups (see Figure 4.7 for chemical formulation of metal ionomer polyethylene resin). Sodium ionomers are known for exceptional toughness and resistance to fats and oils while zinc ionomers exhibit outstanding direct adhesion and possess excellent chemical resistance. Figure. 4.8 shows the sandwiched electrodes.

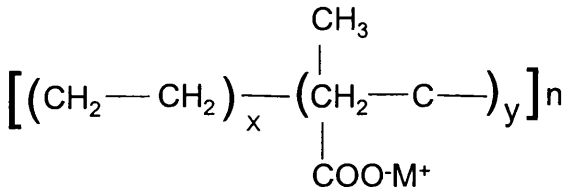

M = Sodium, Zinc

Figure 4.7 *Chemical formula of metal ionomer polyethylene resin.*

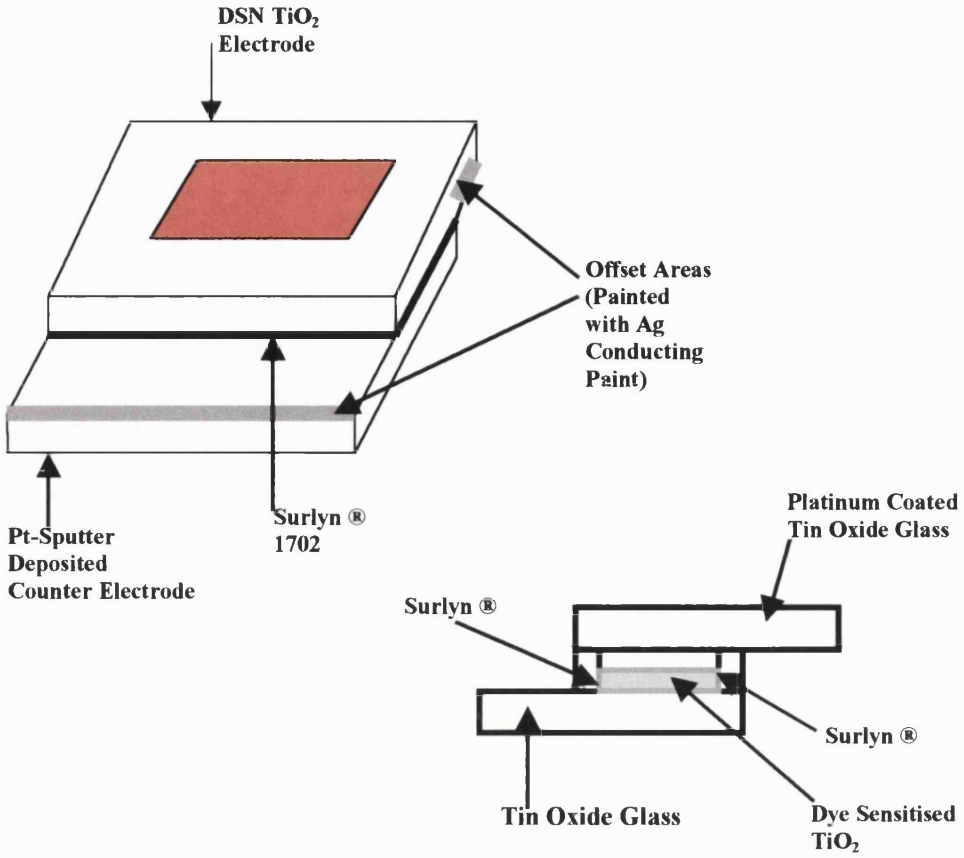

Figure 4.8 *Construction of the sandwiched electrodes showing the offset areas in both electrodes and electrode separating Surlyn® 1702 ionomer polyethylene film. (**upper** : side view and **lower** : cross sectional view)*

The sandwiched electrodes were tightly clamped together between a domestic electric iron surface and a hot plate surface. The electrode clamping apparatus is shown in Figure 4.9.

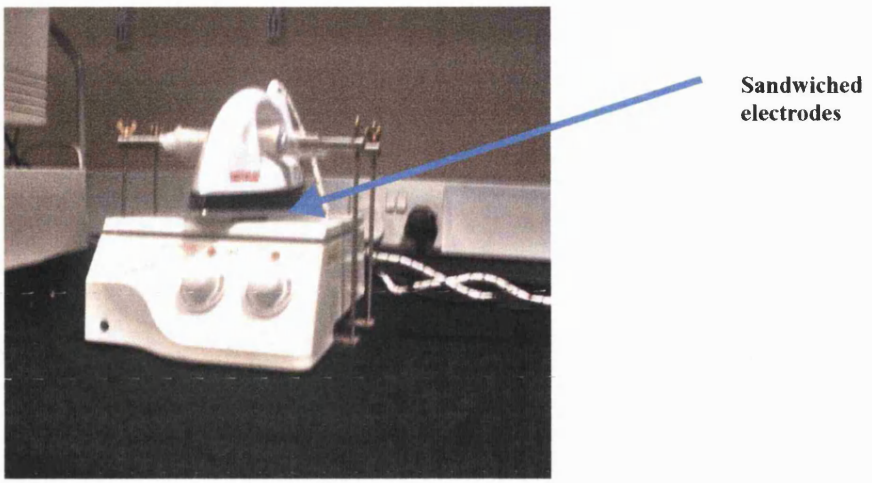

Figure 4.9 *The electrode clamping apparatus*

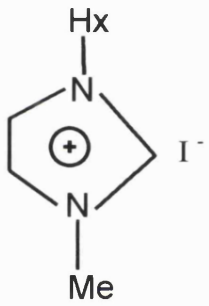

Figure 4.10 *The molecular structure of methylhexylimidazolium iodide (MHImI).*

Heat was gradually applied from either side by the hot iron and hot plate so that the Surlyn melted and sealed the electrodes together. The sandwiched cell was left clamped until the cell cooled down. Then the cell was flushed with argon and electrolyte solution was introduced through the holes drilled in the counter electrode. The electrolyte solution was composed of 0.85 M methylhexylimidazolium iodide (MHImI) (see the Figure 4.10 for molecular structure of MHImI), 0.05 M iodine (Aldrich, anhydrous, beads, 10 mesh, 99.999%), 0.1 M LiI and 0.2 M tert-butylpyridine (Aldrich, 99%) in acetonitrile (Aldrich, 99.93+%, HPLC grade). Acetonitrile was further dried with Al_2O_3 (BDH, high surface area, active, neutral) followed by filtration Other chemicals were used without further

purification. MHImI was received from Institut fur Angewandte Photovoltaik, Germany. Subsequently the two holes were sealed with microscope cover plates and Surlyn hot melt by using the homemade apparatus, constructed from two soldering irons shown in Figure 4.11. Figures 4.12a and 4.12b show completed dye-sensitised nanocrystalline TiO_2 solar cells.

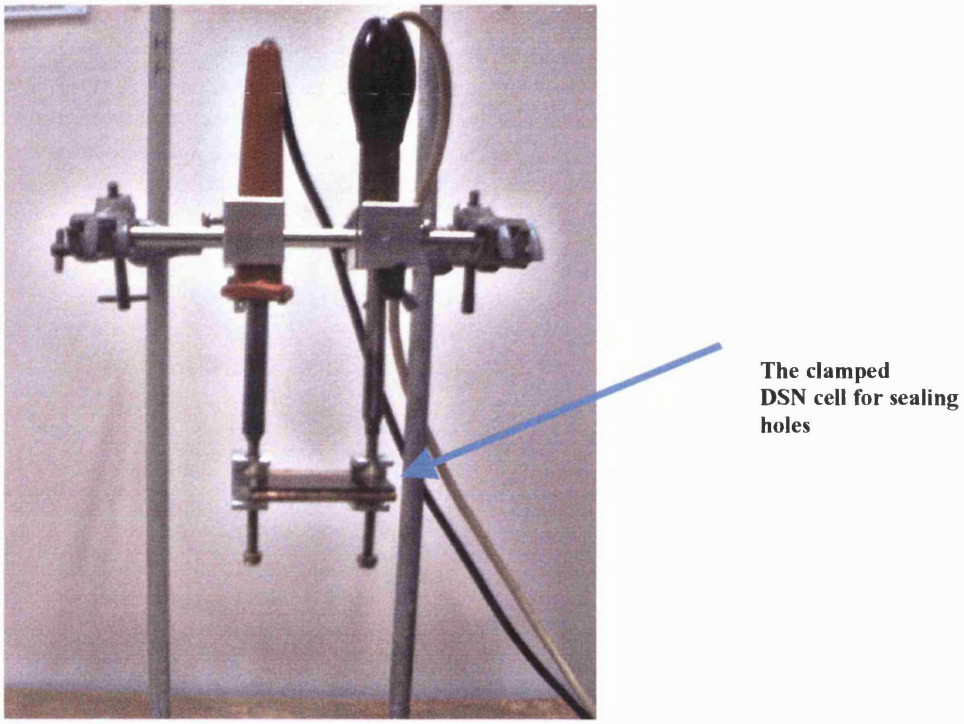

Figure 4.11 *The homemade apparatus that was used for sealing the counter electrode holes.*

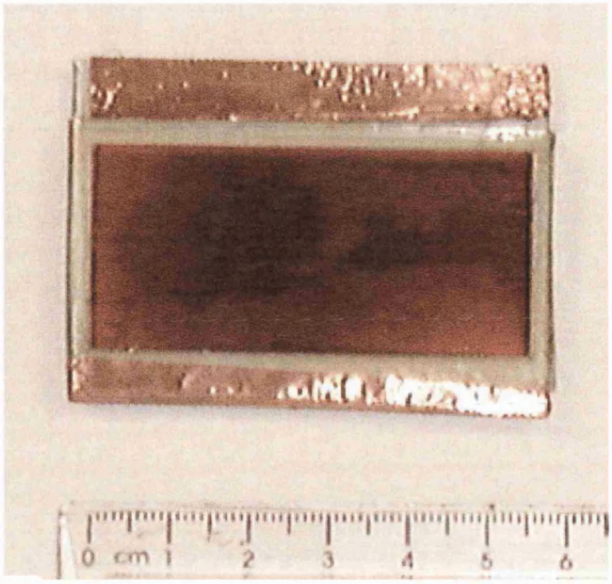

Figure 4.12a *The completed dye-sensitised nanocrystalline TiO_2 solar cell.*

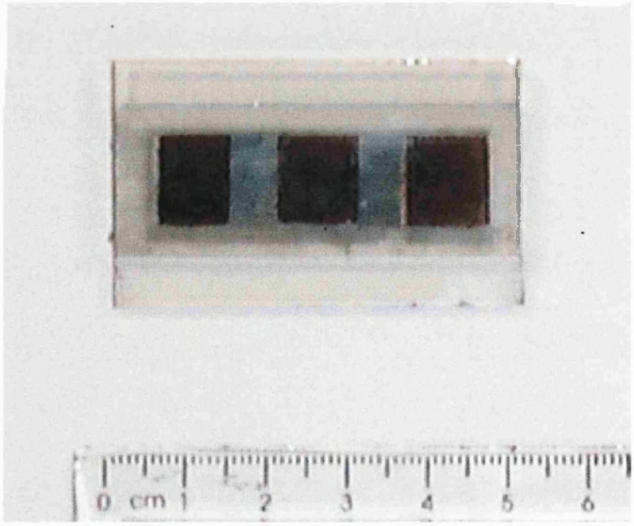

Figure 4.12b *Completed 3 active area dye-sensitised nanocrystalline TiO_2 solar cell.*

4.3 Construction of Dye sensitised Solid State Photovoltaic cells

4.3.1 Dye sensitised Solid State Photovoltaic cell made with CuI as the p-type semiconductor.

A porous thin layer of TiO_2 was deposited on fluorine-doped SnO_2 conductive glass substrates by the following method. Titanium (IV) isopropoxide (5 mL) (Aldrich, 99.9%), glacial acetic acid (5 mL) (BDH, 100%) and isopropanol (20 mL) (Aldrich, anhydrous 99.8+%) were vigorously mixed together. Then 5 mL of deionised water was added to the above mixture drop by drop while stirring. A fine crystallite TiO_2 colloidal solution was obtained by this procedure. Fluorine-doped conductive glass substrates (Libby Owens Ford TEC 10, 10 Ω SnO_2) were cleaned by overnight immersion in a solution of KOH (Aldrich, 85+%) in isopropanol, rinsed with deionised waster, and dried in an air stream. The conductive glass substrate was placed on the surface of a hot plate (surface temperature ~ 125 °C) and a few drops of colloidal TiO_2 solution was spread evenly on the surface of it and allowed to dry. Then the plate was sintered at 450 °C for 20 minutes and the process repeated until a semi-transparent porous TiO_2 film has been deposited. Care was taken to keep a bare SnO_2(F) site (TiO_2-free site) in an edge on the SnO_2(F) conductive substrate so that it can be used to make the electrode contacts with the external circuit later.

The TiO_2 film was immersed in a 3 x 10^{-4} M solution of the N3 dye (cis-di (thiocyanato)-N, N-bis (2,2'-dicarboxylate) ruthenium (II)) (SOLARONIX SA) in dry ethanol (Aldrich, anhydrous, denatured with 5% isopropyl alcohol and 5% methyl alcohol) while the film was still hot (~ 80 °C). Dry argon was bubbled through the ethanolic N3 dye solution for 30 min to remove all traces of oxygen just prior to immerse the TiO_2 film. After being immersed, the TiO_2 electrode was left for overnight in the dark for dye adsorption. The dye coated TiO_2 film was rinsed with ethanol and dried in an air stream.

0.63 M solution of CuI was prepared by dissolving 0.6 g of CuI (Alfa, 99.9984% metals basis) in 50 mL of dry acetonitrile (Aldrich, 99.8+%). Then the dye coated TiO_2 film was

placed on a surface of a hot plate (surface temperature ~ 80 °C) which was kept inside an argon purged glove box. The CuI solution was carefully spread over the dye coated porous TiO_2 surface and allowed to dry. This procedure was repeated until the pores filled with CuI and the surface resistance of CuI film was reduced to 50-60 Ω/cm^2. Care was taken to avoid directly contacting the bare $SnO_2(F)$ site and CuI layer. Electrical contact to the CuI surface was made by evaporation of gold. In some cells, the electrical contact was made by pressing a gold coated conductive $SnO_2(F)$ glass plate. Figure 4.13 shows a constructed dye sensitised solid state solar cell.

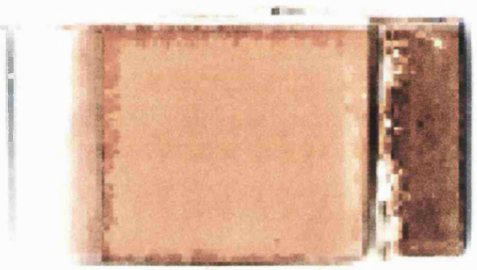

Figure 4.13 *The completed dye sensitised solid state photovoltaic cell made with CuI as the p-type semiconductor.*

4.3.2 Dye sensitised Solid State Photovoltaic cells made with conducting polymers as hole transport materials.

Both types of TiO_2 films (transparent nanocrystalline TiO_2 films made by the procedure given in section 4.2.2 and semi-transparent porous TiO_2 films made by the procedure described in section 4.3.1) were tested in the dye sensitised solid state photovoltaic cells that replaced the liquid electrolyte by a conductive polymer. Both types of TiO_2 electrodes were coated with N3 sensitiser dye following the procedures described in section 4.2.3 and 4.3.1. Attempts were taken to employ Poly(p-phenylene vinylene) (PPV), Poly(vinylcarbazole) (PVK) and Poly(aniline) (PANI) as hole transport materials in the construction of dye sensitised solid state photovoltaic devices as given below.

Fabrication of devices with Poly(p-phenylene vinylene) (PPV)

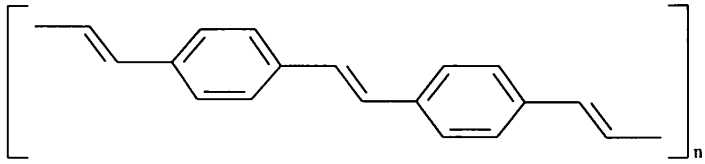

Figure 4.14 *Poly(p-phenylene vinylene) (PPV)*

Calculations were done to find out the volume remain in porous dye sensitised electrode that has to be filled with the PPV, taking in to account the average TiO_2 particle size and assuming that they are spherical. Then a series of PPV solutions in Tetra Hydro Furan (THF) (Aldrich, 99+%) with different concentrations were prepared. (PPV concentrations were selected in a way that number of THF drops require to fill the porous space in dye coated electrode is different from solution to solution. The idea of doing this is to obtain the best penetration of PPV into porous network). A thin layer of PPV was deposited on dye coated porous TiO_2 electrode using the homemade spin coating system. Series of cells were constructed repeating the same procedure using PPV solutions with different concentrations. The back electrical contact was made by pressing a gold coated conductive $SnO_2(F)$ glass plate.

Fabrication of devices with Poly(vinylcarbazole) (PVK)

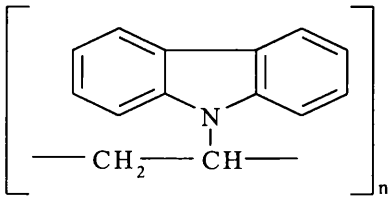

Figure 4.15 *Poly(vinylcarbazole) (PVK).*

A series of PVK solutions in Toluene (Aldrich, anhydrous, 99.8%) with different concentrations were prepared and dye adsorbed porous TiO_2 electrodes were coated with

PVK by spin coating method as described in previous case. Gold back electrical contact was made same as the previous case. In some cases, PVK doped with iodine under vacuum condition first and then prepared the solution series. The purpose of doing that is to enhance to hole conductivity in PVK polymer chains.

Fabrication of devices with Poly(aniline) (PANI)

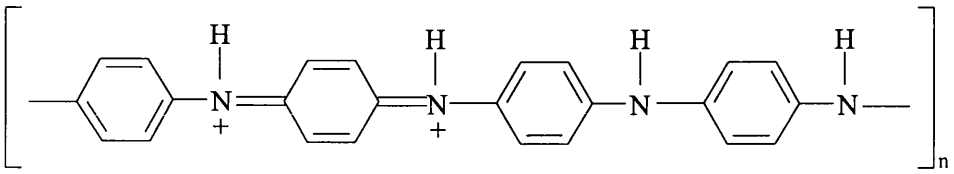

Figure 4.16 *Partially oxidised form of Poly(aniline) (also known as Emeraldine Salt)*

Emaraldine salts with protonic dopants containing different types of counter-ion possess electrical conducting properties. In fact, Emeraldine Camposulfate has shown very good electrical conducting properties Therefore, Emeraldine Camposulfate was chemically prepared by the following method.

Anilinium sulfate was prepared by mixing Aniline (BDH, AnalaR) and sulfuric acid in equi-molar ratio. The resulting solid, anilinium sulfate was washed and dried. This was mixed with $(NH_4)_2S_2O_8$ aqueous solution in 2:1 molar ratio to obtain the greenish colour poly(aniline) (emaraldine salt with the counter ion SO_4^{2-}). This product was converted to blue coloured emaraldine base by adding NaOH and then washed and dried. This was dissolved in 1-Methyl-2-pyrrolidinone (Aldrich, 99+%). Camphorsulfonic acid (Aldrich, 98%) was also dissolved in 1-Methyl-2-pyrrolidinone separately and both solutions were mixed each other to obtained Emeraldine Camposulfate solution in 1-Methyl-2-pyrrolidinone. The number of moles of Camphorsulfonic acid that dissolved in 1-Methyl-2-pyrrolidinone was adjusted to the same mole number of $(NH_4)_2S_2O_8$ that used in polymerisation process so that there is no excess Camposulfate ions trapped in polymer strands. This solution was used to fill the remaining porous space in dye coated porous

TiO_2 electrodes by spin coating method. Gold back contact was made as described in previous cases.

In some cases, PANI was reduced, reacting with Hydrazine (Aldrich) to obtain the Leucoemeraldine form. Then Emaraldine salt and Leucoemeradine were mixed in equi-molar ratio in 1-Methyl-2-pyrrolidinone. Then, this solution was used to deposit a PANI layer on dye coated porous TiO_2 electrodes by spin coating method.

4.3.3 Dye sensitised Organoceramic Nanocomposite Photovoltaic Devices

Attempts were also taken in this work to construct dye sensitised organoceramic nanocomposite photovoltaic devices. First, dye-coated nanocrystalline particles were obtained as follows.

The nanocrystalline TiO_2 colloidal solution prepared by sol gel method (see section 4.2.1) was dried and ground (in a motor pestle) to obtain nanocrystalline TiO_2 powder. The powder was heated upto 100 ^oC and transferred into a 3 x 10^{-4} M ethanolic solution of N3 dye while the powder was still hot and left it for overnight. The resulting deep reddish dye coated nanocrystalline TiO_2 powder filtered by a 20 nm pore size filter paper and dried in a desicator under N_2.

2 g of dye-coated nanocrystalline TiO_2 powder was mixed with PPV, PVK and PANI solutions (prepared in different concentrations as in the case of spin coating solutions) separately. A thin layer of nanocrystalline TiO_2/dye/polymer paste was coated onto a SnO_2(F) conductive glass plate and allow to dry. This was sandwiched with a second SnO_2(F) conductive glass plate. Care was taken to prevent directly contacting two conductive glass plates. In some cases, nanocrystalline TiO_2/dye/polymer layer was heated upto 80 ^oC first and then sandwiched with a second SnO_2(F) conductive glass plate. The purpose of heat treatment was, sintering the TiO_2 particles for the better electrical contacts.

4.4 Surface Morphology and Particle size Measurements

In order to observe the surface morphology and determine the average particle size of the nanocrystalline TiO_2 electrode, the electrode microstructure was studied using a high-resolution scanning electron microscope (JEOL 6330F Field emisson SEM with an Oxford Instruments Energy Dispersive X-ray Analyser). Figure 4.17 shows a SEM micrograph of a TiO_2 film. It clearly shows that the TiO_2 films are nano-porous and the average particle size is ~50 nm.

The TiO_2 films were also characterised by Atomic Force Microscopy (Omicron UHV chamber, Scan speed 850 nm / s, SiN cantilever). A typical AFM micrograph of a Bath TiO_2 film is shown in Figure 4.18. The AFM micrograph further confirms that Bath TiO_2 films are nano-porous and the average particle size is ~50 nm.

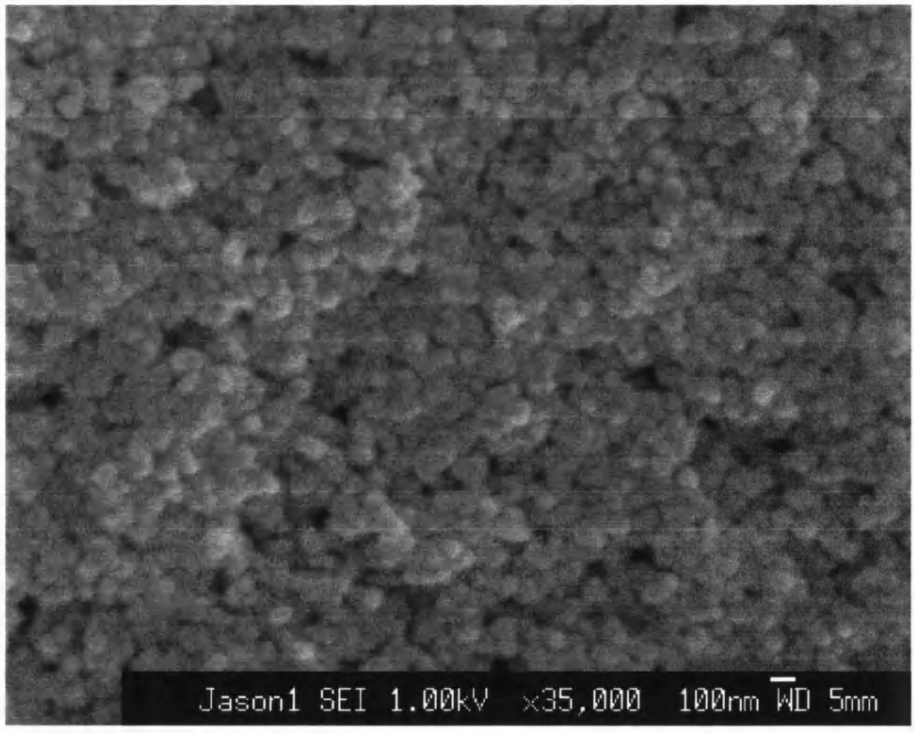

Figure 4.17 *SEM micrograph of TiO_2 film*

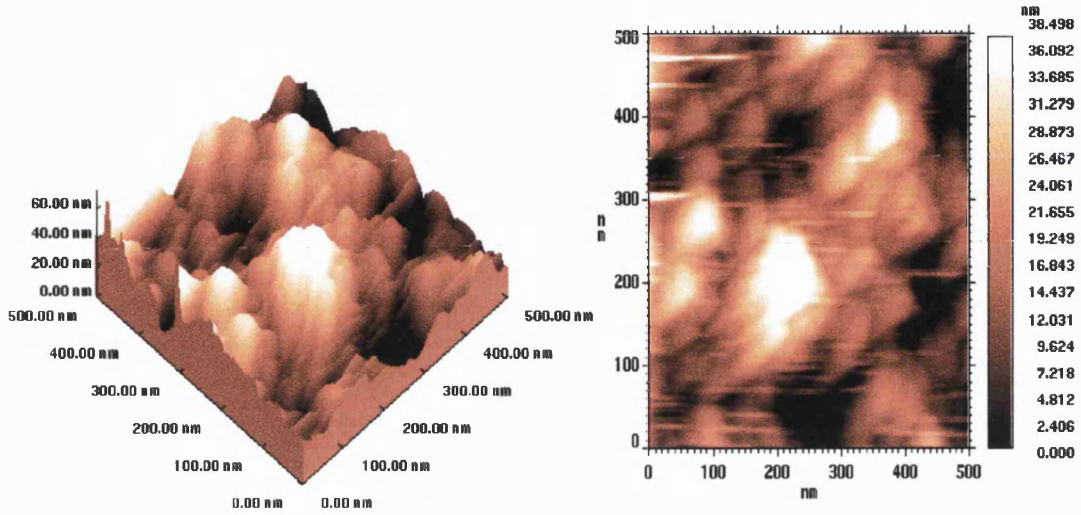

Figure 4.18 *AFM micrograph of TiO_2 film.*

4.5 Film thickness Measurements

4.5.1 Talysurf Measurements

Film thickness measurements were done using a Talysurf instrument (Taylor Hobson, Form Talysurf-50). First, the TiO_2 coated electrode was fixed on a horizontal adjustable flatform that was connected to the Talysurf instrument. The tip of the probe of the Talysurf was lowered so that it touched the bare surface (TiO_2-free SnO_2 surface) of the electrode. Then the tip was scanned across the electrode so that the scanning covered the TiO_2 free surface as well as the TiO_2 film. During the scan the tip of the probe is automatically adjusted so that it just touches the surface of the electrode. When the tip

reaches the TiO_2 film, it moves upwards. The upward movement is equivalent to the TiO_2 film thickness. The average upward movement that the tip of the probe of Talysurf makes is taken as the average film thickness. A typical film thickness profile that was recorded by the Talysurf is shown in Figure 4.19. Note that the Figure 4.19 only shows the thickness profile at an edge of a TiO_2 film. To get the average film thickness, scan needs to be performed further on the TiO_2 film.

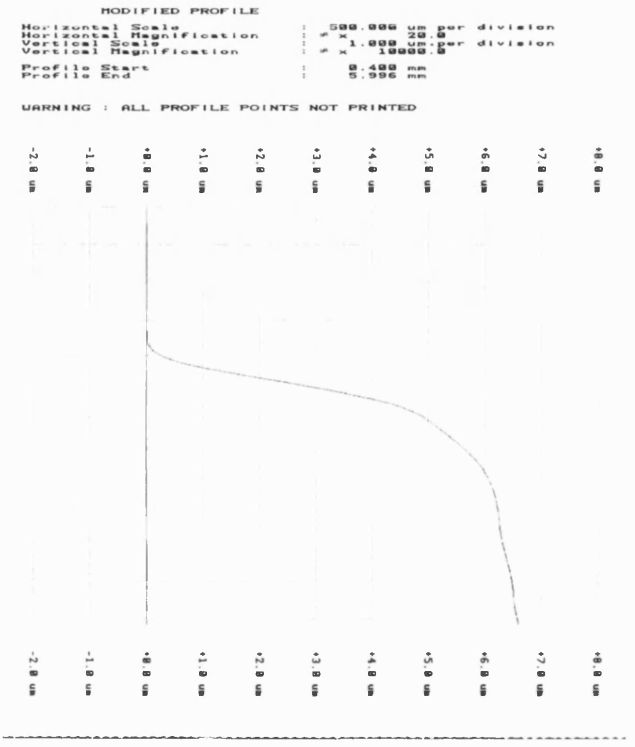

Figure 4.19 *A typical film thickness profile recorded by the Talysurf instrument.*

4.5.2 SEM Measurements

For comparision with the Talysurf film thickness measurements, the cross section of the TiO_2 coated electrode was observed by Scanning Electron Microscopy (JEOL JSM-T330 Scanning Electron Microscope) and the film thickness was evaluated. A typical SEM micrograph of the cross section of the TiO_2 coated SnO_2 substrate is shown in Figure 4.20.

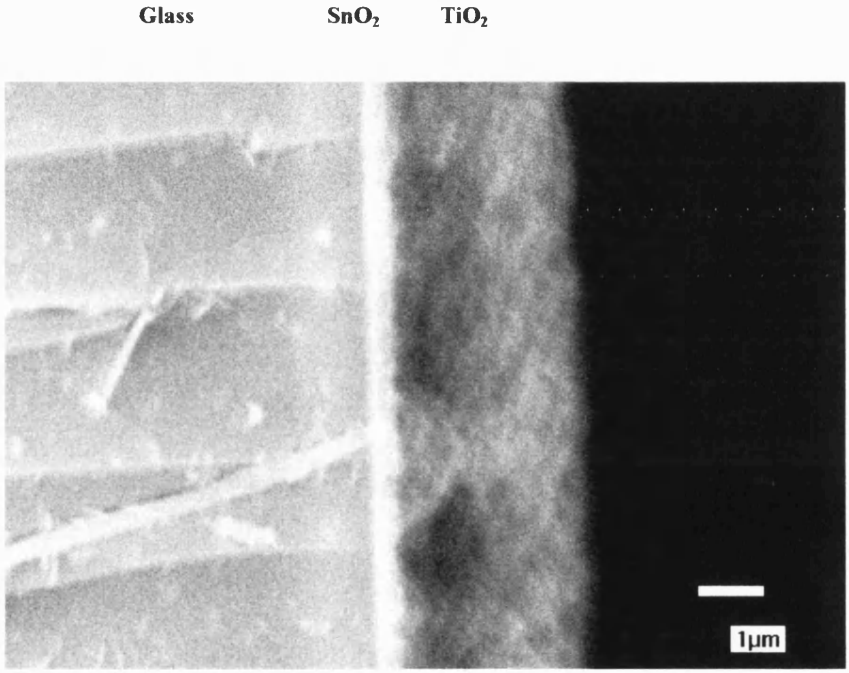

Figure 4.20 *A SEM micrograph showing the cross section of TiO_2 film*

4.6 Absorption/Transmission Spectroscopy

In order to determine the light absorption and transmission by the DSN TiO_2 solar cell absorption and transmission measurements were performed. Absorption and transmission spectra were acquired using a UV-Vis spectrometer (*PERKIN ELMER, Lambda 40*). First the spectrometer was auto-zeroed in air with no samples placed in the sample holders. The measurements required a Pt sputter-coated SnO_2 + SnO_2 sandwich to act as the

reference cell affixed in the reference compartment. The Pt sputter-coated SnO_2 + SnO_2 sandwich takes into account the reflections of the light beam from the glass electrodes and any light absorption and reflection due to the platinum. This ensures that any measured light absorption can be attributed to the TiO_2, ruthenium N3 dye and liquid electrolyte. The solar cell was then placed in the sample holder with the correct orientation for substrate-side illumination. The absorption/transmission spectrum of the cell was recorded using a PC interfaced to the UV-Vis spectrometer.

4.7 Photocurrent Spectroscopy

Measurement of steady state photocurrent spectra is a basic technique for photoelectrochemical characterisation of semiconductor electrodes. This involves measuring the photocurrent of a semiconductor electrode as a function of illumination wavelength. The potential of the semiconductor electrode is kept at a constant value by a potentiostat while the wavelength of the incident light is scanned over the range of interest by a monochromator. The potentiostat also provides the facility to record steady state photocurrent spectra in two or three electrode mode. Generally photocurrent spectroscopy uses chopped light and lock-in detection. However, the typical slow response time of dye-sensitised nanocrystalline TiO_2 solar cells prevents using the lock-in technique for photocurrent spectroscopy. (The reason for the slow response time in DSN solar cells is discussed in chapter 5).

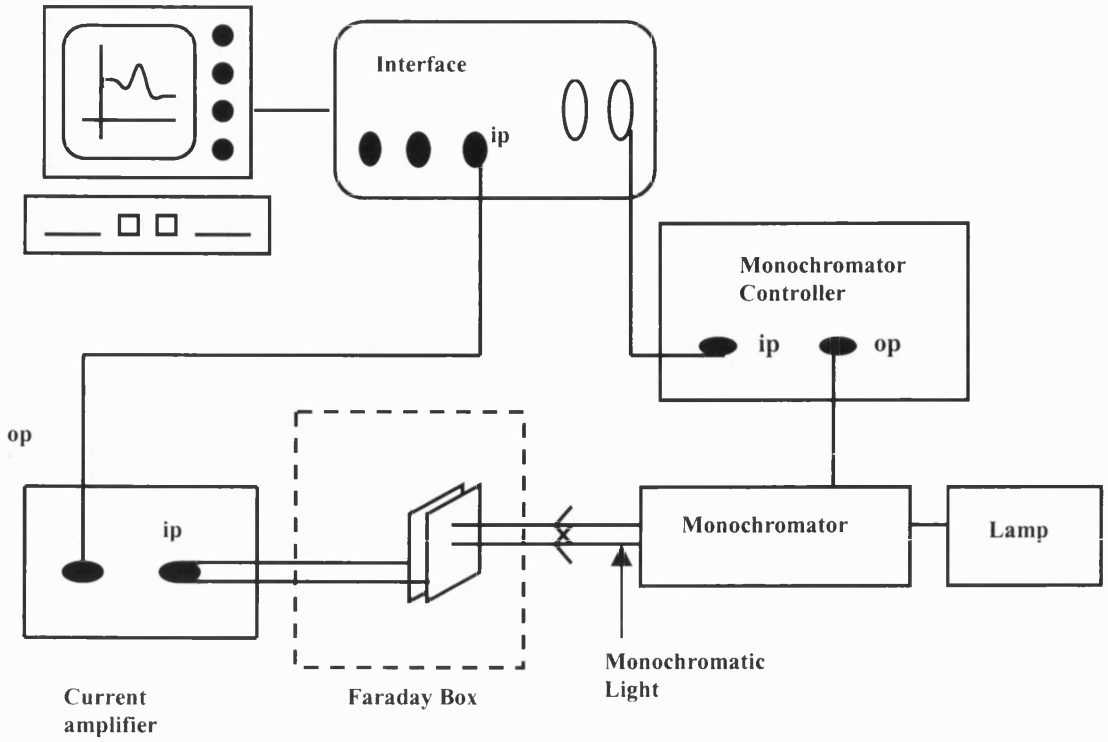

Figure 4.21 *The experimental set-up for photocurrent spectroscopy*

In the present experimental set up no chopper or lock-in amplifier was used. The monochromator was interfaced to a BBC microcomputer to enable automatic scanning of the wavelength of illumination. The DSN solar cell was connected to a current amplifier and the output of current amplifier was fed directly into the BBC computer interface. The computer records the steady-state photocurrent while it controls the illumination light wavelength. Then the DSN TiO_2 solar cell was replaced by a calibrated silicon diode (± 5%, traceable to NBS) and the current amplifier output was fed to the BBC computer. The photodiode spectra were recorded in the wavelength range where the photocurrent spectra were recorded under the same conditions. Then the computer converts the photocurrent of the cell into the conversion efficiency at each wavelength using stored values of the photodiode sensitivity. In this way incident photon to current conversion efficiency (IPCE) plots were recorded for the dye-sensitised nanocrystalline TiO_2 thin layer solar cells.

4.8 DC Current-Voltage Measurements

Recording a current-voltage curve is another basic technique that is generally used in the characterization of solar cells. From the current-voltage curve one can calculate the overall power conversion (global) efficiency of a solar cell. This is perhaps a more important measurement than the monochromatic efficiency as it reflects how the cell would operate under standard outdoor conditions. The experimental set up for the apparatus to record current-voltage curves is shown in Figure 4.22.

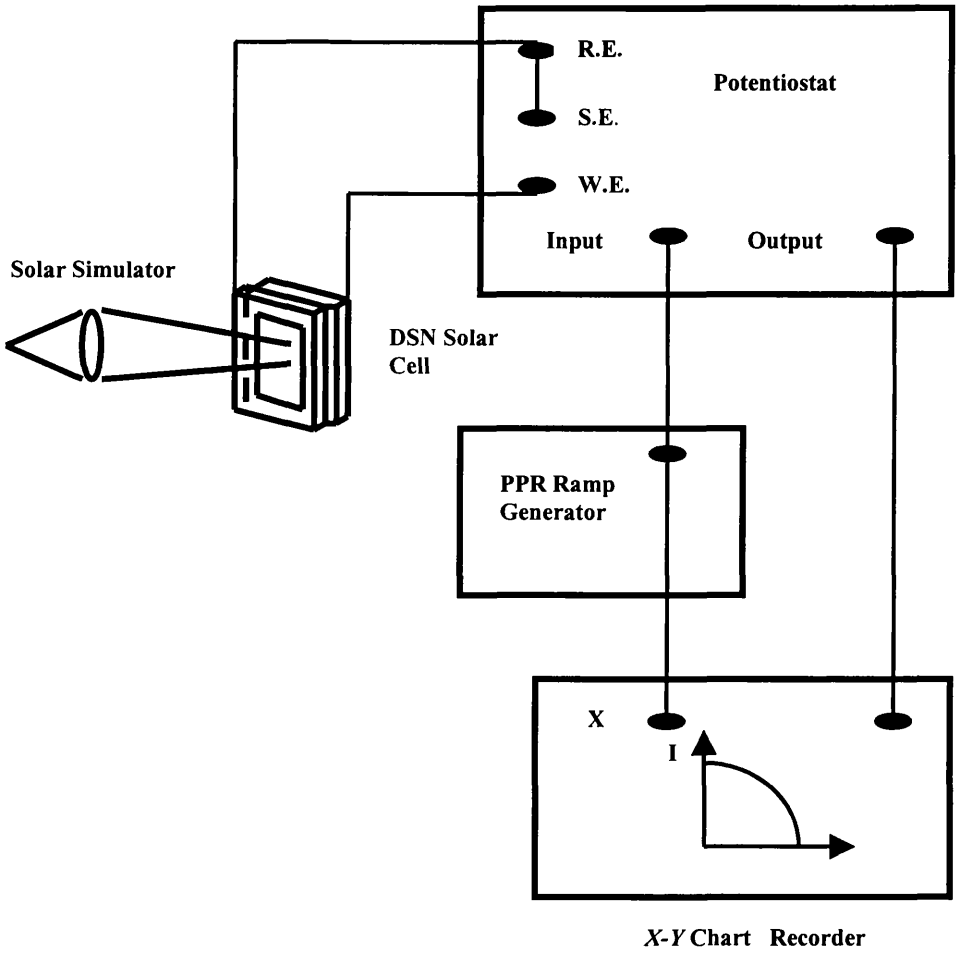

Figure 4.22 *Experimental set up for recording current-voltage curves.*

The solar cell was connected to a potentiostat (home made mains power supplied potentiostat), which operated in two-electrode mode while the output of the potentiostat was fed into one input of an *X-Y* chart recorder (Philips, M 8271). The potential applied to the solar cell was swept using a waveform generator. (HI-TEK INSTRUMENTS, PP R1) The applied potential was also fed into the input of *X-Y* chart recorder. The power of the illumination lamp for recording the global efficiency was set to 1 Sun (AM 1.5 simulated light) as described below, which corresponds to 100 mW/cm^2 output power. The solar simulator (MÜLLER, ELLSOL 1000) was calibrated using a calibrated GaAs solar cell, which had previously been tested for global efficiency. The calibration method is as follows.

The short circuit photocurrent for the calibrated GaAs solar cell was measured as a function of power supply current for the solar simulator lamp. Knowing the short-circuit photocurrent for the GaAs solar cell under AM 1.5 simulated light intensity, the supply current for the solar simulator lamp was adjusted so that the power output of the lamp was equivalent to AM 1.5 simulated light (1 Sun).

4.9 Intensity Modulated Photocurrent Spectroscopy (IMPS)

One of the frequency-resolved techniques that was used to characterise the dye-sensitised nanocrystalline solar cells is IMPS. Measurements were performed using a frequency response analyser (FRA) (Solartron, 1250) that was used to drive a light emitting diode (LED). The generation part of the FRA can provide an AC voltage output (sinusoidal, square wave etc.) that is superimposed on a DC voltage output. This is very convenient as a LED can be driven directly by a sinusoidal output superimposed on a DC voltage with an appropriate series resistor. As an alternate light source, a CW laser can be used in combination with an acousto-optic modulator driven by the FRA.

In the present work, the dye-sensitised nanocrystalline solar cell was connected to a battery-operated potentiostat constructed using low-noise operational amplifiers, which operated in two-electrode mode while the output of the potentiostat was connected to the

FRA. In the potentiostat, the applied DC potential for the working electrode of DSN cell was adjusted to 0 V for all the measurements. The DSN solar cell was illuminated from the substrate side with a blue LED (λ_{max} 470 nm, I_{max} 30 mA, V_{max} 5 V and view angle 30°) that provided a modulated AC illumination flux superimposed on a DC illumination flux. The AC voltage output of the generation part of the FRA was adjusted so that the AC component of the incident photon flux was less than 10% of the incident DC photon flux. In order to get a linear response from DSN solar cells it is important to perturb the steady state electron density by less than 10% (see section 3.2 for more details). The modulated photocurrent measured by the low-noise battery-operated amplifier was fed to the FRA. The FRA measures the amplitude and the phase shift of the small AC photocurrent. The IMPS responses were recorded over the appropriate frequency range using the FRA under computer control. The software used for these measurements was written in home by M.Bailes. The modulated frequency range used depended on the DC light intensity. Since measurements were made down to very low light intensities, special precautions were needed to eliminate electrical noise. Measurements were performed in an earthed Faraday box, and computer equipment was shielded to prevent interference. The light intensity incident on the DSN solar cell was adjusted by the insertion of a series of calibrated neutral density filters (Schott NG3). Since some measurements were extended to high light intensities, an additional DC light source (20 W tungsten halogen lamp) was used to increase the incident DC light intensity in such cases. However, care was taken to maintain the DC to AC ratio at ~ 10%. The DC light intensity was measured using a calibrated silicon diode (traceable to NBS). Figure 4.23 shows the experimental set-up that was used for IMPS measurements.

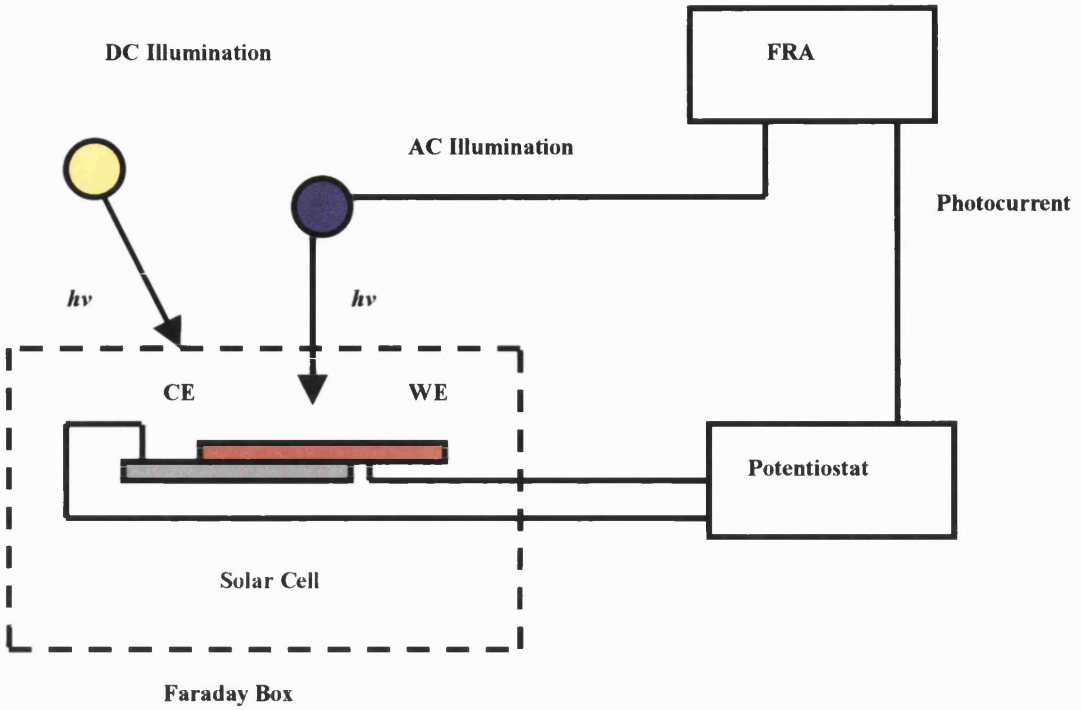

Figure 4.23 *The experimental set-up for IMPS measurements.*

4.10 Intensity Modulated Photovoltage Spectroscopy (IMVS)

The other frequency-resolved technique that was used to characterise the dye-sensitised nanocrystalline solar cells in the present work was IMVS. IMVS measurements were performed using the same set-up as for IMPS measurements, except that the potentiostat was replaced by a high-impedance low-noise battery operated preamplifier (Stanford model SR560, input impedance 10^8 Ω). The high-impedance low-noise preamplifier also served as a filter to minimise noise. The working and counter electrodes were connected to the inputs of the preamplifier. Under illumination consisting of a modulated AC photon flux superimposed on a DC flux from the substrate side, the DSN solar cell generates an AC photovoltage on top of a steady state photovoltage. The FRA only detects the AC photovoltage and measures the amplitude and the phase shift of the response. The IMVS responses were recorded over the desired frequency range using the

FRA under computer control. Figure 4.24 describes the experimental set-up that was used for IMVS measurements.

In some experiments a homemade voltage follower was used instead of the Stanford model SR560 preamplifier with input impedance 10^8 Ω. The voltage follower has made with an operational amplifier (Farnell, AD 645) that possesses input impedance of 10^{12} Ω. Therefore, the homemade voltage follower possesses 10^{12} Ω input impedance and very low output impedance. It was very useful in very low voltage measurements as well as voltage measurements on highly resistive samples. Figure 4.25 shows an electronic circuit diagram for the homemade voltage follower.

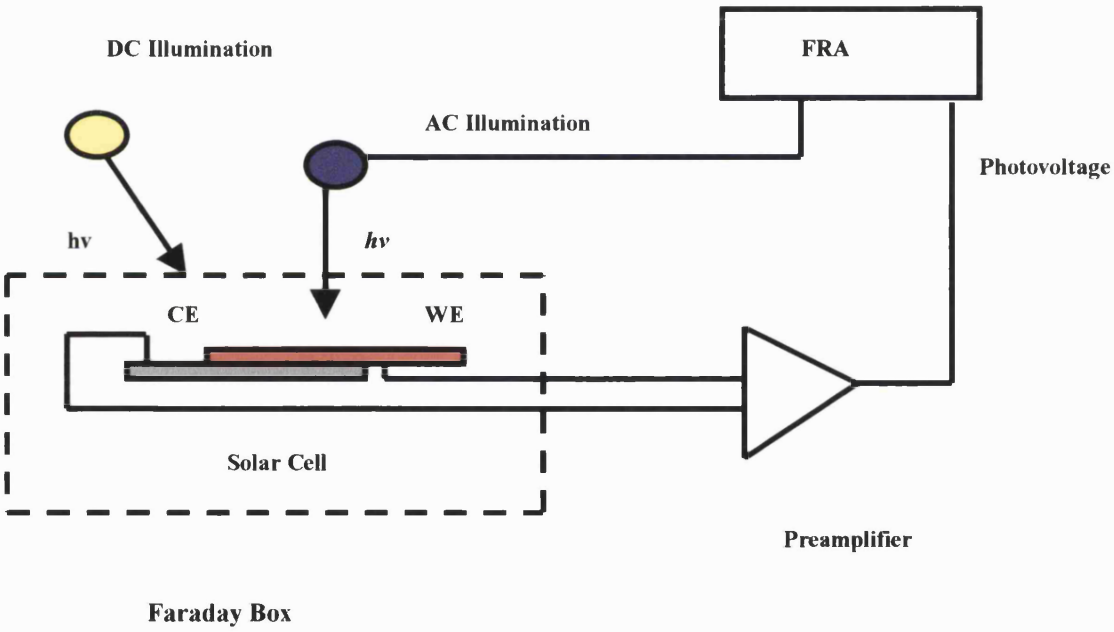

Figure 4.24 *The experimental set-up for IMVS measurements*

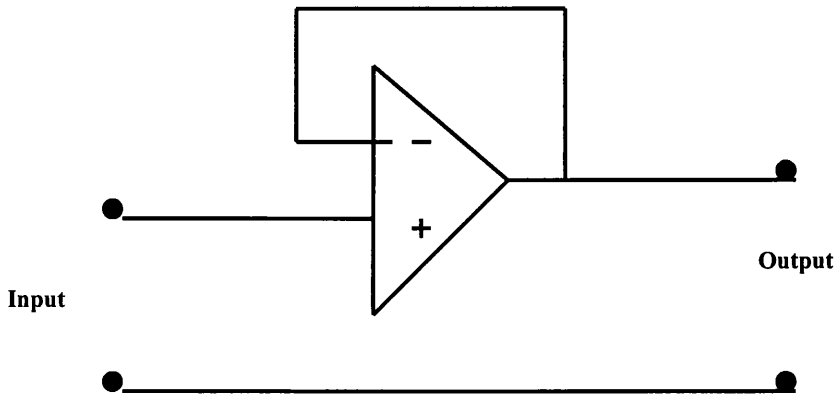

Figure 4.25 *The electronic circuit for the homemade voltage follower*

4.11 Small Amplitude Laser pulse Excitation Transient Measurements

The small amplitude laser pulse excitation transient measurement technique involves illumination of the DSN solar cells by a pulsed photon flux that is superimposed on a steady state photon flux illumination. This is an approach very similar to the small amplitude periodic perturbation techniques such as IMPS and IMVS. The technique was performed to record the photocurrent transients as well as photovoltage transients. The experimental set-up for photocurrent transient measurements is shown in Figure 4.26.

4.11.1 Photocurrent Transient Measurements

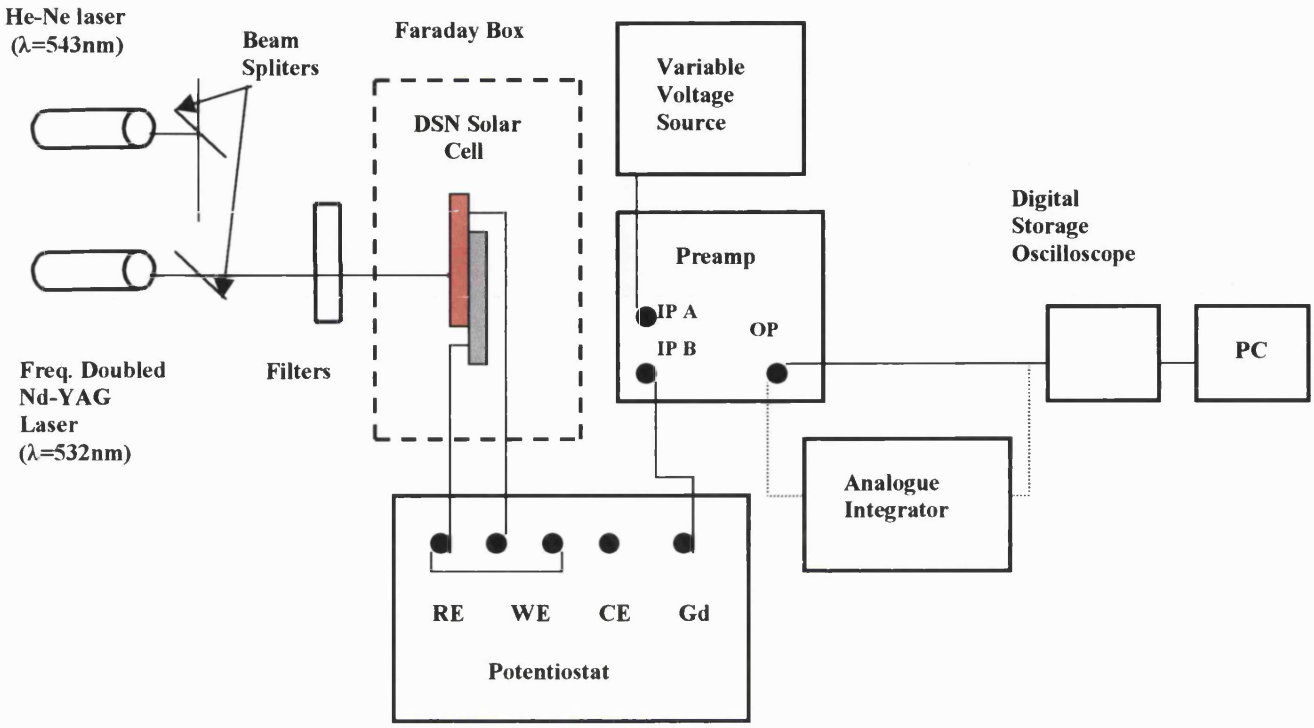

Figure 4.26 *The experimental set-up for small amplitude laser pulse excitation photocurrent transient measurements.*

The dye-sensitised nanocrystalline TiO_2 solar cell was illuminated from the substrate side by a steady state photon flux provided by a green CW He-Ne laser (λ = 543 nm) while a frequency-doubled Nd-YAG laser (λ = 532 nm) was used to provide the small amplitude pulsed photon fluxes. The intensity of the Nd-YAG laser was made sufficiently small in comparison to the intensity of the He-Ne laser so that the pulse-generated photocurrent was less than 1% of the steady state photocurrent. Laser pulses were fired singly at sufficiently long intervals to guarantee that the photo-generated electrons relax before the next pulse. Both laser beams incident on the DSN solar cell were attenuated by insertion of a series of calibrated neutral density filters (Schott). The DSN cell was connected to a battery-operated potentiostat constructed using low-noise operational amplifiers, which operated in two-electrode mode and the output of the potentiostat was connected to a dc voltage preamplifier (Stanford Research Systems SR 560) operating in differential mode.

A variable voltage source was connected to the other input of the preamplifier to offset the dc component of the photocurrent signal in order to enhance the sensitivity of transient current measurements. The current transients from the amplifier were recorded using a digital storage oscilloscope (Hitachi, VC265) interfaced to a computer. Charge transients were recorded at the same time by connecting the preamplifier output to the second input of the digital storage oscilloscope through an analogue integrator. Care was taken to offset the steady state photocurrent accurately to eliminate integrator drift during the charge transient measurements.

Care must be taken to prevent the photo-degradation of organic sensitiser dye during photocurrent and photovoltage transient measurements. Therefore, before starting the measurements, a calculation was performed to ensure that the incident photons-to-available dye molecules (steady state + pulse) ratio is sufficiently small to guarantee that the saturation of the dye is negligible. This was done as follows.

The light energy that is incident on the cell is calculated as 3.68×10^{-19} J/photon. The power of the Nd-YAG pulse laser on its standard setting is ca. 10μJ/pulse. This corresponds to 1.36×10^{13} total photons incident on the cell. As we know from section 1.4.1, the surface area/volume in nanocrystalline TiO_2 is of the order of 10^6 cm^{-1}. (The calculation was done assuming that the average radius of the spherical TiO_2 particles is ~ 10 nm.) Suppose that the laser spot size is about 5 mm^2. So, the 5 mm^2 area 10 micron thick nanocrystalline TiO_2 electrode can in principal have an internal surface area of 50 cm^2. It was reported that the average molecular coverage for two-ligand anchored ruthenium N3 sensitiser dye on flat TiO_2 surface is ~ 100 $Å^2$ (1.0×10^{-14} cm^2) [18]. Therefore the total number of dye molecules that are available within the area of laser spot size for the highest reported dye molecular coverage is 50 $cm^2/1.0 \times 10^{-14}$ cm^2 (50×10^{15} molecules). So, the number of available dye molecules per incident photon is 50×10^{15} molecules/1.36×10^{13} photons (3.6×10^3 molecules/photon). Therefore saturation of the dye can be neglected.

4.11.2 Photovoltage Transient Measurements

Small amplitude laser pulse excitation photovoltage transient measurements were performed using the same set-up as for photocurrent transient measurements, except that the DSN solar cell was directly connected to the high-impedance low-noise battery operated preamplifier (Stanford model SR560) in differential dc mode. As for the photocurrent transient measurements, a variable voltage source was used to offset the dc photovoltage component to enhance the sensitivity of transient voltage signal measurements. Fast photovoltage transients (at high photon intensity levels) were obtained using the digital storage oscilloscope. Slow photovoltage transients (at low intensity illumination levels) were recorded on a *XYt* chart recorder (Philips, M 8271). Figure 4.27 describes the experimental set-up for photovoltage transient measurements.

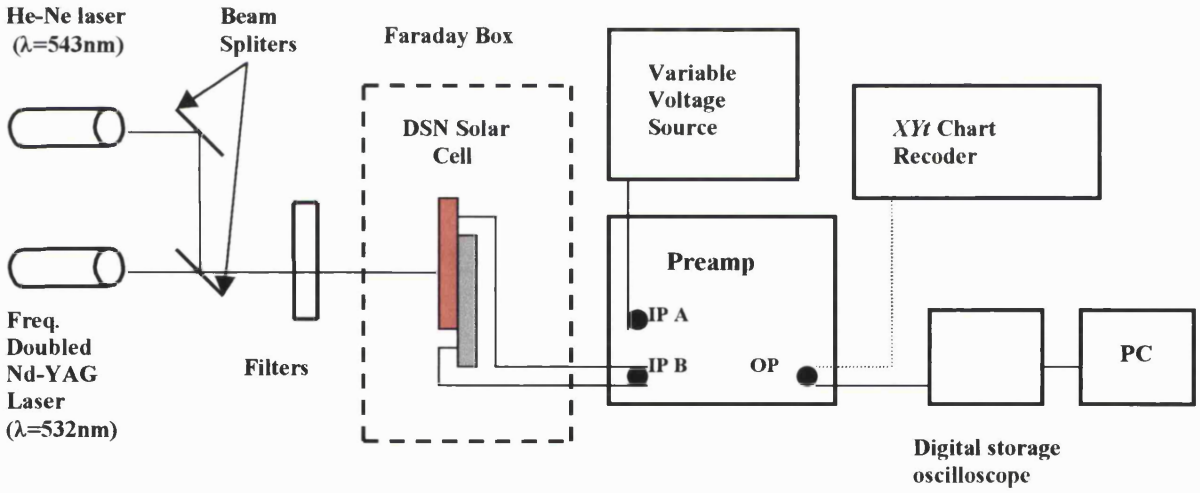

Figure 4.27 *The experimental set-up for small amplitude laser pulse excitation photovoltage transient measurements.*

4.12 Charge Extraction Technique

4.12.1 Charge Extraction Measurements

The DSN solar cell was illuminated from the substrate side with a blue LED (λ_{max} 470 nm: maximum power output 2 mW). The LED was mounted close to the cell so that the centre of the DSN TiO_2 film of the cell was illuminated with a spot having a diameter of about 8 mm. The dimensions of the active area of a measured cell were ~ 5 mm x 5 mm. All measurements were done in a screened dark box. Care was taken to eliminate stray light. The LED was driven by a pulse generator that allowed synchronization of the illumination pulse with the switching of the cell between open circuit and short circuit. The cell was controlled using an electronic circuit that was developed for potentiostatic/galvanostatic switching measurements [19]. This equipment was based on an operational amplifier and contained a fast VMOS (V - Metal Oxide Semiconductor) switch that changes the controlled variable from potential (potentiostatic mode) to current (galvanostatic mode) and then back again. This sequence can be controlled by external trigger signals.

The measurement sequence of the charge extraction method is as follows. Initially the DSN solar cell was in the potentiostatic mode (applied voltage is 0 V: short circuit) in the dark. Then the cell was switched to the galvanostatic mode (zero current: open circuit) and illuminated by the LED for 550 ms. The 550 ms illumination time is well above the rise time of the cell so there is adequate time for the DSN cell to reach the steady state photovoltage. The increase in the photovoltage towards its steady state value was recorded by a digital storage oscilloscope (DSO) (Hitachi, VC-6265). In some measurements the Tektronix (TDS 200) digital real-time oscilloscope was also used. Then the LED was switched off and the photovoltage decay was recorded by using the DSO. The cell was then switched back to the potentiostatic mode (applied voltage is 0 V: short circuit) at different points along the photovoltage decay curve by varying the delay time after switching off the LED. This could be done by a series of different

measurements, as the steady state photovoltage as well as photovoltage decay curve for the cell, was highly reproducible.

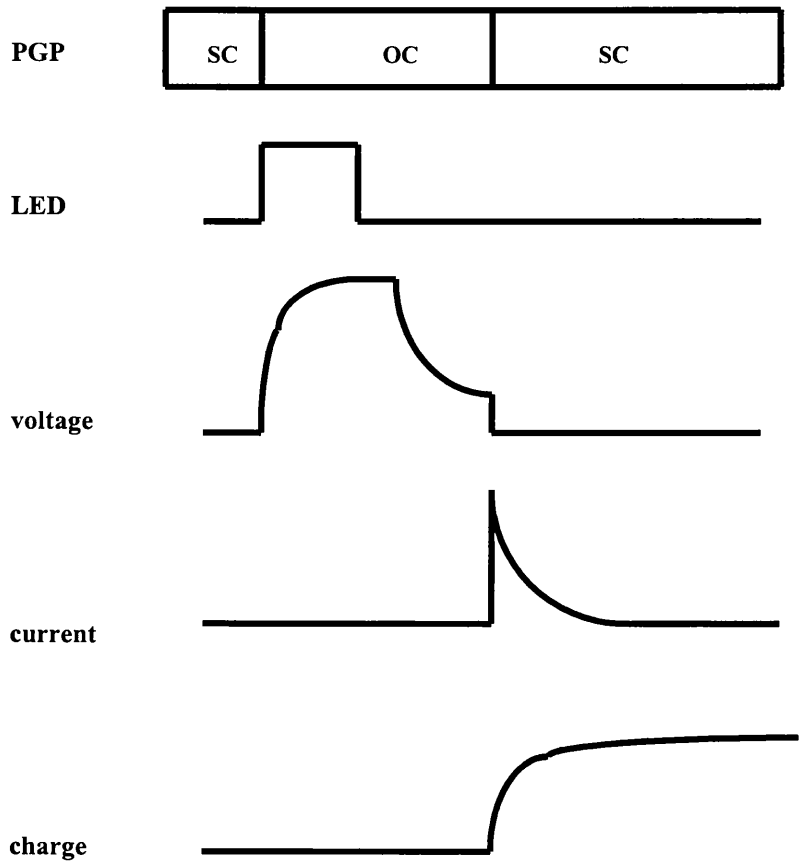

Figure 4.28 *The typical shapes of voltage, current and charge vs time plots in charge extraction technique.*

As shown in Figure 4.28, a current transient was observed as a result of electron extraction from the DSN TiO_2 film when the cell was switched from open circuit to short circuit. The output of the potentiostat current amplifier was simultaneously integrated using an operational amplifier integrator and the charge extraction was recorded by the DSO. The charge integration was done for only 3 s as longer integration times could introduce an error due to the offset drift of the current amplifier (The residual current

from the cell at longer times was smaller than the offset of the current amplifier: less than ~ 10 nA). However, measurements were performed in a temperature-controlled room at 24 °C so that the drift could be minimised. The equipment set-up for the charge extraction technique is shown in Figure 4.29.

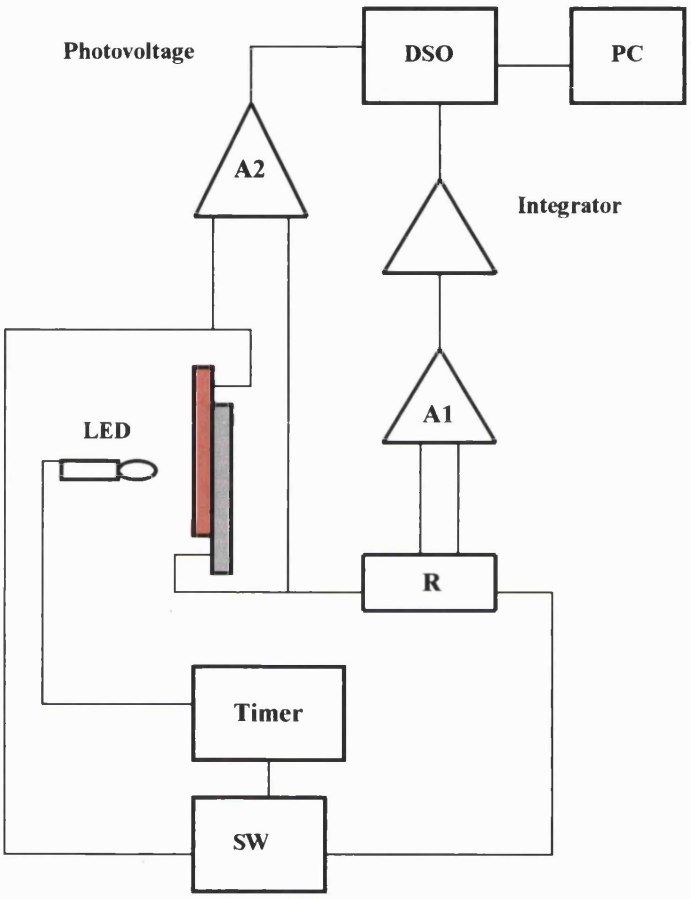

Figure 4.29 *The equipment set-up for the charge extraction technique (PGP). A1 high impedance differential amplifier to measure voltage across the series resistor R. A2 high impedance amplifier to measure the cell voltage. SW solid-state switched potentiostat galvanostat. DSO digital storage oscilloscope.*

However, at a later stage, a specially designed instrument was constructed and the integrator and measurements were carried out using it. This instrument is designed for measurements on a DSN TiO_2 solar cell connected to the cell socket. The cell can be connected either in open circuit or via a mercury relay to a known resistor to measure the current drawn through it. A socket (labeled as v) is available to read the voltage across the cell when it is open circuit or connected across the known resistor. A second socket (labeled as I) is available to read the current drawn across the known resistor. There is also a third socket (labeled as Q) is available to read the integrated current drawn across the known resistor. The fourth socket that with a controlled current (0 to 30 mA) is available for powering a LED which illuminates the DSN TiO_2 solar cell. Measurements sequence of this newly designed instrument is as follows. The DSN solar cell was initially connected in short circuit (across a known resistor) and the LED and the integrator are both off. Then the cell was switched to the open circuit and the LED was switched on for the time set by the LED time switch (0.1, 1, 10 or 100 s) simultaneously by pressing the initiate button. As already explained, it was at this stage the open circuit voltage started to rise. The LED is then automatically switched off after a time set by one of the delay time switches and the open circuit voltage started to fall off. After a fixed time the cell was connected across the known resistor and the integrator was switched on. Same as the experimental procedure with the previous set up the charge extraction was done only for 3 s.

4.12.2 Sources of Errors and Methods to overcome them

There are several sources of errors in charge extraction technique. Careful experiments are needed to eliminate the errors and calibrate the system. One of the errors is the offset current that generated by the PGP instrument at its input. As a result of this, the recorded photovoltage decay curve, current pulse and charge extraction plot may not be accurate. For accurate measurements, the system has to be zeroed precisely and calibrated.

The system was calibrated and zeroed accurately by replacing the cell with a 1 μF capacitor. The offset current in the galvanostatic mode (applied voltage 0 V) gave rise to

a ramping of the voltage output at a rate given by $dV/dt = i_{offset}/C$, where $C = 10^{-6}$ F. The ramping of the voltage output was recorded on a digital storage oscilloscope and the offset current was adjusted until the ramp rate was less than 1 mV s^{-1}, which corresponds to a residual current of less than 1 nA.

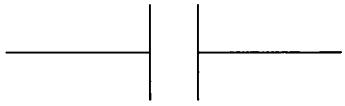

$$Q = CV$$

$$dQ/dt = C\ dV/dt$$

$$i = C\ dV/dt$$

$$dV/dt = i_{leak}/C$$

If the leakage current of the system is 1 nA, the rate of the voltage ramp fot $c = 10^{-6}$ F is 1 mV s^{-1}.

The analogue integrator connected to the output of the potentiostat current amplifier was also zeroed accurately to eliminate the drift. The digital storage oscilloscope was interfaced to a PC using an IEEE interface.

The other problem that experienced with the PGP measurements was the excess charge extraction due to the discharge of the SnO_2 surface. When the DSN solar cell was in the galvanostatic mode, the SnO_2 surface was also charged in addition to the photogenerated electron concentration build up (photovoltage). When the system was switched into potentiostatic mode, we extract photogenerated electrons as well as electrons due to the discharge of SnO_2 the substrate. This can be written as follows.

$$Q_{photo(actual)} = Q_{photo(observed)} - Q_{substrate}$$

Therefore, to get the actual value of Q_{photo} , the Q_{charge} must be detected. The approach to determine the $Q_{substrate}$ will be treated in chapter 7.

4.13 References

1. B. Oregan and M. Gratzel, Nature 353:737 (1991).
2. A. Kay and M. Gratzel, Journal of Physical Chemistry 97:6272 (1993).
3. M. K. Nazeeruddin, A. Kay, I. Rodicio, R. Humphrybaker, E. Muller, P. Liska, N. Vlachopoulos, and M. Gratzel, Journal of the American Chemical Society 115:6382 (1993).
4. M. Gratzel and K. Kalyanasundaram, Current Science 66:706 (1994).
5. M. Yanagida, L. P. Singh, K. Sayama, K. Hara, R. Katoh, A. Islam, H. Sugihara, H. Arakawa, M. K. Nazeeruddin, and M. Gratzel, Journal of the Chemical Society-Dalton Transactions:2817 (2000).
6. S. E. Lindquist, Solar Energy Materials and Solar Cells 38:335 (1995).
7. N. G. Park, G. Schlichthorl, J. van de Lagemaat, H. M. Cheong, A. Mascarenhas, and A. J. Frank, Journal of Physical Chemistry B 103:3308 (1999).
8. K. Tennakone, G. Kumara, K. G. U. Wijayantha, I. R. M. Kottegoda, V. P. S. Perera, and G. Aponsu, Journal of Photochemistry and Photobiology a-Chemistry 108:175 (1997).
9. A. Hagfeldt and M. Gratzel, Chemical Reviews 95:49 (1995).
10. L. M. Peter and D. Vanmaekelbergh, in Advances in Electrochemical Science and Engineering, Vol. 6 (D. M. Alkire and D. Kolb, eds.), VCH Wiley, New York, 1999, p. 77.
11. A. C. Fisher, L. M. Peter, E. A. Ponomarev, A. B. Walker, and K. G. U. Wijayantha, Journal of Physical Chemistry B 104:949 (2000).
12. N. W. Duffy, L. M. Peter, and K. G. U. Wijayantha, Electrochemistry Communications 2:262 (2000).
13. M. Turrion, B. Macht, P. Salvador, and H. Tributsch, Zeitschrift Fur Physikalische Chemie-International Journal of Research in Physical Chemistry & Chemical Physics 212:51 (1999).
14. E. V. Stefanovich and T. N. Truong, Chemical Physics Letters 299:623 (1999).
15. E. Depauw and J. Marien, Journal of Physical Chemistry 85:3550 (1981).
16. A. L. Linsebigler, G. Q. Lu, and J. T. Yates, Chemical Reviews 95:735 (1995).

17. K. Tennakone, G. Kumara, A. R. Kumarasinghe, K. G. U. Wijayantha, and P. M. Sirimanne, Semiconductor Science and Technology 10:1689 (1995).

18. R. Hengerer, B. Bolliger, M. Erbudak, and M. Gratzel, Surface Science 460:162 (2000).

19. G. J. Hills, L. M. Peter, B. R. Scharifker, and M. I. D. Pereira, Journal of Electroanalytical Chemistry 124:247 (1981).

Chapter 5

Studies of Electron Transport and the Back reaction in the Dye-Sensitised Nanocrystalline TiO_2 Solar Cells by Small Amplitude Periodic Techniques

5.1 Introduction

In the DSN TiO_2 solar cell, the physical and chemical processes include the charge injection from the photoexcited surface adsorbed dye molecules and their regeneration by electron transfer from liquid electrolyte based iodide ions. The dye regeneration reaction is coupled to the regeneration of iodide from tri-iodide ions at the counter electrode and is also linked to the electron transport in the nanocrystalline TiO_2. The photo-injected electrons travel through the porous nanocrystalline TiO_2 solid before they are collected at the SnO_2 substrate, while a fraction of them undergo back reaction with tri-iodide ions in the liquid electrolyte. The physical and chemical processes involved in the cell operation take place in a two-phase system consisting of a porous nanocrystalline matrix interpenetrated by liquid based iodide/tri-iodide redox electrolyte.

Despite the complicated processes that are involved, the DSN TiO_2 cell has shown very high photocurrent quantum yields and has received much attention as an alternative to existing solar cells [1-4]. Therefore, there is a great deal of interest in electron transport and back reaction in the DSN TiO_2 solar cell. In the present study, intensity modulated photocurrent spectroscopy and intensity modulated photovoltage spectroscopy have been used to characterise the electron transport properties and back reaction kinetics over five orders of magnitude of illumination intensity. Experimental details of these techniques are given in sections 4.9 and 4.10. The numerical solutions of the generation, collection and back reaction problem in DSN solar cells for intensity modulated periodic illumination techniques (i.e. IMPS and IMVS) are treated in section 3.3.

5.2 Theory

5.2.1 Factors Determining the IPCE

The incident photon to current conversion efficiency (IPCE) of the DSN solar cell is determined by the wavelength-dependent light harvesting efficiency (*LHE*), the net electron injection efficiency (ϕ) and the collection efficiency (η).

$$IPCE(\lambda) = LHE(\lambda)\phi\eta \tag{5.1}$$

As shown in section 1.6.1, the net injection efficiency ϕ is determined by the competition between regeneration of sensitiser dye, D by recombination of photo-injected electrons with D^+ and electron transfer from I^- to D^+. Previous studies have provided experimental evidence for the formation of $I_2^{\bullet-}$, as an intermediate in the dye regeneration process [5, 6]. Therefore, a possible reaction scheme of electron injection and dye regeneration is as follows

$D^* \rightarrow D^+ + e_{cb}$	electron injection	(5.2*a*)
$D^+ + e_{cb} \rightarrow D$	D^+ / electron recombination	(5.2*b*)
$D^+ + I^- \rightarrow D + I^\bullet$	dye regeneration	(5.2*c*)
$I^\bullet + I^- \rightarrow I_2^{\bullet-}$	formation of $I_2^{\bullet-}$	(5.2*d*)
$2I_2^{\bullet-} \rightarrow I_3^- + I^-$	disproportionation of $I_2^{\bullet-}$	(5.2*e*)

Step (5.2*b*) can be important at high intensities under open circuit conditions where stationary electron densities in excess of 10^{17} cm^{-3} are expected [7-9]. It is convenient to term it *geminate recombination* (i.e. the injected electron is still located in the conduction band of the TiO_2 particle to which D^+ is attached, and it returns to D^+ before being trapped) or recombination of D^+ with any of a larger number of electrons already present in the particle depending on the electron concentration in the TiO_2 film [7-9]. However,

the net result of either case is suppression of the net electron injection efficiency, ϕ in equation (5.1). The reaction scheme does not distinguish between free and trapped electrons, but in principle electrons trapped at surface sites may be involved in interfacial electron transfer (recall reaction (2.37b) in chapter 2) and electrons trapped in the bulk can only react after thermal detrapping (recall reaction (2.41) in chapter 2).

By contrast, ϕ may increase if the dye regeneration reaction that involves iodide, is efficient. However, this process is complicated by the fact that the overall reaction of iodide to tri-iodide involves the transfer of two electrons (see the step (5.2*c*) – (5.2*e*) in the proposed scheme).

The other term in equation (5.1), the electron collection efficiency, η, depends on the competition between electron diffusion toward the SnO_2 substrate and back reaction with tri-iodide ions. The reduction of I_3^- is not a simple one-step electron transfer process. At platinum electrodes, dissociative chemisorption of I_2 allows facile electron transfer to $I_{ads}^{\bullet}$. By contrast, the electron transfer rate constant at SnO_2(F) is over 10^5 times slower [10]. This is attributed to the fact that the iodine atom intermediate is not stabilised by chemisorption on the TiO_2/SnO_2(F) electrode as is the case for the Pt electrode. This large difference in rate constants of the I_3^-/I^- reaction at Pt and at TiO_2/SnO_2(F) is essential for power generation in the DSN cells. When the DSN cell is illuminated, the I_3^-/I^- reaction remains close to equilibrium at the platinum electrode, whereas it deviates far from equilibrium at the TiO_2 and SnO_2 surfaces, allowing the electrochemical potential of electrons in the TiO_2 to rise to qU_{photo}, where U_{photo} is the open circuit potential (recall equation (3.59)). It is also worth noting here that for illumination from the substrate side, the condition for efficient electron collection ($\eta \rightarrow 1$) can be expressed by the inequality $L_n > \alpha^{-1}$. Here, L_n is the electron diffusion length and α^{-1} is the light penetration depth.

5.2.2 The Electron Diffusion Length

As electrons diffuse through the TiO_2 network by a random walk process, they may become trapped at the surface of the TiO_2 particles and back react with tri-iodide in electrolyte solution. In principle, this back reaction determines the electron lifetime, τ_n. The diffusion process can be described in terms of the electron diffusion coefficient D_n. Recalling the equation (2.35), this allows one to define the electron diffusion length as $L_n = (D_n \tau_n)^{1/2}$ in the DSN solar cell. In terms of cell performance, the condition that must be satisfied is $L_n \geq d$, where d is the thickness of the TiO_2 film. Otherwise, a substantial number of photo-injected electrons are lost through the back reaction with tri-iodide ions decreasing the IPCE of the cell. Since the TiO_2 film thickness must be sufficient to guarantee that most of the incident light is absorbed, DSN TiO_2 solar cells are usually constructed with the TiO_2 film thickness, $d \geq 10$ μm. Therefore, efficient DSN cells require that $L_n \geq 10$ μm.

Several early studies have shown that both D_n and τ_n depend on illumination intensity [11-14]. Since the electron diffusion length in the DSN TiO_2 solar cell, L_n is given by the square root of the product of the electron diffusion coefficient, D_n and the electron lifetime, τ_n, L_n should also depend on illumination intensity. An important question that arises from the intensity dependence of D_n and τ_n whether this will result in an intensity-dependent IPCE. The present work addressed this question by measuring D_n and τ_n over a wide range of illumination intensities using intensity modulated photocurrent spectroscopy and intensity modulated photovoltage spectroscopy. These values were then used to obtain L_n. The experimentally determined values of L_n were used in analytical solutions of the generation/collection/back reaction problem that include either first-order or second-order back reaction kinetics, to calculate the IPCE at different illumination intensities. These predictions were then compared with the experimentally determined IPCE values. The theoretical and experimental values agree quite well and show that the IPCE varies only weakly with light intensity because D_n and τ_n vary in opposite senses

with light intensity: D_n increases with increasing light intensity, whereas τ_n decreases. As a consequence, the electron diffusion length remains almost constant.

However, it will be clear from Figure 5.1 that the steady-state component of the electron density is not identical in IMPS and IMVS experiments (i.e. short circuit and open circuit conditions), even if the dc illumination intensity is identical. This means that even if the electron lifetime is inversely proportional to the square root of the illumination intensity (i.e. second order electron decay), the use of the τ_n value obtained at open circuit in the calculation of $L_n = (D_n \tau_n)^{1/2}$ will result in underestimation of the electron diffusion length at short circuit. Nevertheless the characteristic behavior that is observed for the electron diffusion length should be the same.

5.2.3 Kinetics of the Back reaction of Electrons with Tri-iodide

It is clear that the back reaction of photo-injected electrons with tri-iodide plays an important role in determining the electron collection efficiency, η. Several studies have paid attention to the back reaction kinetics, in terms of understanding the limiting factors of the DSN TiO_2 solar cell [13-15]. In fact, determination of the reaction order with respect to individual species (i.e. electrons and tri-iodide ions) is very important in establishing the back reaction mechanism. Therefore, the periodic responses in the present study were used to investigate the reaction order with respect to electron concentration in the back reaction process, which was then used in the prediction of possible reaction mechanisms.

The possible back reaction mechanism if $I^\bullet$ is an intermediate

If the back reaction pathway involves dissociative chemisorption of I_2 as in the case of tri-iodide reduction on Pt electrodes [16], the possible back reaction sequence is as follows.

$$I_3^- \leftrightharpoons I_2 + I^- \qquad K_1 \qquad (5.3a)$$

$$I_2 \rightleftharpoons 2\,I^{\bullet} \qquad K_3 \qquad (5.3b)$$

$$I^{\bullet} + e \rightarrow I^- \qquad k_a \qquad (5.3c)$$

In this case the rate of decay of electron density is first order with respect to electron density

$$\frac{dn}{dt} = -k_a n \sqrt{\frac{K_1 K_3 [I_3^-]}{[I^-]}} \qquad (5.4)$$

Therefore, the pseudo first order electron lifetime, τ_n can be defined as follows

$$\tau_n = \frac{1}{k_a \sqrt{\frac{K_1 K_3 [I_3^-]}{[I^-]}}} \qquad (5.5)$$

It should be noted that in this case the electron lifetime, τ_n is independent of the net electron injection rate G (given in $cm^3\ s^{-1}$). Furthermore, the steady state excess electron density, n increases linearly with illumination intensity according to the expression, $G = kn$ provided that ϕ is constant. Here, k is the first-order back reaction rate constant.

The possible back reaction mechanism if $I_2^{\bullet-}$ is an intermediate [13-15]

$$I_3^- \rightleftharpoons I_2 + I^- \qquad K_1 \qquad (5.6a)$$

$$I_2 + e \rightleftharpoons I_2^{\bullet-} \qquad K_2 \qquad (5.6b)$$

$$2\,I_2^{\bullet-} \xrightarrow{k_{dsp}} I_3^- + I^- \qquad (5.6c)$$

$$I_2^{\bullet-} + e \xrightarrow{k_{et}} 2\,I^- \qquad (5.6d)$$

The equilibrium constant of step (5.6*a*) is $\approx 10^{-7}$ mol dm^{-3} [17]. In this back reaction transfer scheme, the disproportionation reaction (5.6*c*) competes with the direct electron transfer (5.6*d*). However, if reaction (5.6*b*) is in equilibrium and reaction (5.6*d*) is neglected, the rate of decay of electron density can be given by

$$\frac{dn}{dt} = -2k_{dssp}K_1^{\,2}K_2^{\,2}\frac{\left[I_3^-\right]^2 n^2}{\left[I^-\right]^2} \tag{5.7}$$

Interestingly, Schlichthörl *et al.* have reported that dn/dt $\propto$ $n^{2.2}$ [14]. However, it is also possible that the reaction (5.6*d*) is the predominant route in this scheme. If this is the case, the rate of decay of electron density is given by

$$\frac{dn}{dt} = -k_{et}K_1K_2\frac{\left[I_3^-\right]n^2}{\left[I^-\right]} \tag{5.8}$$

Therefore, it is clear that in both cases, the decay of electron density is second order with respect to electron density. Section 3.3.2 shows that in the second order case, the effective electron lifetime can be defined for small amplitude perturbations of n as follows.

$$\tau_n = \frac{1}{2kn} \tag{5.9}$$

Section 3.3.1 provides further details of the derivation of equation (5.9). If step (5.6*c*) of the proposed scheme is the predominant route, the rate constant, k in equation (5.9) is given by

$$k = 2k_{dssp}K_1^{\,2}K_2^{\,2}\frac{\left[I_3^-\right]^2}{\left[I^-\right]^2} \tag{5.10}$$

However, if step (5.6*d*) is the predominant route, rate constant, k in equation (5.9) is given by

$$k = k_{et}K_1K_2\frac{\left[I_3^-\right]}{\left[I^-\right]} \tag{5.11}$$

In the second-order decay of electron density, the steady state excess electron density at open circuit is given in either case by $n = (G/k)^{1/2} = G\tau_n$. It follows that the electron lifetime in the small amplitude limit is given by $\tau_n = (Gk)^{-1/2}$. This means that if ϕ is constant, the electron lifetime is inversely proportional to the square root of the light intensity.

Equations (5.9)-(5.11) also show that the determination of back reaction orders with respect to other species (i.e. $[I_3^-]$ and $[I^-]$) from small amplitude IMVS measurements must be done at constant steady state electron density (n), not at constant illumination intensity.

5.2.4 Electron Transport

The photogenerated electrons that have survived the back reaction with tri-iodide are collected at the SnO_2(F) substrate electrode. Since the contribution of electric fields to electron transport in the bulk of the nanocrystalline TiO_2 layer is thought to be negligible, the photo-injected electrons reach the back contact by diffusion [18, 19]. However, electron diffusion in the nanocrystalline TiO_2 phase is very slow. For example, at typical solar illumination levels, the electron diffusion coefficient for nanocrystalline TiO_2 is typically 5×10^{-5} cm^2 s^{-1}, whereas for bulk rutile it is 0.02 cm^2 s^{-1} [7] and for bulk anatase it is 0.01 cm^2 s^{-1} [20]. This suggests that the electron transport through the nanocrystalline TiO_2 is a trapping/detrapping dominant process. This may be the reason why the *apparent electron diffusion coefficient*, determined by intensity modulated photocurrent spectroscopy, is an intensity dependent quantity (the following paragraph will discuss more details of the term '*apparent diffusion coefficient*') [11, 12]. It is therefore reasonable to assume that the majority of electrons are trapped, and that the trapping/detrapping processes determine the effective diffusion coefficient. The upper limit of the diffusion coefficient should correspond to the movement of free conduction band electrons. Alternatively, one can also argue that the relatively low electron mobility in the nanocrystalline TiO_2 (compared to the bulk oxide) is a result of solvent polarisation effects. The present study shows that the electron diffusion coefficient never reaches an

upper limit, suggesting that the reason for the slow transport is the trapping/detrapping process.

Several previous studies have used large amplitude light pulses to perturb the DSN TiO_2 system from an initial dark condition in order to study electron transport [21-23]. In such cases, electron transport in the nanocrystalline phase will be influenced by the wide range of residence times of electrons in traps. Under these non-stationary conditions, the concept of effective diffusion coefficient is not useful, and the electron transport is best described in terms of a distribution of residence times [23, 24]. However, in the case of a small amplitude periodic perturbation of the illumination superimposed on a much larger steady state illumination level, the electron diffusion coefficient can be regarded as an intensity dependent quantity that is determined by the position of ${}_nE_F$, the electron quasi Fermi level (QFL) [25]. The density of trapping states located at the QFL determines the apparent diffusion coefficient for electrons [25]. This means that an *apparent diffusion coefficient* can be defined for a particular illumination level and measured by IMPS.

The shape of the IMPS response is expected to be the same as in the absence of trapping, provided that the first order rate constants for trapping (k_{trap}) and detrapping (k_{detrap}) satisfy the conditions $k_{trap} >> k_{detrap}$ and $k_{detrap} > \omega$. In this case, the IMPS frequency response is determined by the effective diffusion coefficient, D_n given by the following relationship.

$$D_n = \left(\frac{k_{detrap}}{k_{trap}} \right) D_{cb} \tag{5.12}$$

where D_{cb} is the diffusion coefficient of electrons in the conduction band. This means that the fraction of electrons that are free in the conduction band is determined by the dimensionless ratio k_{detrap}/k_{trap}. Therefore, the observed low D_n compared to D_{cb} even at typical solar illumination levels, indicates that the dimensionless ratio k_{detrap}/k_{trap} is small, even at high light intensities [12, 26]. One can therefore expect D_n to vary with light intensity as ${}_nE_F$ moves through a distribution of trapping levels since k_{detrap} depends

exponentially on (E_c - ${}_nE_F$) (recall equation (2.41)) and k_{trap} depends on the density of vacant trapping states at the electron quasi Fermi level (recall equation (3.42)).

5.2.5 Steady State Electron Concentration Profiles

As already discussed in detail in section 3.3.1, the generation, collection and back reaction of electrons in the DSN TiO_2 solar cell can be described by the continuity equation [12, 18, 25, 27].

$$\frac{\partial n}{\partial t} = \eta\alpha I_0 e^{-\alpha x} + D_n \frac{\partial^2 n}{\partial x^2} - \frac{n - n_0}{\tau_n} \tag{5.13}$$

The last term of this equation considers the decay of electrons by the reaction with I_3^- assuming that the process is pseudo first-order with respect to electron density. As described in section 5.2.3, this can also be second order in electron density. If this is the case, as discussed in section 3.3.1, equation (5.13) can be rewritten as

$$\frac{\partial n}{\partial t} = \eta\alpha I_0 e^{-\alpha x} + D_n \frac{\partial^2 n}{\partial x^2} - k(n - n_0)^2 \tag{5.14}$$

where k is defined by equation (5.10) or (5.11) depending on whether step (5.6*c*) or (5.6*d*) is the dominant route in the proposed second order back reaction scheme in section 5.2.3.

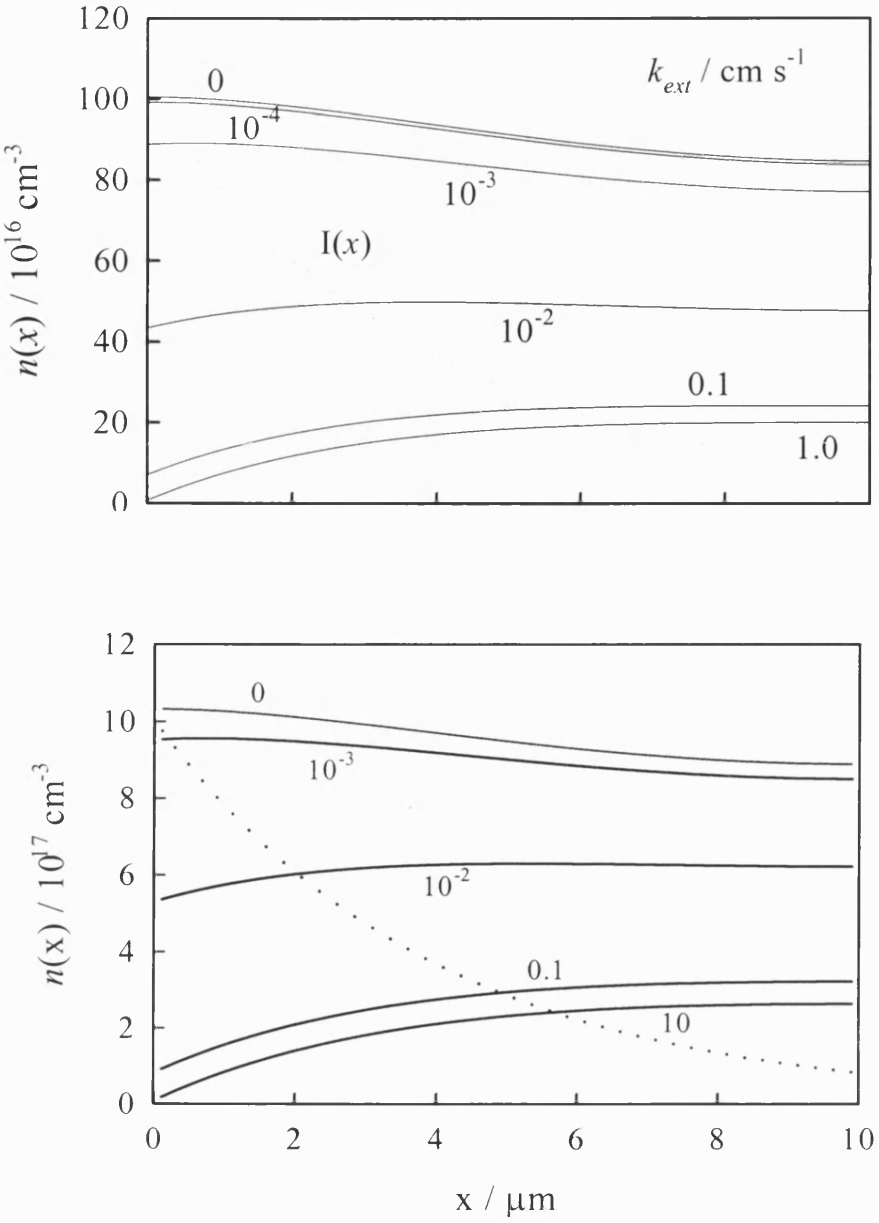

Figure 5.1 *Electron density profiles calculated for illumination of the DSN cell from the substrate side for a range of k_{ext} values between the limits of open circuit (k_{ext} = 0) and short circuit (large k_{ext}) with $I_0 = 10^{16}$ cm^2 s^{-1}, α = 2500 cm^{-1}, $D_n = 10^{-5}$ cm^2 s^{-1}, d = 10 μm, k_{ext} is given in cm s^{-1}: **(Upper)** first-order back reaction of electrons with tri-iodide where τ_n = 0.1 s; **(Lower)** second-order back reaction of electrons with tri-iodide where $k = 10^{-17}$ cm^3 s^{-1}.*

Figure 5.1 compares the calculated steady state electron density profiles for the first and second order cases. Two extreme situations (open and short circuit) have been obtained by setting k_{ext} = 0 and k_{ext} = a large value (i.e. 10) respectively for both first and second order electron decay. Conditions between these two extremes were obtained by setting different values for the electron extraction rate, k_{ext} where $0 < k_{ext} < 10$. To make the comparison easy, the first and second order rate constants for the back reaction of electrons with tri-iodide have been chosen to correspond to the same small-amplitude electron lifetime (recall equations (5.9)-(5.11)).

Equation (3.58) in chapter 3 introduced the following expression, which describes the electrochemical potential of electrons in the nanocrystalline TiO_2 corresponding to the electron QFL, ${}_nE_F$.

$$\frac{n_0 + \Delta n}{N_C} = e^{-\frac{(E_C - {}_nE_F)}{kT}} \approx \frac{\Delta n}{N_C} \tag{5.15}$$

It is reasonable to assume that Δn (the excess electron density generated by illumination) is much greater than n_0, the equilibrium electron density (in the dark), for all intensities of practical interest. The position of the electron quasi Fermi level (QFL) at $x = 0$ under illumination is given by the relation $qU_{photo} = ({}_nE_F - E_F)$ (recall equation (3.59)). Assuming n_o is equal to 10^5 cm^{-3} (based on the position of the I_3^-/I^- redox Fermi level relative to the conduction band of TiO_2), the electron quasi QFL has been calculated for different electron extraction rates (ranging from short circuit to open circuit). Figure 5.2 contrasts the QFLs obtained for different electron extraction rates for both first and second order electron recombination with tri-iodide. Interestingly, the plots show no difference beteen the electron QFLs for first and second order decay under open circuit and short circuit conditions, except close to the SnO_2 substrate.

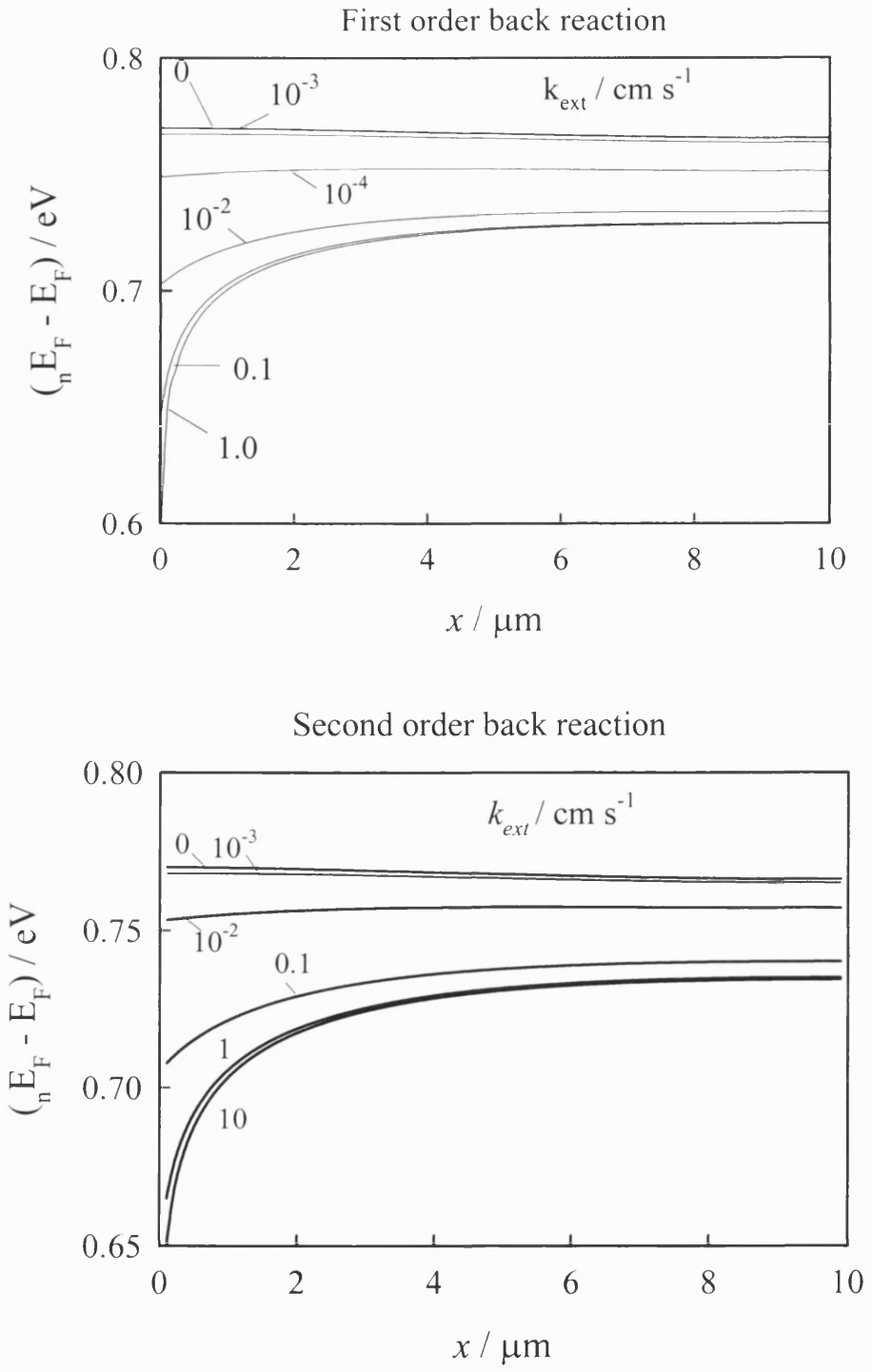

Figure 5.2 *QFLs calculated from electron density profiles in Figure 5.1:* ***(upper)*** *first-order back reaction of electrons with I_3^-;* ***(lower)*** *second-order back reaction of electrons with I_3^-. Equlibrium electron density in the dark (n_0) is 10^5 cm^{-3}. Values of k_{ext} are shown in plots.*

Increasing the rate of back reaction (and hence reducing the diffusion length) introduces a peak in the electron concentration profile as depicted in Figure 5.3. The photo-injected electrons deeper in the TiO_2 film will diffuse away from the substrate and be lost by back reaction with tri-iodide. Figure 5.4 shows how decreasing the electron diffusion length affects the IPCE of a typical DSN TiO_2 cell.

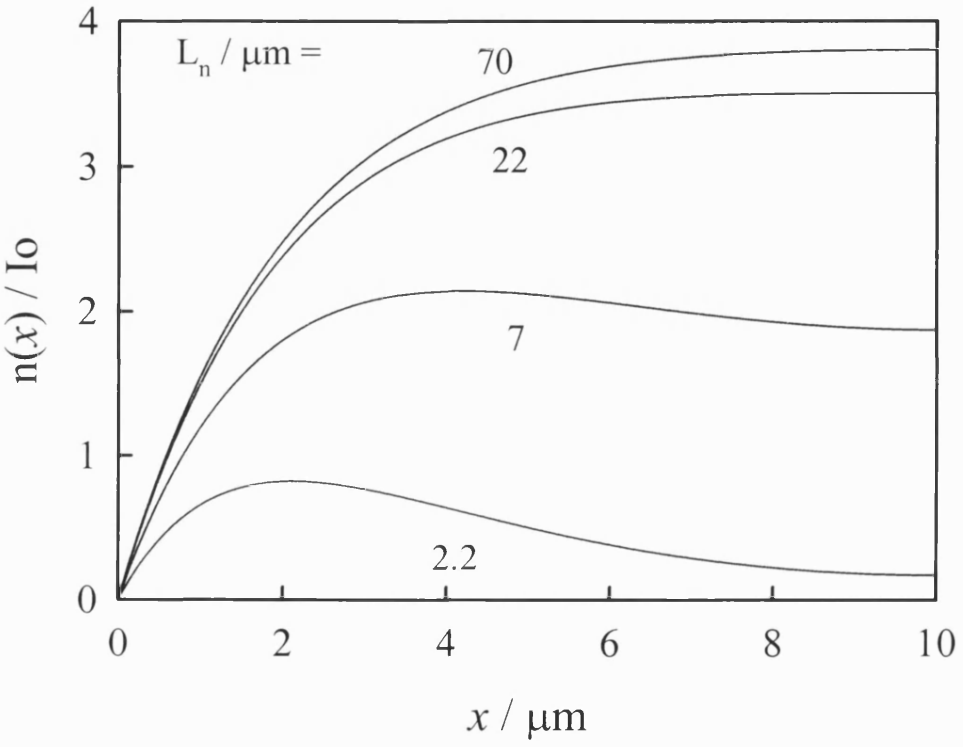

Figure 5.3 *Influence of L_n on normalised steady-state electron density profiles at short circuit; calculated for first-order back reaction, with d = 10 μm, α = 3000 cm^{-1}.*

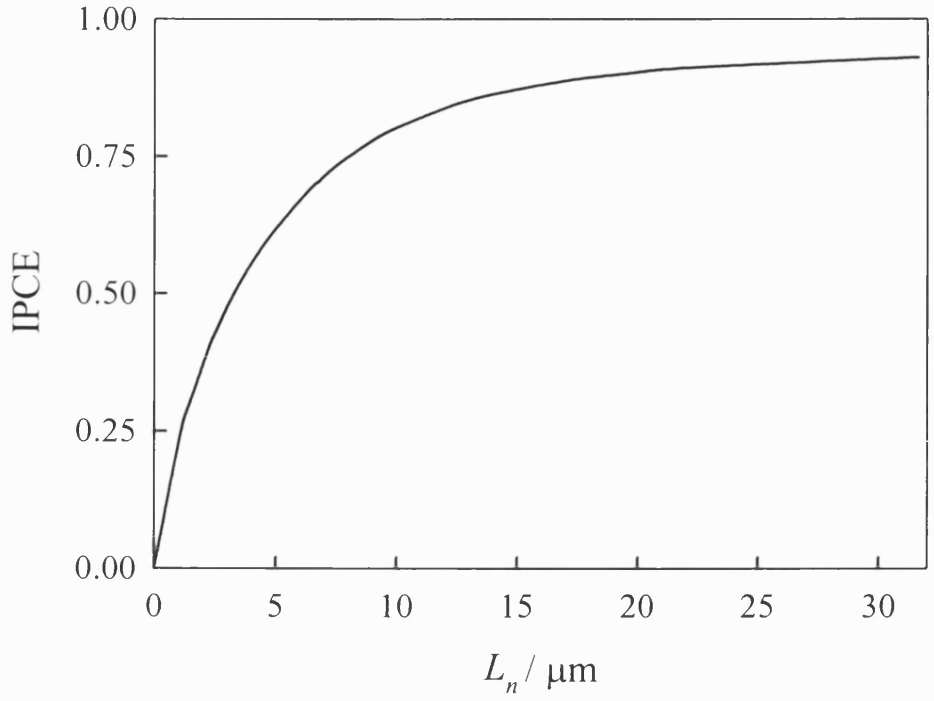

Figure 5.4 *Calculated IPCE as a function of electron diffusion length, with* $d = 10\ \mu m$, $\alpha = 3000\ cm^{-1}$.

5.3 Results and Discussion

A typical example of an experimentally determined IMVS plot is shown in Figure 5.5. Clearly, the photovoltage lags behind the illumination. Because at open circuit, photo-injected electrons are not extracted at the SnO_2 substrate, the phase lag is associated with the relaxation of the electron concentration by back reaction with I_3^-. Unless the light absorption profile is very non-uniform ($\alpha d >> 1$), the IMVS response is expected to be a semicircle in the lower quadrant with $\omega_{min} = 1/\tau_n$ (recall the details of theoretical IMVS plots given in section 3.3.2). This characteristic is clearly indicated by the experimentally observed IMVS plots (see Figure 5.5 for an example). This means that the electron lifetime can be obtained from ω_{min}(IMVS).

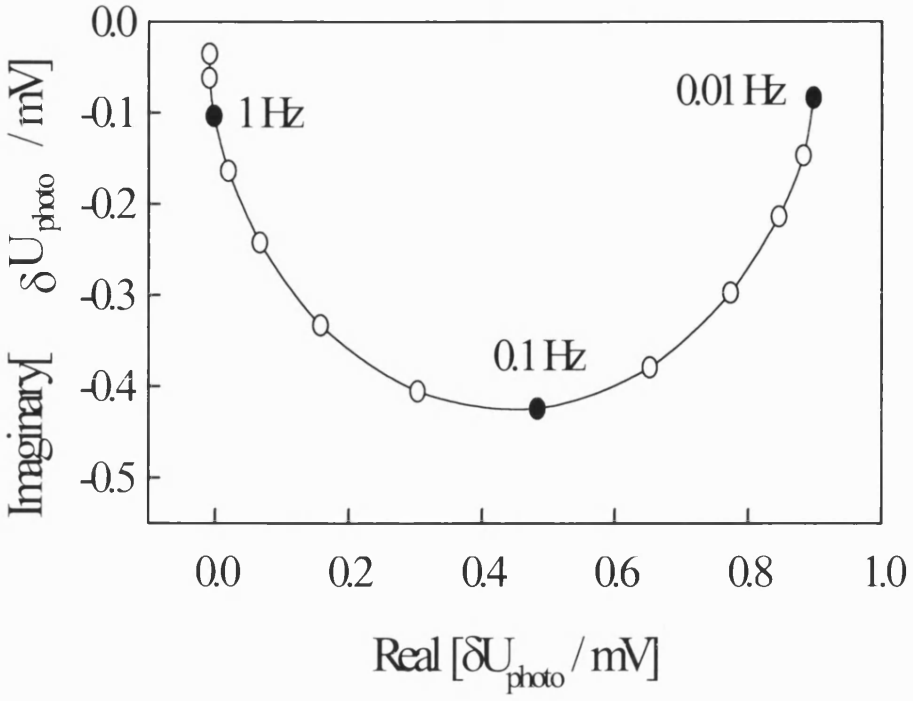

Figure 5.5 *A typical IMVS response of a DSN TiO_2 solar cell. d = 6 μm, α = 2300 cm^{-1}, $I_0 = 4 \times 10^{13}$ cm^{-2} s^{-1}, λ = 470 nm, IPCE = 0.75.*

Figure 5.6 illustrates a typical example of an experimentally obtained IMPS plot. The photocurrent lags behind the illumination. This phase lag arises mainly due to the delay time associated with electron transport from the injection site to the SnO_2 substrate, if most photo-injected electrons are collected. However, if the electron lifetime is so short that a substantial number of the photo-injected electrons are lost on their passage to the SnO_2 substrate (i.e. the collection efficiency, $\eta << 1$ in equation (5.1)), the IMPS phase lag is determined by the electron lifetime.

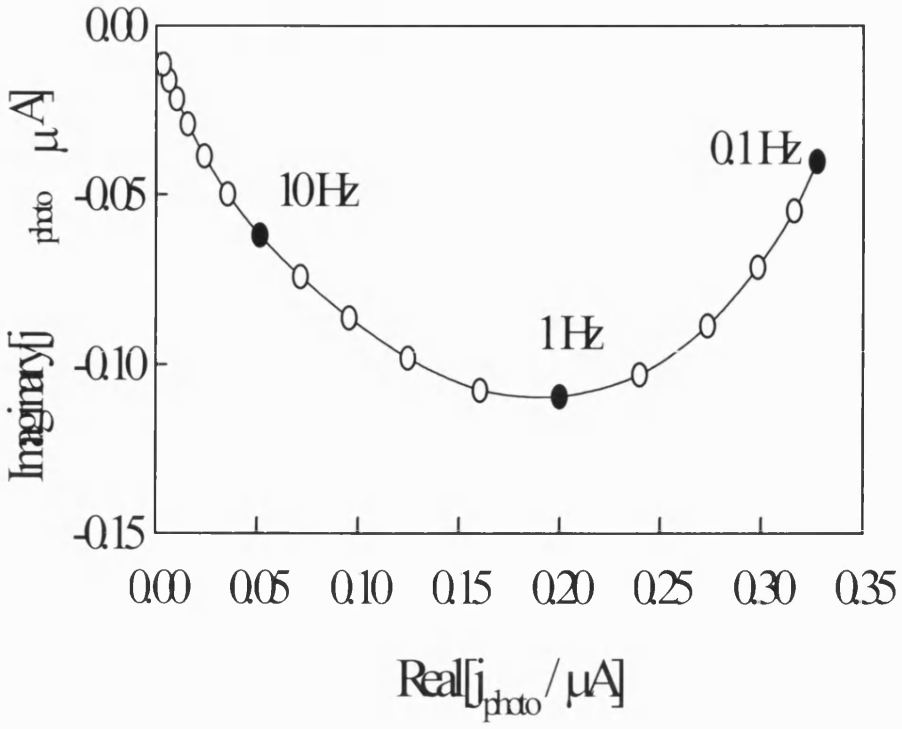

Figure 5.6 *A typical IMPS response of a DSN TiO_2 solar cell. d = 6 μm, α = 2300 cm^{-1}, I_0 = 4 x 10^{13} cm^{-2} s^{-1}, λ = 470 nm, IPCE = 0.75.*

The delay time, t_d, associated with diffusion of an electron injected at a distance x from the SnO_2 substrate, is given by

$$t_d = \frac{x^2}{D_n} \tag{5.16}$$

where D_n is the electron diffusion coefficient. This means that the delay time depends on the injection position in the TiO_2 film. For a DSN cell with a TiO_2 film thickness of d, where $d \leq 1/\alpha$, the IMPS response is composed of a distribution of delay times. This may be the reason why the IMPS response is not a perfect semicircle (see the typical IMPS plot illustrated in Figure 5.6). $2\pi/\omega_{min}$ is a good estimate of the electron transit time.

Electron lifetimes derived for particular illumination intensities from ω_{min}(IMVS) values were employed to fit the IMPS response in order to obtain the corresponding electron diffusion coefficient, D_n (according to the small amplitude solutions of the continuity equation in the Dloczik model).

The experimental IMVS and IMPS plots shown in Figures 5.5 and 5.6 were obtained for a constant level of background illumination, satisfying the condition of $\delta << 1$ (cf. equation (3.22)). IMVS and IMPS measurements were performed over a wide range of illumination intensities using a constant value of $\delta = 0.025$. The shapes of the IMPS and IMVS responses remained unchanged. However, it was noticed that the values of f_{min} change as the illumination intensity is adjusted to different levels for both IMVS and IMPS. These changes are demonstrated by the observed dependence of f_{min} ($f_{min}=\omega_{min}/2\pi$) on illumination intensity. Figure 5.7 depicts f_{min}(IMVS) and f_{min}(IMPS) as a function of the illumination intensity (over five orders of magnitude change) in double logarithmic form.

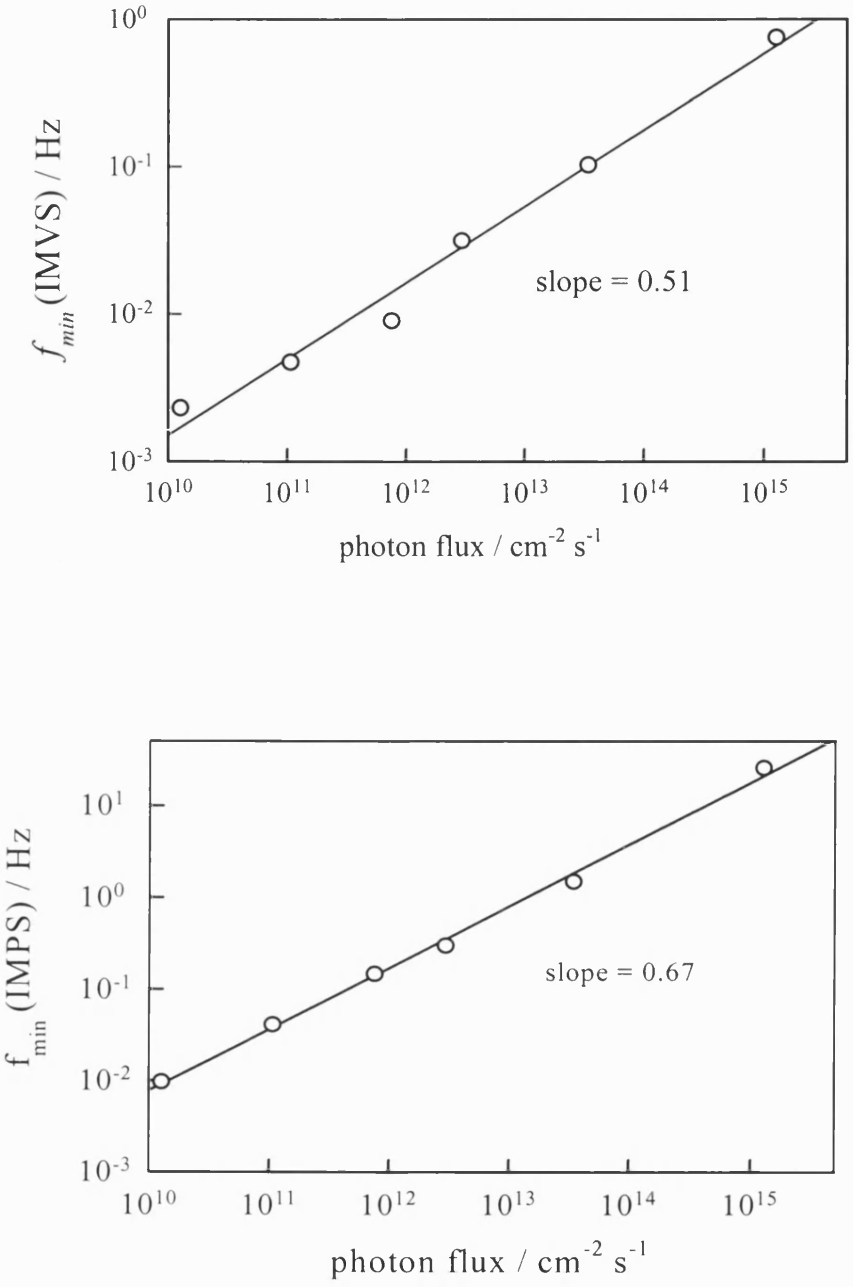

Figure 5.7 *Double logarithmic representation of variation of* ***(upper)*** f_{min}*(IMVS) and* ***(lower)*** f_{min}*(IMPS) with incident steady-state photon flux.*

Clearly, f_{min}(IMPS) increases as the illumination intensity is adjusted to higher levels. The increase in f_{min}(IMPS) indicates that photo-injected electrons take shorter times to reach the SnO_2 substrate at relatively high illumination intensities. This means that the electron

diffusion coefficient, D_n rises as the illumination intensity is gradually adjusted to higher levels. In other words, electrons diffuse faster with an increase of illumination intensity. The trend is in the opposite direction for IMVS as electron lifetime decreases with an increase of illumination intensity (see Figure 5.8). This behavior indicates that not only the photo-injected electrons move more slowly at low illumination intensities, but also they live longer. At the lowest illumination intensity measured in the present study, the time taken for photo-injected electrons to reach the SnO_2 substrate is of the order of minutes, whereas the corresponding electron lifetime is about 100 s. This is very surprising as the observed electron lifetime measured at the highest illumination intensity was 0.2 s. (see Figure 5.8).

The IMPS responses were fitted using the analytical solution of the continuity equation for the small amplitude modulation case (see section 3.3 for details). Values of the electron diffusion coefficient, D_n, were obtained by fitting the IMPS response. These values were related to the conduction band free electron diffusion coefficient, D_{cb}, in the nanocrystalline oxide by the relation $D_n = (k_{detrap}/k_{trap})D_{cb}$ (recall the equation (5.12)) [25].

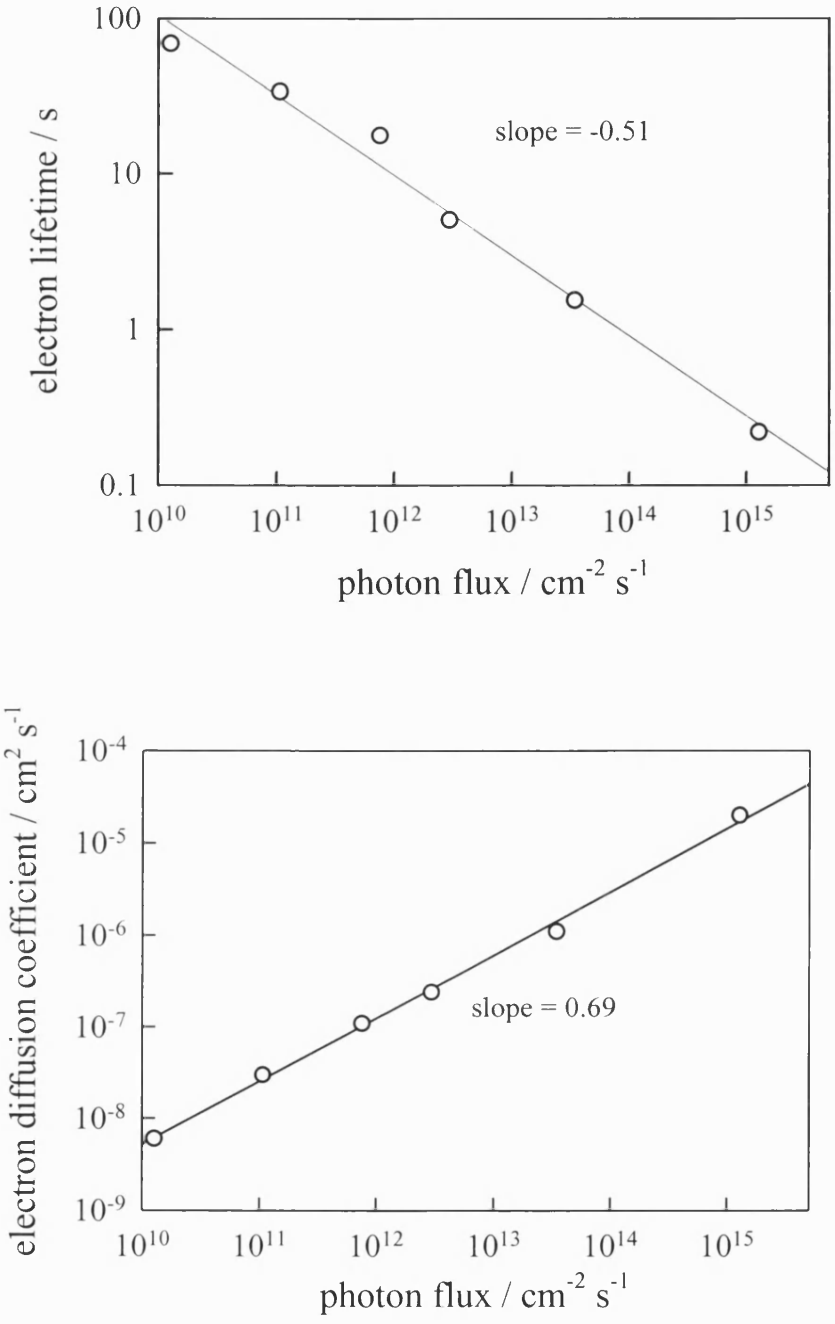

Figure 5.8 *Double logarithmic representation of variation of* ***(upper)*** τ_n, *and* ***(lower)*** D_n *with incident steady-state photon flux.*

The values of τ_n and D_n obtained by fitting the IMVS and IMPS responses respectively and plotted as a function of illumination intensity in double logarithmic form are depicted in Figure 5.8. These double logarithmic representations allow the intensity dependence of D_n to be expressed in the form of the power law $D_n \propto I_o^{0.69}$, where I_o is the dc component of the incident photon flux density. The corresponding intensity dependence of τ_n is $\tau_n \propto I_o^{-0.51}$. As described in the preceding section, the intensity dependence of the electron diffusion length, L_n, can be obtained from relation $L_n = (D_n \tau_n)^{1/2}$. The intensity dependence of the electron diffusion length can be described in the form of the power law as $L_n \propto I_o^{0.085}$. Figure 5.9 illustrates this rather weak intensity dependence of L_n in a semi-logarithmic form. Unlike double logarithmic representations of τ_n and D_n against illumination intensity, which exhibit strong intensity dependence, the semi-logarithmic representation is more convenient for the case of L_n as it only varies by less than a factor of 2.5 over more than five decades of illumination intensity change.

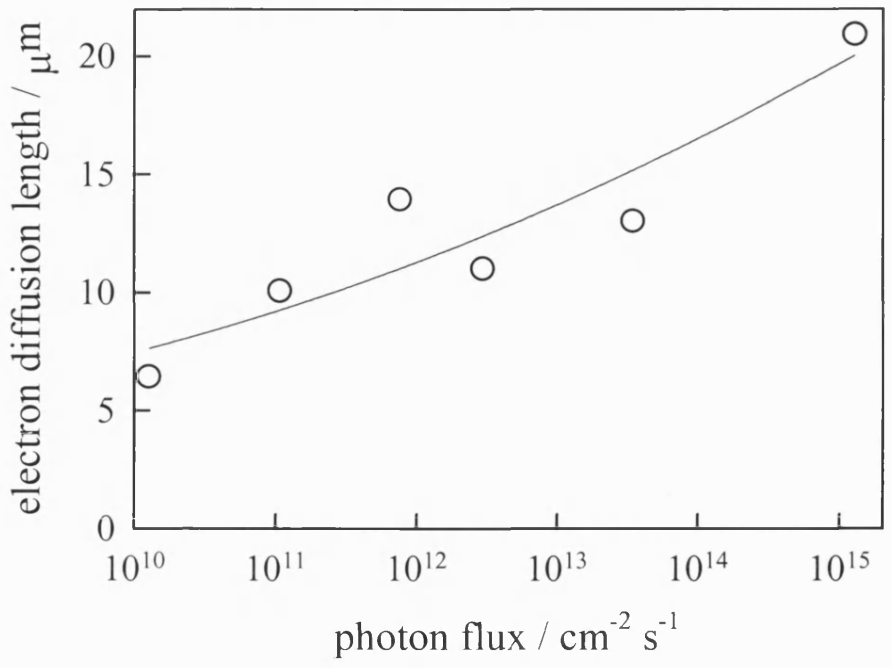

Figure 5.9 *Variation of estimated electron diffusion length $L_n = (D_n \tau_n)^{1/2}$ with incident photo flux. (Points were calculated from D_n and τ_n values determined by IMPS and IMVS. Line represent the polynomial fit).*

This weak intensity dependence of L_n arises from the compensation of the decrease in τ_n with increasing illumination intensity by a corresponding increase in D_n (recall the relation $L_n = (D_n \tau_n)^{1/2}$). The intensity dependent values of D_n and τ_n were used in equation (3.37) to calculate the IPCE as a function of illumination intensity. The calculated IPCE hardly varies over five orders of magnitude of illumination intensity change. Values of the predicted IPCE were then compared with experimental IPCE results.

However, experimental determination of reliable IPCE values for the DSN TiO_2 solar cell over five orders of magnitude of illumination intensity is a really challenging task. The main problem is the very slow photocurrent response of these cells particularly at very low illumination intensities. For example, the photocurrent densities at the lowest illumination intensity measured in the present study are below 10^{-9} A cm^{-2}, so there are experimental difficulties in obtaining reliable values. It is worth noting here that the very slow photocurrent response of these cells prevents use of the conventional photocurrent

detection technique, which involves a mechanical chopper and a lock-in amplifier. The experimental difficulties of obtaining reliable photocurrent values at low illumination intensities stimulated the application of two independent methods for determining the IPCE experimentally so that finally they could be compared. Reasonably accurate experimental IPCE values were obtained by doing this. The first experimental method involved obtaining the steady-state photocurrent from the difference between the current under illumination and the current in the dark, allowing sufficient time to achieve steady state values. The second approach involved obtaining the low frequency intercept on the IMPS plot. In some cases the low frequency intercept was obtained by extrapolating the frequency response to the real axis, as the recorded minimum frequency does not cross the real axis. The IPCE was then calculated from the known value of δI_o. Both approaches gave very similar IPCE values as a function of the illumination intensity. Figure 5.10 compares the experimental IPCE values obtained by the first method with the values predicted theoretically using the experimentally determined D_n and τ_n values. The theoretical data have been fitted to a polynomial curve to aid comparison. From Figure 5.10, it is clear that the experimentally determined and calculated IPCE values agree quite well. The most important outcome of the present analysis is, the IPCE is almost independent of illumination intensity over the entire measured intensity range.

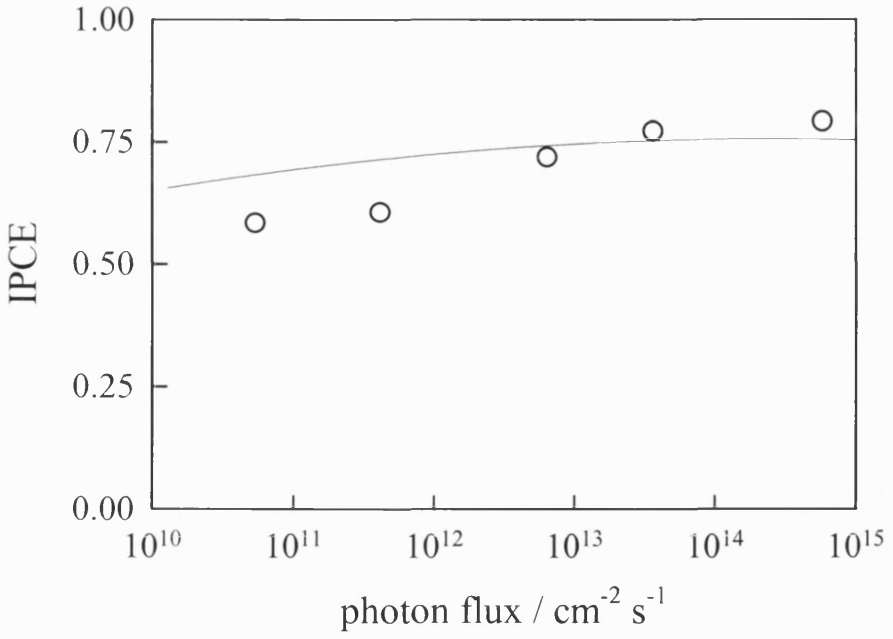

Figure 5.10 *Comparison of experimental IPCE of DSN TiO_2 solar cell (**open circles**) the behavior predicted from the observed intensity dependence of D_n and τ_n. (**line**) the polynominal fit of L_n as a function of illumination intensity shown in Figure 5.9.*

Several previous studies have reported electron transport in nanocrystalline phases that involves a trapping/detrapping process [12, 23, 28]. Dloczik *et al.* considered a single trapping/detrapping level [12] and Vanmaekelbergh and de Jongh treated trapping/detrapping with a distribution of energy levels [28]. However, latter neglected the effect of the back reaction on electron transport in their studies. Nelson has proposed an alternative method based on a random walk model, which simulates electron transport through nanocrystalline media for a distribution of waiting times [23]. In this approach, an exponential density of trap states $g(E) \propto \exp[\beta(E_c - E)/kT]$ is used giving rise to a power-law waiting time distribution [23].

As shown in Figure 5.8, the apparent electron diffusion coefficient, D_n varies from 10^{-5} to 10^{-8} cm^2 s^{-1} with a slope of 0.69 for the double logarithmic plot over the measured illumination intensity range. This intensity dependence of D_n indicates an increase in the ratio of k_{detrap}/k_{trap} in equation (5.12) as the electron quasi Fermi level moves upwards

(towards the conduction band) with increasing illumination intensity. Since D_{cb} is of the order of 10^{-2} cm^2 s^{-1} for bulk anatase [19, 29], and D_n varies from 10^{-5} to 10^{-8} for the measured light intensity range, the ratio k_{detrap}/k_{trap} lies in the range 10^{-3} to 10^{-6} depending on illumination intensity (recall equation (5.12) and Figure 5.8). It is very important to note here that the use of the D_{cb} value reported for bulk anatase [19, 29] to obtain the ratio of k_{detrap}/k_{trap} for the measured intensity range does not effect the value D_n, provided that $k_{trap} >> k_{detrap}$ (i.e. most electrons are trapped). This was confirmed as the values of D_n obtained by this approach (i.e.considering trapping/detrapping process) were almost identical to those obtained using the expressions for the trap-free case in the limit of negligible back reaction of electrons. Recalling the preceding section, it can be shown that k_{detrap} depends exponentially on the trap depth, $(E_c - E_T)$ (also recall equation (2.41)) and k_{trap} depends linearly on the density of vacant trapping states, $(1-f_T)N_t$ (also recall equation (3.42)) [25]. Here, f_T is the Fermi Dirac function defined for $E = E_T$:

$$f_T = \frac{1}{1+\exp\left[\dfrac{E-E_T}{k_BT}\right]} \tag{5.17}$$

The ratio k_{detrap}/k_{trap} is obtained by integrating the trapping and detrapping rates over the energy range E_v to E_c, for a distribution of traps [25]. An exponential density of states distribution of traps can be described by the expression [24]

$$_S(E_T) = \frac{N_{T0}}{k_BT_T}\exp\left[-\beta\left(\frac{E_c-E_T}{k_BT}\right)\right] \tag{5.18}$$

Here $\beta = T/T_T$ and T_T is a characteristic temperature that determines the broadening of the exponential distribution. Evaluation of the ratio k_{detrap}/k_{trap} for this distribution of traps shows that the variation of the effective diffusion coefficient with the electron quasi-Fermi level (and hence with the dc photovoltage) is given by [25]

$$\frac{\partial \log D_n}{\partial U_{photo}} = (1-\beta)\frac{q}{2.303 k_B T} \tag{5.19}$$

Equation (5.19) can be related to the observed intensity dependence of D_n and U_{photo} in the present study as follows

$$\frac{\partial \log D_n}{\partial U_{photo}} = \frac{\partial \log D_n}{\partial \log I_0} \times \frac{1}{\frac{\partial U_{photo}}{\partial \log I_0}} \tag{5.20}$$

Figure 5.11 depicts the plot of U_{photo} vs. log(I_0). Despite the observed steep fall of U_{photo} at low illumination intensities, which may arise due to the internal shunt resistance of the DSN TiO_2 cell, $dU_{photo}/dlog(I_0)$ can be obtained from the slope of the plot of U_{photo} vs. log(I_0) as 0.085 V. Figure 5.8 shows that the slope of the plot of log D_n vs. log(I_0) ($dD_n/dlog(I_0)$) is 0.69. From equations (5.19) and (5.20) the value of β was calculated and found to be 0.57. However, further work is required to establish how β and IPCE depend on different oxide materials and preparation methods.

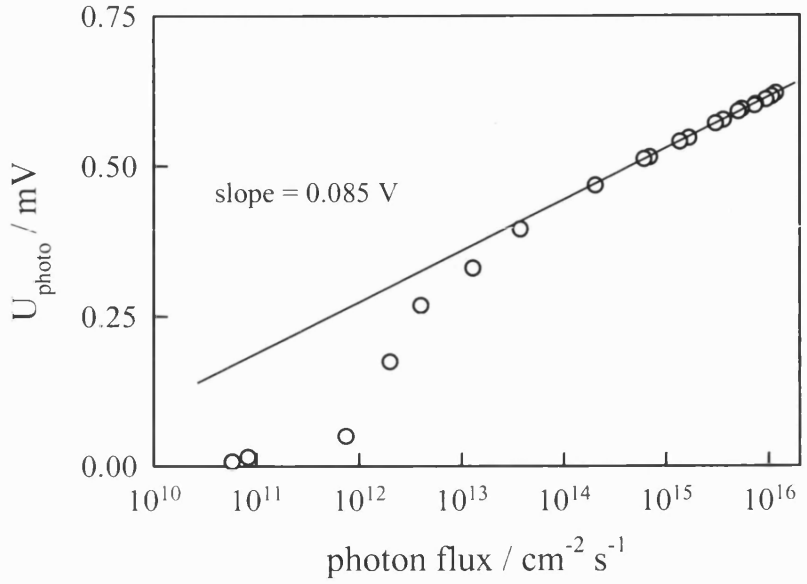

Figure 5.11 *Intensity dependence of the open circuit photovoltage.*

Several previous studies have considered the intensity dependence of the electron lifetime, τ_n in DSN TiO_2 solar cells [13, 14, 30]. Schlichthörl *et al.* have attributed the intensity dependence of τ_n to the variation of the electron transfer rate with the energy level of trapped electrons [13, 14]. They also showed that a fivefold increase in the I_3^-/I^- concentration lowered the electron lifetime by a factor of 25 at a constant open circuit voltage (i.e. for constant n in equation (5.9)) [13, 14]. This study shows that the back reaction of photo-injected electrons with tri-iodide is second order in I_3^- concentration and corresponds to reaction steps (5.6*a*) – (5.6*c*). In fact, it shows that the rate of electron decay is proportional to $n^{2.2}$ [14]. This finding is very interesting as the formation of $I_2^{\bullet-}$ during the photo-oxidation of iodide at bare and dye coated TiO_2 colloids is already well established [5, 31]. However, Liu *et al.* reported that the reaction is first order in $[I_3^-]$, and proposed that the mechanism involves dissociative chemisorption of I_2 [30] (recall reaction steps (5.3a) – (5.3c) and equations (5.4) – (5.5)) which contradicts to the results of Schlichthörl *et al.* [13, 14].

As shown in Figure 5.8, the electron lifetime is inversely proportional to the illumination intensity with a slope of 0.51 for the measured intensity range in the present study. For a second order electron decay, the half lifetimes of electrons ($t_{1/2}$) is described by equation (5.21).

$$t_{1/2} = \frac{1}{kn} \tag{5.21}$$

where k is the second order rate constant with respect to electron density and n is the initial electron density. This means that as the initial electron density decreases (i.e. illumination intensity reduces) the electrons live longer. It was observed in the present study that the electron lifetime varies with illumination intensity in a similar fashion (see Figure 5.8). In fact, τ_n is inversely proportional to the square root of the illumination intensity (hence the electron concentration, as IPCE is constant) and this is consistent with the proposed second order mechanism involving $I_2^{\bullet-}$ as an intermediate (i.e. reaction steps 5.6*a* – 5.6*d*) since $\tau_n = (Gk)^{-1/2}$ [25, 32, 33]. However, it is important to note here that the $I_2^{\bullet-}$ can decay either by disproportionation (recall reaction step (5.6*c*)) or by back reaction with electrons in surface traps (recall reaction step (5.6*d*)).

Fitzmaurice and Frei [5] reported a value of 3×10^9 dm^3 s^{-1} for the rate constant for disproportionation of $I_2^{\bullet-}$ into I_3^- (recall k_{dssp} in proposed back reaction scheme) for colloidal suspensions of phenylfluorone sensitised TiO_2 in aqueous media. The formation constant for tri-iodide in acetonitrile is of the order of 10^7 mol dm^{-3}, so that K_1 in reaction step (5.6*a*) is equal to 10^{-7} mol dm^{-3}[17]. A rough estimate of the second order rate constant, k can be obtained from the relation $k = \frac{1}{\tau_n^2 G}$ considering the facts that the measured electron lifetime is around 1 s for an incident photon flux of 6×10^{13} cm^{-2} s^{-1}, 70% of the incident light is absorbed by the 6 μm thick DSN TiO_2 film and, the mean electron injection rate G is 7.3×10^{16} cm^{-3} s^{-1}. The resulting value of the second-order rate constant $k = 1.4 \times 10^{-17}$ cm^3 s^{-1} (equal to 8.4×10^3 dm^3 mol^{-1} s^{-1}) can be substituted in

equation (5.10) to obtain $K_2 \approx 6.57 \times 10^2$ mol^{-1} dm^3. This means that the equilibrium reaction (5.6*b*) favours the right hand direction suggesting the formation of $I_2^{\bullet-}$ as an intermediate in the back reaction process with tri-iodide [25, 33].

The results obtained in the present study are consistent with the second order back reaction kinetics scheme presented by Huang *et al.* [15]. However, at present it is not possible to distinguish between the different mechanisms with certainty. It is important to measure the reaction order with respect to iodide and tri-iodide, and this must be done for constant n, not for constant intensity. The distinction between the two mechanisms discussed above is important for future development of DSN cells. If the kinetics of the back reaction depend on intensity as a result of second order back reaction kinetics for the iodide/tri-iodide redox couple at the TiO_2 surface, attempts to replace the iodide/tri-iodide couple by simple one electron redox systems are likely to be unsuccessful, since in this case one would expect the lifetime to be independent of intensity. However, if the observed intensity dependence of the lifetime arises from the distribution of electron trap levels, other redox systems might be expected to exhibit similar behavior.

5.4 Conclusions

The rates of electron transport and back reaction in the dye sensitised nanocrystalline cell have been characterised by IMPS and IMVS over more than five orders of magnitude of light intensity. It was found that the electron diffusion coefficient increases with increasing light intensity ($D_n \propto I^{0.68}$), and the electron lifetime falls according to the power law relation $\tau_n \propto I^{-0.51}$. The consequence of the variation of D_n and τ_n in opposite directions is that the electron diffusion length $L_n = (D_n \tau_n)^{1/2}$ is only weakly dependent on light intensity. This means in practice that the IPCE of the cell hardly varies over five orders of magnitude of light intensity. Further work is required to establish whether this effect is a unique feature of the current dye sensitised nanocrystalline cells that employ the iodide/tri-iodide redox couple. The observation that the IPCE is almost independent of illumination intensity in the DSN TiO_2 cells provides further evidence for the second order back reaction kinetics with respect to electron density. However, recently Trupke *et*

al. reported [34] strong dependence of the IPCE on illumination intensity. This observation is totally contradicted to the results obtained in the present study. Therefore, a comparison work carried out in both labs (in Karlsruhe and Bath). Following this comparison work, it was understood that performance of the DSN TiO_2 cells heavily depends on the preparation methods which explains the reason why the Bath cells exhibit weak dependence of IPCE with illumination intensity.

5.5 References

1. B. Oregan and M. Gratzel, Nature 353:737 (1991).
2. M. K. Nazeeruddin, P. Liska, J. Moser, N. Vlachopoulos, and M. Gratzel, Helvetica Chimica Acta 73:1788 (1990).
3. M. K. Nazeeruddin, A. Kay, I. Rodicio, R. Humphrybaker, E. Muller, P. Liska, N. Vlachopoulos, and M. Gratzel, Journal of the American Chemical Society 115:6382 (1993).
4. M. Gratzel, Progress in Photovoltaics 8:171 (2000).
5. D. J. Fitzmaurice and H. Frei, Lanumuir 7:1120 (1991).
6. C. Nasr, S. Hotchandani, and P. V. Kamat, Journal of Physical Chemistry B 102:4944 (1998).
7. B. Oregan, J. Moser, M. Anderson, and M. Gratzel, Journal of Physical Chemistry 94:8720 (1990).
8. S. A. Haque, Y. Tachibana, D. R. Klug, and J. R. Durrant, Journal of Physical Chemistry B 102:1745 (1998).
9. G. Franco, J. Gehring, L. M. Peter, E. A. Ponomarev, and I. Uhlendorf, Journal of Physical Chemistry B 103:692 (1999).
10. N. J. Show, in Chemistry, University of Bath, Bath, 1999.
11. F. Cao, G. Oskam, G. J. Meyer, and P. C. Searson, Journal of Physical Chemistry 100:17021 (1996).
12. L. Dloczik, O. Ileperuma, I. Lauermann, L. M. Peter, E. A. Ponomarev, G. Redmond, N. J. Shaw, and I. Uhlendorf, Journal of Physical Chemistry B 101:10281 (1997).

13. G. Schlichthorl, S. Y. Huang, J. Sprague, and A. J. Frank, Journal of Physical Chemistry B 101:8141 (1997).
14. G. Schlichthorl, N. G. Park, and A. J. Frank, Journal of Physical Chemistry B 103:782 (1999).
15. S. Y. Huang, G. Schlichthorl, A. J. Nozik, M. Gratzel, and A. J. Frank, Journal of Physical Chemistry B 101:2576 (1997).
16. V. A. Macagno, M. C. Giordano, and A. J. Arvia, Electrochimica Acta 14:335 (1969).
17. I. V. Nelson and R. T. Iwamoto, Journal of Electroanalytical Chemistry 7:218 (1964).
18. L. M. Peter and D. Vanmaekelbergh, in Advances in Electrochemical Science and Engineering, Vol. 6 (D. M. Alkire and D. Kolb, eds.), VCH Wiley, New York, 1999, p. 77.
19. D. Vanmaekelbergh and P. E. de Jongh, Journal of Physical Chemistry 103:747 (1999).
20. B. Enright and D. J. Fitzmaurice, Journal of Physical Chemistry 100:1027 (1996).
21. A. Kay, R. Humphrybaker, and M. Gratzel, Journal of Physical Chemistry 98:952 (1994).
22. A. Solbrand, A. Henningsson, S. Sodergren, H. Lindstrom, A. Hagfeldt, and S. E. Lindquist, Journal of Physical Chemistry B 103:1078 (1999).
23. J. Nelson, Physical Review B-Condensed Mater 59:15374 (1999).
24. J. M. Marshall, Reports on Progress in Physics 46:1235 (1983).
25. A. C. Fisher, L. M. Peter, E. A. Ponomarev, A. B. Walker, and K. G. U. Wijayantha, Journal of Physical Chemistry B 104:949 (2000).
26. L. Forro, O. Chauvet, D. Emin, L. Zuppiroli, H. Berger, and F. Levy, Journal of Applied Physics 75:633 (1994).
27. S. Sodergren, A. Hagfeldt, J. Olsson, and S. E. Lindquist, Journal of Physical Chemistry 98:5552 (1994).
28. D. Vanmaekelbergh and P. E. de Jongh, Physical Review B-Condensed Mater 61:4699 (2000).

29. L. Kavan, M. Gratzel, S. E. Gilbert, C. Klemenz, and H. J. Sceel, Journal of the American Chemical Society 118:6716 (1996).
30. Y. Liu, A. Hagfeldt, X. R. Xiao, and S. E. Lindquist, Solar Energy Materials and Solar Cells 55:267 (1998).
31. D. J. Fitzmaurice, M. Eschle, H. Frei, and J. Moser, Journal of Physical Chemistry 97:3806 (1993).
32. L. M. Peter and K. G. U. Wijayantha, Electrochemistry Communications 1:576 (1999).
33. L. M. Peter and K. G. U. Wijayantha, Electrochimica Acta 45:4543 (2000).
34. T. Trupke, P. Wurfel, and I. Uhlendorf, Journal of Physical Chemistry B 104:11484 (2000).

Chapter 6

Small Amplitude Laser pulse Excitation Transient Measurements on Dye Sensitised Nanocrystalline TiO_2 Solar Cells

6.1 Introduction

The limitations of steady-state methods for characterisation of electrochemical systems are well known, and progress in understanding the kinetics and mechanism of electrode processes depends to a large extent on the development of non-stationary techniques which involve measurement of the potential or current response of the system to transient or periodic excitation. However, characterisation of the transport and interfacial reaction of electrons in systems such as dye sensitised nanocrystalline solar cells is complicated by the non-linearity of these processes. Using frequency-resolved techniques, this problem has been overcome by superimposing a small ac perturbation of the illumination light intensity on top of a steady dc illumination level in the previous study (chapter 5). The dc illumination controls the occupancy of electron traps, so that the electron diffusion coefficient can be treated as a constant. Similarly, the kinetics of the back reaction of electrons with I_3^- can be linearised for small perturbations about a dc illumination level, allowing the definition of a small amplitude pseudo first order electron lifetime τ_n (i.e.IMVS) [1-4].

The previous work reported in chapter 5 has shown that the incident photon to current conversion efficiency (IPCE) of these cells is almost independent of the illumination level over a wide range of intensity [5-7]. This result is surprising, since it has been established that the collection of electrons at the substrate electrode can be described by an intensity dependent diffusion coefficient D_n. At low light intensities, D_n becomes very small ($10^{-8}cm^2s^{-1}$), and photogenerated electron collection can take several minutes [5-7]. The fact that the IPCE remains nearly constant over at least five orders of magnitude of light intensity is explained by the observation that the electron lifetime τ_n increases as the intensity is adjusted lower [5-7]. The increase in τ_n and the decrease in D_n almost

compensate each other, so that the electron diffusion length $L_n = (D_n \tau_n)^{1/2}$ is only weakly dependent on intensity.

The present study has extended the same approach to the time domain. The electron occupancy (i.e. the electron quasi Fermi level ${}_nE_F$) was fixed by the dc illumination level, and nano-second laser pulses were then used to create a small excess of electrons. The electron transport behaviour was characterised by measuring the current and charge transients at short circuit. The back reaction of electrons with I_3^- was characterised by measuring the photovoltage transients with the system at open circuit. It is very important to note that in both short circuit and open circuit cases in the present small amplitude approach, following the nano-second laser pulses the current and voltage transients relax back to a steady-state level. This contrasts with the previous studies that used large amplitude laser pulses with an initial dark condition of the system so that the current and voltage transients relax back to the dark condition [8-10]. The small amplitude responses of the system have been calculated from the continuity equation using an approximate analytical solution of the boundary value problem as well as by a finite difference method. The experimental methods of the present approach have already been discussed in section 4.11.

6.2 Theory

The generation and collection of electrons in dye-sensitised nanocrystalline solar cells is commonly described using the continuity equation [11-13]. The analytical solutions of the continuity equation for small amplitude periodic perturbations (i.e. IMPS and IMVS) have already been discussed in section 3.3. The present approach is analogous to the above system but in the time domain. In the present study, a small laser pulse was superimposed on a larger steady dc illumination level, i.e.

$$I(t) = I[1 + \delta(t)] \tag{6.1}$$

where $\delta(t)$ is the delta function. The power of the pulse is small enough that the steady state electron density is perturbed only by less than 1%. The time-dependent solution of the continuity equation can then be obtained by considering that D_n and τ_n are functions only of the dc illumination level I_0, and are not affected by the perturbation.

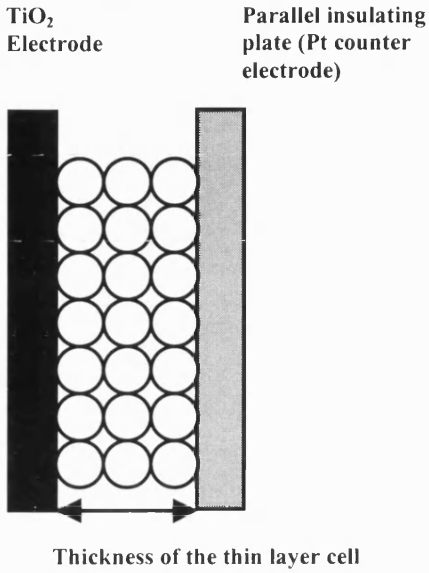

Figure 6.1 *Thin layer configuration of DSN solar cell.*

The general features of the time dependent photocurrent solution for pulse excitation can be obtained analytically by considering that the cell behaves like an electrochemical thin layer cell consisting of one electrode and a parallel insulating plate [14] (see Figure 6.1). The analogy is exact if illumination is homogenous (i.e. $\alpha d << 1$) provided that the back reaction of photogenerated electrons is zero. Then, a uniform concentration of excess electrons can be expected at time $t = 0$.

In that case, the electron extraction occurs under diffusion control and the transient photocurrent is given by

$$j_{photo}(t) = \frac{2qn_{t=0}}{d} \sum_{k=0}^{\infty} \exp\left[\frac{-D_n(2k+1)^2\pi^2 t}{4d^2}\right] \qquad (6.2)$$

where d is the thickness of the dye sensitised nanocrystalline TiO_2 film and $n_{t=0}$ is the electron density immediately after the pulse. At short times, equation (6.2) reduces to the familiar Cottrell equation and the current decay is proportional to $t^{-1/2}$:

$$j_{photo}(t) \rightarrow \frac{qD_n n_{t=0}}{\pi^{1/2} t^{1/2}} \tag{6.3}$$

At longer times, the decay becomes exponential. Integration of equation (6.2) gives the corresponding time dependent photocharge:

$$Q_{photo}(t) = qn_{t=0}d\left[1 - \frac{8}{\pi^2}\sum_{k=0}^{\infty}\frac{1}{(2k+1)^{1/2}}\exp\left(\frac{-D_n(2k+1)^2\pi^2 t}{4d^2}\right)\right] \tag{6.4}$$

At short times, equation (6.4) reduces to

$$Q_{photo}(t) = \frac{2qn_{t=0}D_n t^{1/2}}{\pi^{1/2}} \tag{6.5}$$

At long times the charge tends towards

$$Q_{photo}(t \rightarrow \infty) = qn_{t=0}d \tag{6.6}$$

Equation (6.4) can be recast in the useful dimensionless form

$$\frac{Q_{photo}(t)}{Q_{photo}(t \rightarrow \infty)} = 1 - \frac{8}{\pi^2}\sum_{k=0}^{\infty}\frac{1}{(2k+1)^{1/2}}\exp\left[(2k+1)^2\pi^2 T\right] \tag{6.7}$$

where the reduced time T is defined as

$$T = \frac{tD_n}{d^2} \tag{6.8}$$

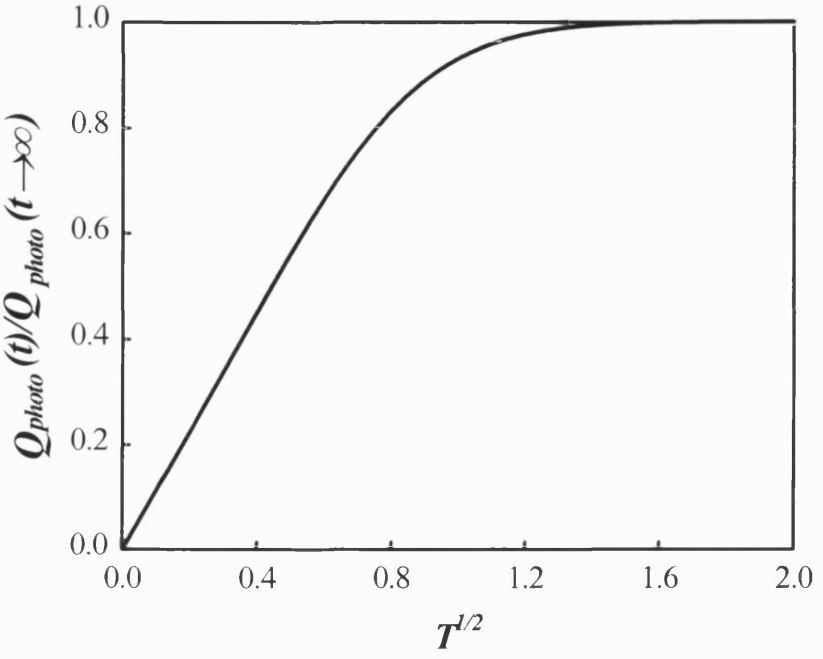

Figure 6.2 *The normalised charge transient calculated from the approximate analytical solution (equation (6.4)) showing the linear variation with $T^{1/2}$ at short times.*

Figure 6.2 illustrates the plot of the normalised charge versus $T^{1/2}$. It is clear that the plot is linear for $T<0.75$. Figure 6.2 can be used to estimate D_n if the dye sensitised TiO_2 film thickness, d is known. However, if d is unknown, equation (6.5) can be used to determine D_n, and d can then be estimated using equation (6.6). This is more convenient since determination of d by SEM requires destruction of the cell.

As already noted, the preceding analytical expressions are only valid if illumination is homogeneous and the back reaction of photogenerated electrons (with I_3^- or oxidised dye molecules) can be neglected. The fully implicit finite difference method was used to obtain solutions of the continuity equation for comparison with the analytical expression for homogenous illumination. For the present analysis, it is assumed that illumination is from the substrate side, and the back reaction effect is negligible although in reality the effect of the back reaction is substantial especially for low intensity illumination (see also chapters 5 and 7). Figure 6.3 shows how increasing the absorption coefficient (and hence the inhomogeneity of the initial electron density distribution) affects the current transients. For convenience, the results are shown in the form of Cottrell plots of j_{photo} vs. $t^{-1/2}$. It can be seen that the deviations from linearity become important for α>1000.

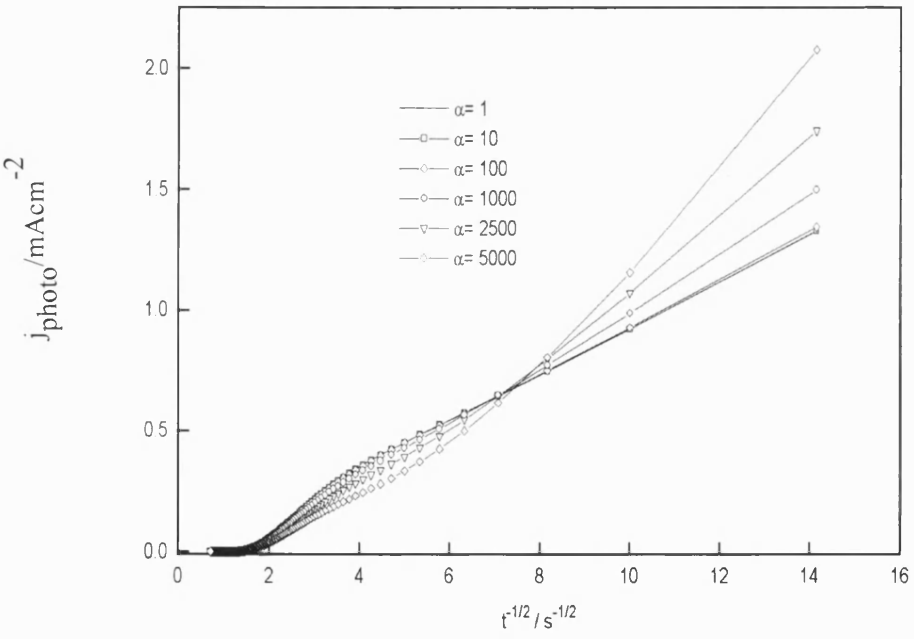

Figure 6.3 *Cottrell plots of the photocurrent transients calculated by the finite difference method as a function of different values of the absorption coefficient, α for 5 μm film thickness, electron diffusion coefficient =10^{-5} cm^2 s^{-1}, $n_{t=0}$=10^{18} cm^{-3}.*

As already shown in section 3.3.2, the decay of the photovoltage is related to the change in the electron quasi Fermi energy ${}_nE_F$, which is related to the free electron density n by

$$\frac{n-n_0}{n_0} = \exp\left[\frac{{}_nE_F - E_F}{k_BT}\right] \tag{6.9}$$

Here n_0 is the equilibrium (dark) density of free electrons that depends on E_F, the equilibrium (dark) Fermi energy determined by the I^-/I_3^- redox couple. The photovoltage is given by $U_{photo} = q({}_nE_F - E_F)$. For small changes in the photovoltage ($\delta U_{photo} << U_{photo}$), it can be shown that the decay of the photovoltage is a linear function of the total electron density [15] (recall section 3.3.2). Linearisation of the decay kinetics allows definition of an effective first order electron lifetime, τ_n. As shown in section 3.3.2, if the recombination of photogenerated electrons with I_3^- is second order in electron concentration, the effective electron lifetime is inversely proportional to the steady-state electron concentration (recall the equation (3.56)).

6.3 Results and Discussion

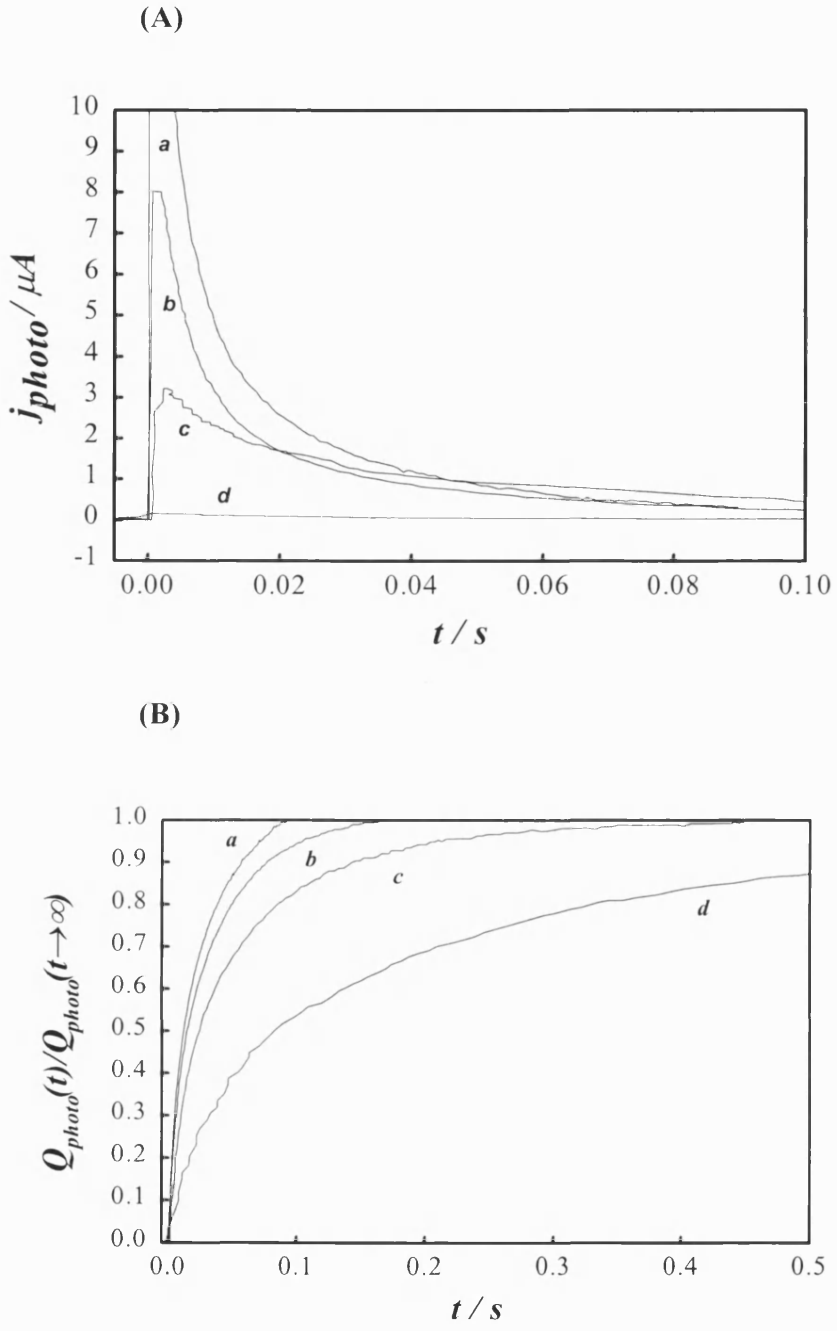

Figure 6.4 *(A) Photocurrent transients for different dc illumination intensities (Photocurrent densities have given in μA cm-2): (a) 71, (b) 43, (c) 25, (d) 3.6.* ***(B)*** *Photocharge transients corresponding to the photocurrent transients in* ***(A)****.*

Figure 6.4(A) shows photocurrent transients obtained at different dc illumination levels. The influence of the dc illumination is clearly apparent as at higher intensities the photocurrent decays faster. This indicates that at higher light intensities, the electron collection is rapid. This shows that the electron diffusion coefficient, D_n is intensity dependent. The photocharge transients corresponding to the photocurrent transients shown in Figure 6.4(A) are depicted in Figure 6.4(B).

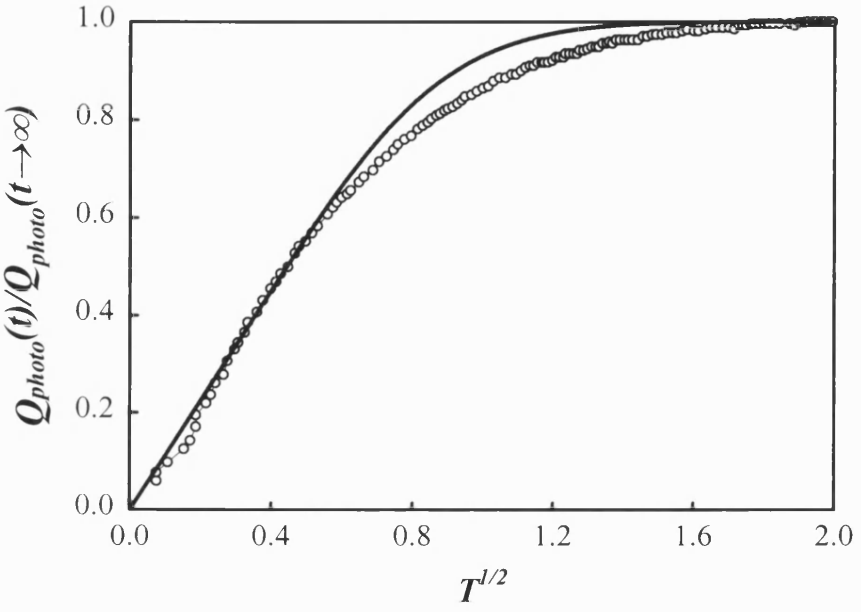

Figure 6.5 *Typical normalised charge plot illustrating the fit to the linear part used to derive the electron diffusion coefficient.*

Figure 6.5 illustrates an example of $Q_{photo}(t)/Q_{photo}(t\rightarrow\infty)$ vs $T^{1/2}$, which corresponds to the integrated Cottrell equation (c.f. equation 6.5). The value of electron diffusion coefficient, D_n can be estimated from the slope of the plot. This value of D_n can now be used to obtain a fit of the entire charge transient. This is done by noting that the reduced

time $T = \frac{tD}{d^2}$, where d is the thickness of the film. For this particular dc illumination intensity, the electron diffusion coefficient obtained from the fit shown is 2.4 x 10^{-6} cm^2 s^{-1}. The same procedure was used to obtain D_n values for a range of dc illumination intensities. The observed intensity dependent D_n values are summarised in Figure 6.6. The power law dependence of $D_n \propto I_o^{0.68}$ derived from the slope of the plot of the D_n versus j_{dc} (illumination intensity) is in excellent agreement with the results obtained using intensity modulated photocurrent spectroscopy reported in chapter 5 [5-7].

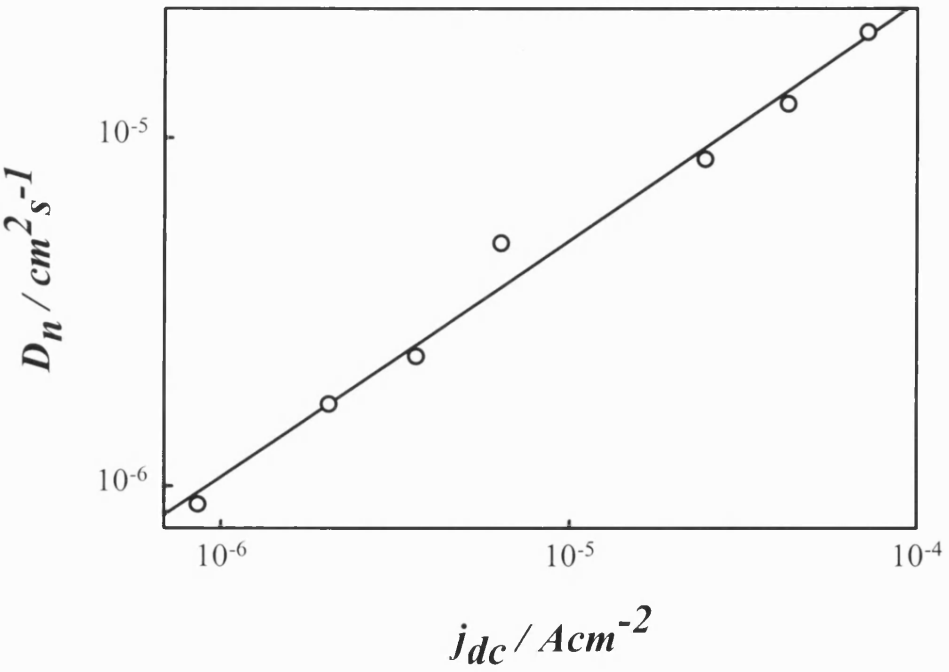

Figure 6.6 *Experimental dependence of electron diffusion coefficient on dc short circuit photocurrent density, j_{dc}. (Since the IPCE is constant, j_{dc} is linearly proportional to light intensity).*

A linear and semi-logarithmic representation of typical photovoltage transients is shown in Figure 6.7. It can be seen that the photovoltage decays more steeply at short times. This can be explained as follows. Since the initial electron density profile is determined

by the Beer Lambert law, $n(x) = n_{x=0}e^{-\alpha x}$, the electron concentration will be highest near the substrate electrode. After the laser pulse, the electron profile will relax by diffusion of electrons towards the bulk. So the rapid relaxation of the initial electron density profile by diffusion may be the reason for the steep photovoltage decay at short times. A similar influence of transport has been previously predicted and detected in several studies [16].

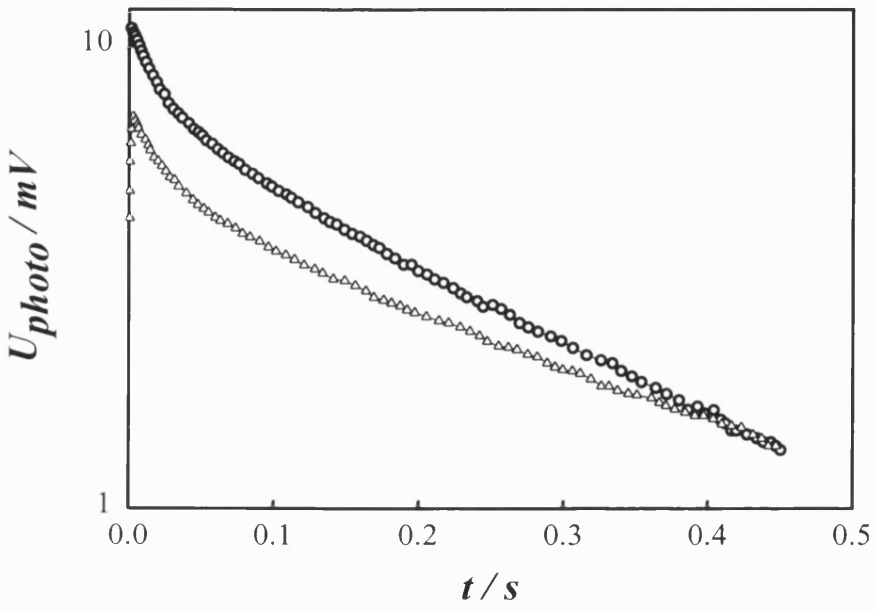

Figure 6.7 *Typical voltage photovoltage transients at different light intensities.*

Figure 6.8 shows how τ_n varies with dc light intensity. The slope of the double logarithmic plot is –0.62. This slope is higher than the slope of the similar plot (-0.51) obtained previously by IMVS (see Figure 5.8 of chapter 5), but the trend is identical. It follows from the present results that the electron diffusion length, $L_n = (D_n \tau_n)^{1/2}$ is only weakly intensity dependent. Interestingly, this confirms the conclusion of a weak intensity dependence of the electron diffusion length obtained using modulated illumination in chapter 5 [5-7].

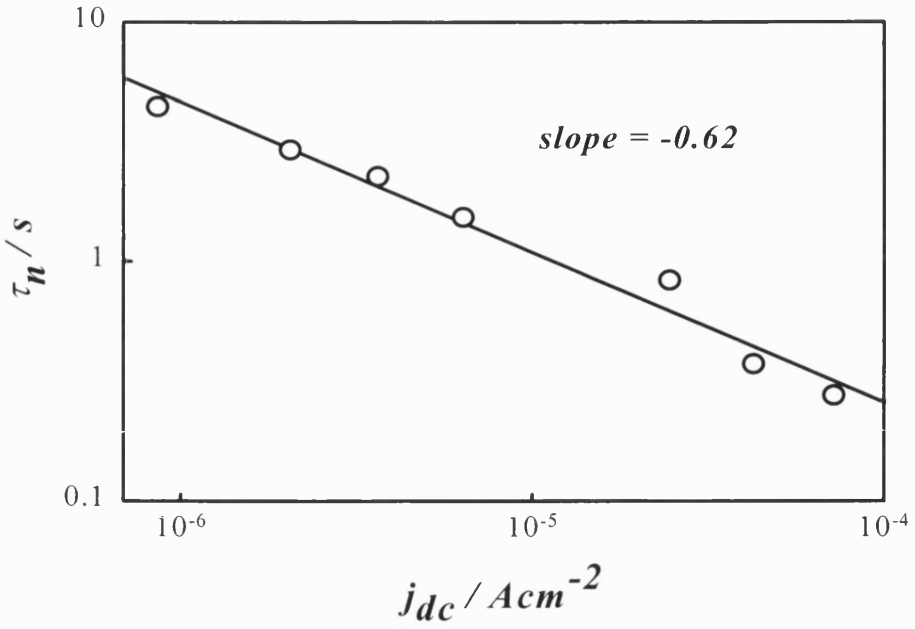

Figure 6.8 *Experimental dependence of electron lifetime on the dc short circuit photocurrent density, j_{dc}.*

6.4 Conclusions

The present work has demonstrated that linearisation of the photocurrent and photovoltage response of dye sensitised nanocrystalline cells can be achieved. The key feature of the present study is the use of small perturbations of electron density superimposed on a larger steady state condition. The results confirm the conclusions reached in chapter 5 that the electron diffusion coefficient, D_n and the electron lifetime, τ_n are functions of light intensity, whereas the electron diffusion length, L_n is only weakly intensity dependent. This unusual feature of the Grätzel cell explains why the IPCE is almost independent of illumination intensity.

6.5 References

1. B. O'Regan and M. Gratzel, Nature 353:737 (1991).
2. M. Gratzel, Coordination Chemistry Reviews 111:167 (1991).

3. M. K. Nazeeruddin, P. Liska, J. Moser, N. Vlachopoulos, and M. Gratzel, Helvetica Chimica Acta 73:1788 (1990).
4. M. K. Nazeeruddin, A. Kay, I. Rodicio, R. Humphrybaker, E. Muller, P. Liska, N. Vlachopoulos, and M. Gratzel, Journal of the American Chemical Society 115:6382 (1993).
5. L. M. Peter and K. G. U. Wijayantha, Electrochemistry Communications 1:576 (1999).
6. A. C. Fisher, L. M. Peter, E. A. Ponomarev, A. B. Walker, and K. G. U. Wijayantha, Journal of Physical Chemistry B 104:949 (2000).
7. L. M. Peter and K. G. U. Wijayantha, Electrochimica Acta 45:4543 (2000).
8. A. Kay, R. Humphrybaker, and M. Gratzel, Journal of Physical Chemistry 98:952 (1994).
9. A. Solbrand, A. Henningsson, S. Sodergren, H. Lindstrom, A. Hagfeldt, and S. E. Lindquist, Journal of Physical Chemistry B 103:1078 (1999).
10. J. Nelson, Physical Review B-Condensed Matter 59:15374 (1999).
11. L. Dloczik, O. Ileperuma, I. Lauermann, L. M. Peter, E. A. Ponomarev, G. Redmond, N. J. Shaw, and I. Uhlendorf, Journal of Physical Chemistry B 101:10281 (1997).
12. L. M. Peter and D. Vanmaekelbergh, in Advances in Elecrochemical Science and Technology (R. C. Alkire and D. M. Kolb, eds.), VCH Wiley, 1999.
13. S. Sodergren, A. Hagfeldt, J. Olsson, and S. E. Lindquist, Journal of Physical Chemistry 98:5552 (1994).
14. W. R. Heinemann and P. T. Kissinger, Laboratory Techniques in Electroanalytical Chemistry, Marcel Dekker, New York, 1984.
15. G. Franco, J. Gehring, L. M. Peter, E. A. Ponomarev, and I. Uhlendorf, Journal of Physical Chemistry B 103:692 (1999).
16. F. Cao, G. Oskam, G. J. Meyer, and P. C. Searson, Journal of Physical Chemistry 100:17021 (1996).

Chapter 7

Characterisation of Dye-sensitised Nanocrystalline TiO_2 Solar Cells by the Charge Extraction Technique

7.1 Introduction

In the DSN TiO_2 solar cell the photoinjected electrons reach the SnO_2 substrate by trap controlled diffusion through the TiO_2 network [1-4]. As described in Chapter 5, the time required for this diffusion process depends upon the illumination intensity. At very low light intensities, the charge collection in a cell with a typical thickness TiO_2 film (i.e. 10 microns), can take several minutes, whereas at solar intensities it requires only several milliseconds [1, 2, 5-8]. One remarkable feature of the optimised DSN TiO_2 solar cell is, in spite of this slow transport process, almost all the photogenerated electrons are collected at the SnO_2 substrate. Therefore, the back reaction of photogenerated electrons with I_3^- must be very slow at the TiO_2/electrolyte interface compared with that at the platinum counter electrode. This indicates that the performance of the cell depends on differential electron transfer kinetics. The observed weak intensity dependence of IPCE and intensity dependence electron diffusion coefficient, D_n in DSN TiO_2 solar cells (recall the results in chapter 5) implies that the photogenerated electrons travel more slowly at low light intensities, but at the same time they back react with I_3^- even more slowly [6, 7]. However, these conclusions have been reached using small amplitude perturbations of the illumination intensity that are either periodic (intensity modulated photocurrent or photovoltage spectroscopy [6, 7]) or pulsed [8]. In these techniques, the small amplitude perturbations are superimposed on a much larger steady-state illumination component to ensure that the systems can be linearised (recall section 3.2).

Undoubtedly, small amplitude modulation techniques are more powerful than steady-state techniques as they can be used to obtain kinetic information for systems of interest (i.e. the dye-sensitised TiO_2 PEC cell). However, there is also speculation that small

amplitude methods linearise the system response in a way that may obscure the electron transfer mechanism and kinetics [11, 12]. One purpose of the present study is to investigate how far the newly developed large amplitude charge extraction method provides information about the electron transfer mechanism and kinetics of the back reaction of photogenerated electrons with I_3^- in the DSN TiO_2 solar cell. Another purpose of the present work is the comparison of kinetic information obtained from the charge extraction technique and small amplitude methods. Section 7.3 of this chapter deals with this comparison. A detailed description of this newly developed large amplitude charge extraction technique is given in the section 4.12 where it is also discussed the experimental details.

7.2 Results and Discussion

Initially the DSN TiO_2 solar cell is in the potentiostatic mode in the dark and just before illuminating the cell, it is switched to the open circuit mode. When the light emitting diode is switched on, the photovoltage quickly attains a steady-state value close to 700 mV (the corresponding incident photon flux for illumination by the LED is 9.22×10^{15} cm^{-2} (3.9 mW cm^{-2})). The illumination area and the TiO_2 film thickness of the cell is 0.25 cm^2 and 18 μm respectively. When the LED was switched off, the photovoltage starts to decay. The decay occurs over a period of seconds and is very reproducible. The experiment was repeated in a way that the decay curve was interrupted at different delay times, t_d, by switching the DSN TiO_2 solar cell from open circuit mode to short circuit mode. These interrupted points are illustrated on the trace in Figure 7.1 by the vertical lines where the voltage falls to zero.

When the DSN TiO_2 solar cell was switched from galvanostatic mode (open circuit) to potentiostatic mode (short circuit) at different time intervals along the photovoltage decay curve (i.e. Figure 7.1), relevant current transients were observed. However, the quantity of interest in the present work was the amount of excess charge (i.e. excess electrons) in the dye-sensitised TiO_2 film. Therefore, the output of the current amplifier is simultaneously integrated using an operational amplifier for a period of 3 s. By doing

this, a set of charge transients relevant to each delay time was obtained. Figure 7.2 illustrates a family of such charge transients that were obtained for different delay times.

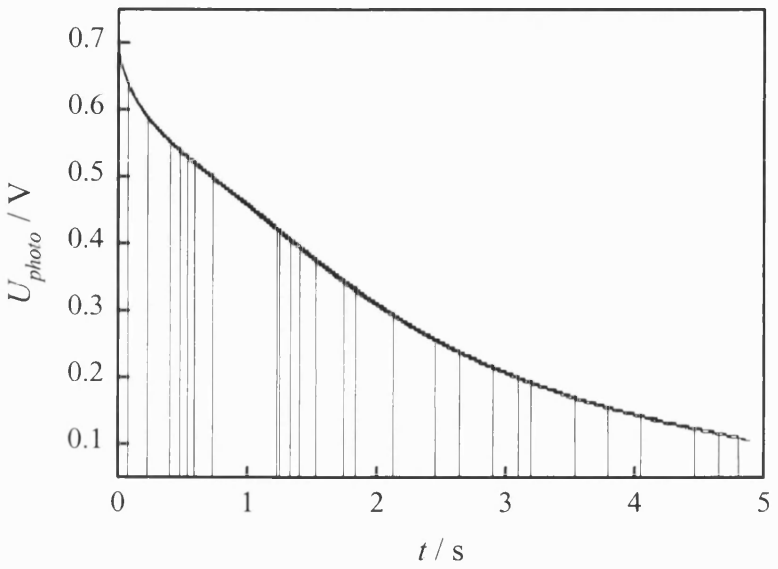

Figure 7.1 *Time-dependent photovoltage decay curves for a DSN TiO_2 solar cell illuminated from the substrate side for 550 ms at 470 nm. The vertical lines indicate the points at which the cell was short-circuited after a delay time, t_d to extract the remaining charge.*

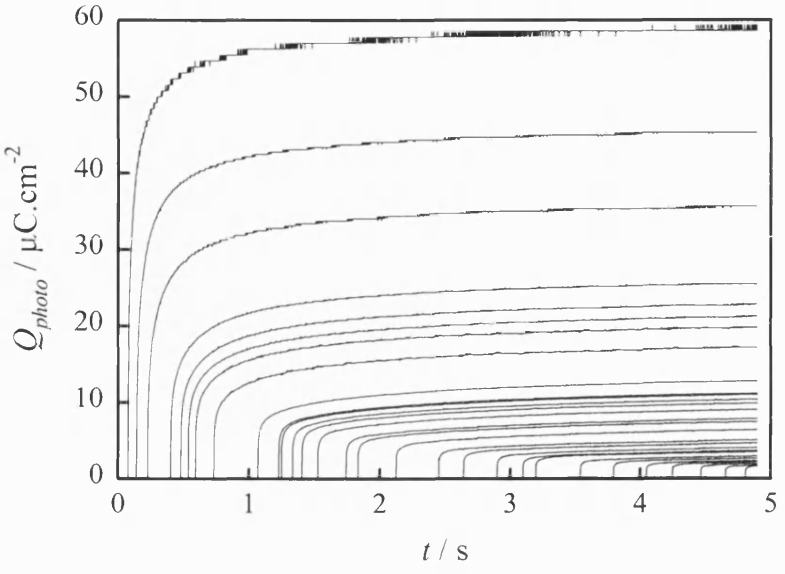

Figure 7.2 *Corresponding charge-extraction transients for the DSN TiO_2 cell.*

By switching to the potentiostatic mode from the galvanostatic mode immediately after the interruption of the illumination, it was found that the total excess electron charge in the cell under photostationary condition was 5 x 10^{-2} C cm^{-3} (which is equivalent to 90 μC cm^{-2} for 18 micron TiO_2 film). Figure 7.2 illustrates the charge extraction transients corresponding to time-dependent photovoltage curves given in Figure 7.1. Figure 7.3 shows how the extracted charge varied with delay time. The charge per unit volume has been calculated by taking into account the illuminated area of the cell (0.25 cm^2) and the film thickness (18 μm).

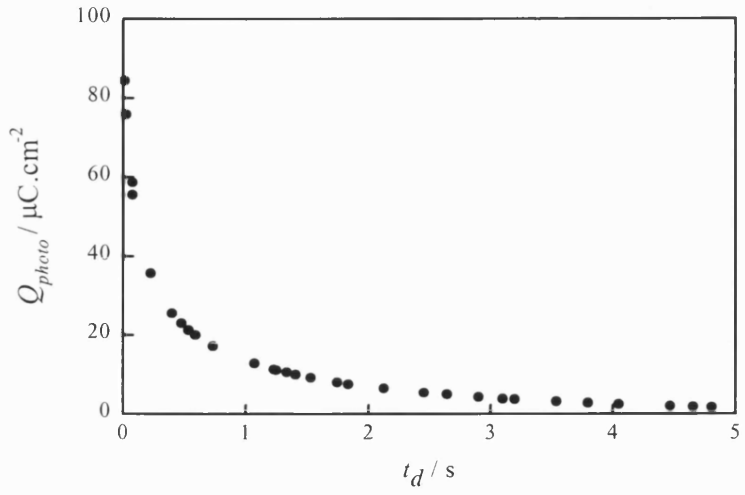

Figure 7.3 *Extracted photocharge as a function of delay time for the DSN TiO_2 cell.*

Figure 7.4 shows the $1/Q_{photo}$ vs t_d plot from t = 0 s to t = 5 s. To make it clearer, the U_{photo} decay curve at open circuit is also indicated in Figure 7.4. Notably, the $1/Q_{photo}$ vs t_d plot deviates positively from linearity beyond the delay time, t_d = 2 s. As this positive deviation of $1/Q_{photo}$ could result from losing some amount of extracted excess electrons at long delay times, it is important to consider the factors that could influence the charge extraction at long delay times.

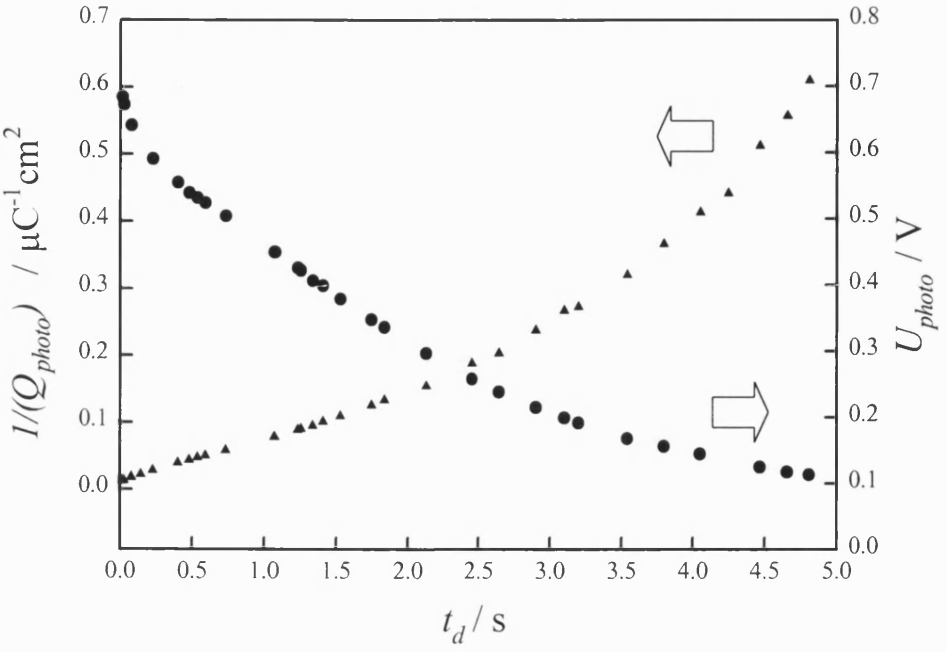

Figure 7.4 *The behavior of $1/Q_{photo}$ with decay time, t_d from $t = 0$ s to $t = 5$ s. The plot deviates from linearity after $t = 2$ s possibly indicating an underestimation of the extracted charge. To make it clearer, the U_{photo} decay curve at open circuit is also indicated here.*

As far as the amount of extracted charge is concerned, three important questions arise. The first is, how long a current transient can be integrated to obtain reliable charge data? As the time required to collect electrons in deep trap states may exceed the integration time (3 s in the present study), longer integration times may be required to collect all the relevant photogenerated electrons. The second question is, how does the back reaction of photogenerated electrons with I_3^- affect the amount of extracted charge? Some photogenerated electrons could possibly be lost due to back reaction with I_3^- while they are on the way to the SnO_2 substrate. When the delay time is longer, the number of electrons that are lost due to the back reaction could be higher, as the electron diffusion length could become less than the TiO_2 film thickness (i.e. at small excess electron concentrations). As described in Figure 7.10, the back reaction effect may be

considerable in cells made with thick TiO_2 films (In fact, the TiO_2 film thickness of the cell used in the present study was 18 μm). The charge extraction was done during the first 3 s in short circuit mode and was used in the subsequent analysis without making any correction. This could be a reason for the observed positive deviation of the $1/Q_{photo}$ vs t_d plot from linearity beyond 2 s delay time. Finally the third question is, does all the extracted charge in short circuit mode come purely from the TiO_2 film? Obviously, an excess amount of charge due to the discharging of the SnO_2 substrate ($Q_{substrate}$) was also extracted in short circuit mode. An estimate suggests that the required correction for $Q_{substrate}$ is about 8%, and it has been neglected in the present analysis (please refer to section 7.4 for more details of this estimation where it is discussed the possible sources of error in this method).

Figure 7.5 illustrates the $1/Q_{photo}$ vs t_d plot (from t_d = 0 to 2 s). As already explained in the region where t_d = 0 to 2 s back reaction effect could be minimal. At open circuit, the decay of the total electron concentration in the film is determined by the rate of the back reaction

$$I_3^- + 2e^- \rightarrow 3I^- \qquad (7.1)$$

If the rate of the back reaction with respect to electron concentration is first-order (the simplest case), the decay in the electron concentration should be exponential. If, on the other hand, the back reaction is second-order with respect to electron concentration, the decay should be hyperbolic, and the plot of $1/Q_{photo}$ vs t_d should be linear (note that in both cases, this conclusion is only valid if the rate constants are independent of mean electron energy (i.e. of electron quasi-Fermi level)). The observed linearity of the $1/Q_{photo}$ vs t_d plot in the delay time region where photo-injected electrons lost due to back reaction could be neglected, suggests that the rate of the back reaction could be second-order with respect to the electron concentration. The slope of the plot gives the second-order rate constant k = 6.5 x 10^4 C^{-1} cm^2 s^{-1}. By considering the TiO_2 film thickness (18 μm), the rate constant can be converted to conventional units and it is found that k = 1.9 x 10^{-17}

$cm^3\ s^{-1}$ which is equivalent to 1.1 x $10^4\ dm^3\ mol^{-1}\ s^{-1}$. Therefore, the rate of the back reaction can be written as follows

$$\frac{dn}{dt} = kn^2\left[I^-\right]^a\left[I_3^-\right]^b\left[Li^+\right]^c \tag{7.2}$$

where a, b and c are the reaction orders with respect to I^-, I_3^- and Li^+ concentrations of the electrolyte respectively. Here, the term n^2 represents the second order back reaction kinetics with respect to electron concentration. Interestingly, the observed second order dependence of the decay rate on electron density is consistent with the results obtained from small amplitude methods and the proposed back reaction mechanism in section 5.3, which involves the formation of $I_2^{\bullet-}$ as an intermediate.

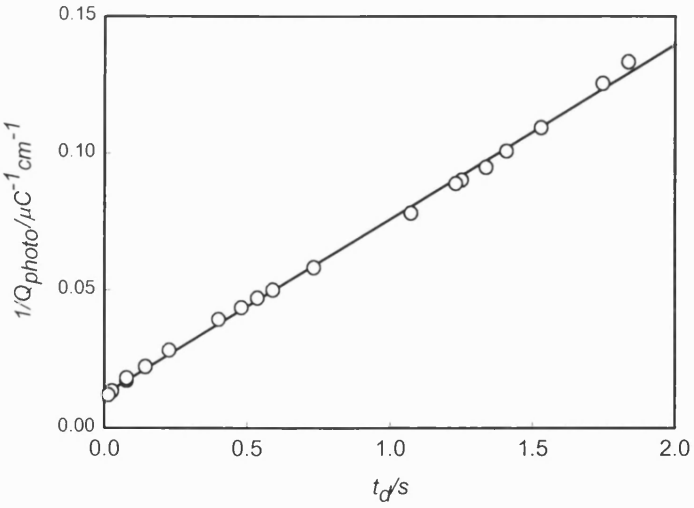

Figure 7.5 *The behavior of $1/Q_{photo}$ with delay time in the region where electron lost due to back reaction could be neglected*

The charge extraction method also provides a direct link between the total stored charge density and the photovoltage, U_{photo}. Under conditions where the majority of electrons are located in trapping states (recall Figure 7.8), the charge is given by

$$Q_{photo} \approx Q_{trap} = \int_{E_F}^{{}_nE_F} N_{trap}(E)dE \tag{7.3}$$

Where N_{trap} (E) is the density of states function of traps (cm^{-3} eV^{-1}). The measured photovoltage is given by

$$qU_{photo} = {}_nE_F - E_F \tag{7.4}$$

The density of states function for electron traps as a function of energy is given by

$$N_{trap}(qU_{photo}) = \frac{1}{q}\frac{dQ_{photo}(U_{photo})}{dU_{photo}} \tag{7.5}$$

Therefore, the density of states function can be obtained by differentiating the plot of $Q(t)$ versus $U_{photo}(t)$ obtained by the series of measurements illustrated in Figure 7.1. Figure 7.6 shows the density of states that was obtained for the DSN TiO_2 cell. From Figure 7.6, it is clear that the density of states decreases exponentially with the trap depth.

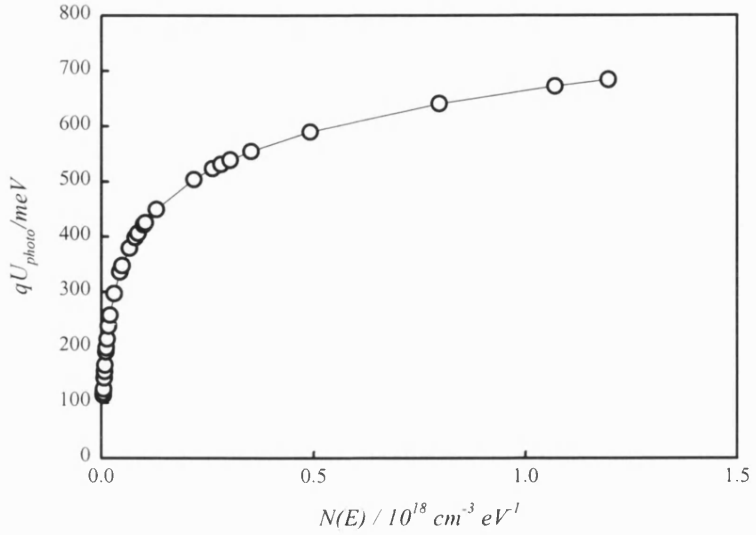

Figure 7.6 *Density of states functions for electron traps for the DSN TiO_2 cell derived by fitting the electron charge as a function of photovoltage and taking the derivative with respect to electron energy.*

7.3 Comparison of Kinetic Information obtained from the Charge Extraction Technique and Small Amplitude Methods

The back reaction of the same cell was also studied by intensity modulated photovoltage measurements and the electron lifetime was determined from the angular frequency of the minimum in the semicircular IMVS response as described in chapter 5. The electron lifetime for the second-order case under these conditions can be derived by the expansion and linearisation of the response for small perturbations. In this small amplitude limit, τ_n is given by

$$\tau_n = \frac{1}{2kn} \tag{7.6}$$

where k is the second order rate constant and n is the electron concentration. Equation (7.6) allows τ_n to be calculated as a function of n using the value k obtained from the $1/Q_{photo}$ vs t_d plot. For a second order electron decay, the steady-state electron density at

open circuit is expected to vary with the square root of the light intensity (recall section 5.3). Therefore, if the IPCE is constant, τ_n should decrease with the inverse square root of the short circuit photocurrent. The calculated variation of τ_n with short circuit photocurrent is compared with values determined by IMVS. Figure 7.7 compares the τ_n values measured by IMVS with the behavior calculated from the second order rate constant derived from charge extraction measurements.

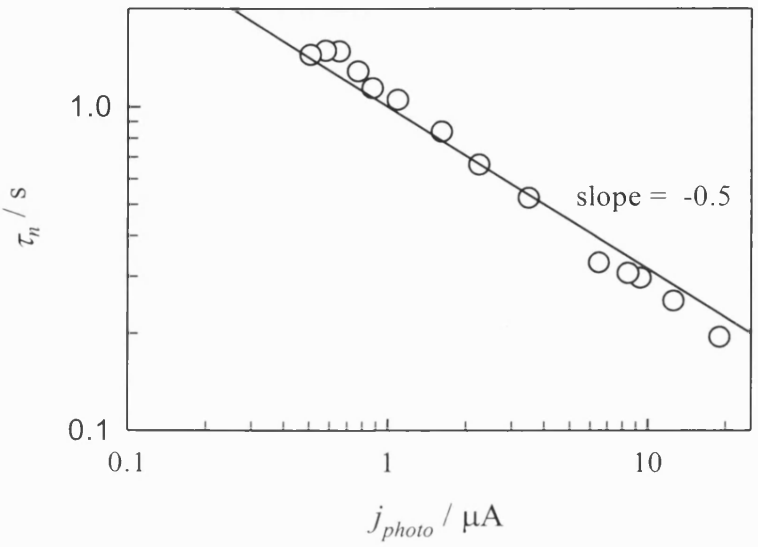

Figure 7.7 *Comparison of electron lifetimes measured by IMVS (**open circles**) with the behavior calculated from the second-order rate constant derived from charge-extraction measurements (**line**). Second-order kinetics gives rise to an inverse square root dependence of τ_n on the photon flux (or short circuit current), provided that IPCE is almost constant. This corresponds to the slope of –0.5 in the double logarithmic plot observed experimentally.*

It is clear that the electron lifetime values determined by IMVS correspond closely to the values calculated from the second order rate constant equation (7.6). However, the slope of the IMVS plot is slightly higher than the value of –0.5 that would be expected for

second order kinetics. This slight difference may indicate that electron occupancy exerts a weak but measurable effect on the rate constant for back electron transfer.

7.4 Sources of Errors

As far as the amount of extracted charge is concerned, three sources of error must be taken into account. The first error arises from the fact that not all photogenerated carriers are extracted at short circuit mode because the time required to collect excess electrons in deep trapping states may exceed the integration period. In fact, the transit time for electrons to reach the SnO_2 substrate under short circuit condition depends on the electron quasi-Fermi level (i.e., on the trap occupancy). As the charge is extracted, the electron quasi-Fermi level goes down and the remaining excess charge in deep trapping states may take a time longer than the integration time (3 s in the present experiment) to reach the SnO_2 substrate. Figure 7.8 illustrates this situation. This may be one reason for the observed positive deviation in the $1/Q_{photo}$ vs t_d plot (Figure 7.4) from the second order behavior. However, taking into account the experimentally determined trap distribution, the amount of lost charge can be quantified and the required correction can be made at each reading (i.e. correct the individual readings considering the relevant electron quasi-Fermi level).

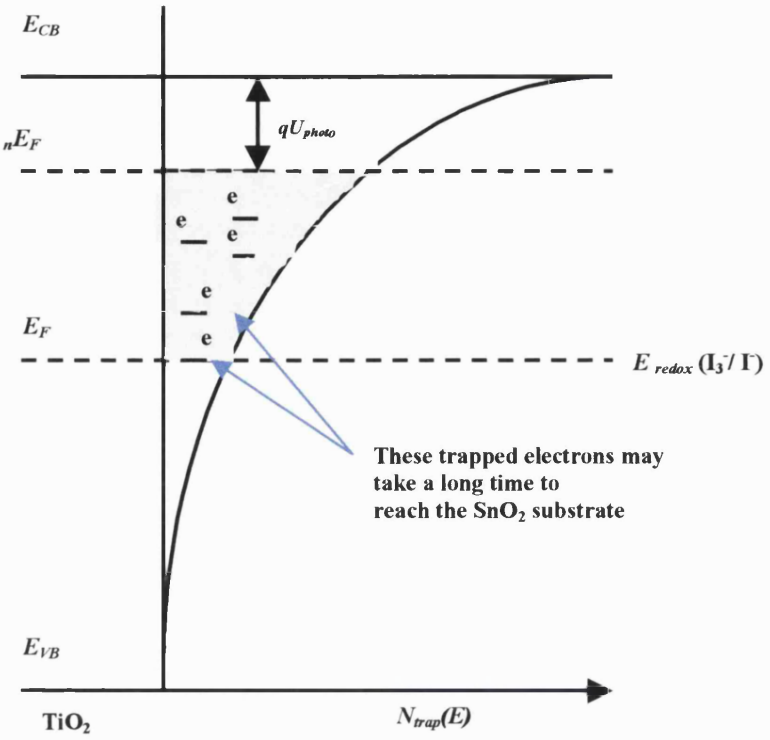

Figure 7.8 *As described here, when the electron quasi-Fermi level goes down and the remaining excess charge in deep trapping states may take a time longer than the integration time.*

The second problem is, electrons may back react with I_3^- before they reach the SnO_2 substrate. As the charge is extracted (i.e. as excess electron density falls in the TiO_2 film) the electron diffusion length, L_n decreases (recall Figure 5.9 in section 5.3). When the electron diffusion length becomes smaller than the film thickness, some fraction of the electrons will back-react before they reach the SnO_2 substrate. This will also lead to an underestimate of the extracted charge at long integration times. This could also be a reason for the observed positive deviation of the $1/Q_{photo}$ vs t_d plot from the second order behaviour (recall that the TiO_2 film thickness of this particular cell is 18 μm). However, for thin efficient cells this error is negligible (see Figure 7.10).

The third and most important source of error, associated with the extraction of the excess charge in the TiO_2 film is, the discharging of the SnO_2 coated substrate when the cell is switched from open circuit mode to short circuit mode. At open circuit the $SnO_2(F)$ substrate is also charged to some extent. When the cell is switched from open circuit mode to short circuit mode, the charged $SnO_2(F)$ substrate is discharged. Therefore, the operational amplifier integrator measures an excess amount of charge. By considering the $SnO_2(F)/TiO_2$ interface under open circuit and short circuit conditions, Figure 7.9 illustrates this situation.

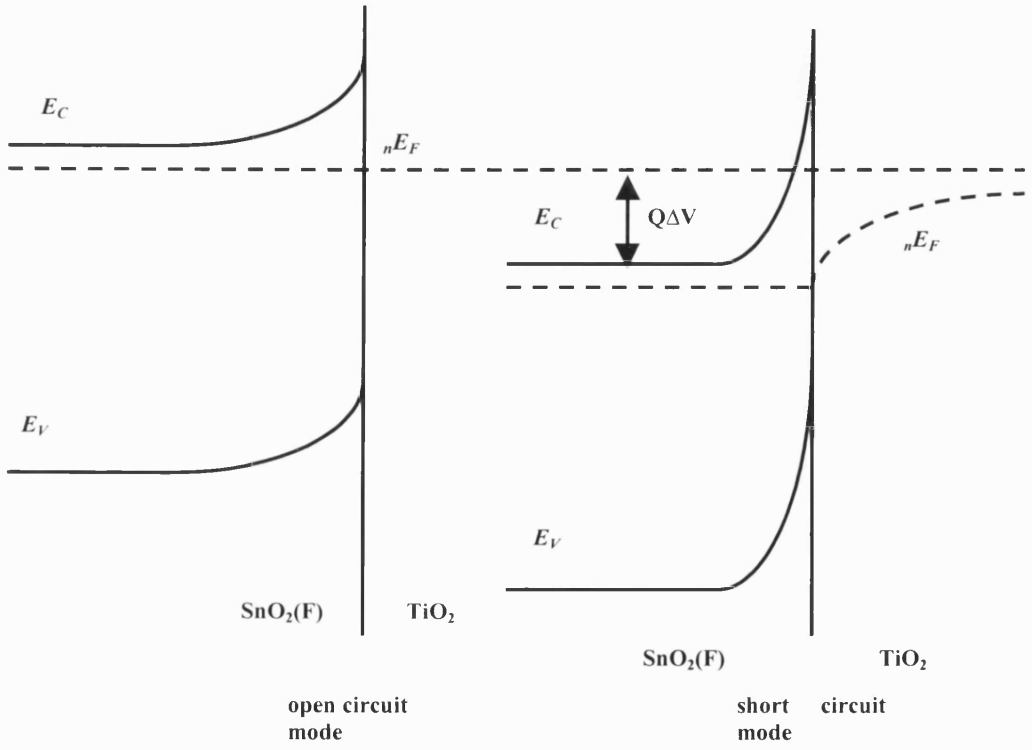

Figure 7.9 *When the cell is switched from open circuit mode to short circuit mode, the charged $SnO_2(F)$ substrate is discharged.*

This excess amount of charge is given by

$$Q_{(substrate)}(t) = \int_{Uphoto(t)}^{0} C_{sc}(U)dU \qquad (7.7)$$

where $C_{sc}(U)$ is the potential dependent space charge capacitance of the $SnO_2(F)$ substrate, $U_{photo}(t)$ is the time dependent photovoltage during the open circuit decay and the potentials are referred to the equilibrium potential of the I_3^-/I^- redox couple. Once the excess amount of charge is determined, the correction can be done as follows.

$$Q_{TiO_2}(t) = Q_{photo(observed)}(t) - Q_{substrate}(t) \qquad (7.8)$$

Here, the $Q_{substrate}$ is not detectable. For example, if the sheet resistance of SnO_2 substrate is 10 $\mu F\ cm^{-2}$ and the known measuring resistor is 100 Ω, the RC time constant of the electrochemical system is 1 ms. On the other hand, the transit time of an injected electron in an outermost TiO_2 particle in the film is about 10 ms (assuming that the diffusion coefficient is around $5 \times 10^{-5}\ cm^2\ s^{-1}$). Therefore, the RC time constant of the electrochemical system and the transit time of an injected electron in an outermost TiO_2 particle in the film are very close. This situation makes it very difficult to distinguish $Q_{substrate}$ from Q_{TiO2}.

However, it is considered that $C_{sc}(U)$ is typically of the order of 10 $\mu F cm^{-2}$ for the $SnO_2(F)$ substrate used in this study. This means that at t = 0, $Q_{substrate}$ is of the order of 10×10^{-6} F cm^{-2} x 0.7 V = 7 $\mu C\ cm^{-2}$. This is around 8% of the extracted charge (recall the total excess electron charge density in the cell under photostationary condition is 5×10^{-2} Ccm^{-3} which is equivalent to 90 $\mu C\ cm^{-2}$ for 18 μm TiO_2 film). For thin TiO_2 film cells, although the majority of TiO_2 phase electrons (Q_{TiO2}) are collected before they back react with I_3^-, $Q_{substrate}$ is considerable compared with Q_{TiO2}. In this case, the $1/Q_{photo}$ vs t_d plot can deviate negatively from second order behavior on a shorter time scale.

Figure 7.10 illustrates the possible deviations of the second order $1/Q_{photo}$ vs t_d plot due to all sources of error discussed in this section.

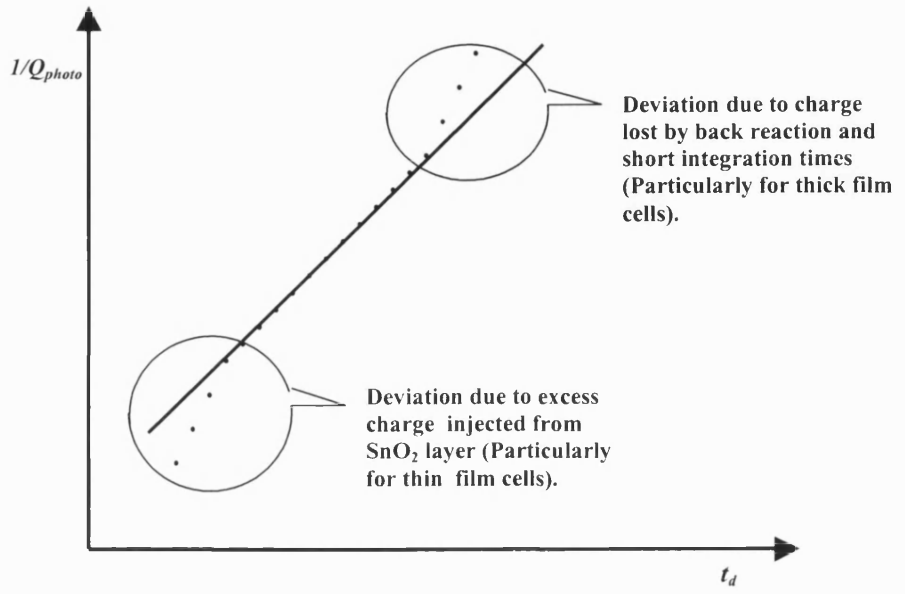

Figure 7.10 *The possible deviations of the second order $1/Q_{photo}$ vs t_d plot.*

7.5 Conclusions

The charge extraction method offers a new approach to the characterisation of DSN solar cells. It provides direct access to the electron density as a function of illumination intensity and decay time, so that the kinetics of the back reaction of photogenerated electrons with tri-iodide ions can be studied. The back reaction rate depends on the square of the electron density, suggesting second order kinetics. The calculated electron lifetime varies with the inverse square root of the illumination intensity (short circuit photocurrent). The values of τ_n determined experimentally by intensity modulation techniques agree well with the values calculated from the second order rate constant for the back reaction (k) the total electron concentration at open circuit in the dark (n).

The method also allows a direct correlation to be made between the photovoltage and the total electron density. Analysis of this relationship leads to the density of states function for trapping states. The distribution functions obtained in this way can be used to model trap-controlled electron transport in the nanocrystalline oxides.

7.6 References

1. F. Cao, G. Oskam, G. J. Meyer, and P. C. Searson, Journal of Physical Chemistry 100:17021 (1996).
2. L. Dloczik, O. Ileperuma, I. Lauermann, L. M. Peter, E. A. Ponomarev, G. Redmond, N. J. Shaw, and I. Uhlendorf, Journal of Physical Chemistry B 101:10281 (1997).
3. L. M. Peter, E. A. Ponomarev, G. Franco, and N. J. Shaw, Electrochimica Acta 45:549 (1999).
4. J. Nelson, Physical Review B-Condensed Matter 59:15374 (1999).
5. G. Schlichthorl, N. G. Park, and A. J. Frank, Journal of Physical Chemistry B 103:782 (1999).
6. L. M. Peter and K. G. U. Wijayantha, Electrochemistry Communications 1:576 (1999).
7. A. C. Fisher, L. M. Peter, E. A. Ponomarev, A. B. Walker, and K. G. U. Wijayantha, Journal of Physical Chemistry B 104:949 (2000).
8. N. W. Duffy, L. M. Peter, and K. G. U. Wijayantha, Electrochemistry Communications 2:262 (2000).
9. G. Schlichthorl, S. Y. Huang, J. Sprague, and A. J. Frank, Journal of Physical Chemistry B 101:8141 (1997).
10. G. Schlichthorl, N. G. Park, and A. J. Frank, Zeitschrift Fur Physikalische Chemie-International Journal of Research in Physical Chemistry & Chemical Physics 212:45 (1999).
11. N. W. Duffy, L. M. Peter, R. M. G. Rajapakse, and K. G. U. Wijayantha, Journal of Physical Chemistry 104:8916 (2000).
12. N. W. Duffy, L. M. Peter, R. M. G. Rajapakse, and K. G. U. Wijayantha, Electrochemistry Communications 2:658 (2000).

Chapter 8

Studies of Dye Sensitised Solid-state Photovoltaic cells

8.1 Introduction

So far the present study has mainly considered dye sensitised nanocrystalline TiO_2 liquid junction solar cells. Section 1.7 of this thesis discuss the future prospects for dye sensitised nanocrystalline solar cells in detail including existing problems and strategies to overcome them. Section 1.7 also introduces solid state analogies of dye sensitised nanocrystalline solar cells. Clearly, most of the existing problems in DSN TiO_2 solar cells are due to the presence of the liquid electrolyte phase. Therefore, the obvious solution for these problems should be replacement of the troublesome liquid layer by a suitable solid material. Several attempts have been reported for filling the dye-coated porous TiO_2 nanocrystalline phase with a hole conducting material, but the power conversion efficiencies of these dye sensitised nanocrystalline solid state versions are still poor [1-13]. A solid electrolyte may not be a suitable candidate because of its low ionic mobility [1].

Alternative approaches to thin film cells involving the use of organic compounds [14] or of polymer materials [15, 16] have excited considerable interest since they offer the possibility of fine-tuning material properties via chemical substitution. In this type of device, charge generation/separation and transport occur at interfaces between different organic phases and in bulk phases respectively. However, a key feature that is responsible for the success of the dye sensitised nanocrystalline TiO_2 liquid junction solar cell is its use of a very high internal interfacial area to obtain efficient photosensitisation from only a monolayer of adsorbed dye. Clearly, any alternative solid state device based on photosensitisation should incorporate this strategy of improving efficiencies. A detailed introduction to the solid state versions of dye sensitised nanocrystalline solar cells is given in section 1.7. Attempts were made in the present study to replace the liquid electrolyte with suitable hole conducting media such as p-type semiconductors (see

Figure 1.8) and conducting polymers (either electronically or redox conducting polymers) (see Figure 1.9). The experimental details of these attempts are discussed in section 4.3. This chapter discusses the results of the characterisation of fabricated dye sensitised solid state devices.

8.2 Results and Discussion

Dye Sensitised Solid State Photovoltaic cells made with CuI as the p-type semiconductor

Figure 1.8 in chapter 1 shows the schematic representation of the photoexcited charge injection and transport mechanism in the n-type semiconductor (TiO_2)/dye (N3)/p-type semiconductor (CuI) photovoltaic device. In this device, the photoexcited dye molecules sandwiched between the two semiconductors inject electrons into the conduction band of the n-type semiconductor material. The regeneration takes place by injecting holes into the valence band of the p-type semiconductor material. It can be described by the following scheme.

$$D + hv \rightarrow D^* \tag{8.1}$$

$$D^* \rightarrow D^+ + e_{TiO_2(CB)} \tag{8.2}$$

$$D^+ \rightarrow D + h_{CuI(VB)} \tag{8.3}$$

The objective of the present work was to fabricate and characterise electron transport and back reaction in this n-type semiconductor (TiO_2)/dye (N3)/p-type semiconductor (CuI) photovoltaic cell. The photocurrent voltage characteristics of this type of solid state dye sensitised photovoltaic cell are shown in Figure 8.1. The fill factor is ~ 0.4 and the overall solar conversion efficiency is ~ 0.7%. The difficulties of achieving full

penetration of CuI into the dye coated porous TiO_2 network may be reflected in the poor fill factor. The poor fill factor may also be due to the resistance of the CuI film.

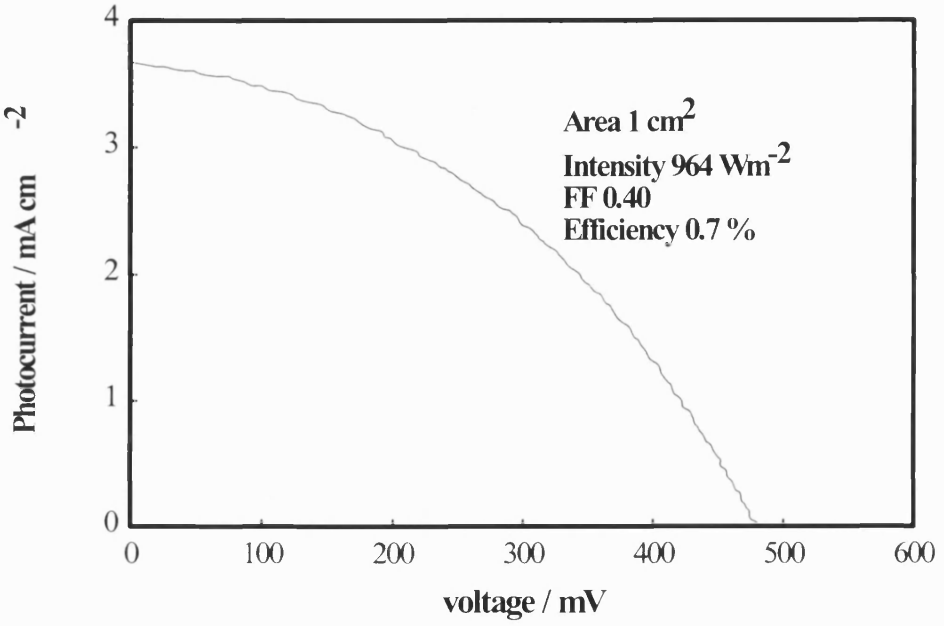

Figure 8.1 *Current-voltage characteristics of a dye sensitised solid state photovoltaic cell fabricated with p-type CuI semiconductor as the hole transport material.*

The semi logarithmic representation of the variation of IPCE with illumination intensity over 3 orders of magnitude in this dye sensitised solid state photovoltaic cell is illustrated in Figure 8.2. The IPCE at 470 nm is ~ 22% and it is low compared to dye sensitised

liquid electrolyte based cells for which the IPCE is about 70%. In fact, the IPCE of the cell hardly changes over the whole of the measured intensity range.

Despite the poor current-voltage characteristics and low IPCE, these types of cells can be used to investigate the electron transport properties and recombination kinetics. Therefore, these cells were characterised by intensity modulated photocurrent spectroscopy and intensity modulated photovoltage spectroscopy.

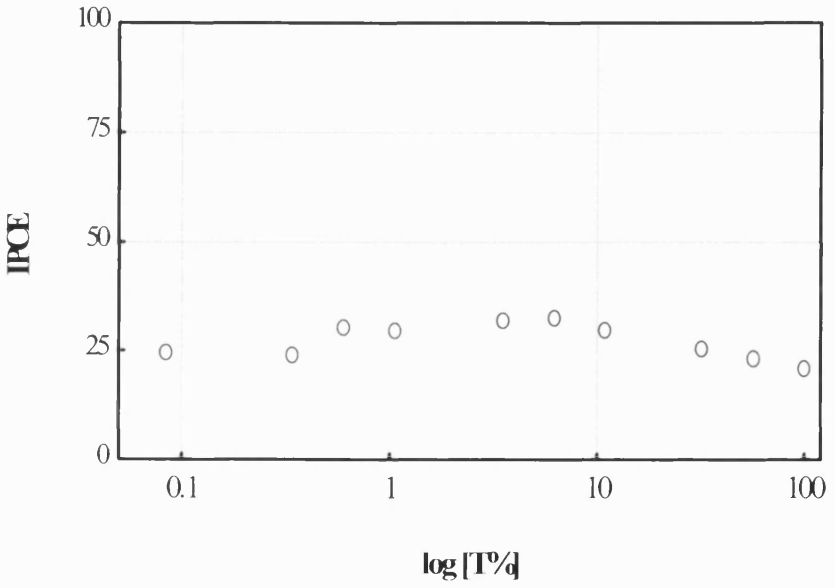

Figure 8.2 *Semilogarithmic representation of the variation of IPCE with light intensity over 3 orders of magnitude in a dye sensitised solid state photovoltaic cell fabricated with p-type CuI semiconductor as the hole transport material.*

Figure 8.3 illustrates typical examples of experimentally obtained IMPS response and IMVS response for dye sensitised solid state photovoltaic cells fabricated with p-type CuI

semiconductor as the hole transport material. Both IMPS and IMVS measurements resulted in two semicircles in the complex plane similar to the responses for liquid junction cells. However, a notable difference in IMPS and IMVS responses of dye sensitised solid state cells compared to that of the liquid junction counterpart is, the unusual behavior at low frequencies. This plots bend in before the low frequency response approaches the real axis. This may be due to the strong recombination.

In liquid electrolyte cells, at open circuit the IMVS phase lag is mainly associated with the relaxation of photoinjected electrons by back reaction with tri-iodide ions. However, the situation in dye sensitised solid state cells could be quite different due to the lack of full penetration of CuI in the porous TiO_2 phase. Therefore, in dye sensitised solid state cells, at open circuit the relaxation can take place either by electron recombination with valence band holes in the CuI phase or back electron transfer to oxidised dye molecules. The degree of penetration of CuI into the dye coated porous TiO_2 phase determines which process is dominant in the electron relaxation at open circuit. For example, if full penetration is achieved the main electron recombination route would be with valence band holes in CuI. On the other hand, if full penetration is not achieved a considerable number of photo-injected electrons would back react with oxidised dye molecules.

In the IMPS response at closed circuit, the phase lag arises mainly due to the delay time associated with electron transport from the injection site to the SnO_2 substrate, provided that the majority of photo-injected electrons are collected. If most photo-injected electrons are lost on their passage to the SnO_2 substrate, the IMPS phase lag determined by the electron lifetime. A rough estimate can be done to make sure whether the majority of photo-injected electrons collect at the SnO_2 substrate or are lost substantially on their passage to the SnO_2 substrate, if the degree of absorption can be measured accurately. However, TiO_2 films used in the fabrication of solid state dye sensitised solar cells are opaque and prevent accurate absorption measurements.

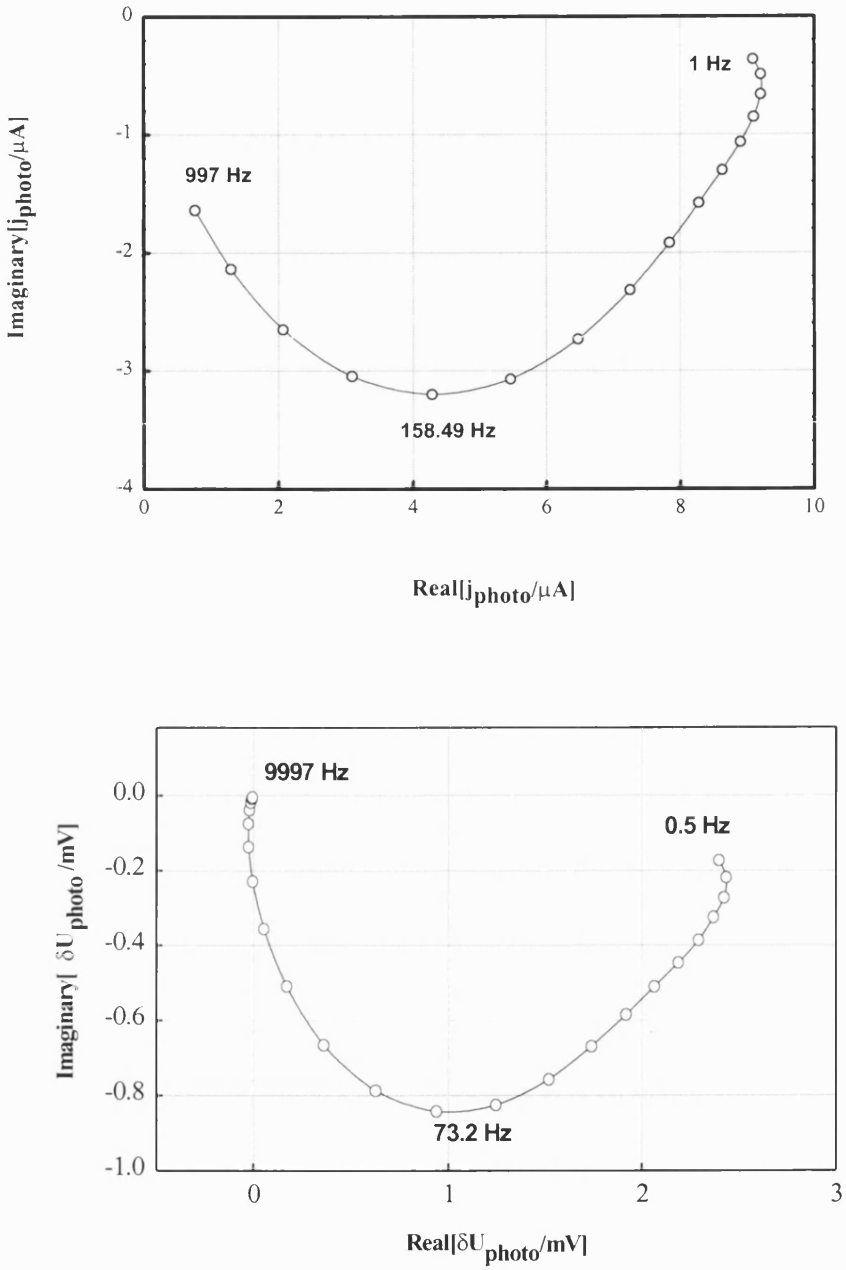

Figure 8.3 *A typical IMPS response (**upper**) and a typical IMVS response (**lower**) for a dye sensitised solid state photovoltaic cell fabricated with p-type CuI semiconductor as the hole transport material.*

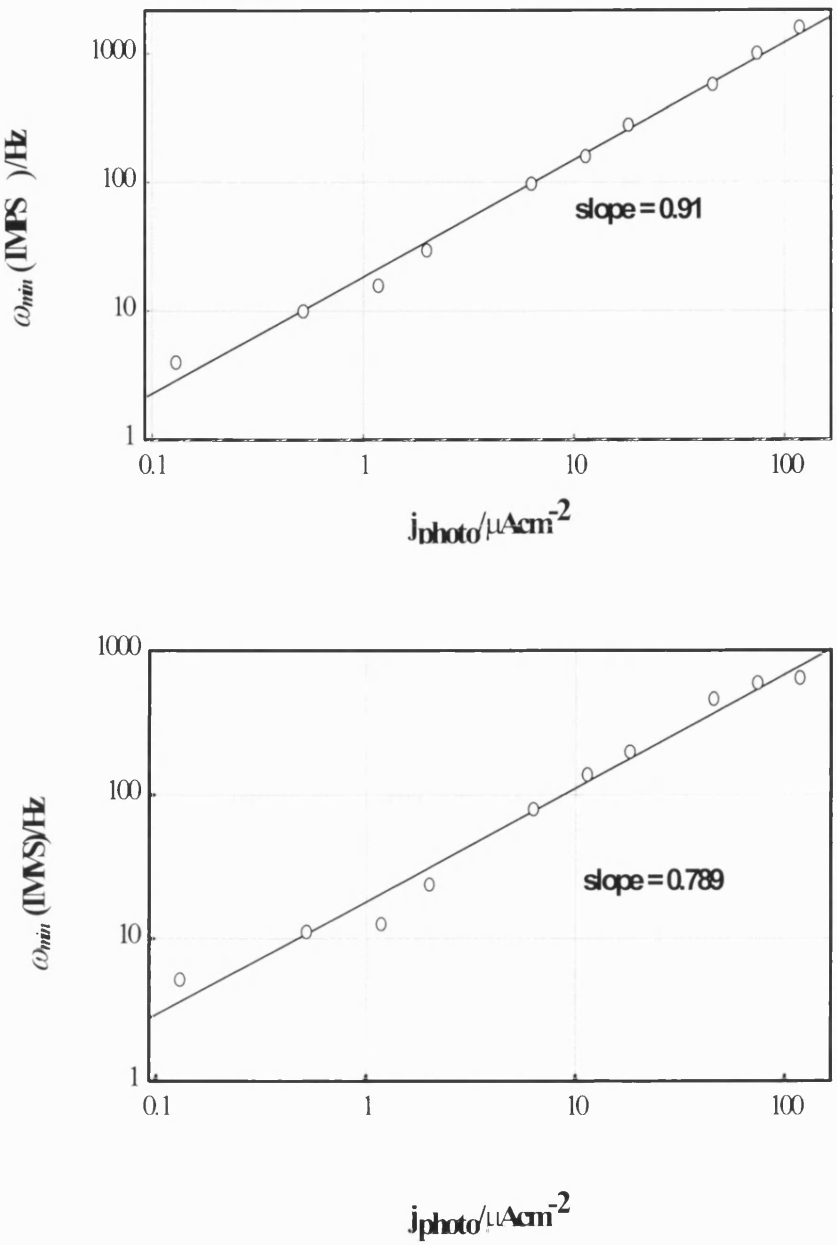

Figure 8.4 *Double logarithmic representation of variation of* ***(upper)*** ω_{min}*(IMPS) and* ***(lower)*** ω_{min}*(IMVS) with short circuit photocurrent in a dye sensitised solid state photovoltaic cell fabricated with p-type CuI semiconductor as the hole transport material.*

Figure 8.4 shows a double logarithmic representation of the variation of ω_{min}*(IMPS)* and ω_{min}*(IMVS)* with short circuit photocurrent in this CuI based dye sensitised solid state

photovoltaic cell. The variation of $\omega_{min(IMPS)}$ with short circuit photocurrent (i.e. with illumination intensity) indicates that the electron transport in the porous TiO_2 phase is dominated by trapping, leading to an intensity dependent apparent diffusion coefficient. For a typical dye sensitised liquid electrolyte cell, the $\omega_{min(IMPS)}$ (or electron diffusion coefficient) changes with the illumination intensity according to the power law relationship, $I_0^{0.68}$. However, for CuI based cells, the fall of $\omega_{min(IMPS)}$ with decrease of illumination intensity is more steep with a slope of 0.91 suggesting a strong trap dominant charge transport. Perhaps, this steep slope arises due to the effect of trap controlled limited hole transport in the CuI phase (also see Figure 1.8). To compare the electron diffusion coefficient value in this solid state device, a liquid junction cell was fabricated using a dye sensitised film identical to that used in the solid state cell. The IMPS measurements on this cell gave similar electron diffusion coefficient values to those shown by dye sensitised nanocrystalline liquid electrolyte cells. This means that the electron transport occurs in a similar time scale in both dye sensitised nanocrystalline liquid electrolyte cells and CuI based solid state cells. This shows that the observed strong intensity dependence of D_n in CuI based cells may be due to the trap controlled limited hole transport in the CuI phase (see Figure 1.8).

The intensity dependence of the electron lifetime, τ_n in liquid electrolyte cells is close to a square root dependence (recall Figure 5.8 in chapter 5) suggesting that the back reaction of photo-injected electrons with tri-iodide is second-order with respect to electron concentration. If the observed intensity dependence of τ_n in liquid electrolyte cells is a consequence of second-order back reaction kinetics in the iodide/tri-iodide redox couple, cells made with a one electron transfer redox system should not exhibit intensity dependent electron lifetimes. The electron lifetime in the CuI based solid state dye sensitised cell also varies with illumination intensity with a slope of 0.79 (see Figure 8.4). At this stage it is very difficult to make any conclusion based on the observed intensity dependence of electron lifetime in these cells without an extensive study. In fact, CuI is a well-known material for its ionic conduction properties. Therefore, the charge transport properties and recombination paths of these cells could be different from liquid electrolyte based dye sensitised solar cells.

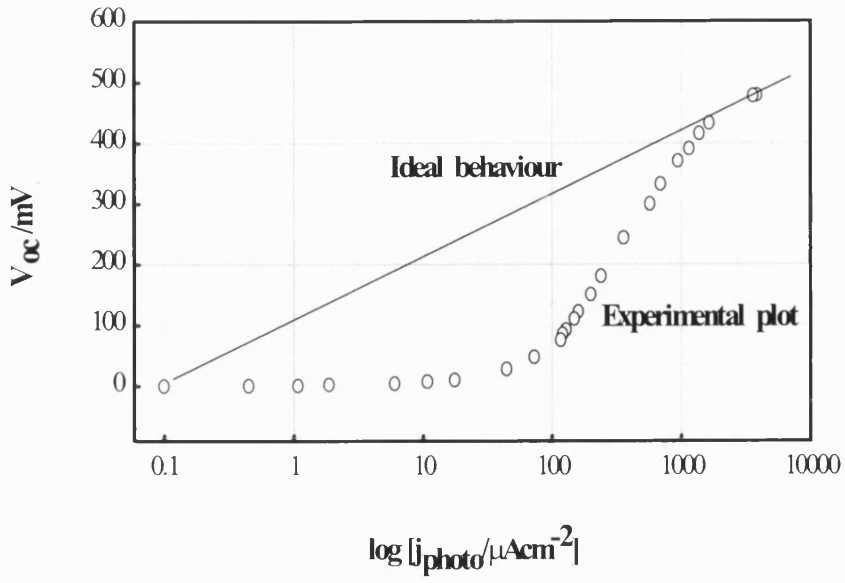

Figure 8.5 *Intensity dependence of the open circuit photovoltage for a dye sensitised solid state photovoltaic cell fabricated with p-type CuI semiconductor as the hole transport material.*

Figure 8.5 illustrates the photovoltage variation with short circuit photocurrent. The non-ideal intensity dependence of the photovoltage suggests that internal shunting may occur by direct contact between CuI and SnO_2(F). As with the liquid electrolyte counterpart, the photovoltage falls with a decrease of light intensity in this cell. However, the photovoltage fall in this cell is much more steep than that for the dye sensitised nanocrystalline liquid electrolyte cells. This means that the internal shunting between CuI and SnO_2(F) is substantial in this device. This is rather confusing as the observed low fill factor suggests poor penetration of the CuI phase into the porous TiO_2 network.

Dye sensitised Solid State Photovoltaic cells made with conducting polymers as hole transport materials.

Figure 8.6 shows the current-voltage plots for the TiO_2/N3 dye/PPV solid state device and the TiO_2/N3 dye/PVK solid state device. These plots indicate that these assemblies do not show photovoltaic characteristics although both devices exhibit measurable photovoltages (~ 400 mV). PPV and PVK are well-known for their hole conducting

properties [15-18]. Therefore, the problem of these devices may be that the HOMO-LUMO energy levels of PVK and PPV are mismatched with the N3 dye energy levels so that dye regeneration does not takes place.

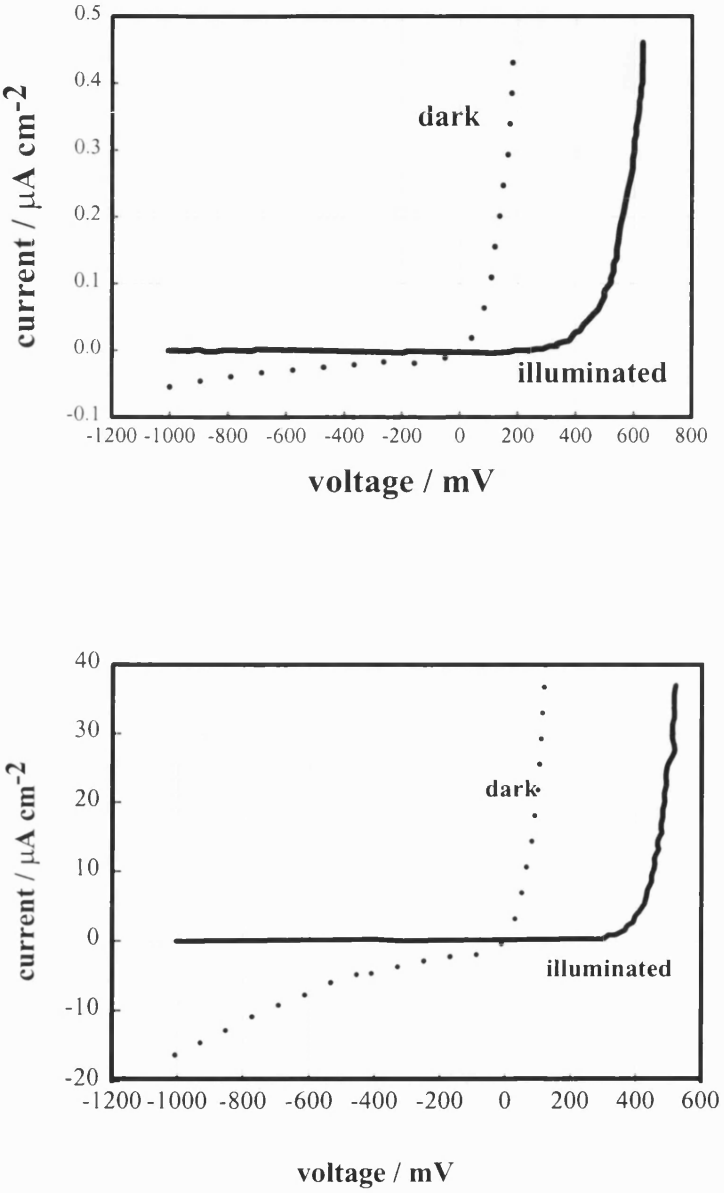

Figure 8.6 *Current-voltage characteristics under 1 sun illumination* ***(upper)*** *TiO_2/N3 dye/PPV assembly.* ***(lower)*** *TiO_2/N3 dye/PVK assembly.*

The dye sensitised solid state photovoltaic cells fabricated with PANI as the hole transport material show appreciable current-voltage characteristics under 1 sun illumination as shown in Figure 8.7. (During the current-voltage measurements an IR filter (1.5 cm water filter) was used to prevent heat effects). The light-induced charge transfer mechanism of this device can be explained as follows. Once the sensitiser dye gets excited it injects electrons into the conduction band (sensitisation). The resulting oxidised dye molecule relaxes back to the ground state by accepting an electron from partially oxidised PANI strands. The electron transport within the PANI phase may be due to a hopping type transport mechanism (see Figure 1.9).

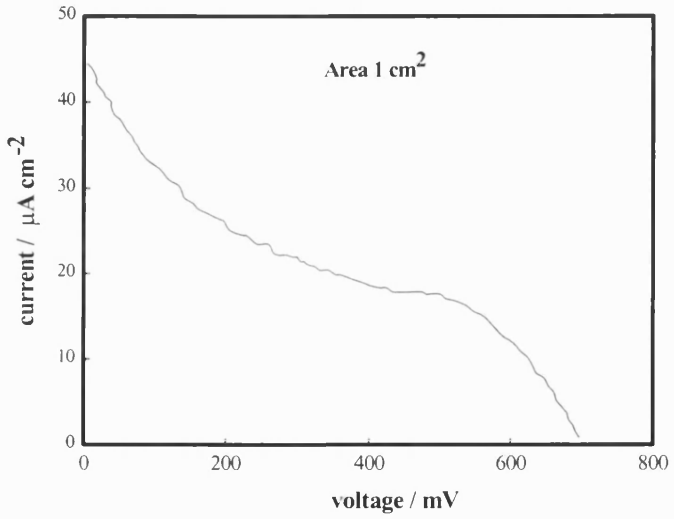

Figure 8.7 *Current-voltage characteristics of TiO_2/N3 dye/PANI photovoltaic cell under 1 sun illumination.*

The small photocurrent observed for this device is possibly due to the resistance of the poly(aniline) film. However, it is very difficult to understand the reason for the steep photocurrent drop at the beginning of the negative voltage polarisation (note that in the current-voltage plot, the cell voltage is shown instead of negative voltage polarisation).

Characterisation of this solid state device using IMPS is very difficult due to the small photocurrent. However, photogenerated charge recombination was studied by IMVS and Figure 8.8 shows a typical IMVS plot obtained for this solid state device. IMVS studies were also performed at different light intensities and interestingly it was observed that ω_{min}(IMVS) is an intensity dependent parameter. As shown in Figure 8.9, ω_{min}(*IMVS*) varies with illumination intensity with a slope of ~ 0.7. Poly(aniline) is well-known for its redox properties and there is no evidence for its ionic conductivity properties. Furthermore, the TiO_2 conduction band electron can recombine either with oxidised dye molecules or with oxidised PANI. So, the recombination of TiO_2 conduction band electrons could be a one electron transfer process provided that the recombination reaction between electrons and oxidised dye molecules are negligible. According to the argument brought in chapter 5, if the electron recombination is a simple one electron transfer process, the electron lifetime may not be changed with the electron density (light intensity). Therefore, the observed intensity dependent ω_{min}(*IMVS*) may be due to the variation of the electron transfer rate at different trapped electron energy levels (i.e. at different ${}_nE_F$ in TiO_2) as explained by Schlichthörl *et al.* [19, 20].

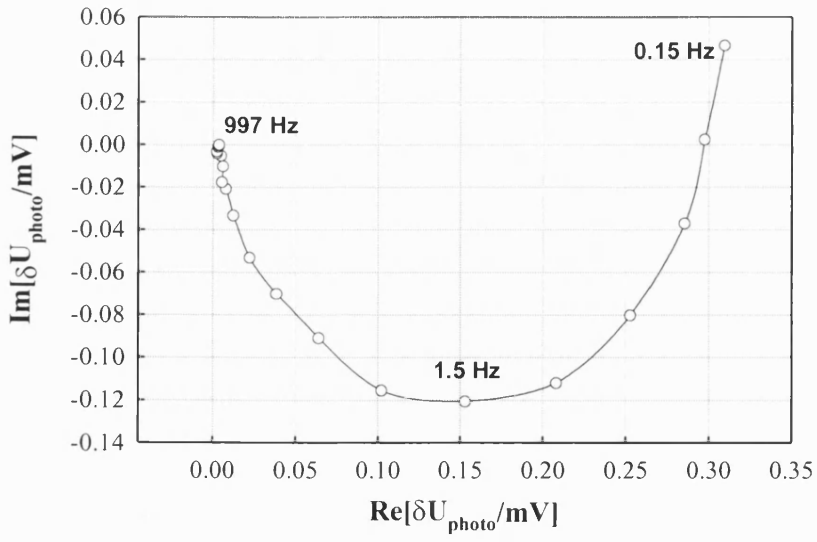

Figure 8.8 *A typical IMVS response obtained for a TiO_2/N3 dye/PANI photovoltaic cell.*

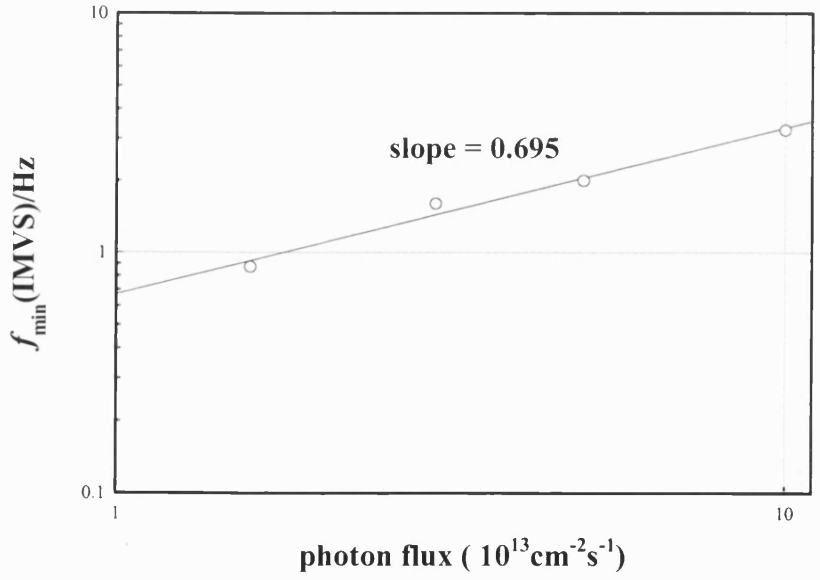

Figure 8.9 *Double logarithmic representation of variation of ω_{min}(IMPS) and ω_{min}(IMVS) with incident photon flux in TiO_2/N3 dye/PANI photovoltaic cell.*

8.3 Conclusions

Two solid state versions of dye sensitised photovoltaic cells were fabricated and electron transport properties and recombination kinetics were studied. In the n-TiO_2/N3 dye/p-CuI solar cell, the electron transport in TiO_2 phase occurs on a similar time scale to that observed in its liquid junction counterpart. Electron transport in the TiO_2 phase and hole transport in the CuI phase are dominated by trapping, leading to strong intensity dependent apparent diffusion coefficients. In addition to the proposed charge transfer mechanism, other different routes (such as ionic transport in CuI) may also be involved in this device. Internal shunting appears limit the dye sensitised solid state TiO_2/N3 dye/CuI photovoltaic cell performance. Further work is needed to optimise the three way contact TiO_2/dye/CuI (such as employing a blocking layer) to retard the electron-hole recombination at TiO_2/CuI junction. Other p-type semiconductor materials are also need to be tested for the filling of 3-dimensional dye sensitised nanocrystalline TiO_2 network.

In the TiO_2/N3 dye/PANI photovoltaic cell, further work is needed to optimise the cell performance and to explore the reason for the steep photocurrent drop at the beginning of negative voltage polarisation. The variation of the electron transfer rate at different trapped electron energy levels (i.e. at different ${}_nE_F$ in TiO_2) could be the reason for the observed intensity dependent $\omega_{min}(IMVS)$ in this device.

8.4 References

1. F. Cao, G. Oskam, and P. C. Searson, Journal of Physical Chemistry 99:17071 (1995).
2. K. Tennakone, G. Kumara, A. R. Kumarasinghe, K. G. U. Wijayantha, and P. M. Sirimanne, Semiconductor Science and Technology 10:1689 (1995).
3. B. Oregan and D. T. Schwartz, Journal of Applied Physics 80:4749 (1996).
4. K. Tennakone, G. Kumara, and K. G. U. Wijayantha, Semiconductor Science and Technology 11:1737 (1996).
5. J. Hagen, W. Schaffrath, P. Otschik, R. Fink, A. Bacher, H. W. Schmidt, and D. Haarer, Synthetic Metals 89:215 (1997).

6. K. Tennakone, G. Kumara, K. G. U. Wijayantha, I. R. M. Kottegoda, V. P. S. Perera, and G. Aponsu, Journal of Photochemistry and Photobiology a-Chemistry 108:175 (1997).
7. K. Tennakone, G. Kumara, I. R. M. Kottegoda, and K. G. U. Wijayantha, Semiconductor Science and Technology 12:128 (1997).
8. U. Bach, D. Lupo, P. Comte, J. E. Moser, F. Weissortel, J. Salbeck, H. Spreitzer, and M. Gratzel, Nature 395:583 (1998).
9. K. Murakoshi, R. Kogure, Y. Wada, and S. Yanagida, Solar Energy Materials and Solar Cells 55:113 (1998).
10. B. Oregan and D. T. Schwartz, Chemistry of Materials 10:1501 (1998).
11. K. Tennakone, G. Kumara, I. R. M. Kottegoda, K. G. U. Wijayantha, and V. P. S. Perera, Journal of Physics D-Applied Physics 31:1492 (1998).
12. K. Tennakone, G. Kumara, K. G. U. Wijayantha, I. R. M. Kottegoda, V. P. S. Perera, and G. Aponsu, Semiconductor Science and Technology 13:134 (1998).
13. J. Kruger, U. Bach, and M. Gratzel, Advanced Materials 12:447 (2000).
14. D. Wohrle and D. Meissner, Advanced Materials 3:129 (1991).
15. G. Yu and A. J. Heeger, Journal of Applied Physics 78:4510 (1995).
16. J. J. M. Halls, C. A. Walsh, N. C. Greenham, E. A. Marseglia, R. H. Friend, S. C. Moratti, and A. B. Holmes, Nature 376:498 (1995).
17. G. Wang, S. Qian, J. Xu, W. Wang, X. Liu, X. Lu, and F. Li, Physica B 279:116 (2000).
18. J. Kido, K. Hongawa, K. Okuyama, and K. Nagai, Applied Physics Letters 63:2627 (1993).
19. G. Schlichthorl, N. G. Park, and A. J. Frank, Journal of Physical Chemistry B 103:782 (1999).
20. G. Schlichthorl, S. Y. Huang, J. Sprague, and A. J. Frank, Journal of Physical Chemistry B 101:8141 (1997).